Ekman transport : a trigger of interannual extreme formation rates of eighteen degree water

Ke Li

DOCTORAT SCIENCES BRETAGNE DE LA MER LOIRE ET DU LITTORAL

UBO Université de Bretagne Occidentale

THESE DE DOCTORAT DE

L'UNIVERSITE
DE BRETAGNE OCCIDENTALE

ECOLE DOCTORALE N° 598
Sciences de la Mer et du littoral
Spécialité : Océanographie Physique et Environnement

Par **Ke LI**

Le transport d'Ekman comme déclencheur des extrêmes de formation de l'Eau Modale à 18 degrés aux échelles de temps interannuelles

Thèse présentée et soutenue à Brest, le 15 Décembre 2020
Unité de recherche : IFREMER, Laboratoire d'Océanographie Physique et Spatiale (LOPS), IUEM

Rapporteurs avant soutenance:

LAZAR, Alban	Maître de conférences, Université Pierre et Marie Curie - Paris 05ème
REVERDIN, Gilles	Directeur de Recherche, Université Pierre et Marie Curie - Paris 05ème

Composition du Jury:

Président:	CARTON, Xavier	Professeur des universités, Université de Bretagne Occidentale - Plouzané
Examinateurs:	SPEICH, Sabrina	Professeur des universités, Ecole Normale Supérieure - Paris 05éme
	TREGUIER, Anne-Marie	Directrice de Recherche, Université de Bretagne Occidentale - Plouzané
	LAZAR, Alban	Maître de conférences, Université Pierre et Marie Curie - Paris 05ème
	REVERDIN, Gilles	Directeur de Recherche, Université Pierre et Marie Curie - Paris 05ème
Dir. de thèse:	MERCIER, Herlé	Directeur de Recherche, IFREMER-Centre de Bretagne - Plouzané
Co-dir. de thèse:	MAZE, Guillaume	Chercheur, IFREMER-Centre de Bretagne - Plouzané

Invité:

KOLODZIEJCZYK, Nicolas	Chercheur, Université de Bretagne Occidentale - Plouzané

Ekman transport: a trigger of interannual extreme formation rates of Eighteen Degree Water

BY

Ke LI

M.Sc. in Atmospheric and Oceanic Sciences, University of Wisconsin-Madison, 2013
B.Eng., University of Science and Technology of China, 2007

THESIS

Submitted to the University of Brest
in partial fulfillment of
the requirements for the degree of

Doctor of Philosophy

in

Physical Oceanography and Environment

December 15th, 2020

Readers before dissertation defense:

LAZAR, Alban	Lecturer, Pierre and Marie Curie University - Paris
REVERDIN, Gilles	Research Director, Pierre and Marie Curie University - Paris

Examining Board:

Chair:	CARTON, Xavier Professor, University of Brest - Plouzane
Examiners:	SPEICH, Sabrina Professor, Ecole Normale Superieure - Paris
	TREGUIER, Anne-Marie Research Director, University of Brest - Plouzane
	LAZAR, Alban Lecturer, Pierre and Marie Curie University - Paris
	REVERDIN, Gilles Research Director, Pierre and Marie Curie University - Paris
PhD Supervisor:	MERCIER, Herlé Research Director, IFREMER Center of Brittany - Plouzane
PhD Supervisor:	MAZE, Guillaume Research Fellow, IFREMER Center of Brittany - Plouzane

Invited examiner:

KOLODZIEJCZYK, Nicolas	Research Fellow, University of Brest - Plouzane

Table of Contents

CHAPTER 1

INTRODUCTION

The upper 1000m subtropical gyre in the North Atlantic region has been experiencing warming since 1970s (Rhein et al., 2018). In the North Atlantic subtropical region, the eighteen degree water (EDW) is found to have the largest heat capacity. Sugimoto et al. (2017) demonstrated that since the 1970s the warming rate of EDW is about 1.31 ± 0.14^{o}C per century, and there is a decreasing trend of dissolved oxygen in EDW.

1.1 North Atlantic subtropical stratification

The EDW is the nearly homogeneous water body found in the western subtropical North Atlantic region. The EDW was named after the fact that it maintains a nearly constant temperature around 18^{o}C. In summer, the EDW is between the seasonal pycnocline and the permanent pycnocline. In the wintertime, the EDW gets ventilated to the surface through the outcropping area. The EDW consists of two types according to their disparate formation dynamics (Joyce, 2011). The first type is the EDW formed near the northern Sargasso Sea, ($73 - 63^{o}$W, 35^{o}N). This type of EDW is away from strong advections and cooling associated with the Gulf Stream. The second type is the EDW formed within frontal region of the Gulf Stream, centered at 55^{o}W. The formation of this type of EDW is predominantly influenced by the vorticity of the flow and cross-frontal mixing. For this reason, this type of EDW is fresher and colder than EDW formed at the northern Sargasso Sea. Based on these two types, Joyce (2011) presented the EDW formation dynamics that involves strong advection, air-sea cooling and cross-front entrainment, as well as the non-advective point of view of EDW formation (Warren, 1972).

In general the EDW bulk volume experienced a decrease since 2010 (Stevens et al., 2020). The EDW formation extreme years are documented as the following: the strong EDW formation winters are 2004-2005, 2009-2010, and the weak EDW formation winters are 2007-2008, 2011-2012, 2013-2014, and 2014-2015 (Billheimer and Talley, 2016a, 2013, 2016b). However, to identify these extreme years, most of the research has used either modeling or sparse observational datasets. The robustness

of these EDW formation extreme years needs to be examined. **First of all, we aim to determine occurrences of the EDW formation extreme years using more various datasets.** We will address this question in detail in Section 4.3.1 and Section 4.3.3.

Billheimer and Talley (2013, 2016b) addressed that a strong (weak) EDW formation extreme winter is correlated with a strong negative (positive) wintertime NAO. Peng et al. (2006) used modeling indicating a lagged correlation between NAO and EDW annual subduction rate at Panulirus station. The Panulirus station (32°10′N, 64°30′W) is near Bermuda, southwestern part of the Sargasso Sea. The lag is 2-3 years with NAO leading. **We aim to investigate the atmospheric patterns that correspond to the extreme occurrences of EDW renewal.** We will address this question in detail in Section 4.3.5, Section 4.3.6, and Section 4.3.7.

1.1.1 EDW subduction and obduction

To properly give measure to the EDW formation, we need to understand some of the complex but important processes associated with EDW. The subduction is the process by which a water parcel that leaves the mixed layer enters the main pycnocline definitively (Marshall et al., 1993; Qiu and Huang, 1995; Williams, 2001; Williams et al., 1995). The subduction takes place in late spring at the subtropical basin in the North Atlantic (Figure 7c in Qiu and Huang 1995; Marshall et al. 1993; Williams et al. 1995). Qiu and Huang (1995) showed that the subduction rate is dominated by the lateral induction in the subtropical basin. Marshall et al. (1993) showed that the subduction in the subtropical gyre is mainly due to the horizontal advection of fluid into the thermocline at the southern flank of the Gulf Stream.

The obduction is the effective entrainment of fluid that originally comes from the permanent pycnocline into the mixed layer (Qiu and Huang, 1995). The obduction occurs when the mixed layer deepens, for example, during late fall to end of winter, mainly in the subpolar basin and the subpolar-subtropical border (Figure 7f, Qiu and Huang 1995). They stressed that obduction is not just a reverse of subduction, but rather, is a completely different physical process that brings water from the permanent pycnocline to the mixed layer.

In short, the EDW renewal in the early spring can be influenced by the EDW obduction, the EDW subduction, and the EDW formation. The early spring EDW ventilation to the sea surface forms fresh EDW. In addition, the EDW ventilation bridges the obduction (coming from the north of the EDW bulk) and the subduction (associated with the subtropical gyre). **In this thesis, we aim to thoroughly determine and analyze a robust time series of freshly ventilated EDW**

volume. We will review how EDW can be identified and we will address in detail how we give measure to the freshly ventilated EDW volume in Section 2.5.

1.1.1.1 Subduction at southern flank of EDW bulk

Marshall et al. (1993) with their Equation (3) estimated the EDW subduction rate at the bottom of the winter mixed layer. They attributed the subduction rate to the vertical velocity across the mixed layer depth and the lateral induction advecting the mixed layer depth horizontal gradient:

$$S_{\text{ann}} = -\left(\bar{w}_{\text{Ek}} - \frac{\beta}{f}\int_{-H}^{0} \bar{v}dz\right) - \bar{\mathbf{u}}_{\text{H}} \cdot \nabla H \tag{1.1}$$

where H denotes the mixed layer depth, S_{ann} denotes the annual subduction rate, $\bar{w}_{\text{Ek}}$ is the averaged Ekman vertical velocity at the mixed layer depth, and $\bar{u}$ denotes the horizontal velocity field that advects the horizontal gradient of mixed layer depth. $\bar{\mathbf{u}}_{\text{H}} \cdot \nabla H$ is the lateral induction term (Figure 1-1b). Marshall et al. (1993) found the lateral induction term at the bottom of the mixed layer the dominant term to the annual subduction rate (Figure 1-1a).

Maze et al. (2013) investigated the EDW formation region using the flux form of the potential vorticity equation (Marshall et al., 2001; Marshall and Nurser, 1992; Maze and Marshall, 2011). The rate of change of PV integrated from surface to the mixed layer depth is attributed to: 1. the PV advection by the horizontal velocity, 2. the diabatic forcing associated with air-sea surface heat fluxes, 3. the mechanical forcing associated with the wind stress inducing Ekman-driven convection. Their assumptions are: 1. the isopycnal surfaces are impermeable to the PV, and 2. the pressure distribution follows the isopycnals, eliminating the thermobaric term (See Equation. 11 in Marshall et al., 2001). The Ekman-driven convection is associated with the along front wind stress interacting with the cross-front density gradient (Joyce et al., 2009; Thomas, 2005; Thomas and Lee, 2005).

The PV is mainly extracted at the northern flank of the EDW bulk, and to the south of the Gulf Stream, through air-sea surface heat loss (Maze and Marshall, 2011). Maze et al. (2013) found that the diabatic forcing associated with the air-sea heat loss is the dominant signal among all the examined terms. This air-sea heat loss is found close to the core of the Gulf Stream.

Maze et al. (2013) showed that the Ekman-driven convection 3-year mean overlaps with the EDW bulk, where its thickness is $> 300\,\text{m}$ (Figure 1-2). The EDW subduction dominated by the lateral induction occurs at the southern edge of the EDW bulk area. This can be observed by comparing the black solid contours in Figure 1-1b and

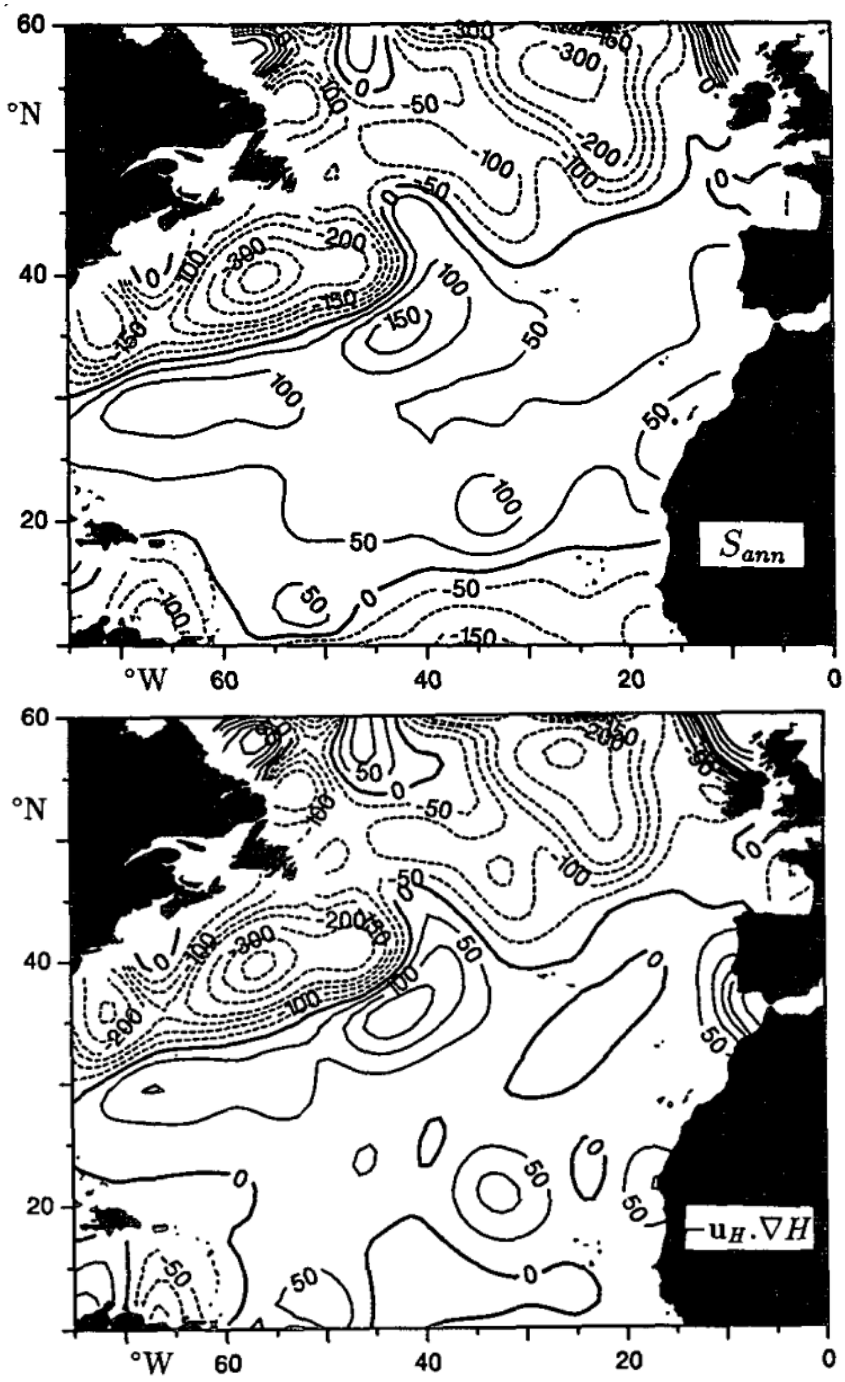

Figure 1-1: (a) Annual subduction rate $S_{\rm ann}$, in the unit of $\mathrm{m\,yr^{-1}}$. Positive values are in solid contours indicating an subduction, going into the thermocline. Negative values are in dashed contours, indicating the entrainment coming from the thermocline into the mixed layer. (b) Annual lateral flux, $-\bar{\mathbf{u}}_{\rm H} \cdot \nabla H$, in the unit of $\mathrm{m\,yr^{-1}}$. Positive (negative) values are in solid (dashed) contours indicating the flux going into (coming from) the thermocline. Source: Marshall et al. (1993)

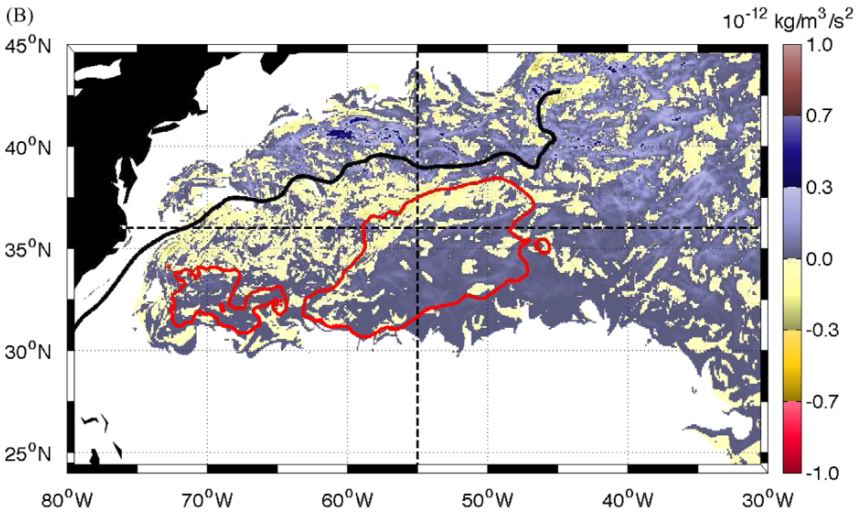

Figure 1-2: Climatological mean (2003-2006) of PV anomaly due to the mechanical forcing associated with the Ekman-driven convection. It is "lagrangian-like", following the EDW outcrop. It shows where lateral Ekman heat fluxes trigger convection in the EDW layer. The solid red line denotes the 300 m EDW mean thickness. The thick black line denotes the Gulf Stream position. Source: Fig. 6b in Maze et al. (2013)

the red contours in Figure 1-2. Marshall et al. (1993) showed that the core of strong subduction is located within the zonal area of $30^o - 35^o$N, south-southeast of the zero subduction contour from 75°W,30°N to 40°W,40°N (the thick black contour in Figure 1-1a). Kelly and Dong (2013) located the subduction region to the south of the EDW formation region (Fig.3c), $27^o - 32^o$N, $75^o - 55^o$W. Qu et al. (2016) observed that the subduction takes place to the east of the EDW formation areas (Fig. 4a), in the northern Sargasso Sea region (32°N, $60^o - 70^o$W), as well as to the southern flank of the Gulf Stream (35°N, $45^o - 55^o$W).

1.1.1.2 Subduction estimates

Liu and Huang (2012) provided a detailed review on the global estimates of subduction/obduction performed since last few decades. To compute the subduction rate, the "Stommel's demon" (Stommel, 1979) was employed by the early literatures (see e.g., Huang 1990; Marshall and Nurser 1991; Marshall et al. 1993; Pedlosky and Robbins 1991; Williams 1989, 1991; Williams et al. 1995). They used the end of winter mixed layer depth and the annual mean circulation to compute the subduction rate. However, they did not consider a seasonally varying mixed layer depth.

Many ocean state variables played a role to the subduction in the subtropical North

Atlantic. Qu et al. (2016) showed the cold (warm) SST anomaly plays a favorable (unfavorable) role to the lateral induction in Subtropical Underwater. Regarding the Subtropical Mode Water, Qu et al. (2016) observed in winter 2010, a negative SST anomaly in the EDW formation region (Fig.11c). However, they did not directly address the EDW subduction. Dong et al. (2007); Kelly and Dong (2013) employed in their model the southward geostrophic advection between the formation region and subduction region as the proxy of the EDW subduction.

Nowadays, many studies use a seasonally varying mixed layer depth and define an annual subduction/obduction rate, depending on the sign of the net rate, as the sum of entrainment into the mixed layer and detrainment out of the mixed layer (Da Costa et al., 2005). In this case people simply drop the idea of "permanently entering the main pycnocline" because it is not necessary anymore. The water that enters the mixed layer is explicitely quantified and removed from the subduction rate. **We aim to understand how subduction has an impact on the freshly ventilated EDW volume on an interannual time scale?** We will discuss this question in detail in Section 4.4.5.

1.1.2 Air-sea heat fluxes

The atmospheric state can impact the ocean through air-sea heat fluxes. Grist et al. (2016) showed that strong winter storms drive large latent and sensible heat fluxes. Piron et al. (2017) showed strong near surface wind drives large air-sea surface heat fluxes in the subpolar region. The ocean state can also impact the air-sea heat fluxes. Dong and Kelly (2004) showed that strong geostrophic heat advection drives strong air-sea surface heat loss.

The EDW is primarily formed to the west of 45°W, between the Gulf Stream and 30°N (Maze et al., 2009). In this region, the air-sea heat flux in EDW is the key driving mechanism in the seasonal time scale (Forget et al., 2011; Maze et al., 2009). Maze et al. (2009) used Argo profiles and the model-interpolated data to quantify the EDW production and destruction through air-sea heat fluxes. They showed that in a typical seasonal cycle, intense winter surface buoyancy loss leads to the outcropping of EDW, which is replenished during this period. In the spring, surface buoyancy flux destroys the EDW. In addition, they reported that the annual EDW formation rate is about $3-5\,\mathrm{Sv}$ (Sverdrup, $1\,\mathrm{Sv} = 1\times10^6\,\mathrm{m}^3$). Forget et al. (2011) examined the EDW production through its volume inventories and air-sea heat fluxes. They showed that in a typical seasonal cycle, the EDW formation rate is dominated by air-sea heat fluxes. They reported that the typical seasonal cycle of EDW overall volume has an amplitude of $8.6\,\mathrm{Svy}$. Each year, the EDW formation due to air-sea heat fluxes is

9.3 Svy. The EDW destruction due to air-sea heat fluxes is −4.6 Svy, and that due to mixing is −2.6 Svy. The net EDW formation each year due to air-sea heat fluxes and mixing is 2.0 Svy, which balances the annual increase of EDW, about 1.4 Svy, and the annual export of EDW, about 0.6 Svy. **We aim to examine whether air-sea heat fluxes are still dominant on the EDW early spring freshly ventilated volume.** We will address this question in detail in Section 4.3.5, 3.3.3, and 3.3.8.

1.1.3 Geostrophic heat advection

On interannual time scales, the geostrophic heat advection is found to be the lead driving force to the subtropical stratification in the North Atlantic subtropical region (Dong and Kelly, 2004). They investigated the roles of geostrophic heat advection associated with the Gulf Stream and air-sea heat fluxes. Subsequently, an algorithm developed in-house was employed to close the heat budget (Dong et al., 2007); however, the usage of historical datasets in the 1990s in their research is not without limits. Roemmich et al. (1999) reported that the ship-of-opportunity based expendable bathythermograph (XBT), developed in the 1960s, limited to the ship lanes and the season, shows coarse spatial and time coverage. In addition, the World Ocean Circulation Experiment (WOCE) developed in the 1990s suffers from sparse spaial coverage, despite the high data quality. The modern datasets based on Argo floats provide more synoptic and pertinent observations of the ocean. Argo floats, being self-drifting devices independent from ship trajectories, overcome some limitations from XBT and WOCE. Moreover, Argo floats evolved from the aforementioned subsurface measuring methods with large spatial coverage and extent, depth and accuracy (Roemmich et al., 1999). Additionally, Dong and Kelly (2004) acknowledged that there are some limitations of the air-sea heat fluxes. They reported an overestimation on the ocean surface heat loss, mainly due to latent heat fluxes (Vivier et al., 2002; Zeng et al., 1998). Fairall et al. (2003) made several changes in the Coupled Ocean–Atmosphere Response Experiment (COARE) bulk algorithm. They corrected the air-sea fluxes for wind speeds exceeding $10\,\mathrm{m\,s^{-1}}$. Yu and Weller (2007) highlighted that progress has been made on air-sea heat constraint estimates after Dong and Kelly (2004), especially on the estimates of latent and sensible heat fluxes. We need to challenge the result of Dong and Kelly (2004) using modern observational datasets. **Given better balanced air-sea heat fluxes than in the early 2000s, we aim to examine, in the subtropical gyre, whether the geostrophic advection is the driving force to the interannual variability of upper ocean heat content (OHC).** We will address this question in detail in Section 3.3.3, Section 3.3.4, Section 3.3.6, and Section 3.3.7.

1.1.4 Ekman current

In multi-decadal time scales, the Ekman current is found to be the lead driving force to the North Atlantic subtropical stratification (Seidov et al., 2018). 2009-10 is a special period, featuring a rapid slowdown of AMOC at 26°N, with the volume transport reduced by 30% (5.6 Sv) over a 15-month period (Bryden et al., 2019, 2014; Häkkinen et al., 2013; McCarthy et al., 2012). Evans et al. (2017) showed this reduction in AMOC corresponds with shoaling of isotherms due to Ekman pumping. The associated heat transport integrated in time over the anomaly is reduced by 14.5 ZJ at 26°N. Bryden et al. (2014) showed that this heat reduction matches the decrease of 13.5 ZJ in upper 1000-m OHC anomaly in the domain of $25-45$°N and $60-20$°W during the same period. On interannual time scales, Evans et al. (2017) showed that the variabilities of both Ekman pumping and thermocline depth are strongly correlated, driving the volume transport anomalies at the subtropical gyre. The horizontal Ekman advection is a buoyancy sink term in the subtropical North Atlantic region, associated with southward advection of cold subpolar surface water (Billheimer and Talley, 2013; Thomas, 2005; Thomas et al., 2013). However, in the study of Billheimer and Talley (2013); Dong and Kelly (2004), the horizontal Ekman advection is within the error bar, thus it is considered negligible on interannual time scales. **We aim to examine if the Ekman current plays an important role in the North Atlantic subtropical stratification on the interannual time scales, particularly during extreme weather events.** We will address this question in detail in Section 4.3.6.

1.1.5 Mesoscale eddies at the Gulf Stream northern flank

The mesoscale eddies at the northern flank of the Gulf Stream can form EDW through surface subduction. At the northern flank of the Gulf Stream, the subduction of EDW occurs at the upper stream part of the meandering trough (the cross-section line 2 in Figure 1-3 and its corresponding vertical velocity field in Figure 1-4 left, Thomas and Joyce, 2010) .

The subduction also takes place underneath the front at the downstream part of the meandering trough (the cross-section line 4 in Figure 1-3 and its corresponding vertical velocity field in Figure 1-4 right, Thomas and Joyce, 2010) .

Using the classic Omega equation to investigate the subduction rate has been done in several studies (Thomas and Joyce, 2010). We rewrote the Equation (1) in Thomas

and Joyce 2010 as an example:

$$f^2\frac{\partial u_{\mathrm{ag}}}{\partial z} - N^2\frac{\partial w}{\partial x_s} = 2\left(\frac{\partial u_{\mathrm{g}}}{\partial x_s}\frac{\partial b}{\partial x_s} + \frac{\partial v_{\mathrm{g}}}{\partial x_s}\frac{\partial b}{\partial y_s}\right) \tag{1.2}$$

where u_{ag} and u_{g} denote the ageostrophic and geostrophic components of the along-front velocity; w is the vertical velocity; x_{s} and y_{s} are the across-front and along-front axes respectively (Figure 1-3). On the LHS, the term $N^2\partial w/\partial x_{\mathrm{s}}$ denotes the across-front horizontal gradient of the vertical velocity tilting (or flattening) the isopycnals. The term $f^2\partial u_{\mathrm{ag}}/\partial z$ denotes the the vertical shear of the across-front ageostrophic velocity tilting (or flattening) the isopycnals.

On the right hand side, the first term, $(\partial u_{\mathrm{g}}/\partial x_{\mathrm{s}})(\partial b/\partial x_{\mathrm{s}})$ positive (negative) denotes the horizontal confluent (difluent) flow by the along-front velocity, "squeezing" ("relaxing") the horizontal isopynals, promoting frontogenesis (frontolysis). The second term $(\partial v_{\mathrm{g}}/\partial x_{\mathrm{s}})(\partial b/\partial y_{\mathrm{s}})$ signifies the horiziontal shearing of the isopycnals by the along-front velocity. When this term is positive, that signifies the tightening of isopycnals, promoting frontogenesis, and negative for promoting frontolysis.

The Omega equation was firstly employed in meteorology to understand the formation of a storm front associated with a meso-scale atmospheric cyclone. Typically, when the front passes, the warm air rises and cold air sinks, forming a thermally direct process. This process is expressed in the term $N^2\partial w/\partial x_{\mathrm{s}}$. This thermally direct process corresponds with the geostrophic confluent flow "squeezing" the isopycnals, expressed in the term $(\partial u_{\mathrm{g}}/\partial x_{\mathrm{s}})(\partial b/\partial x_{\mathrm{s}})$.

Note that Thomas and Joyce (2010) only considered the part of the subduction ascribable to the adiabatic process. Equation 1.2 should have included a term that describes the diabatic heating, which can be written as:

$$\frac{\partial}{\partial x_{\mathrm{s}}}\frac{Db}{Dt} \tag{1.3}$$

This term is important in the mesoscale/sub-mesoscale meteorology (Chapter 7 "the Vertical Circulation at Fronts" in Martin, 2013). Imagine a summer thunderstorm passing. The x_{s} is the across-front axis pointing towards the warmer side. On the warmer side of the associated front, ascending air forming precipitation releases latent heat, $\frac{\partial}{\partial x_{\mathrm{s}}}\frac{Db}{Dt} > 0$. The warm air ascending more rapidely, this promotes frontogenesis. If applied to the Gulf Stream, this terms would be associated with the across-front gradient of the air-sea surface heat loss. If the Gulf Stream frontal region loses more heat than the its northern flank, $\frac{\partial}{\partial x_{\mathrm{s}}}\frac{Db}{Dt} < 0$. This promotes frontolysis, undermining the northern flank subduction due to the ageostrophic flow, This can be another reason that Thomas and Joyce (2010) overestimated the subduction rate.

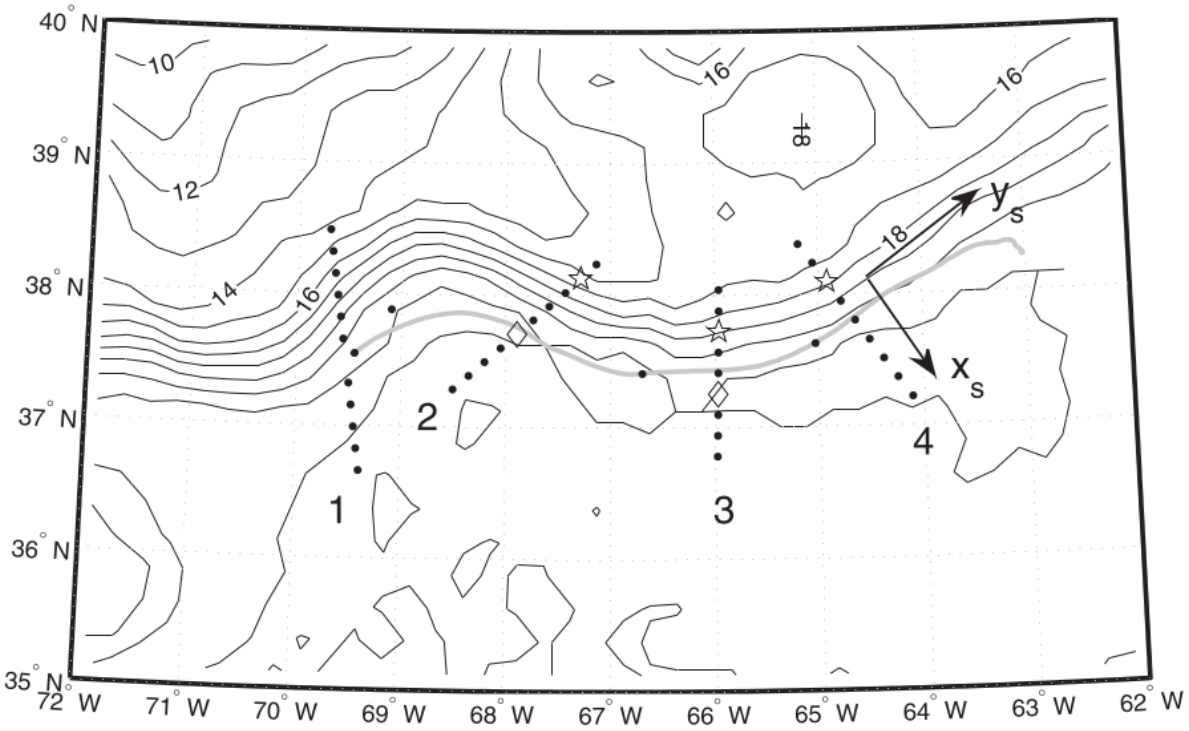

FIG. 1. The SST (contours) on 24 Jan 2006 and the locations of the hydrographic stations (dots) occupied during the cruise. Stations where a thermohaline intrusion was observed (i.e., 22, 31, and 41 on lines 2, 3, and 4, respectively) are denoted with stars. Stations where a pycnostad was observed on the southern edge of the Gulf Stream (i.e., 18 and 28 on lines 2 and 3, respectively) are denoted with diamonds. The contour interval for the SST is 1°C. The thick gray line marks the trajectory of the spar buoy. The arrows indicate the direction of the cross-stream x_s and along-stream y_s coordinates.

Figure 1-3: Source: Thomas and Joyce (2010)

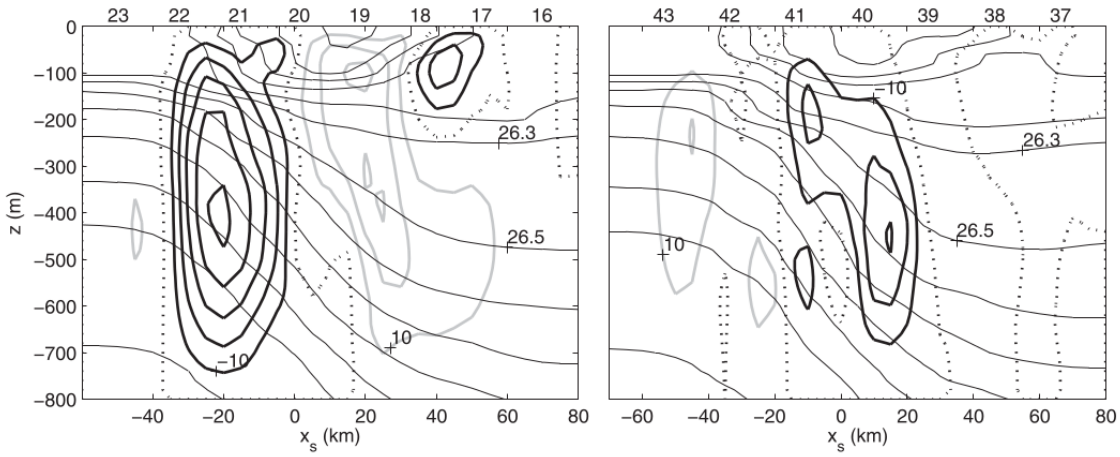

FIG. 6. The inferred vertical velocity along lines (left) 2 and (right) 4. Thick black, gray, and dashed contours denote negative, positive, and zero values for the vertical velocity, respectively. The contour interval for w is 10 m day^{-1}. The potential density is shown (thin contours) at an interval of 0.2 kg m^{-3}.

Figure 1-4: Source: Thomas and Joyce (2010)

1.1.6 Mesoscale/submesoscale eddies at the southern flank

The Gulf Stream interacts with the EDW subduction, through mesoscale, submesoscale eddies (Williams et al., 1995). They found that the eddy stirring enhances the subduction rate. The baroclinic instability serves to transform available potential energy (APE) from the Gulf Stream to eddy kinetic energy (EKE) of mesoscale eddies (Thomas et al., 2013). Thomas et al. (2013) addressed that the PV associated with baroclinicity of a water column is always negative, and that strong baroclinicity corresponds with more negative PV. Herbette et al. (2004) showed that the anticyclonic eddies with negative PV enter underneath a front through baroclinic instability. They showed that the strong dissipation is able to fully consume the subducted low PV eddies.

The baroclinic instability works to restratify the mixed layer and creates mesoscale eddies. There is a transfer from the potential energy, associated with the slope of isopycnal, to eddies. The baroclinic instability of the Gulf Stream results in the formation of cold-core rings for this region south of the Gulf Stream (Figure 1-5, or Fig. 2a in The Ring Group 1981). These cold-core rings are more stratified and colder than its surrounding in the Sargasso Sea (Figure 1-5b, or Fig. 2b in The Ring Group, 1981). In these cyclonic (counterclockwise) cold-core eddies dense water is found closer to the surface and the thickness of the EDW is reduced to close to zero. Kang and Curchitser (2013) showed that the baroclinic instability associated with the

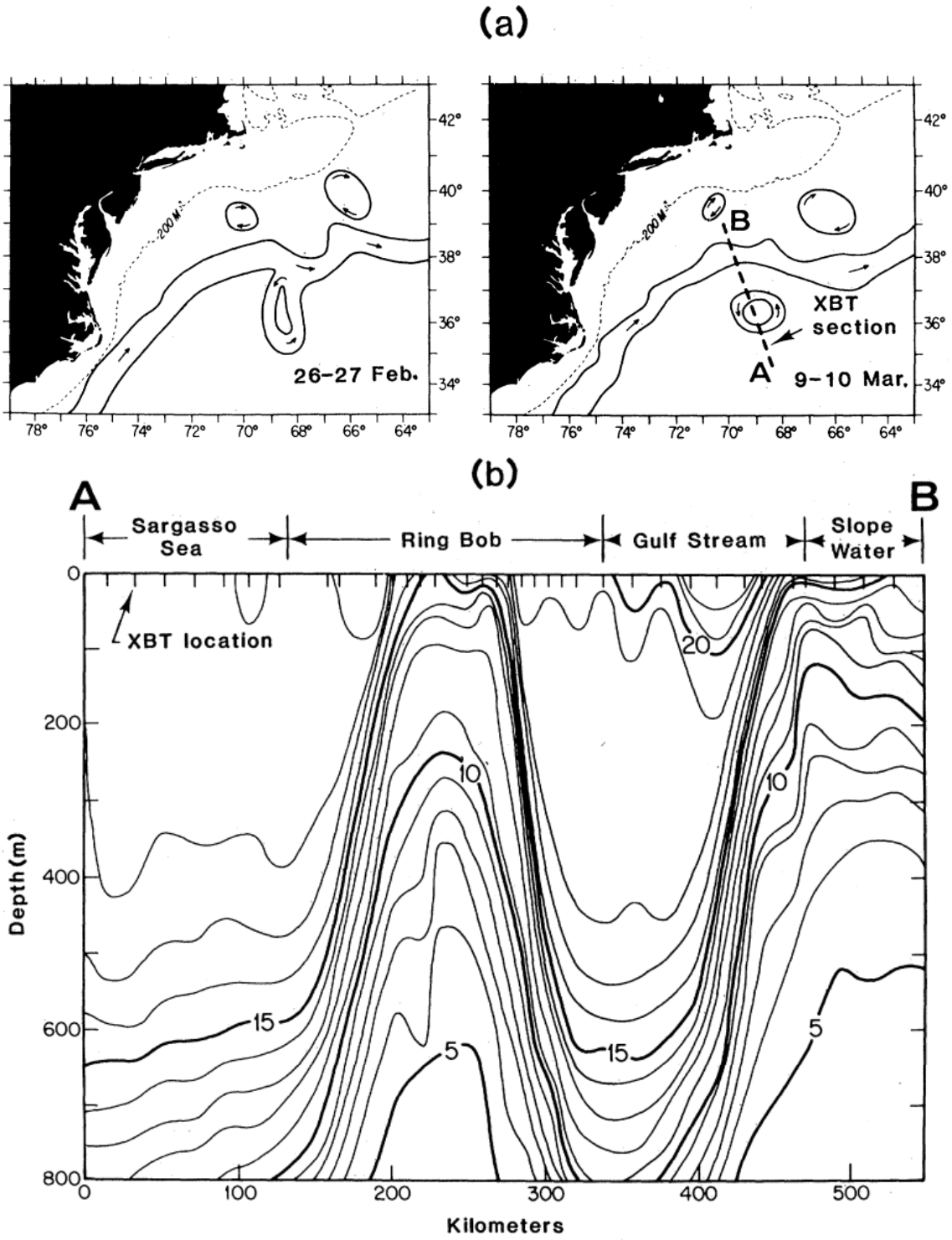

Fig. 2. (a) Diagrams showing the formation of cyclonic Gulf Stream ring Bob in February–March 1977 based on infrared images from the NOAA-5 satellite. Two anticyclonic (warm-core) rings were observed north of the Gulf Stream. (b) Vertical temperature section through ring Bob and the Gulf Stream on 12 March 1977. Ring Bob can be seen as the area of raised isotherms and cool surface temperatures.

Figure 1-5: Source: The Ring Group (1981)

Gulf Stream reaches its seasonal maximum in strength in early spring (March), when the upper thermocline near the Gulf Stream is the most tilted. The eddy kinetic energy at the southern flank of the Gulf Stream reaches seasonal maximum in spring / early summer (Fig. 13 in Kang and Curchitser, 2013). Maze and Marshall (2011) showed in their Fig 5c that in summer (June) the PV flux at the northwest part of the Sargasso Sea, south of the Gulf Stream is the strongest. They addressed that this summer strong PV flux is associated with vigorous mesocale eddies. Callies and Ferrari (2018) showed that even in the winter time, in the presence of convection, the baroclinic instability can still take place, serving as a buoyancy source. They stressed that the mixed layer baroclinic instability can still persist through the strong convection in the winter time, generating submesoscale turbulence in the mixed layer.

Of the submesoscale processes, the Symmetric Instability is found in the Gulf Stream region, penetrating down to 100-200m in depth (Thomas et al., 2013). The water column with strong enough baroclinicity would have a PV negative enough to overbalance the PV due to vertical stratification, susceptible to a Symmetric Instability (Thomas et al., 2013). They defined the Richardson number (Ri) as the ratio between the PV due to vertical stratification and the absolute value of PV due to baroclinicity. When Ri < 1, the water column is symmetrically unstable. Capuano et al. (2018) investigated the Agulhas Rings mode water formation and subduction in the southern Atlantic region. They found that in winter, the convective instability prevails, the Symmetric Instability (Ri < 1), associated with a front (the western boundary current, in this case, the Agulhas Current) in summer, and the baroclinic instability (Ri > 1) between the two seasonal regimes.

The meridional heat transport due to mesoscale / submesoscale eddies is important, making up 1/4-1/3 of the total meridional heat transport at the Gulf Stream extension region (Hecht and Smith, 2009; Smith et al., 2000; Tréguier et al., 2012). This eddy heat transport at 36.6°N is about 0.3 PW on average, with the strongest at the cross-section of coast-70°W, reaching 0.5 PW (Figure 1-7 or Fig. 4b in Tréguier et al., 2017). This eddy heat transport can penetrate to a depth of 500 m. It is deep enough to allow these mesoscale / submesoscale eddies interacting with the EDW bulk (The red contour in Figure 1-2 or Fig. 6b in Maze et al., 2013).

The meridional heat advection due to geostrophic velocity comprises the part due to the mean and the part due to the eddies (See details in Equation 1 in Tréguier et al., 2017):

$$\overline{VT} = \overline{\bar{V}\bar{T}} + \overline{V'T'} \tag{1.4}$$

where, V denotes the meridional geostrophic velocity, and T denotes the temperature. V' and T' are the fluctuations of velocity and temperature due to eddies. $\overline{V'T'}$ denotes

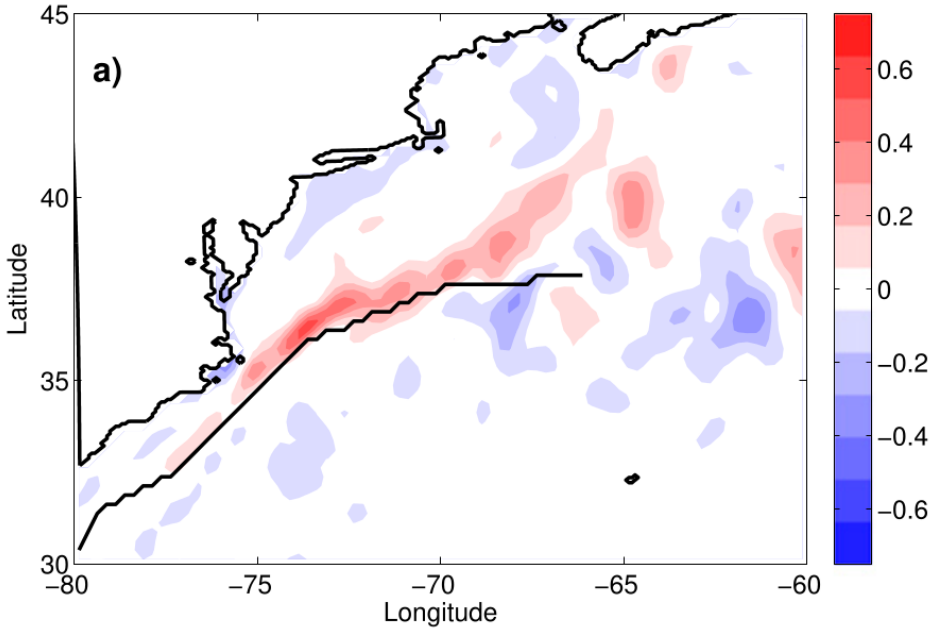

Figure 1-6: 2003-2012 averaged surface eddy heat flux $\overline{V'T'}$ in Equation 1.4 at the Gulf Stream region, in the unit of $^{o}\mathrm{C\,m\,s^{-1}}$, calculated based on observational datasets. Source: (Tréguier et al., 2017)

the eddy heat flux at the ocean surface.

Tréguier et al. (2017) calculated the eddy heat flux at the ocean surface according to Equation 1.4. Figure 1-6 shows the map of this surface eddy heat flux. The 10 year mean (2003-2012) shows large northward heat transport due to eddies along the northern flank of the Gulf Stream (75°W,35°N - 67°W, 38°N), as well as negative surface eddy flux centered at 67°W, 36°N and at 63°W, 36°N. These patches of cooling due to mesoscale/submesoscale eddy heat flux are at the northern flank of the EDW bulk (Figure 1-2 or Fig. 6b in Maze et al., 2013). **We aim to further discuss the role of the mesoscale / submesoscale eddies in the EDW formation.** We will address this question in detail in Section 3.4.2.

1.2 Air-sea coupling near Gulf Stream

The upper ocean mixed layer responds to atmospheric events with a persisting memory. Frankignoul and Hasselmann (1977) employed linear stochastic climate models (Hasselmann, 1976) showing that the decay of the SST anomaly associated with an atmospheric disturbance has an e-folding scale of 1/2 year (6 months). In their model, they used the white-noise as the input for atmospheric forcing, and yielded

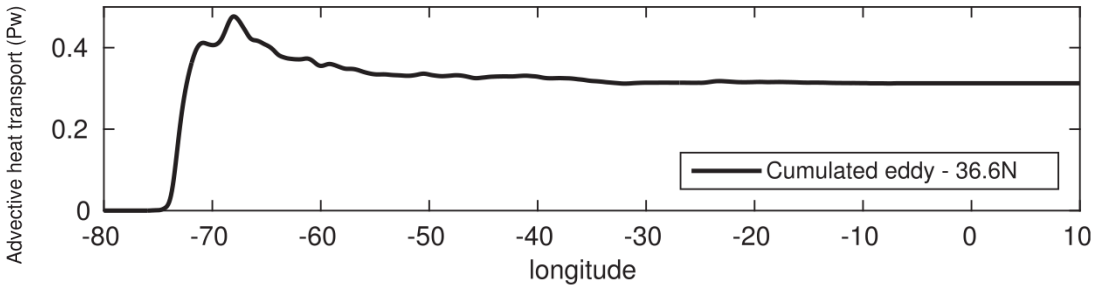

Figure 1-7: 2003-2012 averaged meridional heat transport due to eddies at 36.6°N along the longitude. It is accumulated from the west, in the unit of PW. Source: (Tréguier et al., 2017)

the red-noise response for SST anomalies. They found a negative feedback following a period of temporary incoherence, asymptotically approaching to the stationary SST anomalies. They showed that this enhanced persistance is imposed by the upper ocean heat capacity. Meanwhile, the model results of Grötzner et al. (1998); Latif and Barnett (1994) demonstrated a positive feedback, indicating unstable SST anomalies responding to atmospheric forcing. Both views stressed that the nonlinear terms are important in the air-sea coupling. Frankignoul and Hasselmann (1977) discussed that the nonlinear terms in the ocean-atmosphere coupling can possibly stabilize the positive feedback coupling . The nonlinear terms in the atmosphere forcing can generate low-frequency disturbance, possibly resulting in an unstable coupling (Grötzner et al., 1998; James and James, 1989).

The AMOC strength has an impact on the subtropical gyre heat content. The low frequency (multidecadal) variability of AMOC strength, measured at 26°N, reached a trough in the 1990s and a peak in the 2009-2010 (the lines in shades of blue in Figure 1-8). **We aim to investigate if the change of AMOC has an impact on the interannual extreme occurrences of EDW formation extremes.** We will address this question in Section 3.4.1.

1.2.1 Impact by NAO

The Gulf Stream meridional positioning is reported to have an impact on the OHC (Frankignoul et al., 2001; Joyce et al., 2000, 2019; Taylor and Stephens, 1998). Joyce et al. (2019) showed that a more northward (southward) shift of the Gulf Stream corresponds with an increase (decrease) in OHC. Frankignoul et al. (2001); Taylor and Stephens (1998) showed that a more northward (southward) shift of the Gulf Stream is found to respond to the NAO+(−) extreme occurrences with a lag of

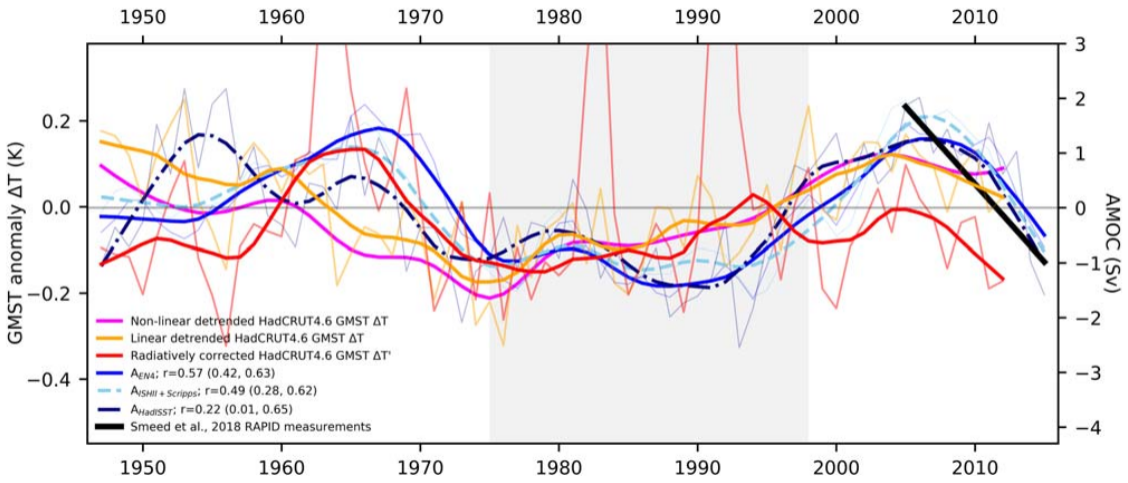

Figure 1. Time evolution of the multidecadal variability of the AMOC compared to the global mean surface temperature adjusted by the historical forcing for the time period 1948–2012. In grey the time period from 1975 to 1998 is marked during which the AMOC was in a relatively weak state. Proxies for the AMOC are the salinity based proxies $A_{ISHIIS+Scripps}$, A_{EN4} and the temperature based proxy $A_{HadISST}$ (shades of blue), which are compared to the linear trend of the 2005–2015 measurements form the RAPID array (thick black line). The global mean temperature deviation is based on HadCRUT4.6 data and is corrected for the linear, long-term warming trend (ΔT, orange), the nonlinear trend as done by Chen and Tung (2018) (ΔT, magenta) or adjusted by the historical forcing used for CMIP5 ($\Delta T' = \Delta T - 1/\lambda \, \Delta Q_{rad}$, red line). The default value for the feedback parameter is $\lambda = 2.3 \pm 0.7$ W K^{-1} m^{-2} and the numbers in brackets give the range of correlation coefficients resulting from other values for λ that are additionally shown in table 1. Thin lines are annual values; thick lines are 10 year LOWESS smoothed values. The LOWESS (Locally Weighted Scatterplot Smoothing) filter fits a regression curve to a scatterplot using weighted local linear regressions depending on the smoothing span, in this case 10 years (Cleveland 1979). The correlation coefficients r were calculated with the smoothed time series. (To remove any correlations due to common trends the time series were first linearly detrended.)

Figure 1-8: 1948-2012 multidecadal variability of AMOC, estimated using different proxies. Notice the blue solid line indicates the salinity based AMOC index A_{EN4}. The blue dashdot line indicates the SST based AMOC index $A_{HadISST}$. The light blue solid line indicates the salinity based AMOC index $A_{ISHIIS+Scripps}$. The multidecadal variabilities of these three proxies show a local minimum AMOC strength in the 1990s, and a local maximum AMOC strength in the period of 2009-2010. Source: Caesar et al. (2020)

11 months to 2 years with NAO leading. Joyce et al. (2000) showed that a more northward (southward) shift of the Gulf Stream is found to be correlated with high NAO+(−) in multi-decadal time scales. The Gulf Stream strength can be impacted by NAO (Bryden et al., 2014; Frankignoul et al., 2001). Bryden et al. (2014) showed that the Ekman divergence associated with NAO− in the North Atlantic subtropical region relaxes the horizontal temperature gradient, and slows down the Gulf Stream. Frankignoul et al. (2001) showed that a larger NAO index is found to correspond with a weaker Florida Current transport at 26°N. The Gulf Stream, as part of the subtropical MOC, can be impacted by the anomalous deep convection in the subpolar gyre (Robson et al., 2016). They suggested that AMOC shows a ∼10-year delayed dampening response to the anomalous deep ventilation of Labrador Sea Water (LSW) in the 1990s. The structure of the Gulf Stream system can impact the subtropical OHC (Bryden et al., 2014). They showed the 2009-2010 slowdown of AMOC at 25°N, and that the corresponding enhanced recirculation brought cooling to the subtropical gyre (north of 25°N) in 2009-10 and 2010-11.

In short, research shows the ocean reacts to the atmosphere with 0-year, 2-year, 5-10 year lags. We aim to examine the heat budget around the EDW formation region, namely, the western subtropical North Atlantic. **To understand this complex atmospheric impact to this region, we start off by examining the 0-year lag impact of the atmosphere to the ocean heat content.** We will address this question in detail in Section 4.3.9.

1.2.2 Feedback to NAO

The Gulf Stream system can have an effect on the NAO (Joyce et al., 2019). They provided the evidence that the Gulf Stream has a 0-year lag correlation with NAO, and they suggested the ambiguity of the impact's direction. The Gulf Stream positioning is found to lead the North Atlantic wintertime storm track and Greenland Blocking by 3 months (Joyce et al., 2019). The Florida Current transport at 26N is found to lead NAO by 3-10 months (DiNezio et al., 2009). Bryden et al. (2019) showed that during the slowdown of AMOC since 2008, the heat transport due to the Gulf Stream is not necessarily decreased. Rather, more warm current from the Gulf Stream is recirculated within the subtropical gyre, less warm current enters the subpolar gyre. Correspondingly, this ocean heat redistribution has an impact on the NAO. Bryden et al. (2014) reported that the rapid slowdown of AMOC in 2009-10 results in record-low NAO− in 2010-11. They showed that this intensified NAO− contributes to the high intensity of the 2010 Atlantic hurricane season, as well as severe winter conditions over northwestern Europe. **On the interannual time scales, we aim to**

investigate how the Gulf Stream connects the NAO anomalies to OHC in the subtropical gyre. This more prospective question will be discussed in Appendix A.

1.3 Preconditioning

To form large volume of mode water, a vigorous wintertime deep convection can be facilitated by a light stratification near the surface in the precedent fall. In this case, we call the light stratification a favorable preconditioning for the mode water formation. In the subtropical region, the preconditioning impacts the EDW formation unsystematically (Billheimer and Talley, 2013). They showed years of strong (weak) EDW renewal with favorable (unfavorable) preconditionings. Yet, they also showed that a year with strong EDW renewal experienced an unfavorable preconditioning (for example, the winter of 2009-2010), as well as a year with weak EDW renewal experienced a favorable preconditioning (for example, the winter of 2011-2012). However, they only used the buoyancy content in September to evaluate a preconditioning.

Preconditioning is important for the mode water formation, as it connects the remnant mode water formed from the previous year to the year following. Research about the preconditioning's role to the mode water formation is more thoroughly done in the subpolar North Atlantic. For example, the formation of the Irminger Sea Water, a subpolar mode water, experienced the most intensified ventilation in the winter 2014-2015 (Piron et al., 2017). Apart from a strong wintertime air-sea heat loss, Piron et al. (2017) showed a favorable preconditioning in the late fall of 2014, an aiding factor to this intense ventilation. The 2015-2018 consecutive intensified deep convection took place southeast of Cape Farewell (Zunino et al., 2019). Apart from the large storm-induced surface cooling, Zunino et al. (2019) showed a favorable preconditioning, an aiding factor to this consecutive intense ventilation.

The preconditioning can be ascribable to many physical processes. It can be due to a local process associated with the eddy advections. For example, the lateral advection of fresher Labrador Sea Water, freshening its adjacent Cape Farewell basin was a favorable preconditioning for the consecutive 2015-2018 intense deep convection (Zunino et al., 2019). The preconditioning can be due to a sub-annual and intermittent weather anomaly. For example, a lightly stratified near surface water at Labrador Sea in the late fall 2014 was a favorable preconditioning for the winter 2014-2015 (Piron et al., 2017). This favorable preconditioning in the Piron et al. (2017)'s analysis is associated with a strong air-sea heat loss associated with the area of cold anomaly in 2014, situated at the southern tip of Greenland and Iceland (namely, the

"Cold Blob", Duchez et al., 2016; Rahmstorf et al., 2015). despite the diverse arguments behind on the cause of the "Cold Blob" itself. This local anomalously cold area was shown possibly resulting from a multidecadal/decadal and non-local process, such as the AMOC slowdown (Bryden et al., 2019; Rahmstorf et al., 2015), or, possibly and more plausibly accepted by the community, resulting from local and sub-annual processes (Duchez et al., 2016), such as a storm-induced air-sea surface heat loss and an enhanced convection of cold water (Grist et al., 2016; Josey et al., 2018; Lozier et al., 2019).

To quantify the preconditioning, Billheimer and Talley (2013) investigated the buoyancy content of the water column above the permanent pycnocline in September. Piron et al. (2017); Zunino et al. (2019) investigated the preceeding late fall vertical density profiles of the mode water ventilation region. They showed the contribution of the vertical entrainment of cold water of the permanent pycnocline. For example, Piron et al. (2017) examined a less stratified water column near the bottom in the late fall of 2014. Indicated by this profile, the large entrainment of cold water from the bottom of the mode water bulk promoted an intensification of the wintertime convection at the Labrador Sea in 2014-2015.

In general, the subpolar convection (800-1000m in depth) is deeper than the subtropical convection (300-400m). It requires a much stronger atmospheric forcing. In comparison, to form less deep subtropical convection (300-400m) it is reasonable that atmospheric forcing is relatively weaker. In addition, in the subtropical region, the Gulf Stream interacts strongly with the EDW formation. It is expected that the preconditioning together with other physical processes contribute to the EDW ventilation in a more complex manner. **Given some well-investigated studies on preconditioning in the subpolar gyre, we aim to re-evaluate the role of preconditioning in the EDW formation.** We will address this question in detail in Section 4.3.8 and Section 4.3.9.

CHAPTER 2

Data and Method

1. How do we define the interannual variability in this study?

    - Interannual: the variability within 6-50 month window
    - Low frequency signal: > 50 month

2. What's the domain of study?

    - The domain of study is a fixed region where the EDW formation mainly takes place in the western subtropical gyre. The northern boundary is at the northern flank of the Gulf Stream. The southern boundary is at 30°N, near the Bermuda station. The western boundary is at 75°W, where the Gulf Stream curves eastward away from the US eastcoast. The eastern boundary is at 35°W, near the standing Mann Eddy, where the Gulf Stream curves northward partaking of the North Atlantic Current. The vertical domain is from the sea surface to 800m in depth, which extends near the depth of the permanent pycnocline and contains the EDW bulk.

3. What are the datasets that we used?

    - For the ocean state variables, namely the temperature and the salinity, we used the gridded observational datasets such as ISAS, EN4, SCRIPPS, and IPRC. For the SSH, we used the altimetry datasets. For the atmospheric variables, namely, the surface wind stress, the air-sea heat fluxes, and the sea level pressure, we used the atmopsheric reanalysis datasets, such as ERA and NCEP.

4. What's the governing equation?

    - We employed the heat equation in the domain of analysis, stating that the rate of the temperature change depends on the external heat flux through the air-sea boundary, the geostrophic and ageostrophic advections of heat, and the heat diffusion due to mixing.

5. Which criteria do we employ to estimate the Eighteen Degree Water (EDW)?

   - To estimate the total EDW volume, we employed the density criteria ranging from $26.2 - 26.6\,\mathrm{kg\,m^{-3}}$ and stratification criteria of the potential vorticity $\mathrm{PV} < 1.5 \times 10^{-10}\,\mathrm{s^{-1}\,m^{-1}}$. To estimate the ventilated EDW volume, we selected the winter surface EDW outcropping region, with a sea surface density ranging from $26.2 - 26.6\,\mathrm{kg\,m^{-3}}$, and integrated this outcrop down to the mixed layer depth.

2.1 Datasets

Dataset	Temporal Coverage	Resolutions	Reference
Ocean Datasets: Temperature and Salinity			
EN4	January 1950-March 2020	1.0°, monthly	Good et al. 2013
ISAS	January 2002-April 2020	0.5°, monthly	Kolodziejczyk et al. 2017
Scripps	January 2004-January 2020	1°, monthly	Roemmich and Gilson 2009
IPRC	January 2005-December 2019	1°, monthly	APDRC 2009
Altimetry Datasets: SSH			
SSH anomaly	January 1993-May 2019	0.25°, monthly	CMEMS 2020
MDT	1993-2012 mean	0.25°, climatology	Rio 2009
Atmosphere Datasets Sea level pressure, Air-sea heat fluxes, Surface wind speed, Surface wind stress momentum flux			
NCEP	January 1948-Febuary 2020	2.5°, 6hr	Kalnay et al. 1996
ERA	January 1979-January 2020	0.75°, daily	Dee et al. 2011

Table 2.1: List of the datasets employed in the analysis.

Regarding the ocean, we used ocean datasets that are based on an optimal interpolation of all available in-situ data. We used ISAS15-ARGO monthly analysis data for the period of 2002-2015 and ISAS-NRTOAGL01 monthly analysis data for January 2016-April 2020 (altogether referred to as the ISAS dataset; Kolodziejczyk et al. 2017; Table 2.1), taking the practical salinity and the sea water temperature. These are gridded datasets with a spatial resolution of 0.5° on average in latitude and about 0.39° in longitude. The meridional spatial resolution of ISAS gridded data varies from 0.45° at a latitude of 25°N to 0.32° at a latitude of 51°N. The maximum depth reached is 2000 m. We used the EN4 dataset for the period of January 1950-March 2020 (Good et al., 2013, Table 2.1), taking the sea water in-situ temperature and the sea water salinity. The EN4 dataset has a horizontal spatial resolution of $1^\circ \times 1^\circ$

and a maximum depth of 5350 m. Meanwhile, we used International Pacific Research Center (IPRC) dataset with a period of January 2005-December 2019. We also used Roemmich-Gilson dataset from the Scripps Institute of Oceanography (the Scripps dataset), a Global gridded 1 degree NetCDF Argo only dataset produced by optimal interpolation (Table 2.1, Roemmich and Gilson 2009). The Scripps dataset contains a period of January 2004-January 2020, taking the ARGO temperature and salinity monthly means. The horizontal spatial resolution of both Scripps and IPRC datasets is $1^{\,o} \times 1^{\,o}$. The maximum depth of Scripps is 1953.01 m, while that of the IPRC dataset is 2000 m.

We calculated the ocean heat content, the EDW volume, and the weather regimes using the datasets in Table 2.1. We focused on the 2002-2019 period, as it is a time period during which the ARGO floats were deployed.

The MLD was defined in various ways. The temperature-mixed layer depth (TMLD) is the depth of upper ocean with a temperature lower than 10-m value by a fixed ΔT (de Boyer Montégut, 2015; Levitus, 1982). Levitus (1982) used $\Delta T = 0.5^{o}$C to calculate the TMLD. de Boyer Montégut et al. (2004) proposed a smaller temperature difference of $\Delta T = 0.2^{o}$C, which better captures the early spring restratification than does $\Delta T = 0.5^{o}$C.

The density-mixed layer depth (DMLD) is the depth of upper ocean with a density larger than 10-m value by a fixed $\Delta\sigma$ (de Boyer Montégut, 2015). $\Delta\sigma = 0.03\,\mathrm{kg\,m^{-3}}$ corresponds with the temperature difference $\Delta T = 0.2^{o}$C, at a 9^{o}C seawater (de Boyer Montégut et al., 2004). de Boyer Montégut et al. (2004) commented that $\Delta\sigma = 0.125\,\mathrm{kg\,m^{-3}}$ can overestimate the mixed layer depth, and may not be able to capture the restratification in the early spring. de Boyer Montégut et al. (2004) showed that this density-based MLD is deeper than the aforementioned temperature-based MLD in certain regions, but more in the subpolar region, such as the Greenland-Iceland-Norway Sea and the Labrador Seas. Moreover, they showed that the density-based MLD has large blank and uninterpolatable area, compared with the temperature-based MLD, located in the central Pacific and the Southern oceans. This is due to the lack of salinity profiles.

We employed the DMLD with the density threshold of $\Delta\sigma = 0.03\,\mathrm{kg\,m^{-3}}$ to estimate the mixed layer depth of the ISAS, EN4, IPRC and Scripps datasets.

We used the Gibbs Seawater Library (GSW) version 3.0.3 to calculate the sea water in-situ density and the potential vorticity (PV) from temperature and salinity.

We used the altimetry datasets that include the SSH anomaly and the SSH annual mean. Regarding the sea surface height (SSH) anomaly, we used the global ocean gridded L4 SSHs and derived variables reprocessed (1993-ongoing; Product ID:

SEALEVEL_GLO_PHY_L4_REP_OBSERVATIONS_008_047) distributed by the Copernicus Marine Environment Monitoring Service (CMEMS, 2020). Regarding the SSH annual mean, we used the CNES-CLS2013 Mean Dynamic Topography (MDT; Rio, 2009). The altimetry datasets have a horizontal spatial resolution of $0.25^\circ \times 0.25^\circ$. We employed the available SSH dataset in the period of January 1993-May 2019.

Regarding the atmosphere, we used the sea level pressure (SLP), the air-sea surface heat fluxes, the surface wind speed, as well as the surface wind stress momentum flux from National Centers for Environmental Prediction-National Center for Atmospheric Research (NCEP-NCAR, or NCEP) reanalysis data (Kalnay et al., 1996). We used the NCEP dataset in the period of 1948-2019 with a 6-hr time resolution and $2.5^o \times 2.5^o$ spatial resolution. In addition we used European Centre for Medium-Range Weather Forecasts (ECMRWF) Re-analysis data (ERA-interim, or ERA5, Dee et al. 2011). We used The ERA dataset in the period of January 1979-January 2020 with a daily time resolution and $0.75^o \times 0.75^o$ spatial resolution.

To calculate the air-sea heat flux, we summed the upward/downward short/long wave radiation fluxes, the latent heat flux, and the sensible heat net flux. Therefore we used SLP for both ERA and NCEP datasets to have a unified naming convention.

2.2 Domain of study

The mixed layer depth in the subtropical North Atlantic region can reach up to a depth of 500 m (the solid black contour in Figure 2-1, Maze et al. 2009). The EDW formation region is located at the southern flank of the Gulf Stream (the dash dotted yellow contour in Figure 2-1).

We chose the domain of analysis (the cyan dashed lines in Figure 2-1) to include the EDW formation region. The northern boundary of the domain of study is at the northern flank of the Gulf Stream (38^oN, 75^oW - 46^oN, 35^oW), to ensure the inclusion of the mode water outcropping area (between the two red contours in Figure 2-1). The southern boundary is 30^oN, and the eastern boundary is located at 35^oW, east of the standing Mann Eddy at the Gulf Stream extension (45^oW, 42^oN, Mann 1967). Surrounding the Mann Eddy, the Gulf Stream turns northward to exit the domain of study from the northern boundary and becomes part of the North Atlantic Current (NAC); and the western boundary is located at 75W at the entrance of the Gulf Stream, with a reasonable distance from the coastal region.

Since 800 m in depth in the subtropical North Atlantic region is below the EDW bulk and this depth cuts through the permanent pycnocline (OACP-Argo, 2020), we

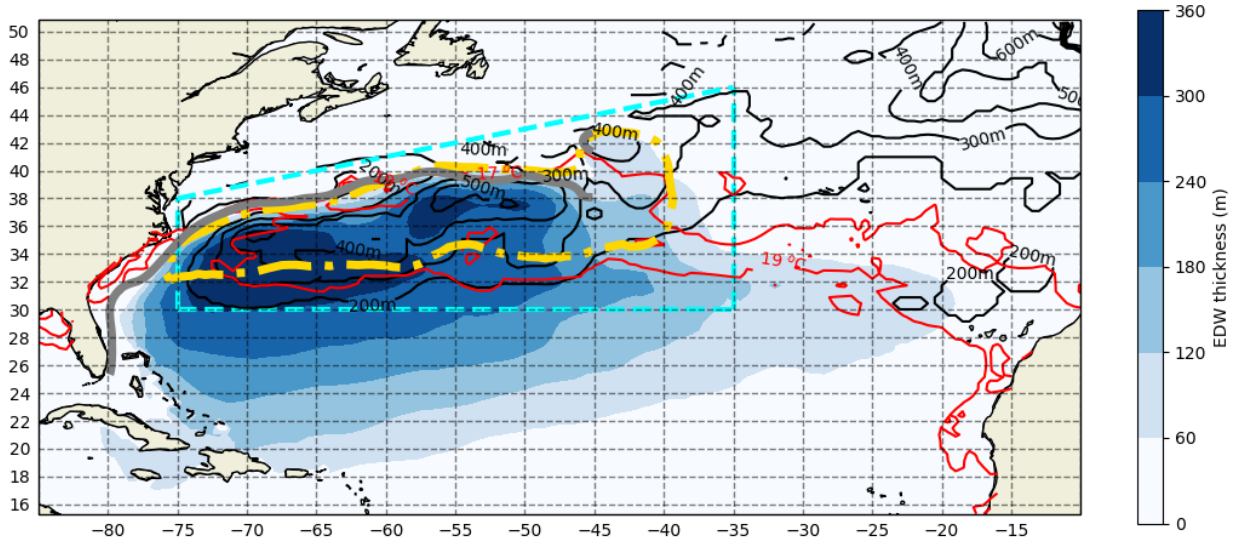

Figure 2-1: The domain of study (the cyan dashed line) and the climatological mean of EDW thickness (color shading in blue) from 2003-2018. The thick solid grey line shows the SSH (sum of the Sea level anomaly, SLA, and mean dynamic topography, MDT, from AVISO Altimetry) at 0.39m, indicating the Gulf Stream position. The red solid contours indicate the 17^{o}C and 19^{o}C outcrops at the time of the deepest mixed layers, and the black solid contours indicate the depth of the deepest mixed layer. The dash dotted yellow line represents the 75 m contour of standard deviation of EDW thickness. We used this contour to indicate the EDW formation region. The EDW thickness is calculated using the potential density layer of $26.2 - 26.6 \mathrm{kgm}^{-3}$, and the PV threshold of PV $< 1.5 \times 10^{-10} \mathrm{m}^{-1}\mathrm{s}^{-1}$. The PV is calculated using the potential density and the Brunt-Väsälä frequency from ISAS15-ARGO data.

chose 800 m as the vertical domain. The total surface area of the domain of analysis is $4.918 \times 10^{12}\,\mathrm{m}^2$, and the total volume of the sea water in the domain of analysis is about $3.93 \times 10^{15}\,\mathrm{m}^3$ (about 127.7 Svy).

2.3 Heat budget calculation

2.3.1 Equations

In the domain of study, the potential temperature change depends on the external heat flux through the air-sea boundary, the geostrophic advection of temperature, the ageostrophic advection of temperature (Ekman heat advection), and diffusion, written as:

$$\frac{\partial \theta}{\partial t} = \frac{1}{\rho_o C_p}\frac{\partial q}{\partial z} - \left[\boldsymbol{\nabla}_{\mathrm{H}} \cdot (\mathbf{u}_{\mathrm{g}}\theta) + \frac{\partial (w\theta)}{\partial z}\right] - \boldsymbol{\nabla}_{\mathrm{H}} \cdot (\mathbf{u}_{\mathrm{Ek}}\theta) + \kappa_{\mathrm{H}}\boldsymbol{\nabla}_{\mathrm{H}}^2\theta + \kappa_{\mathrm{V}}\frac{\partial^2 \theta}{\partial z^2} \tag{2.1}$$

where θ denotes the potential temperature in the unit of $^{\mathrm{o}}\mathrm{C}$, q denotes the vertical heat flux in the unit of $\mathrm{W\,m^{-2}}$, $\mathbf{u}_{\mathrm{g}}$ denotes the horizontal geostrophic velocity vector in the unit of $\mathrm{m\,s^{-1}}$. The vertical velocity w at the bottom of the domain is calculated as:

$$w\Big|_{z=-H} = w_{\mathrm{Ek}} - \frac{\beta}{f}\int_{-H}^{-\delta_e} v_{\mathrm{g}}\, dz \tag{2.2}$$

where β is the Rossby parameter, and f is the Coriolis acceleration. $-w\Big|_{z=-H}$ denotes the volume flux across the interface $z = -H$. This signifies the local subduction rate at given depth H, due to the Ekman pumping with the constraint of the linear vorticity balance (Equation 2 in Marshall et al., 1993). The Ekman layer depth, δ_e, is calculated as $\delta_e = 0.7 f^{-1}\sqrt{|\boldsymbol{\tau}|\rho^{-1}}$ (Maze and Marshall, 2011), where $|\boldsymbol{\tau}|$ is the amplitude of surface wind stress, and ρ is the ocean density.

$\mathbf{u}_{\mathrm{Ek}}$ denotes the Ekman velocity, $\boldsymbol{\nabla}_{\mathrm{H}} = \frac{\partial}{\partial x}\mathbf{i} + \frac{\partial}{\partial y}\mathbf{j}$ denotes the horizontal divergence operator, t denotes time in the unit of s, z denotes the vertical axis with positive direction pointing upwards and its origin fixed at the sea surface, $\rho_o = 1.027 \times 10^3 \mathrm{kg\,m^{-3}}$ is the reference ocean density, $C_p = 4.2 \times 10^3 \mathrm{J\,kg^{-1}\,^{o}C^{-1}}$ denotes the sea water specific heat, κ_{H} and κ_{V} denote the horizontal and vertical diffusivity coefficients, respectively.

2.3.2 Terms

We used V to denote the volume of the domain of analysis, S the horizontal surface of the domain of analysis, and $H = 800\,\mathrm{m}$ the depth of water column. The ocean

heat content (OHC) is defined as:

$$\mathrm{OHC} = \rho_o C_p \int_V \theta \, dV \tag{2.3}$$

We integrated Equation 2.1 over the domain of study:

$$\partial_t \mathrm{OHC} = \int_S Q_{\mathrm{net}} dS + \mathcal{H}_{\mathrm{Geo}} + \mathcal{H}_{\mathrm{Ek}} + \mathcal{H}_{\mathrm{Mix}} \tag{2.4}$$

The heat source due to the convergence of temperature geostrophic advection $\mathcal{H}_{\mathrm{Geo}}$ is:

$$\mathcal{H}_{\mathrm{Geo}} = -\rho_o C_p \int_V \boldsymbol{\nabla}_{\mathrm{H}} \cdot (\mathbf{u}_{\mathrm{g}} \theta) \, dV + \rho_o C_p \int_S (w\theta) \Big|_{z=-H} dS \tag{2.5}$$

The heat source due to the convergence of temperature Ekman advection $\mathcal{H}_{\mathrm{Ek}}$ is calculated as:

$$\mathcal{H}_{\mathrm{Ek}} = -\rho_o C_p \int_S \int_{-\delta_e}^{0} \boldsymbol{\nabla}_{\mathrm{H}} \cdot (\mathbf{u}_{\mathrm{Ek}} \theta) dz \, dS \tag{2.6}$$

And the heat source due to the convergence of horizontal and vertical temperature mixing $\mathcal{H}_{\mathrm{Mix}}$ is calculated as:

$$\mathcal{H}_{\mathrm{Mix}} = \kappa_{\mathrm{H}} \oint_L \int_{-\delta_{\mathrm{ML}}}^{0} (\boldsymbol{\nabla}_{\mathrm{H}} \theta) dz \cdot \mathbf{l} - \kappa_{\mathrm{V}} \int_S \frac{\partial \theta}{\partial z} \Big|_{z=-H} dS \tag{2.7}$$

where L is the circumference of the horizontal edges of the domain of study, and δ_{ML} denotes the mixed layer depth. We chose the vertical diffusivity $\kappa_{\mathrm{V}} = 1.0 \times 10^{-5}\,\mathrm{m^2 s^{-1}}$, a measure that parameterizes the energy diffusion process due to the internal wave breaking in the thermocline (Whalen et al., 2012). We neglected horizontal diffusion below the MLD. We chose the horizontal diffusivity coefficient $\kappa_{\mathrm{H}} = 1.0 \times 10^3\,\mathrm{m^2 s^{-1}}$, a measure that parameterizes the enhancement of lateral meso-scale stirring in the mixed layer (Cole et al., 2015). We integrated the budget over a closed box, to which contributes only the horizontal diffusivity at the boundaries. This excludes a sensitivity of the results to the high κ_{H} values of the Gulf Stream region. Moreover, the diffusion term due to mixing is not included explicitly in the heat budget. It has relatively a smaller magnitude than other terms, comparable to the allowed heat convergence residual (Figure 2-10 and Figure 2-9).

2.3.3 Geostrophic current

The geostrophic current is estimated by combining the $\mathbf{u}_{z=0}$ component and the baroclinic component.

$$\mathbf{u}_{\mathrm{g}} = \mathbf{u}_{z=0}(x, y) + \mathbf{u}_{\mathrm{baroclinic}}(x, y, z) \tag{2.8}$$

We estimated the $u_{z=0}$ component by using the absolute dynamic topography from the altimetry datasets, with the reference level set at the ocean surface (Petit et al., 2018).

$$\mathbf{u}_{z=0} = \Big(-\frac{g}{f}\frac{\partial \eta}{\partial y}, \frac{g}{f}\frac{\partial \eta}{\partial x} \Big) \tag{2.9}$$

where the sea surface absolute elevation η denotes the SSH, the sum of a sea level anomaly (SLA) and a mean dynamic topography (MDT).

We estimated the baroclinic component by calculating the horizontal gradient of the in-situ ocean density $\rho_{\text{in-situ}}$, and then applying the thermal wind relation.

$$\frac{\partial \mathbf{u}_{\text{baroclinic}}}{\partial z} = \frac{g}{f\rho_{\text{ref}}} \Big(\frac{\partial \rho_{\text{in-situ}}}{\partial y}, -\frac{\partial \rho_{\text{in-situ}}}{\partial x} \Big) \tag{2.10}$$

With this algorithm, we calculated the geostrophic velocity using the altimetry data combined with in-situ density from gridded observational ocean datasets, namely, ISAS, EN4, SCRIPPS, and IPRC. We interpolated the altimetry datasets to the ocean datasets. Despite the difference between the effective resolutions (for example, altimetry and ISAS, see details in Appendix C), we chose to combine the baroclinic component and the $\mathbf{u}_{z=0}$ component without performing smoothing to obtain the geostrophic velocity field. We found that directly combining the two datasets best describes the structure as well as the magnitude of the velocity field at the western subtropical North Atlantic.

To verify the geostrophic current calculation, we compared both the yielded 3D structure and the associated amplitude with the existing dataset as well as the literature. We chose one zonal cross-section at 45°N and one meridional cross-section at 70°W. At the zonal cross-section at 45°N, the NAC has a core at the surface with a magnitude of $0.23\,\mathrm{m\,s^{-1}}$, located at 43.5°W, and extends to 2000 m with a magnitude of $0.13\,\mathrm{m\,s^{-1}}$ (Figure 2-2a). The Deep Western Boundary Current (DWBC) at 45°N has a core below 500m with a magnitude of $-0.1\,\mathrm{m\,s^{-1}}$, centered at 46.5°W, and extends to the surface. The Labrador Current (LC) at 45°N has a core of $-0.3\,\mathrm{m\,s^{-1}}$ centered at 48.5°W, separated from DWBC at 47.5°W. Using the ARMOR3D dataset, we yielded consistent magnitudes and positions of NAC, DWBC and LC from our estimate. In addition, we compared our estimate of DWBC and LC and NAC with Desbruyères et al. (2019)'s estimate (their Fig.2) using in-situ hydrographic datasets. In Figure 2-2(b), the LC-and-DWBC-related southward volume transport is about $-25\,\mathrm{Sv}$, zonally extended from 50°W to 45°W. The NAC-related northward volume transport is about 50 Sv, zonally extended from 45°W to 43°W. The recirculation gyre related southward-flowing volume transport is about 20 Sv, zonally extended from 47°W to 36°W. Our estimation of volume transport is well in line with Des-

bruyères et al. (2019), despite an underestimate on NAC northward volume transport by 16%, that is, 10 Sv (see Figure 1 at Desbruyères et al. 2019).

At the meridional cross-section at 70°W in Figure 2-3, the NAC has a core at the surface with a magnitude of $0.8\,\mathrm{m\,s^{-1}}$ located at 37.5°N, and extends to 2000 m with a magnitude of $0.4\,\mathrm{m\,s^{-1}}$. The DWBC at 70°W has a core of $-0.2\,\mathrm{m\,s^{-1}}$ centered at 39°N, and extends to the surface. This profile is in line with the ARMOR3D dataset.

We estimated the Gulf Stream volume transport and compared with the literature. The volume transport passing the Oleander Line (Rossby and Gottlieb 1998) at 55 m depth is examined by Chi et al. (2018) using observations and models. We calculated this volume transport within one layer of unit depth at 55 m (Section 3.3.2 in Chi et al., 2018). We chose the location of this volume transport at 70°W, $34^{\circ} - 38^{\circ}$N. During the period of 2002-2016, our estimate shows an average of $10.3\times10^4\,\mathrm{m^3\,s^{-1}\,m^{-1}}$ (or $\mathrm{m^2\,s^{-1}}$) of Gulf Stream transport, an average of $-3.1\times10^4\,\mathrm{m^2\,s^{-1}}$ of the westward-flowing return flow, and an average of $7.3\times10^4\,\mathrm{m^2\,s^{-1}}$ of the east-flowing net flow (Figure 2-4). The observation of Chi et al. (2018) is shown to have a mean Gulf Stream transport of $13.5\times10^4\,\mathrm{m^2\,s^{-1}}$, and a mean net transport of $8.5\times10^4\,\mathrm{m^2\,s^{-1}}$. The models with resolutions of $0.5^{\circ} - 1^{\circ}$ show, in general, a Gulf Stream transport of $7 - 9\ \times10^4\,\mathrm{m^2\,s^{-1}}$ with an error of $\pm5\times10^4\,\mathrm{m^2\,s^{-1}}$, and a net transport of $5.5 - 8\ \times10^4\,\mathrm{m^2\,s^{-1}}$ with an error of $\pm2\ \times10^4\,\mathrm{m^2\,s^{-1}}$. Using the ARMOR3D dataset, at 70°W, $34^{\circ}-38^{\circ}$N, at depth of 55 m, during the period of 1995-2015, the averaged Gulf Stream transport is $11.9\times10^4\,\mathrm{m^2\,s^{-1}}$, the averaged transport of the westward-flowing return flow is $-3.2\times10^4\,\mathrm{m^2\,s^{-1}}$, and the averaged transport of the eastward-flowing net flow is $8.7\times10^4\,\mathrm{m^2\,s^{-1}}$. The return flow in our estimate well agrees with that at ARMOR3D. Our estimate on the Gulf Stream transport is underestimated compared to ARMOR3D00 by 15% (by $1.6\times10^4\,\mathrm{m^2\,s^{-1}}$ eastward), thus, the net flux of our estimate is underestimated by 20% (by $1.5\times10^4\,\mathrm{m^2\,s^{-1}}$ less eastward) compared to ARMOR3D. Our volume transport estimate of Gulf Stream is in line with the literature.

2.3.4 Ekman current

The Ekman velocity $\mathbf{u}_{\mathrm{Ek}}$ in Equation 2.6 is estimated using the wind stress $\boldsymbol{\tau}$ and the Ekman layer depth δ_e. This Ekman velocity is a depth averaged quantify over the Ekman depth. The domain averaged vertical velocity at the bottom of the Ekman layer depth ($\overline{w_{\mathrm{Ek}}}$) is estimated from the horizontal Ekman velocities using the following equations:

$$\mathbf{u}_{\mathrm{Ek}} = -\frac{1}{\rho_o f \delta_e}\mathbf{k}\times\boldsymbol{\tau} \qquad w_{\mathrm{Ek}} = \frac{1}{S}\int_S\int_{-\delta_e}^{0} \boldsymbol{\nabla}_{\mathrm{H}}\cdot\mathbf{u}_{\mathrm{Ek}}\,dS\,dz \tag{2.11}$$

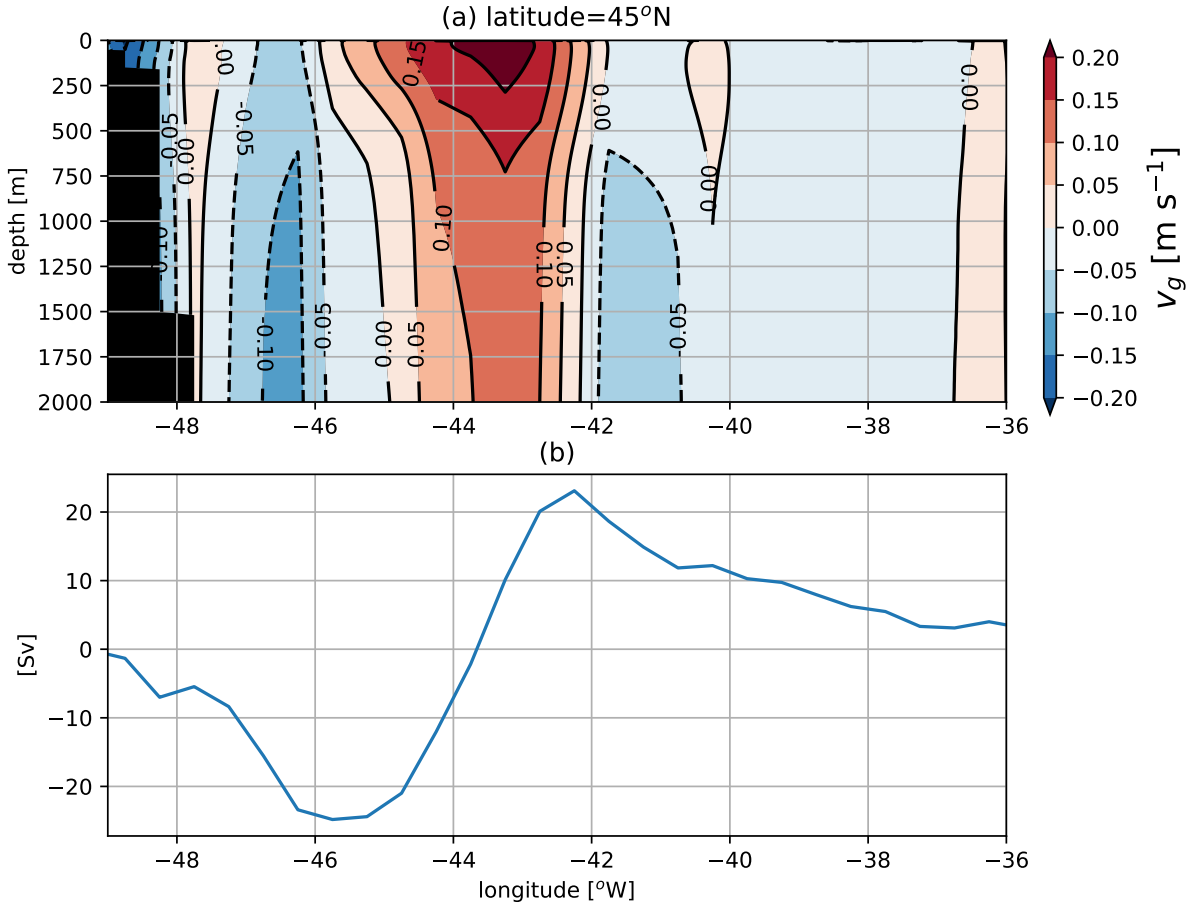

Figure 2-2: (a) Meridional velocity averaged over January 2002-October 2019 at 45°N, and (b) the corresponding accumulated northward transport over the depth of surface-2000 m integrated from the western boundary, using the ISAS dataset for temperature and salinity, as well as the altimetry datasets for SSH. The blue curve denotes the accumulated northward transport in Sverdrup ($1 \times 10^6\,\mathrm{m^3\,s^{-1}}$). The positive value denotes northward-flowing current, and the negative value denotes southward-flowing current.

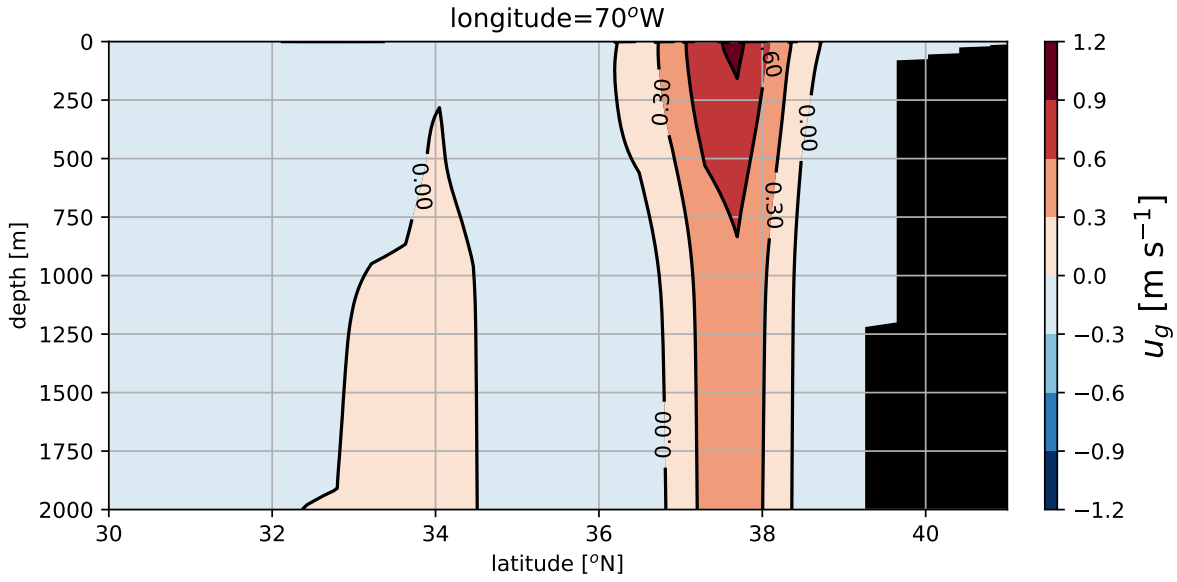

Figure 2-3: The zonal velocity averaged over the period of January 2002-October 2019 at 70°W using the ISAS dataset and the altimetry dataset. The $\mathbf{u}_{z=0}$ and baroclinic components of the velocity are calculated in the same way as Figure 2-2(a). The positive velocity denotes eastward-flowing current, and the negative velocity denotes westward-flowing current.

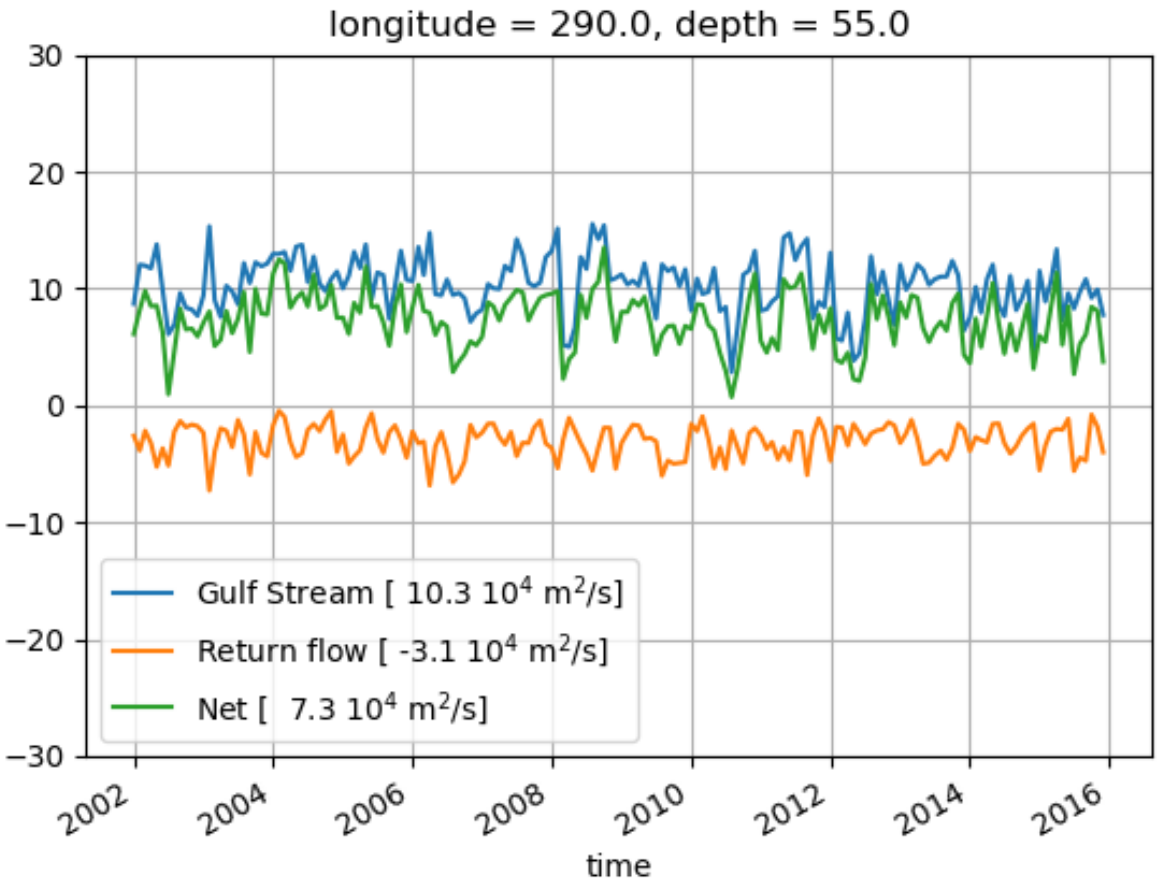

Figure 2-4: The time series of the Gulf Stream transport (blue curve), the return flow transport (orange curve), and net eastward transport (green curve) at the depth of 55 m, at 70°W and 34-38 °N. The $\mathbf{u}_{z=0}$ and the baroclinic components of the velocities are calculated in the same way as Figure 2-2(a).

2.3.5 Volume change estimate due to SSH variability

We examined both the seasonal variability and interannual variability of the SSH volume, in order to compare its order of magnitude with the horizontal geostrophic volume transport convergence over the EDW formation region. During a typical seasonal cycle (for example in 2002 in Figure 2-5), the SSH volume peak-to-peak variablity is about:

$$2.3 \times 10^{12}\mathrm{m}^3 - 1.7 \times 10^{12}\mathrm{m}^3 = 0.6 \times 10^{12}\mathrm{m}^3 = 0.02\,\mathrm{Svy}$$

Given the area of EDW formation region is $4.32 \times 10^{12}\mathrm{m}^2$, the SSH seasonal variability averaged over the EDW formation region is:

$$0.6 \times 10^{12}\mathrm{m}^3/(4.32 \times 10^{12}\mathrm{m}^2) \approx 0.125\mathrm{m}$$

This seasonal variability is due to the thermosteric component of the SSH. During the period of 2002-2015, the change of volume is about:

$$2.3 \times 10^{12}\mathrm{m}^3 - 1.8 \times 10^{12}\mathrm{m}^3 = 0.5 \times 10^{12}\mathrm{m}^3 = 0.016\,\mathrm{Svy}$$

The SSH associated volume in the EDW formation region roughly increased by 0.016 Svy over 14 years. This translates into an annual trend of :

$$0.5 \times 10^{12}\mathrm{m}^3/14\mathrm{yr} \approx 0.036 \times 10^{12}\mathrm{m}^3\,\mathrm{yr}^{-1} = 1.1 \times 10^{-3}\,\mathrm{Sv}$$

That is, on average over the domain, a change of SSH of:

$$0.036 \times 10^{12}(\mathrm{m}^3\,\mathrm{yr}^{-1})/(4.32 \times 10^{12}\mathrm{m}^2) \approx 0.008\mathrm{m}\,\mathrm{yr}^{-1}$$

To summarize, the volume rates of change due to SSH, both in the seasonal cycle and on a decadal scale, are much less in order of magnitude, than the horizontal volume fluxes at the boundaries or than the vertical volume flux at 800 m in depth. This inferiority of SSH's role in volume rate of change holds regardness of its sub-components due to thermal expansion, or due to dynamic factors.

2.3.6 Closing the heat budget: inverse model approach

The direct calculation of the budget from different data sources led to unbalanced volume and heat budget in the domain of study. To ensure that volume and heat are conserved over the domain, we developed an inverse model. The inverse problem serves to solve the problem of inverting a Fredhold integral equation of the first kind. (Jackson, 1979).

$$y(\eta) = \int_a^b x(\zeta)K(\zeta,\eta)d\zeta + e(\eta) \tag{2.12}$$

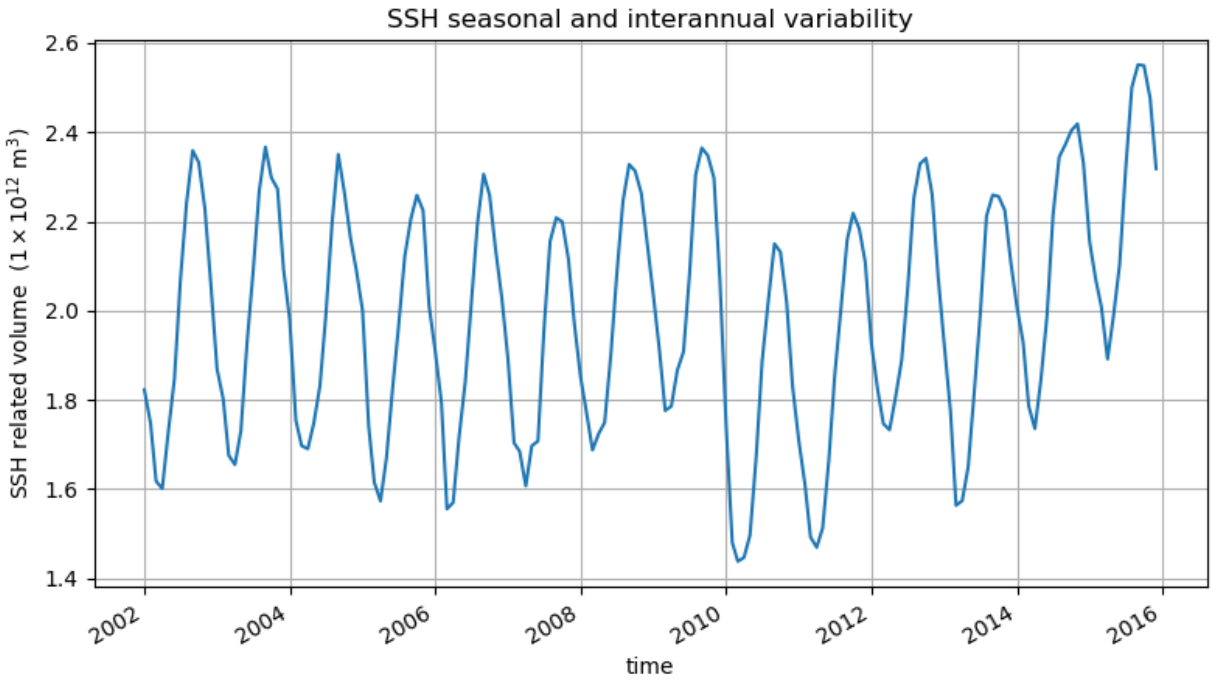

Figure 2-5: SSH volume seasonal and interannual variability during 2002-2015 using monthly data over the domain of analysis

where a and b are fix contants. $x(\zeta)$ is an unknown function, that often describes the "internal" properties, for example, the velocity field, that needs to be corrected. $K(\zeta, \eta)$ is a known Kernel function, which, in the linear case, is a prescribed field (temperature, density, or salinity) , $y(\eta)$ is an observed function, which often describes the measured "external" properties. $e(\eta)$ is a random error function. In the linear space, after discretization in η and ζ, Equation 2.12 is rewritten in the form of

$$\mathbf{Y}(\mathbf{X}) = \mathbf{A}\mathbf{X} \tag{2.13}$$

where $\mathbf{A}$ denotes the known matrix $(n \times m)$, $\mathbf{Y}$ denotes the n vector of observations, $\mathbf{X}$ denotes the m vector of unknown parameters. The *a priori* value for $\mathbf{X}$ is $\mathbf{X_o}$, with an associated error covariance matrix $\mathbf{C_o}$ $(m \times m)$. The *a priori* contraints are $\mathbf{Y}(\mathbf{X_o})$ with an associated error covariance matrix $\mathbf{C_T}$ $(n \times n)$.

The optimized or *a posteriori* estimate is calcuated to minimize the cost function written as the following:

$$\text{Cost Function} = (\mathbf{X} - \mathbf{X_o})^T \cdot {\mathbf{C_o}}^{-1} \cdot (\mathbf{X} - \mathbf{X_o}) + [\mathbf{Y}(\mathbf{X})^T \cdot {\mathbf{C_T}}^{-1} \cdot \mathbf{Y}(\mathbf{X})] \tag{2.14}$$

The first term $(\mathbf{X} - \mathbf{X_o})^T \cdot {\mathbf{C_o}}^{-1} \cdot (\mathbf{X} - \mathbf{X_o})$ is proportional to the square distance between *a priori* and *a posteriori* estimates. The second term $\mathbf{Y}(\mathbf{X})^T \cdot {\mathbf{C_T}}^{-1} \cdot \mathbf{Y}(\mathbf{X})$ is

proportional to the square residuals of the constraints. Both $\mathbf{C_o}$ and $\mathbf{C_T}$ are weighting factors (Mercier, 1986).

The inverse model is a widely used methodology in physical oceanography. For example, Mercier (1986) introduced the inverse method to rectify both the density field and the tracer field. Paillet and Mercier (1997) used a nonlinear inverse method to optimize both the salinity and the velocity fields according to mass, heat, and salt conservations at the eastern North Atlantic region. Dong et al. (2007) used inverse method to close the volume convergence/divergence budget in their numerical model approach. Maze et al. (2012) provided a more detailed description of the inverse model, and applied it to a mass, nutrient, and oxygen budget calculation in the northeast Atlantic.

2.3.6.1 Our model

The volume conservation equation is given by the domain convergence of fluxes due to geostrophic and ageostrophic velocity:

$$U_{\mathrm{Geo}} + U_{\mathrm{Ek}} = \mathcal{V}_{\mathrm{res}} \tag{2.15}$$

where U_{Geo} is the geostrophic convergence term in the domain of analysis $U_{\mathrm{Geo}} = -\int_V \nabla \cdot \mathbf{u_g}\, dV$. U_{Ek} is the Ekman convergence term in the domain of analysis $U_{\mathrm{Ek}} = -\int_V \nabla \cdot \mathbf{u_{Ek}}\, dV$. $\mathcal{V}_{\mathrm{res}}$ denotes the volume flux residual, in the unit of Sv.

Liang et al. (2017) estimated a 20-year-mean total vertical velocity at 1000 m depth with a standard deviation of $O(10^{-7})\,\mathrm{m\,s^{-1}}$. Their estimate on the vertical velocity standard deviation would be responsible for a volume flux of $O(10^{-1}) - O(1)$ Sv in the domain of analysis. Thus its standard deviation is larger than the mean. The volume residual $\mathcal{V}_{\mathrm{res}}$ can be ascribable to this fluctuation of vertical velocity at bottom of the domain.

Among the ocean datasets employed, the total volume convergence $\mathcal{V}_{\mathrm{res}}$ ranges from -6.30 to $11.20\,\mathrm{Sv}$ (Figure 2-6). Since the volume variability of SSH is in the order of $O(10^{-2})$Svy, and the corresponding rate of the volume change due to SSH is in the order of $O(10^{-3})$Sv. The volume change due to SSH is much smaller than the residual. Thus we dropped the volume change due to SSH in Equation 2.15.

The Gulf Stream at 70°W is estimated to have a volume transport of $70 - 119\,\mathrm{Sv}$ (Colin de Verdière and Ollitrault, 2016). The unclosed volume budget has a discrepancy ranging from at least $-5.3\% - 9.4\%$ of the Gulf Stream volume transport.

To calculate the heat budget residual $\mathcal{H}_{\mathrm{res}}$, we re-arranged the heat equation 2.4

into the following:

$$\partial_t \mathrm{OHC} - \int_s Q_{\mathrm{net}} dS - \mathcal{H}_{\mathrm{Geo}} - \mathcal{H}_{\mathrm{Ek}} = \mathcal{H}_{\mathrm{res}} \tag{2.16}$$

where the ocean heat content change over time is mainly impacted by the air-sea surface heat flux, the geostrophic and the ageostrophic heat advections. $\mathcal{H}_{\mathrm{res}}$ denotes the heat residual, in the unit of PetaWatt. Note that we included the mixing term $\mathcal{H}_{\mathrm{Mix}}$ in the residual term $\mathcal{H}_{\mathrm{res}}$.

Among the ocean datasets employed, the total heat residual $\mathcal{H}_{\mathrm{res}}$ ranges from $-208.3 - 47.4\,\mathrm{W\,m^{-2}}$. The negative sign indicates cooling in the domain of study. The *a priori* estimate of the heat residual is unrealistic. Theoretically, according to Equation 2.16, the heat residual should mainly include the mixing term $\mathcal{H}_{\mathrm{Mixing}}$. We estimated that the heat convergence due to horizontal and vertical mixing is about $-0.01\,\mathrm{PetaW}$ ($-2.72\,\mathrm{W\,m^{-2}}$. See details in Section 2.3.6.3). Compared with the mixing, the calculated heat residual is larger by an order of magnitude of $O(10^1) - O(10^2)$. Moreover, the air-sea heat flux at the surface of the domain of study has a climatological mean of about $-78.5\,\mathrm{W\,m^{-2}}$ (using the NCEP dataset, for example). Our estimate on the heat residual is about $0.6-1.7$ times as large as the climatological mean of the air-sea heat flux, one of the major contributors of the OHC.

To close the budget, we employed the inverse method to rectify the geostrophic volume flux at the northern, southern, western, and eastern boundaries of the domain of study.

The *a posteriori* estimate of geostrophic volume convergence consists of the volume convergence U^o_{Geo}, calculated using the *a priori* geostrophic velocity, as well as the rectification terms, displayed as the following:

$$U_{\mathrm{Geo}} = U^o_{\mathrm{Geo}} + U'_{\mathrm{W}} + U'_{\mathrm{E}} + U'_{\mathrm{N}} + U'_{\mathrm{S}} \tag{2.17}$$

where, U'_{W}, U'_{E}, U'_{N}, and U'_{S} denote the rectifications of the geostrophic volume fluxes at the four boundaries, in the unit of Sv. At each boundary, the volume flux entering the domain of study is positive, and exiting from the domain negative. In addition, we believe that it is the current that is the less well known variable in the budget. Thus we only corrected the velocity field, and used the averaged temperature over each cross section to calculate the heat budget. We performed the rectification of the velocity field at each monthly time step.

The *a posteriori* estimate of geostrophic heat convergence consists of the *a priori* estimate of heat convergence $\mathcal{H}^o_{\mathrm{Geo}}$, the heat convergence due to the rectified geostrophic velocity field advecting the temperature averaged over the 0-800m verti-

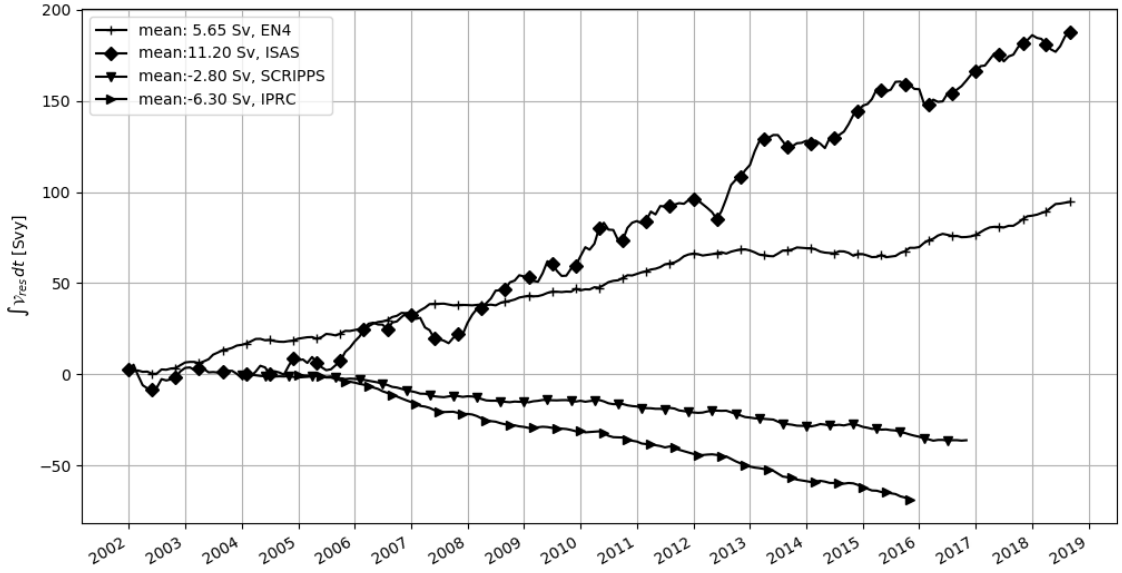

Figure 2-6: The 2002-2019 accumulated domain convergence of volume fluxes due to geostrophic and ageostrophic velocities $\mathcal{V}_{\text{res}}$ (the *a priori* values), calculated using the datasets: EN4 indicated in +, ISAS indicated in ♦, Scripps indicated in ▼, and IPRC indicated in ►. In the legend are shown the mean convergence rates in Sv, with the negative sign indicating the divergence. Using the altimetry data, we calculated the 2002-2015 ocean volume change due to SSH (Figure 2-5). The SSH related ocean volume change is 0.016 Svy, with an associated rate of change of 1.1×10^{-3} Sv, much smaller than the volume residual. Thus, we did not plot the volume change due to SSH.

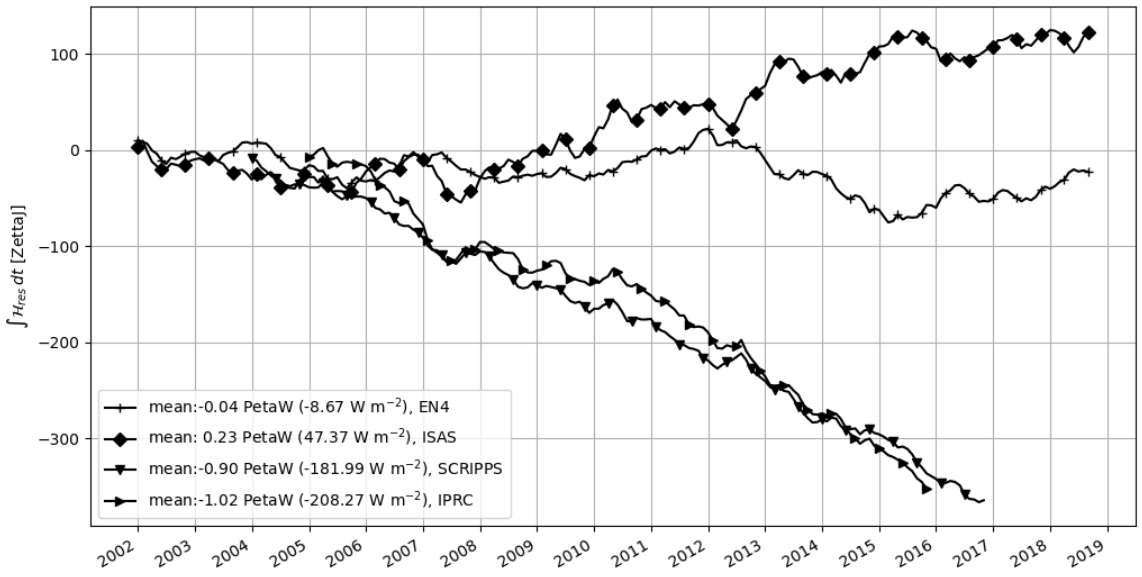

Figure 2-7: Similar to Figure 2-6, except we plotted the heat residual $\mathcal{H}_{\text{res}}$.

cal cross section at each boundary, displayed as the following:

$$\mathcal{H}_{\text{Geo}} = \mathcal{H}^o_{\text{Geo}} + (U'_{\text{W}}\overline{T_{\text{W}}} + U'_{\text{E}}\overline{T_{\text{E}}} \ + U'_{\text{N}}\overline{T_{\text{N}}} + U'_{\text{S}}\overline{T_{\text{S}}})\rho_o C_p \tag{2.18}$$

Combine Equation 2.17 and Equation 2.15, we obtained the rectification terms in the volume constraint.

$$\mathcal{V}_{\text{res}} = U'_W + U'_E + U'_N + U'_S + \mathcal{V}^o_{\text{res}} \tag{2.19}$$

Combine Equation 2.18 and Equation 2.16, we obtained the rectification terms in the heat constraint:

$$\mathcal{H}_{\text{res}} = (U'_{\text{W}}\overline{T_{\text{W}}} + U'_{\text{E}}\overline{T_{\text{E}}} + U'_{\text{N}}\overline{T_{\text{N}}} + U'_{\text{S}}\overline{T_{\text{S}}})\rho_o C_p + \mathcal{H}^o_{\text{res}} \tag{2.20}$$

where $\mathcal{V}^o_{\text{res}}$ and $\mathcal{H}^o_{\text{res}}$ are the volume and heat residual calculated using *a priori* estimate of the geostrophic velocity field. The *a posteriori* residual $\mathcal{V}_{\text{res}}$ and $\mathcal{H}_{\text{res}}$ would be close to zero to be considered a balanced budget. Given such, we employed the linear inverse method to deduct a realistic geostrophic volume transport at four boundaries from its *a priori* estimate. The constraints, Equation 2.19 and Equation 2.20, can be rewritten in the matrix form:

$$\mathbf{Y} = \mathbf{A}\,\mathbf{X}$$

Thus the matrix $\mathbf{A}$ can be written as:

$$\mathbf{A} = \begin{bmatrix} 1 & 1 & 1 & 1 \\ \overline{T_{\text{W}}} & \overline{T_{\text{E}}} & \overline{T_{\text{N}}} & \overline{T_{\text{S}}} \end{bmatrix}$$

The unknown vector $\mathbf{X}$ can be written as:

$$\mathbf{X} = \begin{bmatrix} U'_W & U'_E & U'_N & U'_S \end{bmatrix}^T$$

The measurable variable $\mathbf{Y}$ can be written as:

$$\mathbf{Y} = \begin{bmatrix} \mathcal{V}^o_{\text{res}} & \mathcal{H}^o_{\text{res}}/(\rho_o C_p) \end{bmatrix}^T$$

To solve this problem, we employed the stochastic approach (Jackson, 1979) by assuming the variables and the constraints follow Gaussian distribution. We chose to allow error for volume and heat residuals to tolerate the variability of the unconstrained terms. These terms include: the heat diffusion due to mixing, the ageostrophic vertical velocity at 800 m, etc. We set the volume residual $\mathcal{V}_{\text{res}}$ to have an allowed error of $0.5\,Sv$, 26% of the standard deviation of the geostrophic volume convergence in the domain of study. The heat residual $\mathcal{H}_{\text{res}}$ accordingly has an allowed error of $0.5\overline{T}\,\text{Sv}\,^{\circ}\text{C}$, where $\overline{T}$ denotes the averaged temperature at four boundaries at each time step. The heat residual show a magnitude of $O(1)\,\text{W}\,\text{m}^{-2}$, as converted to the unit of equivalent heat flux. This is set to share the same order of magnitude as the heat diffusion due to mixing (see details in Section 2.3.6.3). We set the allowed error of 20 Sv for the *a priori* geostrophic volume flux at each boundary. During the period of $2003-2018$, the *a priori* estimate of the Gulf Stream volume flux at the western boundary has an overall average of 48 Sv, an underestimate by $15-20$ Sv compared with that estimated by Colin de Verdière and Ollitrault (2016). We used the matrix inverse solver to solve $\mathbf{Y} = \mathbf{A}\,\mathbf{X}$ on a monthly step.

2.3.6.2 Stochastic inversion

We used stochastic inversion (Jackson, 1979; Mercier, 1986) to obtain the optimized estimate, in the condition that the probability density functions of variables and constraints are Gaussian. The unknown $\mathbf{X}$ has the *a priori* estimate $\mathbf{X_o}$ with an associated error covariance matrix of $\mathbf{C_o}$. The *a priori* estimate of the constraints are $\mathbf{Y_o} = \mathbf{A}\mathbf{X_o}$ with an associated error covariance matrix of $\mathbf{A}\,\mathbf{C_o}\,\mathbf{A^T}$. The *a posteriori* estimate $\mathbf{X}_*$ and the associated error covariance matrix $\mathbf{C}_*$ are written as:

$$\mathbf{X}_* = \mathbf{X_o} - \mathbf{Q}\cdot\mathbf{Y}(\mathbf{X_o}) \qquad \mathbf{C}_* = \mathbf{C_o} - \mathbf{Q}\cdot\mathbf{F}\cdot\mathbf{C_o} \tag{2.21}$$

where

$$\mathbf{Q} = \mathbf{C_o}\cdot\mathbf{F^T}\cdot(\mathbf{F}\cdot\mathbf{C_o}\cdot\mathbf{F^T} + \mathbf{C_T})^{-1} \tag{2.22}$$

and $\mathbf{F}$ is the Jacobian matrix, defined as:

$$F^{ik} = \frac{\partial Y^i}{\partial X^k}$$

In the linear case, $\mathbf{F} = \mathbf{A}$.

As a result of this step, we performed this inversion on both volume and heat constraints, yielding a rectification of the horizontal velocities at the four boundaries. We called these rectified fields the *a posteriori* estimate.

2.3.6.3 Validation

Buget residual and mixing The *a posteriori* estimate of volume and heat residuals are calculated using Equation 2.15 and 2.16 respectively. We optimised flux terms at each time steps. The time-averaged *a posteriori* volume residual has a mean of 0.38 Sv. This is of the same magnitude as the allowed error of 0.5 Sv set in the inverse model. The standard deviation of the *a posteriori* volume residual is 1.35 Sv (Figure 2-8), a large fluctuation compared with the allowed volume error of 0.5 Sv.

Figure 2-8: The 2003-2018 *a posteriori* estimate of volume convergence residual. The average volume residual of all datasets is represented in the solid black curve. The unbiased standard deviation is shaded in light blue. It is calculated using ocean datasets ISAS, EN4, Scripps, and IPRC combined with atmosphere reanalysis datasets NCEP and ERA.

The *a posteriori* estimate of the heat residual has a mean of -0.03 PetaW (Figure 2-9). This is in the same order of magnitude as the allowed error of $0.5\,\text{Sv} \cdot \overline{T}$ in the inverse model, $O(10^{-2})$ PetaW. The heat residual mean, converted to the unit of equivalent heat flux, is $-5.45\,\text{W m}^{-2}$. The climatological mean of the heat diffusion due to mixing is about $-2.72\,\text{W m}^{-2}$ (Figure 2-10). On average, 50% of the heat residual is attributed to the heat diffusion due to mixing. The standard deviation of

the heat residual is $9.36\,\mathrm{W\,m^{-2}}$. The standard deviation of the heat diffusion due to mixing is $2.43\,\mathrm{W\,m^{-2}}$, which is contained in the heat residual variability range.

The *a posteriori* estimate does not depend that much on the selected product. Theoretically the method assumes no bias on heat contraint residual. However, the heat residual presented a bias which sign was compatible with the sign of eddy diffusivity. The standard deviation of the heat residuals is about $9.36\,\mathrm{W\,m^{-2}}$, which is not that small. It is about the amplitude of the expected error on the air-sea heat fluxes.

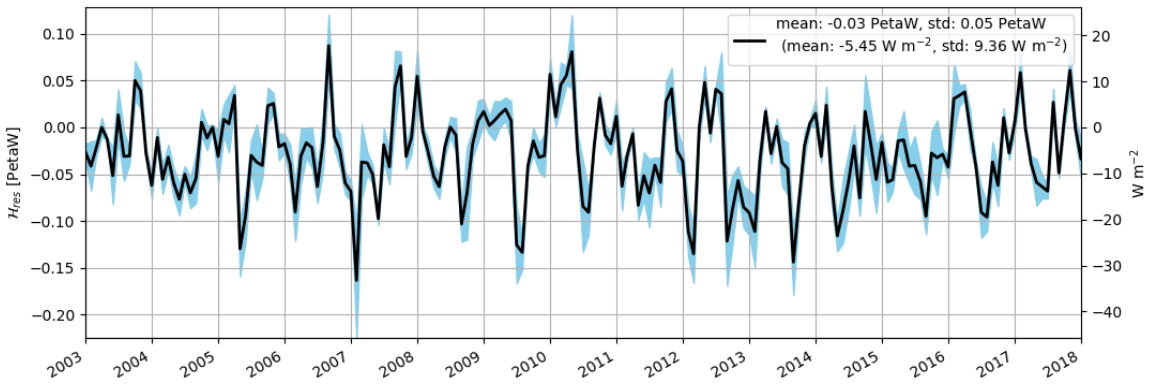

Figure 2-9: The 2003-2018 *a posteriori* estimate of heat convergence residual, using same datasets as in Figure 2-8 The average heat residual of all datasets is represented in the solid black curve. The unbiased standard deviation is shaded in light blue. They are in the unit of both PetaW and $\mathrm{W\,m^{-2}}$, given the surface area of domain of analysis is $S = 4.918 \times 10^{12}\,\mathrm{m^2}$

Volume and heat transport at the western boundary We calculated the inward volume flux at the western boundary of the domain of study (Figure 2-11). The volume flux at the western boundary of the domain of analysis, in the *a posteriori* estimate shows a range of $20.32 - 62.9\,\mathrm{Sv}$ based on different datasets. The estimate calculated using the SCRIPPS and NCEP datasets shows a mean of $20.32 \pm 17.61\,\mathrm{Sv}$ (figure not shown). Admittedly, this estimate of western boundary current volume flux is at the lower end. Along the vertical axis, the last grid point around 800 m in the SCRIPPS dataset is 793.3 m, and the slab thickness around this grid point is about 49.4 m.

The estimate calculated using the EN4 and NCEP datasets shows a mean of

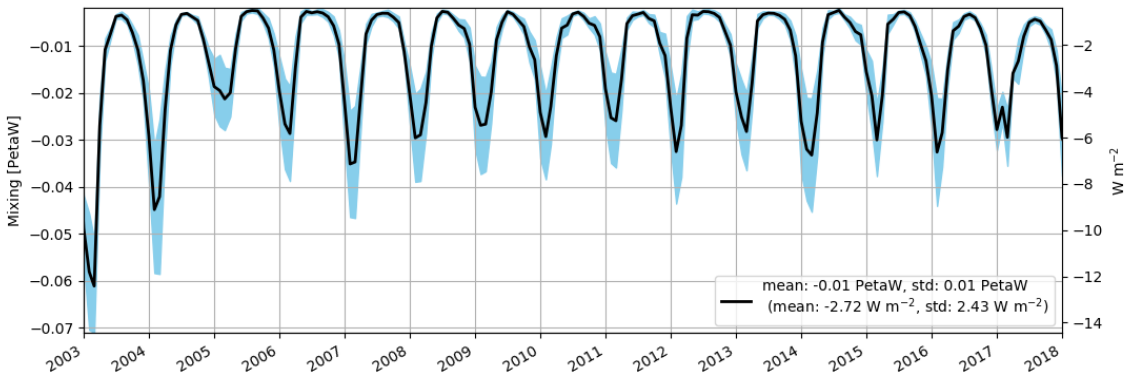

Figure 2-10: The 2003-2018 *a posteriori* estimate of heat diffusion due to mixing, using same dataset as in Figure 2-8. They are in the unit of both PetaW and W m^{-2}, similar to those in Figure 2-9

62.9 ± 14.66 Sv (figure not shown). This estimate is in line with the estimate made by Colin de Verdière and Ollitrault (2016). Along the vertical axis, the last grid point around 800 m in the EN4 dataset is 799.5 m, and the slab thickness around this grid point is about 168.5 m. However, the last grid thickness on the vertical axis around 800m is not responsible for the discrepancies (a factor of 3) among different ocean state estimate datasets.

2.4 Gulf Stream positioning

In the domain of analysis, the Gulf Stream enters from the western boundary, and travels along the northern boundary (Figure 2-1). The recirculation gyre is situated to the south of the Gulf Stream and occupies the southern part of the domain of analysis. To examine the Gulf Stream positioning in the interannual scale, many estimates have been developed. Kelly et al. (1996) used zero surface wind stress curl to indicate the position of Gulf Stream in the ocean. Kelly et al. (2010) used the maximum meridional gradient of SSH around the Gulf Stream region to track the Gulf Stream path. Frankignoul et al. (2001) used the 17°C isotherm at 200 m in the Gulf Stream region to identify the Gulf Stream path. Joyce et al. (2000) used 15°C isotherm at 200 m to indicate the northern boundary of the Gulf Stream.

Here we investigated the Gulf Stream position by adopting the isotherm of 15°C at 200 m as the northern boundary of the Gulf Stream. With this isotherm, we divided our domain of study in "cold part" and "warm part".We define an index α as the ratio between the domain area south of 15°C isotherm, namely, the "warm area"

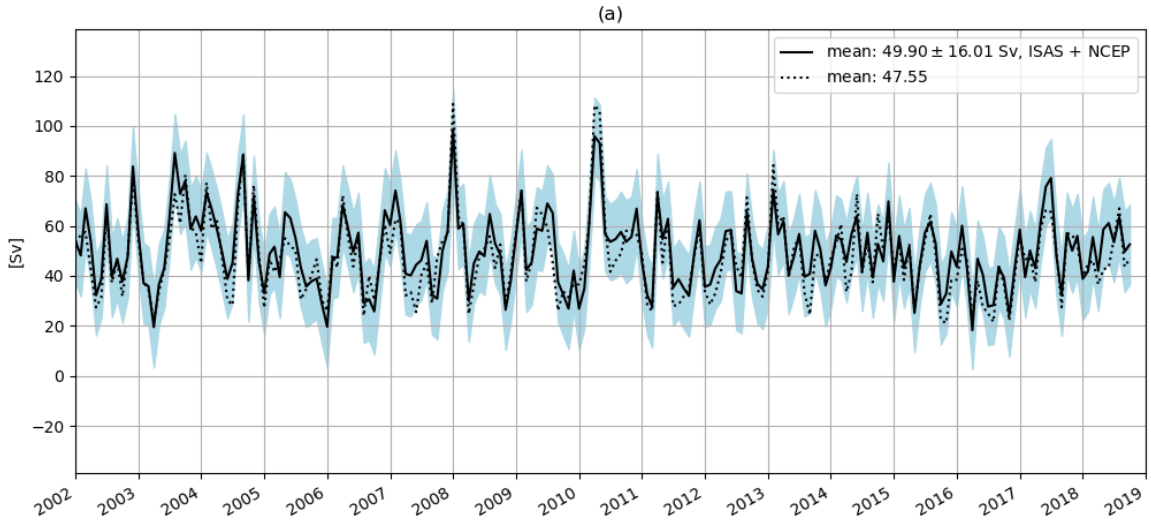

Figure 2-11: The *a posteriori* inward volume flux at the western boundary of the domain of study, in the unit of Sv. For the calculation, we used the ISAS dataset and the NCEP dataset. The solid line indicates the *a posteriori* inward volume flux. The dashed line indicates the *a priori* inward volume flux.

and the overall domain of study. A larger (smaller) α indicates a larger (smaller) "warm area", corresponding with a northward (southward) meridional shift of the Gulf Stream (Figure 2-12).

2.5 To identify EDW

The EDW, on a T/S diagram (Figure 2-13 a and b) is identified as the nearly homogeneous water mass around 18^oC in temperature and $36.0 - 36.7$psu in salinity (Speer and Forget, 2013). To identify the EDW there are different criteria (Forget et al., 2011). The EDW was to the first order selected as the water with temperature between $17 - 19^o$C , a common and rough criteria to identify EDW also used by Worthington 1976, Kwon and Riser 2004, Maze et al. 2009, Forget et al. 2011 etc. Moreover, a stratification criteria is often added to address the homogeneity of the EDW. Kwon and Riser (2004) used vertical temperature gradient $\partial T/\partial z < 0.006^o$C m^{-1}, and Forget et al. (2011) examined the EDW volume using two potential vorticity criteria: PV $< 1.5 \times 10^{-10}$m^{-1}s^{-1} and PV $< 2.0 \times 10^{-11}$m^{-1}s^{-1}.

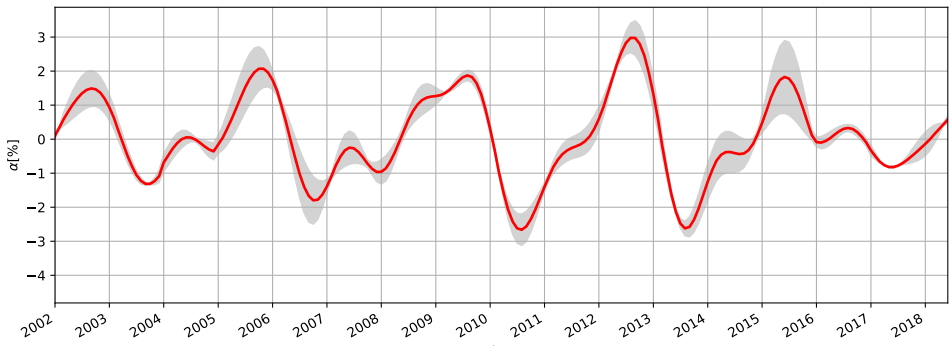

Figure 2-12: 2003-2018 interannual variability (15-50 month band-pass window) of Gulf Stream positioning, measured by index α (as a percentage), details see 2.4. A positive α indicates a northward shifted Gulf Stream. The mean value of all datasets (ISAS, EN4, Scripps, and IPRC) is represented by the solid red curve, and the unbiased standard deviation is shaded in light grey.

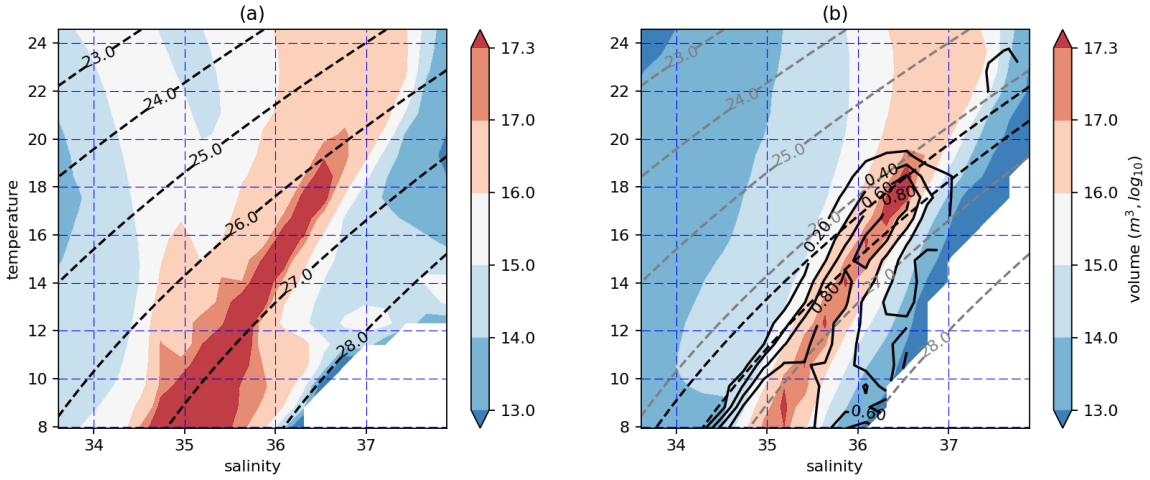

Figure 2-13: Volumetric climatology of North Atlantic waters during the period of 1966-2017 in the T/S plan of: (a) North Atlantic and (b) EDW region ($85^{o} - 40^{o}$W, $15^{o} - 40^{o}$N). The dashed contours are the potential density in $\mathrm{kg\,m^{-3}}$. In (b), the black dashed contours are the potential densities of $26.2\,\mathrm{kg\,m^{-3}}$ and $26.6\,\mathrm{kg\,m^{-3}}$. The solid contours are the percentage of EDW volume over total water volume in each bin. We used data from EN4 and plotted the log volume of each bin with intervals of 0.88^{o}C and of 0.23 psu (20 bins over the temperature of range $7.5^{o} - 25^{o}$C and 20 bins over the salinity of range $33.5 - 38$ psu).

2.5.1 Temperature criteria

We used the 17-19 degree layer to obtain a primary estimate of EDW volume time series. Figure 2-14(a) shows the climatological EDW thickness for the 1966-2017 period. The thickness reaches more than 300m along the equatorward flank of the Gulf Stream Extension, with a monthly standard deviation reaching 80m slightly to the north of climatological mean maximum. Figure 2-14(b) shows the typical seasonal cycle of EDW volume. We see from April to October, a rapid and then steady erosion of the EDW volume mainly driven by mixing with the seasonal pycnocline (Billheimer and Talley, 2016b). From November to March, the EDW volume increases, reaching the largest volume in March. The EDW seasonal formation is primarily driven by surface water mass transformations related to winter time buoyancy loss (Forget et al., 2011; Maze and Marshall, 2011). The seasonal cycle amplitude is $1.55 \times 10^{14}\mathrm{m}^3$, a value that is in line with Forget et al. (2011) estimate. The interannual variability amplitude is $5.0 \times 10^{14}\mathrm{m}^3$, a value that is remarkably larger than the seasonal cycle. Again, our estimate is in line with the bibliography (Kwon and Riser, 2004; Levine et al., 2011).

Figure 2-14 shows the thickness standard deviation pattern, that is mainly associated with the seasonal ventilation of the mode water through the mixed layer seasonal variability (not shown). Indeed, our maximum standard deviation region corresponds to the EDW formation region, as described by Maze et al. (2009) for instance.

Note that we used the seasonal maximum area between $17^{\mathrm{o}}\mathrm{C} - 19^{\mathrm{o}}\mathrm{C}$ as the EDW seasonal maximum outcropping region (referred to as outcropping region).

2.5.2 Density-stratification criteria

We employed the density-stratification criteria to define the EDW to have a more solid understanding on its physical properties, seasonal and interannual variablity.

To generate the time series of total EDW, we used the density criteria ranging from $26.2 - 26.6\,\mathrm{kg\,m^{-3}}$ and stratification criteria from $1.5 \times 10^{-10}\,\mathrm{m^{-1}\,s^{-1}}$ (Forget et al., 2011). The stratification criteria shows that more than 80% of the water with a temperature of $18^{\mathrm{o}}\mathrm{C}$ and a salinity of 36.5 psu in the EDW region is homogeneous (Figure 2-13b). The advantage of adding stratification criteria is that it more precisely captures the EDW.

The time series of EDW using density/PV method is compared with that of the temperature criteria method in both seasonal and interannual time scale (blue and black lines in Figure 2-15 a and b, respectively). The seasonal variability of EDW using density/PV method has a peak-to-peak amplitude of 17.5 Svy, which is in the

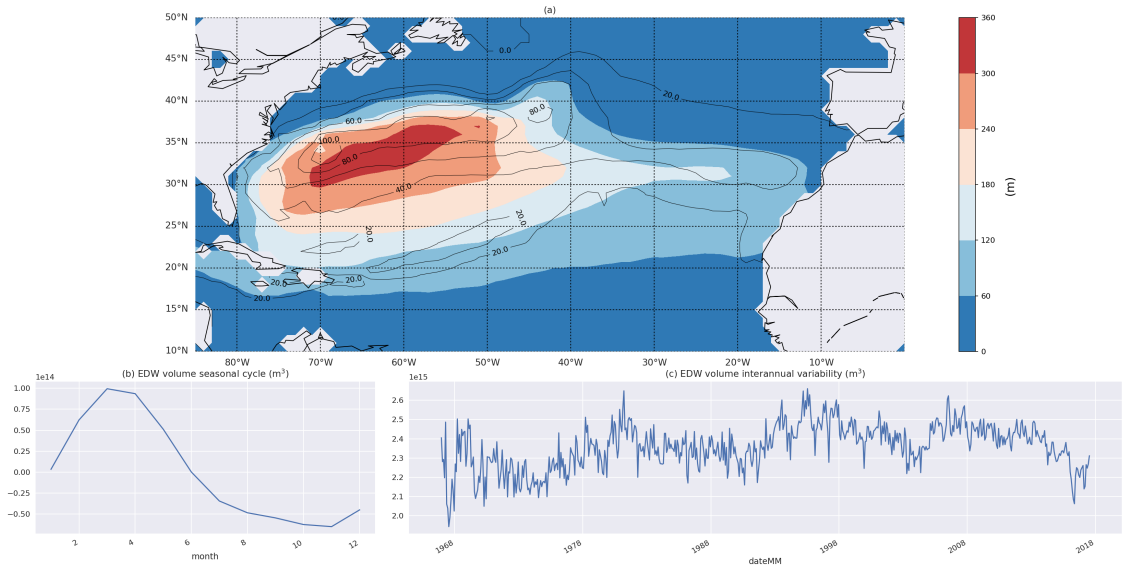

Figure 2-14: Climatological EDW thickness. (a) maps of the mean and standard deviation of the climatological EDW thickness, (b) EDW volume seasonal cycle, and (c) EDW volume interannual variability (seasonal cycle removed). EDW is simply defined as the 17 to 19 ^{o}C layer. This climatology was computed for the 1966-2017 period, using monthly mean values from the EN4 ocean dataset (Good et al., 2013).

range of estimation by Forget et al. (2011). The interannual variability of EDW in March using density/PV method has a peak-to-peak amplitude of 41.2 Svy, within the scales of interannual EDW volume estimates by Kwon and Riser (2004).

Meanwhile, this method presents challenges in practice when we used the EN4 dataset, where the potential vorticity and density were derived variables from temperature and salinity, containing large accumulated uncertainties. For instance, we found density inversion and noisy structures in the upper ocean layers, which were adding difficulties in our interpretation of the signals. To solve this problem, we also employed other observational datasets, such as ISAS, SCRIPPS and IPRC to corroborate the EDW bulk volume time series (Figure 2-15).

2.5.2.1 Ventilated EDW volume

The mixed layer is an ocean surface layer in direct contact with the atmosphere, stirred by turbulence, homogenizing temperature and other properties within some range of depths. Surface ocean cooling and salinization, associated with negative surface buoyancy flux, sensible heat loss, or latent heat loss due to surface evaporation, increase surface water density, leading convective motion within the mixed layer. The

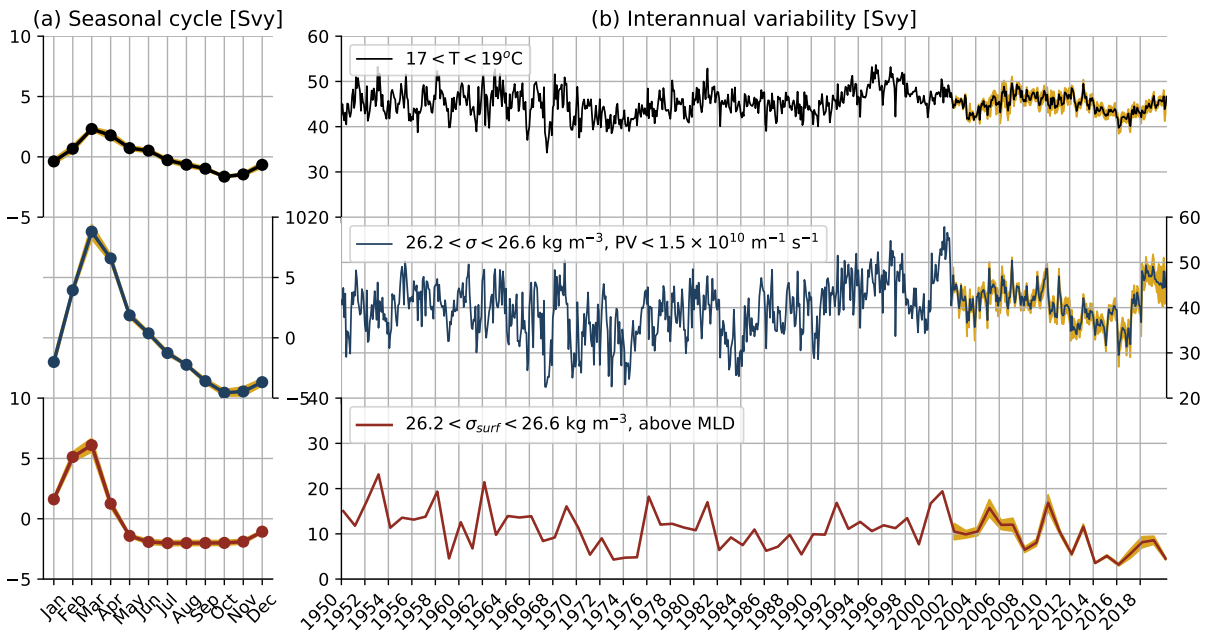

Figure 2-15: (a) The seasonal cycle and (b) the interannual variability of EDW volumes in March calculated using: temperature criteria, ($17 < T < 19$°C, black line), density/PV criteria ($26.2 < \sigma < 26.6\,\mathrm{kg\,m^{-3}}$, PV $< 1.5 \times 10^{-10}\,\mathrm{s^{-1}\,m^{-1}}$, blue line), and outcropping/MLD criteria ($26.2 < \sigma_{\mathrm{surf}} < 26.6\,\mathrm{kg\,m^{-3}}$ above MLD, red line). The shaded areas indicate the standard errors calculated based on the ISAS, EN4, Scripps, and IPRC datasets.

depth of this nearly homogeneous layer, namely the mixed layer depth (MLD), generally is about $50-100$m with large global spatial variation. In northern North Atlantic region, the MLD can exceed 1000 m. In subtropical region, along the equatorward flank of western boundary current, the MLD can reach $300-500$m, which allows the formation of volumnous pycnostad. Note that below the mixed layer, temperature and salinity change rapidly with depth, in the summer time, forming the seasonal pycnocline.

We examined the winter ventilated EDW volume, not including the EDW that is trapped under the mixed layer. We selected the winter surface EDW outcropping regions, with sea surface density ranging from $26.2-26.6\,\mathrm{kg\,m^{-3}}$, and integrating this outcrop down to the mixed layer depth. The mixed layer depth is evaluated using the second criteria developed by de Boyer Montégut et al. (2004), as the depth of the sea water denser than that of 10-meter by $0.02\mathrm{kg/m^3}$.

Concerning a typical seasonal cycle, Maze et al. (2009) showed that from spring to summer air-sea flux destroys the EDW, while the winter air-sea flux helps to form

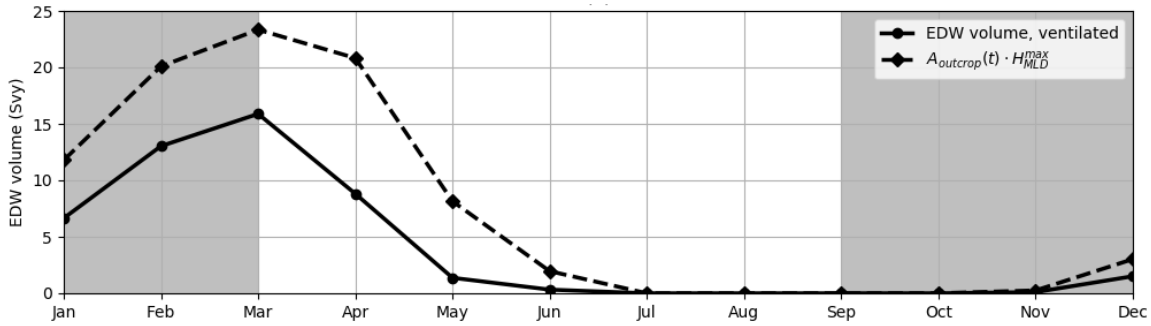

Figure 2-16: The seasonal cycle of the ventilated EDW volume (solid contour), and that of the outcropping area multiplied by the deepest mixed layer depth (dashed contour) in the unit of Svy ($1\,\mathrm{Svy} = 3.154 \times 10^{13}\,\mathrm{m}^3$). The seasonal cycles are calculated in the domain of study with a surface area of ($S = 4.918 \times 10^{12}\,\mathrm{m}^2$). The months of wintertime is shaded in grey.

EDW in the winter time, and the EDW formation rate peaks in early spring. Forget et al. (2011) showed that in a typical seasonal cycle, the EDW formation rate is dominated by air-sea heat flux, while advection and mixing play comparably a minor role. In summer and early fall, the air-sea heat flux is positive (the solid blue line in Figure D-1), warming the ocean surface, and OHC increases over time (the red dashed line with dots in the same Figure). During this time period, the EDW outcropping area and the EDW ventilated volume are both zero (the solid and dashed black lines, respectively, in Figure 2-16). Starting in late fall and early winter, air-sea heat flux is negative, cooling the ocean surface, and OHC decreases over time. The EDW outcropping starts in November (Figure 2-16). In March, the EDW outcropping area expands to the seasonal maximum, corresponding with a seasonal maximum in EDW ventilated volume about 16 Svy. Starting in mid-March, the air-sea heat flux becomes positive, warming the ocean surface, and OHC increases over time. By April, the EDW ventilated volume decreases to 8 Svy, dropping by 50% from March. The seasonal cycle of ventilated EDW volume calculated with this method amplitude of $3.4 \times 10^{14}\mathrm{m}^3$ (10.79Svy) relative to 1 December, in line with Forget et al. (2011).

In summary, to estimate the total EDW volume, we employed the density criteria ranging from $26.2 - 26.6\,\mathrm{kg\,m}^{-3}$ and stratification criteria from $< 1.5 \times 10^{-10}\,\mathrm{s}^{-1}\,\mathrm{m}^{-1}$. To estimate the ventilated EDW volume, we selected the winter surface EDW outcropping region, with a sea surface density ranging from $26.2 - 26.6\,\mathrm{kg\,m}^{-3}$, and integrated this outcrop down to the mixed layer depth.

2.6 Interannual time scales

2.6.1 Signal decomposition

To obtain the interannual variability of time series, we removed from the original time series the climatological mean, the linear trend, and the seasonal cycle. This process can be expressed as:

$$Y = Y_{\mathrm{LT}} + [Y] + Y_{\mathrm{SC}} + Y' \tag{2.23}$$

where Y denotes the raw time series; Y_{LT} denotes the linear trend of Y; $[Y]$ denotes the mean of Y after detrending; and Y_{SC} denotes the typical seasonal cycle. The seasonal cycle Y_{SC} is calculated using the first two annual harmonics. We removed from the original signal the 12-month and 6-month frequency bands.

2.6.2 Time filtering

We applied to the signal Y' a high-pass filter of 50 months (4.2 years) to remove the decadal and multi-decadal variability. We applied to the signal Y' a low-pass filter of 6 months to rid the interannual time series of the high frequency signal. We used running mean method. We refer to as the low frequency variability, the variability of a frequency larger than 50 months. This process can be expressed as:

$$Y' = [Y']_{50\,\mathrm{mo}} + Y''$$

where $[Y']_{50\,\mathrm{mo}}$ denotes the 50-month running mean of Y'. We referred to Y'' the raw interannual signal. Then we smoothed the anomaly Y'', by applying a 6-month running mean:

$$Y'' = [Y'']_{6\,\mathrm{mo}} + Y'''$$

where $[Y'']_{6\,\mathrm{mo}}$ denotes the 6-month running mean of Y'', which we referred to as the interannual signal (6-50 month variability).

In subsequent chapters, we further smoothed the anomaly $[Y'']_{6\,\mathrm{mo}}$, by applying a 15-month running mean. We referred to this signal as the 15-50 month variability.

2.7 Definition of extremes

In the following chapters, I calculate the OHC extremes, the September-March ΔOHC extremes, and the freshly ventilated EDW volume extremes, in the interannual time scales.

I define the monthly OHC extreme occurrences as those whose OHC exceeds ±1.5 times the standard deviation of the interannual variability of OHC monthly time series. The extreme OHC occurrences are the outliers, making up 6.7% of the 1981-2018 monthly OHC values.

I define the September-March ΔOHC extreme as the outliers that exceeds ±1.5 times the standard deviation of the September-March ΔOHCs in the period of 2004-2018.

I define the EDW freshly ventilated volume extreme as the outliers that exceeds ±1.0 the standard deviation of the interannual variability of EDW freshly ventilated volume.

2.8 Buoyancy Budget

2.8.1 Fixed-domain buoyancy content anomaly $\mathbf{BCA_{Sep}}$

To investigate the impact of preconditioning on the EDW winter formation, I examine the buoyancy budget in the mixed layer in the same horizontal region of the domain of study. Billheimer and Talley (2013) used buoyancy content anomaly (BCA) from the surface down to the $26.7\,\mathrm{kg\,m^{-3}}$ isopycnal to give an appropriate measure of the amount of buoyancy that would need to be removed in order for the EDW to be ventilated to the surface.

First of all the buoyancy anomaly b, in the unit of $\mathrm{m\,s^{-2}}$, is the buoyancy difference between the water parcel in upper water column and that at the bottom of the EDW, and it is defined as:

$$b = \frac{g}{\rho_o}(\sigma - \sigma_o)$$

where, g is gravity, $(\sigma - \sigma_o)$ is the relative density difference between a water parcel and that at the bottom of EDW (the upper part of the permanant pycnocline), where $\sigma_o = 26.7\,\mathrm{kg\,m^{-3}}$ (Feucher et al., 2019).

To obtain the BCA, we integrated the buoyancy b over the water column above σ_o isopycnal surface in the domain of study:

$$\text{fixed-domain BCA} = \int_S \int_{-h_{\sigma_o}}^{0} b\,dz\,dS \tag{2.24}$$

The fixed-domain $\mathrm{BCA_{Sep}}$ has a unit of $\mathrm{m^4\,s^{-2}}$. We chose the buoyancy content anomaly in September (fixed-domain $\mathrm{BCA_{Sep}}$) to measure the preconditioning at the beginning of the EDW ventilation season. When the fixed-domain $\mathrm{BCA_{Sep}}$ is high, the preconditioning is unfavorable to the EDW formation, and vice versa.

2.8.2 Relative September buoyancy content anomaly

To investigate factors that would influence the EDW formation, we focused our analysis on the change of buoyancy of the upper water column in the winter period (from September to March the following year). This is primarily driven by: air-sea heat flux, divergence of the horizontal heat advection/diffusion and initial conditions (or preconditioning). Such a buoyancy budget can simply be written as:

$$\mathrm{BCA_{Mar}} - \mathrm{BCA_{Sep}} = \int_S \int_{\mathrm{Sep}}^{\mathrm{Mar}} F_{\mathrm{surf}}\, dS\, dt - \int_S \int_{\mathrm{Sep}}^{\mathrm{Mar}} \int_{\mathrm{MLD_{Mar}}}^{z=0} \nabla \cdot (b\mathbf{U})\, dz\, dS\, dt + \mathrm{Mixing} \tag{2.25}$$

Note that the BCA in this section does not refer to the fixed-domain $\mathrm{BCA_{Sep}}$ from the previous section. Rather, the BCA is defined as:

$$\mathrm{BCA} = \int_S \int_{\mathrm{MLD_{Mar}}}^{z=0} b\, dz\, dS \tag{2.26}$$

The unit of the BCA is $\mathrm{m^4\,s^{-2}}$. Different from the fixed-domain $\mathrm{BCA_{Sep}}$, the BCA in this section has a vertical domain of integration from the sea surface to $\mathrm{MLD_{March}}$. This depth refers to the maximum mixed layer depth reached during the EDW ventilation period (normally in March). This depth is a fixed value for each year, from September-March. F_{surf} is the surface buoyancy flux in the unit of $\mathrm{m^2\,s^{-3}}$ due to net surface heat flux. Here we assumed that the winter surface heat loss is the major contribution to the surface buoyancy flux, other sources (such as the surface salinity flux due to fresh water input or sea surface evaporation/precipitation) that may also contribute to the surface buoyancy flux are neglected.

The BCA change from September to March of the following year (ΔBCA from this point on) is described in $\mathrm{BCA_{Mar}} - \mathrm{BCA_{Sep}}$. The preconditioning at the beginning of the winter EDW ventilation period is described in the term $\mathrm{BCA_{Sep}}$, with an integration over the following March mixed layer each year. We found that $\mathrm{BCA_{Sept}}$ largely depends on the March mixed layer depth.

We referred to $\mathrm{BCA_{Sep}/MLD_{March}}$ as the $\mathrm{BCA^*_{Sep}}$.

$$\mathrm{BCA^*_{Sep}} = \mathrm{BCA_{Sep}/MLD_{March}}$$

where $\mathrm{MLD_{March}}$ refers to the mixed layer depth of March of the current year, while $\mathrm{BCA_{Sep}}$ is the buoyancy content anomaly in September of the previous year. We used $\mathrm{BCA_{Sep}/MLD_{March}}$ to evaluate the preconditioning of the water column in September. To rule out the variability of $\mathrm{MLD_{March}}$, the total winter surface buoyancy loss is the air-sea buoyancy flux integrated over the winter EDW ventilation period, as described

in $\int_{\text{Sep}}^{\text{Mar}} F_{\text{surf}}$. The divergence of horizontal buoyancy advection associated with the Gulf Stream is described in $\int_{\text{Sep}}^{\text{Mar}} \int_{\text{MLD}_{\text{Mar}}}^{z=0} \nabla \cdot (b\mathbf{U})\, dz\, dt$.

All the terms that have impacts on the March ventilated EDW volumes are examined from 1979-2017. Note that we used the year at the end of the ventilation period as the year for the whole period, including the fall and winter of the previous year. For example, Fall 2009-Spring 2010 is denoted as the ventilation period of 2010. All quantities are horizontally integrated over a domain within the 75 m yellow dashed contour in Figure 2-1.

2.9 Weather Regimes

To compute weather regimes, we followed Barrier et al. (2013) methodology, that is based on k-mean clustering of the principal components of the winter time climatological related atmospheric variables (for example, 500mb geopotential height, surface level pressure, etc.)

We utilized December-March in our weather regime calculation to match Barrier et al. (2013). In addition, to have a matched wintertime period, we re-generated a set of weather regimes using the period of September-March. We used the sea level pressure (SLP) and 500 hPa geopotential height from the NCEP dataset and ERA dataset. We selected the region of North Atlantic-Europe ($20 - 80^{o}$N, 80^{o}W $-$ 30^{o}E, Barrier et al. 2013; Cassou et al. 2004), as the domain of calculation. First of all, we obtained the monthly averaged wintertime NCEP time series data. We rid this data of the seasonal cycle. Then we applied the principal component analysis (PCA) weighting. Namely, for each pixel we multiplied with the square root of cosine of latitude to eliminate the unequal weighting on pixels surface area due to map projection from a sphere.

To obtain weather regimes, we performed the k-mean classification on 20 EOFs (explaining 98.5% variance) of the aforementioned pre-processed NCEP data. In the EOF space, the k-means clustering method (Michelangeli et al. 1995; Cassou 2008) is used to categorize the PC samplings around four centroids. Starting with random initialization of centroids, we ran the k-mean classifer 20 times to rule out the impact of initial conditions.

Our computation results are shown in Figure 2-17. Figure 2-17 (left panels) show the Atlantic Ridge regime, and a west-east dipole pattern (also known as the Blocking regime), and the asymmetric negative and positive NAO. Note that the Blocking regime pattern is in opposite sign from traditional Greenland Blocking regime, defined as the high pressure over Greenland (Davini et al., 2012; Hanna et al., 2013, 2014, etc).

Figure 2-17 (right panels) show 1948-2016 daily occurrences of each weather regimes. We see a strong interannual to multidecadal variability of each winter weather regime occurrences with no clear trends. In Figure 2-17, we also superimposed the EOF patterns and their associated principal component time series to highlight the refinement of the weather regime paradigm in allowing asymmetries, especially between the NAO+ and the NAO-. No filter has been applied when we calculated the weather regime. This enable us to keep high-frequency variability (synoptic scale variability of 2-6 days) to low-frequency variability (11-30 days) (Gulev et al., 2002).

We also calculated the weather regimes using other atmospheric variables, such as the 500 hPa and using other datasets, such as ERA. We obtained similar patterns of the weather regimes to those calculated using surface level pressure of the NCEP dataset (Figure 2-17 left panels). The time series corresponding to each weather regime daily occurrences are also consistent among all examined variables and datasets (Figure 2-18).

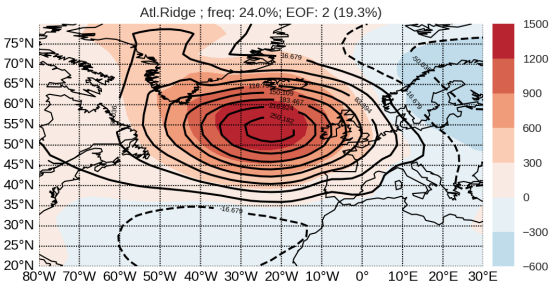
Atl.Ridge ; freq: 24.0%; EOF: 2 (19.3%)

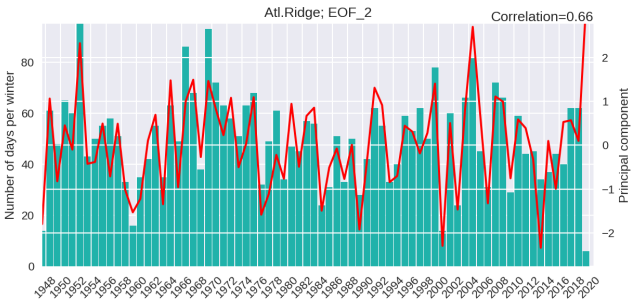
Atl.Ridge; EOF_2
Correlation=0.66
Number of days per winter
Principal component

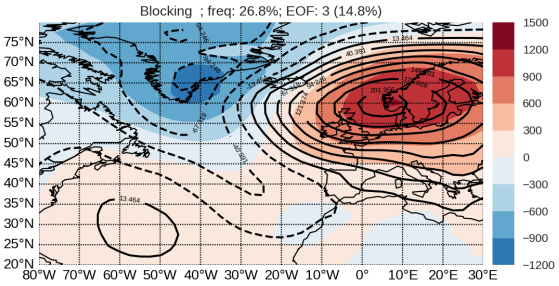
Blocking ; freq: 26.8%; EOF: 3 (14.8%)

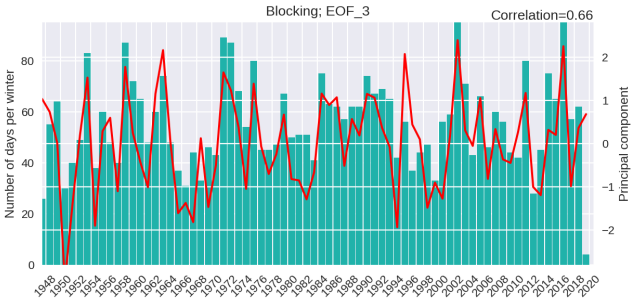
Blocking; EOF_3
Correlation=0.66
Number of days per winter
Principal component

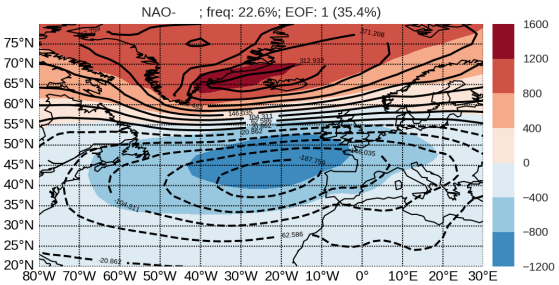
NAO- ; freq: 22.6%; EOF: 1 (35.4%)

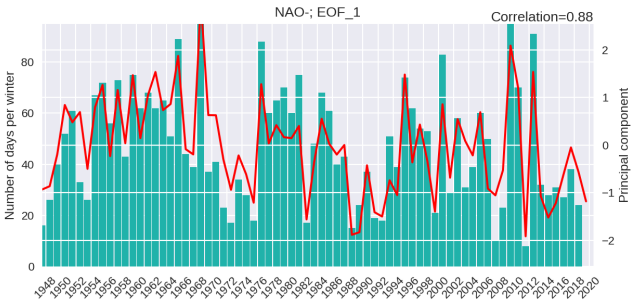
NAO-; EOF_1
Correlation=0.88
Number of days per winter
Principal component

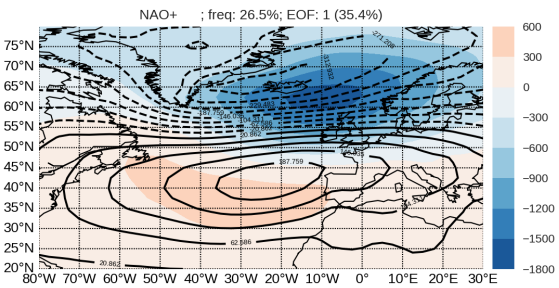
NAO+ ; freq: 26.5%; EOF: 1 (35.4%)

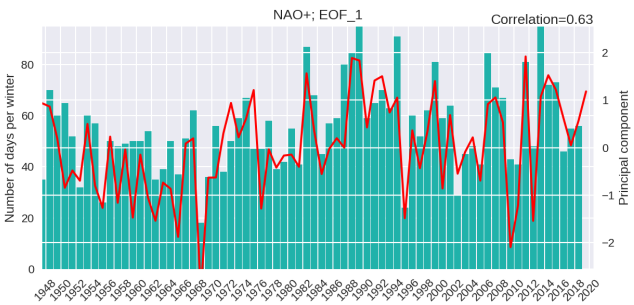
NAO+; EOF_1
Correlation=0.63
Number of days per winter
Principal component

Figure 2-17 *(previous page)*: (Left) Centroids of surface level pressure (SLP) anomalies for the four weather regimes (colors) and EOF-derived modes of variability computed from September-March averaged anomalies of the same variable (black contours). The variance explained by each EOF is indicated between parenthesis (Right). Number of days per winter of WR winter occurrences (bars) and corresponding principal components (PC) from EOF (the red solid line). The correlation between the occurrences and the PCs are indicated. For the last panel, NAO+ patterns in EOF is the NAO-EOF pattern multiplied by -1, and the same for its corresponding time series. This plot is realised using the NCEP dataset.

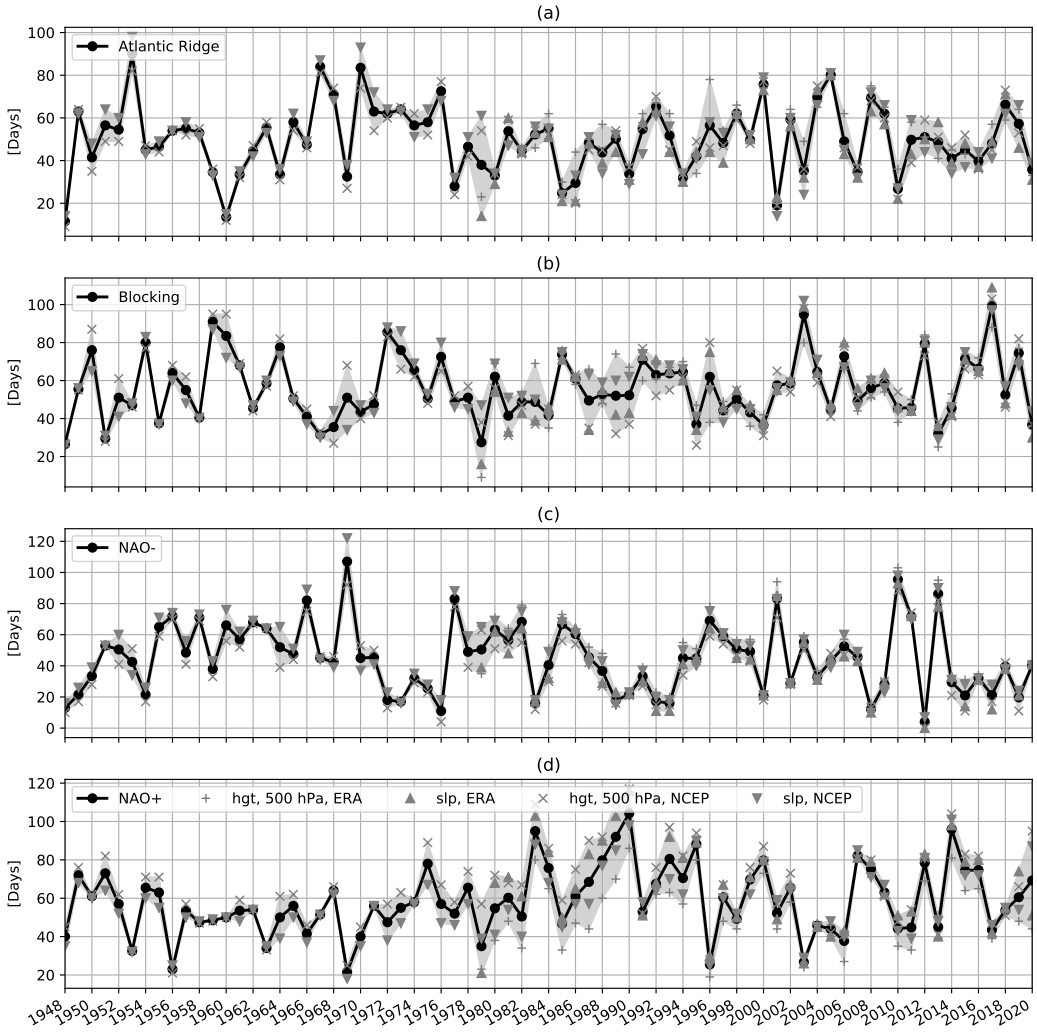

Figure 2-18: The interannual daily occurrences time series of the weather regimes: (a) Atlantic Ridge, (b) Blocking, (c) NAO-, and (d) NAO+. The means over all datasets (SLPs and 500 hPa geopotential heights from the NCEP and ERA datasets) are represented in the black dotted lines. The grey area represents the minimum-maximum range among all aforementioned datasets. The ERA 500 hPa geopotential height is indicated in +. The ERA SLP is indicated in ▲. The NCEP 500 hPa geopotential height is indicated in ×. The NCEP SLP is indicated in ▼.

CHAPTER 3

Heat Budget

3.1 Abstract

The heat in subtropical North Atlantic is mostly stored in the Eighteen Degree Water (EDW). Sitting atop the warming trend since 1970s, the interannual variability of EDW volume contains extreme occurrences, driven by mechanisms that are yet to be clarified. As the first step, we developed an observation-based ocean heat budget integral analysis of the upper 800 m in the western subtropical North Atlantic. We investigated the time series and extremes of OHC integrated over the region of interest. The literature indicates a dominance of geostrophy (i.e. Dong and Kelly, 2004), and of its certain bands of frequency (i.e. Lillibridge III and Mariano, 2013). We examined the heat transport by the Gulf Stream, Ekman-driven heat transport, air-sea heat fluxes, and mixing, the elements of the interannual variability of the ocean heat content (OHC) in frequency band. We will address the following questions:

1. What is the interannual OHC extreme frequency like at a multi-decadal time axis?

2. What are the respective roles of Ekman and geostrophic heat transports, as well as air-sea heat fluxes in wintertime interannual OHC variability?

3. We aim to verify with the bibliography that the Gulf Stream has a frequency band of 18 months, and use it to challenge the results of Dong and Kelly (2004).

4. Are the extreme years becoming more or less frequent since the last decade than before?

5. How would Gulf Stream variability, including meridional positioning and strength be related to the OHC interannual variability?

6. Is there a specific recipe explaining extreme occurrences?

On the interannual time scale, we observed in the western subtropical North Atlantic region, clusters of OHC extreme occurrences centered around 2010, mid 1990s,

and 1980. We observe two periods of absence of the extreme occurrences, from 2000-2006 and from 2014-2019. These two periods correspond with two MOC periods, one after strengthening in the early and mid-1990s, and the other after slowdown in 2009-2010.

The Ekman heat advection and the air-sea heat flux contain a dominant frequency band of > 30 months. Both Ekman heat advection and the air-sea heat flux are the direct indicators of the weather regimes, through surface wind stress, and through latent and sensible heat fluxes respectively. The Gulf Stream positioning drives the interannual variability of air-sea heat fluxes (within a frequency band of 15-50 month).

The geostrophic heat advection contains highly fluctuating frequency bands of 7-10 months, 13 months, and 18 months. The geostrophic heat advection is influenced by the strength of subtropical North Atlantic recirculation gyre.

The extreme occurrences of wintertime OHC have not become more frequent since the last decade. Most recently, we observed no extreme occurrences in the period of 2014-2019, the longest period without OHC extremes since 1950.

The Gulf Stream explains the variance of the air-sea heat flux in the frequency band of 15-50 month, with a correlation coefficient of 0.7. The correlation is larger than with any other major contributing factors. We observed no correlation between the Gulf Stream volume transport and interannual variability of OHC in the western subtropical North Atlantic region. But rather, the strength of its subtropical recirculation gyre impacts the OHC through geostrophic heat advection.

In short, we studied the OHC in the western subtropical Atlantic region to understand the "context" of EDW. This regional OHC is rather complex. Many possible interactions between the components of the OHC budget and/or the atmospheric forcing do not lead to a clear recipe for the OHC extremes.

3.2 Introduction

In the subtropical North Atlantic region, with modern observational datasets, most research has been done on examining the seasonal variability of heat content and its impact on the upper ocean stratification. Maze et al. (2009) studied in 2004–2006 period the seasonal impact of air-sea heat fluxes on subtropical Atlantic stratification. They showed that the air-sea heat flux in western subtropical Atlantic region is the key driving mechanism in the seasonal time scale. Forget et al. (2011) estimated for the 2004-2006 period the change of subtropical Atlantic stratification due to air-sea heat fluxes and ocean mixing. They quantified the seasonal variability of the subtropical Atlantic stratification. Further they attributed this seasonal variability to air-sea

heat fluxes and ocean mixing. Concerning the interannual variability of the heat content in the subtropical Atlantic region, Dong and Kelly (2004) investigated the roles of geostrophic heat advection associated with the Gulf Stream and the air-sea heat fluxes. They showed that the interannual variability of geostrophic heat advection is the dominant signal driving that of OHC in the subtropical Atlantic region. The modern datasets based on Argo floats provide more synoptic and pertinent observations of the ocean. Therefore, the studies in the interannual variability of ocean heat content anomaly (referred to as OHC) in the subtropical North Atlantic region are obliged to be verified using more modern datasets.

Lillibridge III and Mariano (2013) examined 18+ years of altimetry data, and showed that the Gulf Stream north-south positioning has important periods of 10 months, 1.5 years (18 months), and 2.8 years. The northern boundary of our domain of analysis passes the northern flank of the Gulf Stream. We investigated both the Gulf Stream positioning and strength to gain insights of the interannual variability of the geostrophic heat advection.

In this chapter, we employed the Argo data to produce the interannual variabilities of the ocean heat content and its major contributing factors, namely, the geostrophic heat advection, the Ekman heat advection, the air-sea heat fluxes, and mixing. Secondly, we analysed the period with extreme heat content values to understand the regional OHC. We aimed to provide this "context" as a preceding material of the EDW extremes in Chapter 4.

3.3 Direct Results

3.3.1 Periods with and without OHC extremes

We obtained the interannual variability of OHC using the band-pass filter method. Firstly, we removed the seasonal cycle from the detrended OHC signal. The mesoscale eddies have a decorrelation period of 6 months. To remove the mesoscale variability, we applied the low-pass filter of 6 months and high-pass filter of 50 months to rid the lowest frequencies.

Some studies suggest that extreme events are getting more and more frequent or intense. Understanding the dynamics of extreme is a prerequisite to better predict them. In this section, we investigated the interannual OHC extreme occurrences since 1950 (Figure 3-1). The extremes of OHC are chosen to exceed $\pm 3.63\,\mathrm{ZJ}$ (1.5σ) threshold of the interannual variability of OHC. Under this criteria, 112 months out of 840 total monthly samples (13.4% of the total months) are chosen as extremes using 1.5σ, where 6.7% are positive extremes, and the remaining 6.7% are negative.

In Figure 3-1, we observed clusters of extreme occurrences centered around 2010, mid 1990s, 1980, and mid 1960s. To help describe the frequency of extreme occurrences, we divided the time axis into several periods: 1950-1959, 1960-1974, 1975-1989, 1990-2004, and 2005-2019 (Table 3.1).

The period of 1975-1989 has the highest OHC extreme occurrences, 30 months. That indicates on average an extreme occurrence every 6 months. The most recent period of 2005-2019 has an OHC extreme occurrences of 24 months, the lowest of all 15-year periods since 1960s.

Year range	extreme [mo]	frac [mo]	positive	frac	negative	frac
2005-2019	24	7.5	8	22.5	16	11.3
1990-2004	26	6.9	17	10.6	9	20
1975-1989	30	6.0	13	13.8	17	10.6
1960-1974	26	6.9	14	12.9	12	15.0
1950-1959	6	20.0	4	30.0	2	60.0
1950-2019	112	7.5	56	15.0	56	15.0

Table 3.1: Extreme occurrences and corresponding fraction extremes from 1950-2019 in 15-year increments. Fraction extremes are the average number of months between two extreme occurences. For example, from 2005-2019, there is an average of 1 extreme occurence every 7.5 months.

3.3.2 Interannual Variability

In the period of 2002-2019, besides the EN4 dataset, the ISAS, Scripps, and IPRC datasets are also available. With multiple dataset, we examined OHC as well as its major contributing factors. The climatology and the seasonal cycle of the heat budget are presented in detail in Appendix D. In this section, we focused on the OHC interannual signal with ISAS, Scripps, and IPRC datasets (Figure 3-2). To be selected as extremes, all the datasets need to surpass the threshold.

We examined the frequency of extreme occurrences using a 6-year window, namely, 2002-2007, 2008-2013, and 2014-2019 (Table 3.2). In the period of 2014-2019, the interannual variability of OHC displays a total of 0 months of extremes, the lowest among all the three periods examined. In 2009-2010, the wintertime OHC decreases rapidly from positive extremes to negative extremes. The robustness of both these positive and negative extremes are agreed upon by all employed datasets. In the winter of 2004-2005, the OHC decreases, but not to an extreme extent according to

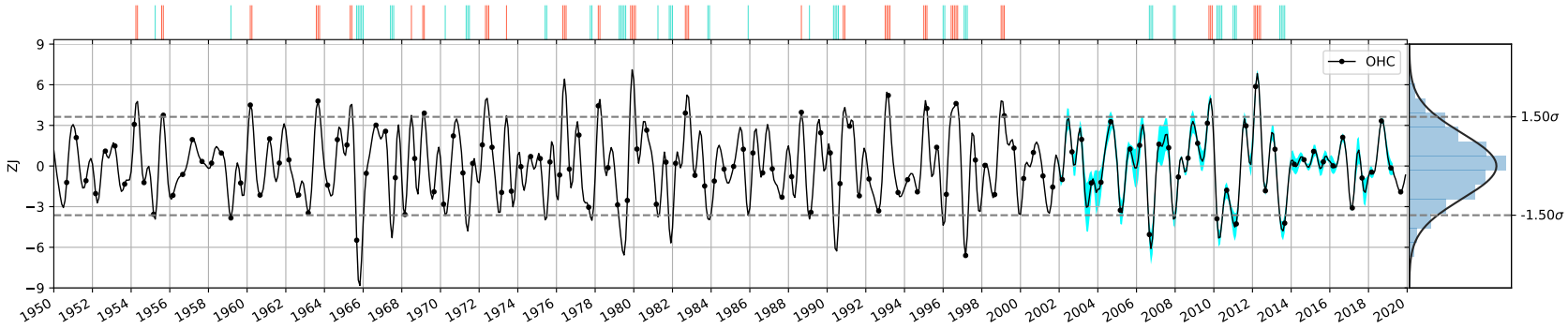

Figure 3-1: 1950-2020 interannual variability of OHC, an average over several products, and its occurrences of extreme months. The interannual variability of OHC is in solid black line with dots. The black dots on the solid black line indicate September and March, in order to highlight the wintertime OHC change. The unbiased standard deviation of OHC among all datasets (ISAS, EN4, Scripps, and IPRC) is shaded in blue. The grey dashed lines are the 1.5 standard deviation ($1.5\sigma = 3.63\,\mathrm{ZJ}$) of the time series. The histogram of interannual OHC values is represented to the right, superimposed with a Gaussian fit (solid black curve). The months with OHC greater than $1.5\,\sigma$ are in short solid red lines in the "rug" plot, and those smaller than $-1.5\,\sigma$ are in cyan.

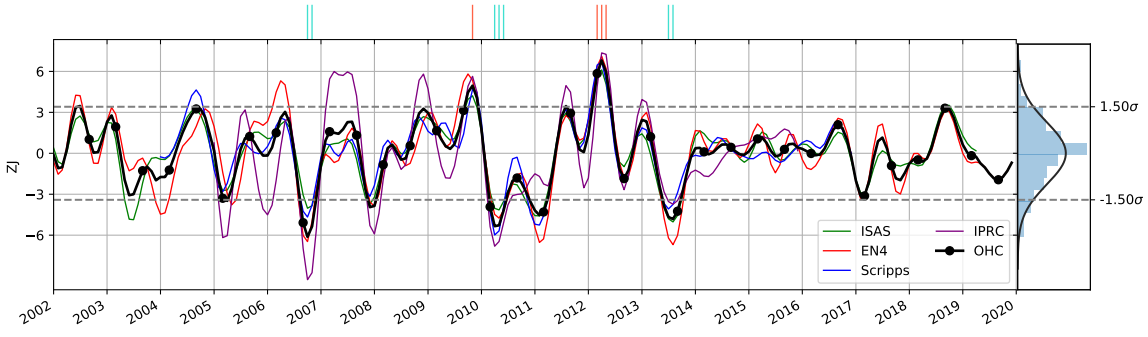

Figure 3-2: 2002-2019 interannual variability of OHC and occurrences of extreme months. The averaged OHC is in solid black line with dots. The black dots on the solid black line indicates the OHC values in September and March. In green is OHC calculated using the ISAS dataset, EN4 in red, Scripps in blue, and IPRC in purple. The grey dashed lines are the 1.5 standard deviation (1.5σ = 3.63 ZJ) of time series. The histogram of interannual OHC values is represented to the right, superimposed with a Gaussian fit (solid black curve). The months with OHC in all examined datasets greater than $1.5\,\sigma$ are in short solid red lines in the "rug" plot, and those smaller than $-1.5\,\sigma$ are in cyan.

some datasets. Only the Scripps dataset shows that OHC reaches a positive extreme in the winter of 2004, and the IPRC and EN4 datasets show that OHC reaches negative extreme in the spring of 2005. In addition, the rapid OHC increase in the wintertime of 2006-2007 have a larger spread among all datasets. In this period, the IPRC dataset shows more rapid OHC increase compared with the other datasets. The flat OHC between 2014-2019 are robust among all the datasets employed.

We observed no OHC extreme occurrences from 2014-2019 from any of the employed datasets (Figure 3-2), the longest period without OHC extreme occurrences since 1950s. In 2000-2005, no OHC extreme occurrences are observed according to the mean (the black lines in Figure 3-1 and in Figure 3-2). However, not all datasets agree upon the absence of the extreme OHC occurrences. For example, the EN4 dataset shows negative extremes in the winter of 2003-2004 (Figure 3-2). The IPRC dataset shows negative extremes in the spring of 2005 and in the winter of 2005-2006.

Year range	extreme [mo]	frac [mo]	positive	frac	negative	frac
2014-2019	0	-	0	-	0	-
2008-2013	9	8.0	4	18.0	5	14.4

2002-2007	2	36.0	0	-	2	36.0
2002-2019	11	19.6	4	54.0	7	30.9

Table 3.2: Similar to Table 3.1, except the period is 2002-2019 in 5-year increments.

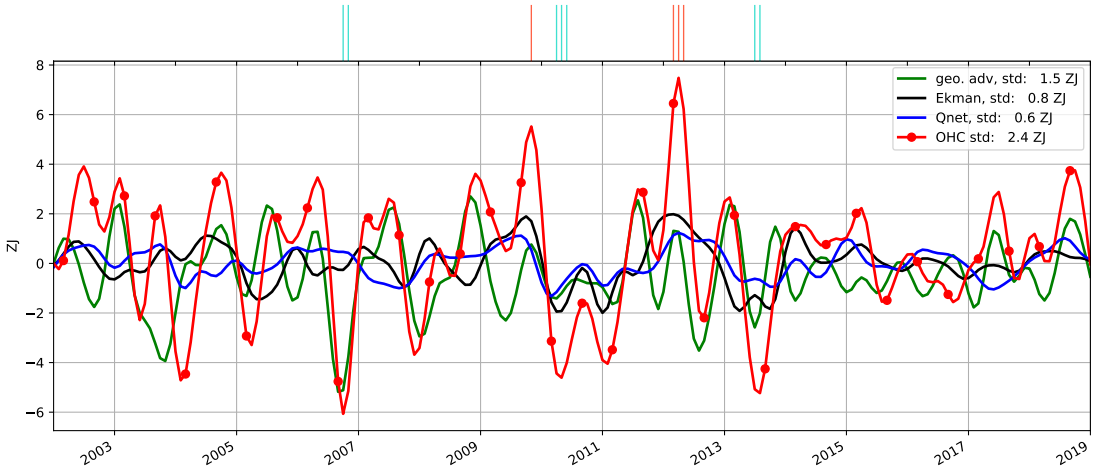

Figure 3-3: 2002-2020 6-50 month variability of OHC and its major comtributing factors, namely, geostrophic heat advection, Ekman heat advection, and air-sea heat flux, in the unit of ZJ. By construction of the inverse model, $\partial_t \mathrm{OHC} = \mathcal{H}_{\mathrm{Qnet}} + \mathcal{H}_{\mathrm{Geo}} + \mathcal{H}_{\mathrm{Ek}}$. The OHC is in solid red line with dots. The geostrophic heat advection is in solid green line. The air-sea surface heat loss is in solid black line. The Ekman heat advection is in solid blue line. To calculate these time series, we employed as the ocean datasets ISAS, EN4, Scripps and IPRC. For Ekman heat advection and air-sea heat flux, we also employed NCEP and ERA as the atmospheric forcing datasets. These variables are calculated as the averages of all employed datasets. The rug plot denotes the monthly occurrences of extreme OHC, same as in Figure 3-2.

3.3.3 Major contributing factors to OHC variability

The OHC interannual variability using a 6-50-month band-pass filter, together with its major contributing factors are shown in Figure 3-3. We calculated the fractions of explained variance in percentage as the square of the correlation coefficient multiplied. The explained OHC variance by each term is summarized in Table 3.3.

The OHC has a standard deviation of 2.3 ZJ. The heat convergence term due to geostrophic advection has a standard deviation of 1.8 ZJ, largest among all major contributing factors (Table 3.3). The geostrophic advection explains 53.0% of the variance of OHC, the largest among all examined contributing terms. In comparison, the Ekman heat advection has a standard deviation of 0.8 ZJ, smaller than that of the geostrophic advection. It explains 28.3% of the variance of OHC, lower than that of geostrophic advection.

The geostrophic heat avection is almost orthogonal to all the examined contributing factors of OHC in the 6-50 month variability. It explains 0.6% of the variance of the Ekman heat advection, 0.7% of the air-sea surface heat flux, and 0.2% of the mixing.

The mixing is not considered as a major contributing factor to OHC. The amplitude of the mixing is small compared with the other terms. Moreover, the mixing is almost orthogonal to OHC, explaining 0.5% of its variance. Similarly, the mixing is orthogonal to the major contributing factors, namely, the geostrophic heat advection, the Ekman heat advection and the air-sea heat flux.

We performed the error estimates of the interannual time series of OHC and its major contributing factors, namely, the geostrophic heat advection, the Ekman heat advection, and the air-sea heat flux. All datasets employed yielded the similar time series for each term on the interannual time scale (see details in Appendix E).

Concerning the Gulf Stream positioning index α, 41.5% of its variance is explained by the geostrophic heat advection. The Ekman heat advection and the air-sea heat flux explains 14.7% and 16.9%, lower than that of geostrophic heat advection.

OHC	2.3ZJ					
$\boldsymbol{\alpha}$	51.4	-				
$\boldsymbol{\mathcal{H}_{\mathbf{Geo}}}$	53.0	41.5	1.8ZJ			
$\boldsymbol{\mathcal{H}_{\mathbf{Ek}}}$	28.3	14.7	0.6	0.8ZJ		
$\mathbf{Q_{net}}$	17.0	16.9	0.7	36.5	0.6ZJ	
$\boldsymbol{\mathcal{H}_{\mathbf{Mix}}}$	0.5	0.9	0.2	5.8	1.2	0.0ZJ
	OHC	$\boldsymbol{\alpha}$	$\boldsymbol{\mathcal{H}_{\mathbf{Geo}}}$	$\boldsymbol{\mathcal{H}_{\mathbf{Ek}}}$	$\mathbf{Q_{net}}$	$\boldsymbol{\mathcal{H}_{\mathbf{Mix}}}$

Table 3.3: The fractions of explained variance (%) among the 6-50 month variabilities of OHC: the Gulf Stream positioning index (α), the heat divergence due to geostrophic advection ($\mathcal{H}_{\text{geo}}$), the heat divergence due to Ekman current ($\mathcal{H}_{\text{Ek}}$), and the air-sea surface heat fluxes (Q_{net}). Note that except OHC, all other terms are integrated in time, in the unit of ZJ. The fractions of explained variance is calculated as the square of the correlation coefficient of each two terms, and then multiplied by 100. The diagonal cells are the standard deviations, in the unit of ZJ. $\mathcal{H}_{\mathbf{Mix}}$ is the mixing term.

3.3.4 Frequency component of OHC and its major contributing factors

In this section, we introduce the spectra of the OHC (Figure 3-4) and its major contributing factors (Figure 3-5). We explore the important frequency bands of the

full time series, as well as the 6-50 month variability (Table 3.4).

The full time-series refers to the detrended and de-seasonalized time series of OHC or its contributing factors, without band-pass window smoothing (also referred to as the "no smoothing" signal, the green line in Figure 3-4a). The spectrum of the OHC "no smoothing" signal shows important periods of: $>$ 30 months, 10 months, 18 months (the green line in Figure 3-4b and Table 3.4). The OHC "no smooth" signal (the green solid line in Figure 3-4a) shows cooling in the period of 2002-2010, as well as warming in the period of 2010-2018. This decadal trend of the OHC in the EDW formation region is anticorrelated with the AMOC strength estimated at 26°N (Figure 1-8 or Fig. 1 in Caesar et al., 2020). On the decadal time scale, we observed that the maxima (minima) of the OHC corresponds with the minima (maxima) of the AMOC strength at 26°N.

Within the frequency band of 30-50 months, the OHC spectrum shows a power spectrum density with an order of magnitude of $O(10^2 - 10^{2.5})\,\mathrm{ZJ}^2\,\mathrm{Month}$. The geostrophic heat advection, the Ekman heat advection, and the air-sea heat flux all have important frequency bands on the spectra at this period range (the green lines in Figure 3-5a, b, and c, Table 3.4). Our research focuses on the interannual variability time scale.

At 10 months, the OHC spectrum has a magnitude of $O(10^2)\,\mathrm{ZJ}^2\,\mathrm{Month}$ (the green line in Figure 3-4b). Only the geostrophic heat advection has at 10 months a comparable magnitude (the green line in Figure 3-5a). In comparison, the spectra of both the Ekman heat advection and the air-sea heat flux show a power spectral density of $O(10^{0.5})\,\mathrm{ZJ}^2\,\mathrm{Month}$ around 10 months, less than that of OHC and the geostrophic heat advection (the green lines in Figure 3-5b and c).

At 18 months, the OHC spectrum shows a power spectrum density with an order of magnitude of $O(10^{1.5})\,\mathrm{ZJ}^2\,\mathrm{Month}$ (the green line in Figure 3-4b). At 18 months, the geostrophic heat advection has a magnitude comparable to that of OHC (the green line in Figure 3-5a).

In short, the geostrophic heat advection is the leading contributing factor to OHC at 18-month, 10-month frequerncy bands, compared with Ekman heat advection and air-sea heat flux. At the frequency band of 30-50 months, OHC is attributed to all its major contributing factors. In our interannual time series, the Gulf Stream shows high fluctuations at high frequency bands, for example 10 months. We aim to examine the lower frequency band part, without this high-frequency fluctuation from the Gulf Stream. Thus we introduce the interannual variability with a 15-50 month window filter to the following analysis.

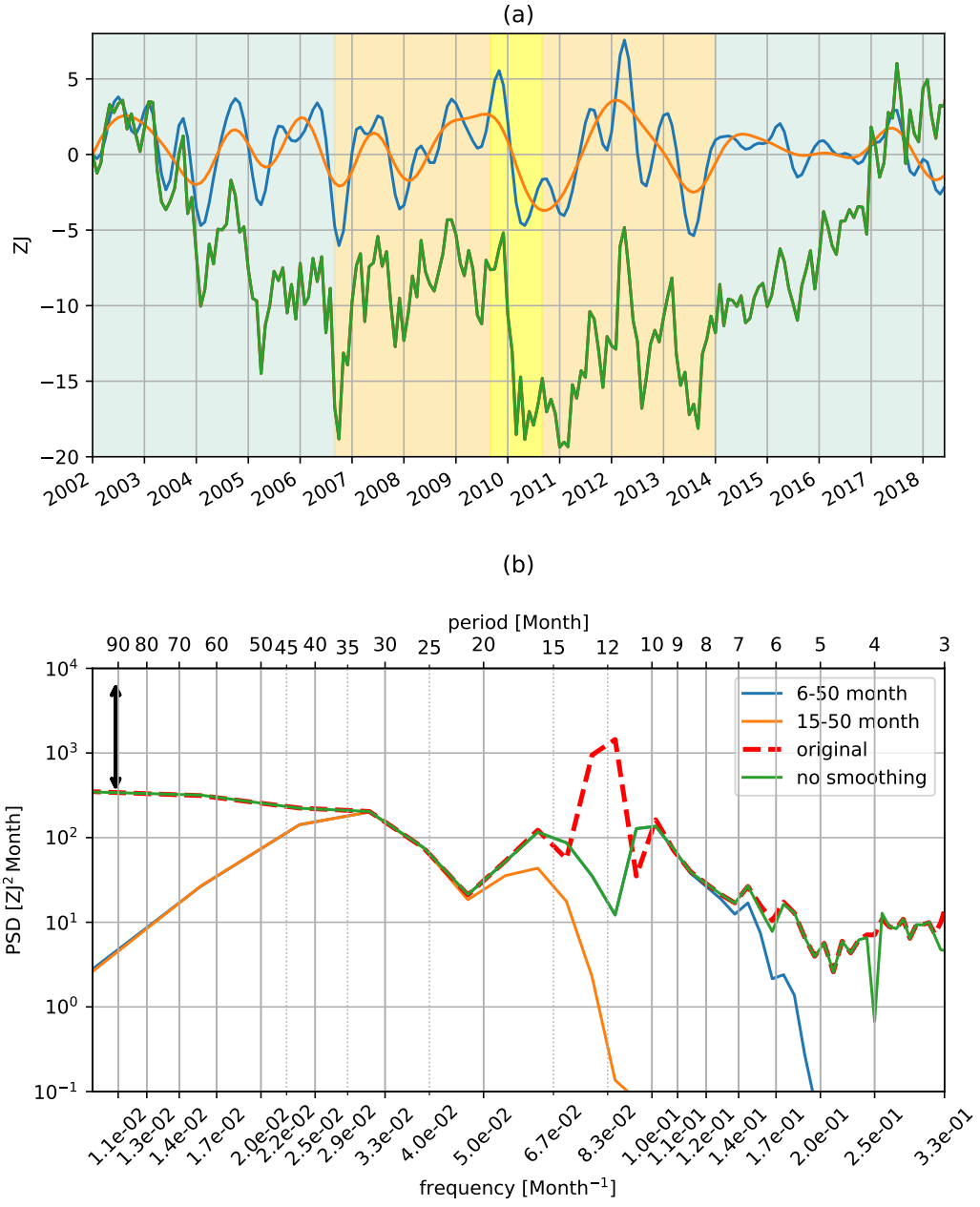
(a)
ZJ
5
0
−5
−10
−15
−20
2002
2003
2004
2005
2006
2007
2008
2009
2010
2011
2012
2013
2014
2015
2016
2017
2018
(b)
period [Month]
90 80 70 60 50 45 40 35 30 25 20 15 12 10 9 8 7 6 5 4 3
PSD [ZJ]² Month]
10^4
10^3
10^2
10^1
10^0
10^{-1}
6-50 month
15-50 month
original
no smoothing
1.1e-02
1.3e-02
1.4e-02
1.7e-02
2.0e-02
2.2e-02
2.5e-02
2.9e-02
3.3e-02
4.0e-02
5.0e-02
6.7e-02
8.3e-02
1.0e-01
1.1e-01
1.2e-01
1.4e-01
1.7e-01
2.0e-01
2.5e-01
3.3e-01
frequency [Month^{-1}]

Figure 3-4

Figure 3-4 *(previous page)*: (a) The 2002-2019 interannual variability of OHC, and (b) The frequency spectra of 2002-2019 OHC variabilities, using 6-50 month filter (blue line), 15-50 month band-pass filter (orange line) and de-seasonalized with no smoothing applied (green line). In (a), shaded in blue are the periods with OHC, namely the green curve, decreasing and increasing. Shaded in red are the periods with relatively "steady". Shaded in yellow is the sudden OHC drop in 2009-2010. In (b), the red dotted line is the orignal signal including the seasonal cycle. The black line with double arrows indicates the 90% confidence interval.

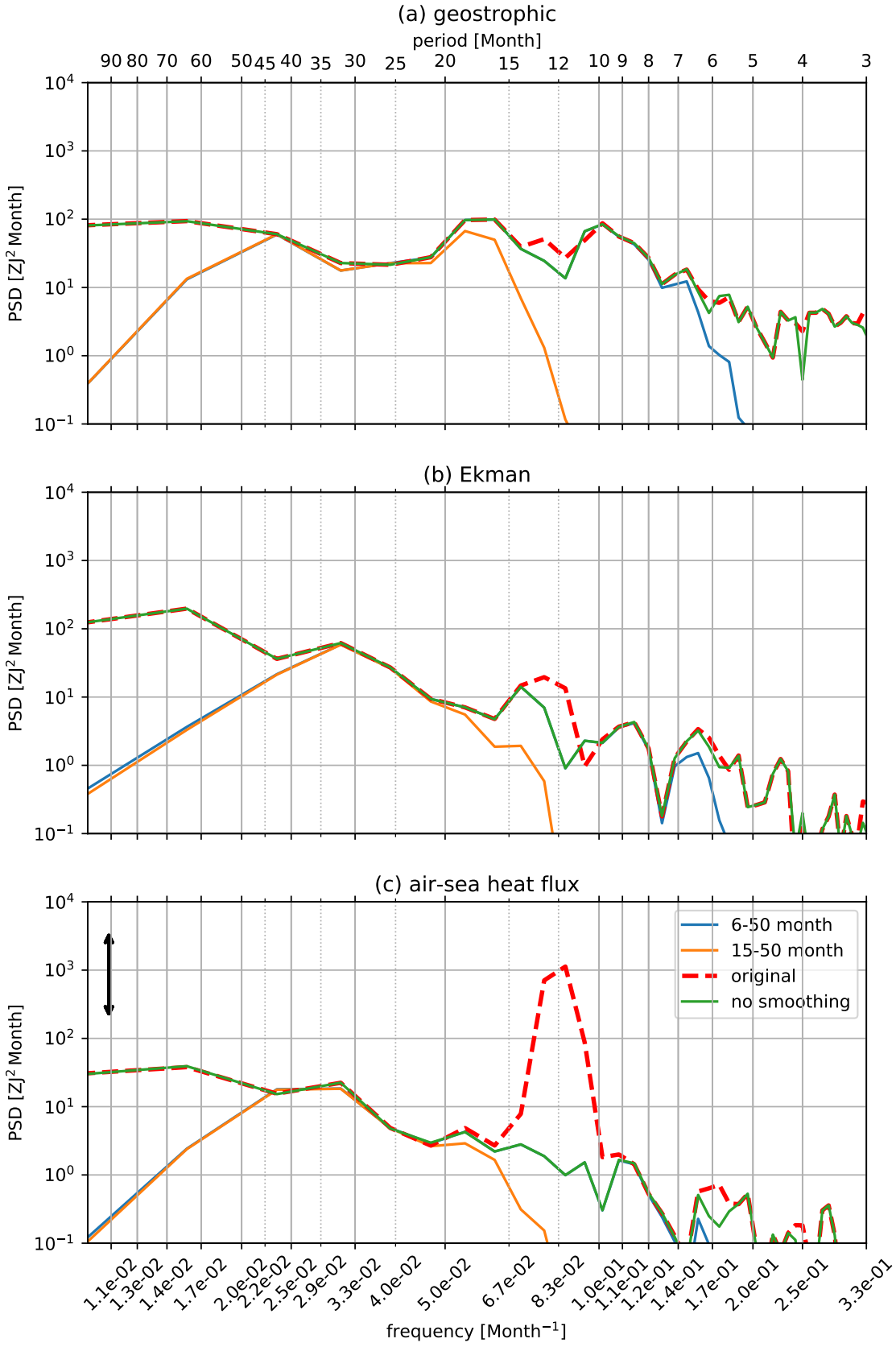
(a) geostrophic
period [Month]
90 80 70 60 50 45 40 35 30 25 20 15 12 10 9 8 7 6 5 4 3
PSD [ZJ]^2 Month]
(b) Ekman
(c) air-sea heat flux
6-50 month
15-50 month
original
no smoothing
1.1e-02 1.3e-02 1.4e-02 1.7e-02 2.0e-02 2.2e-02 2.5e-02 2.9e-02 3.3e-02 4.0e-02 5.0e-02 6.7e-02 8.3e-02 1.0e-01 1.1e-01 1.2e-01 1.4e-01 1.7e-01 2.0e-01 2.5e-01 3.3e-01
frequency [Month^{-1}]

Figure 3-5

Figure 3-5 *(previous page)*: The frequency spectra of: (a) geostrophic heat advection, (b) Ekman heat advection, and (c) air-sea surface heat flux. The orange lines represent the variability using a 15-50 month band-pass filter. The blue lines represent the variability using a 6-50 month band-pass filter. The green lines represent the variability with no smoothing. The red dotted lines represent the original variability including the typical seasonal cycle. The black line with double arrows indicates the 90% confidence interval.

Variable	**"no smoothing"**	**6-50 month**
OHC	$>$ 30mo ($10^2 - 10^{2.5}$), 10mo (10^2), 18mo ($10^{1.5}$)	35mo ($10^2 - 10^{2.5}$), 10mo (10^2), 18mo ($10^{1.5}$)
$\boldsymbol{\mathcal{H}}_{\text{Geo}}$	$>$ 40mo ($10^{1.5} - 10^2$), $>$ 35mo ($10^{1.5}$), 18mo, 10mo ($10^{1.5} - 10^2$)	42mo ($10^{1.5} - 10^2$), $>$ 35mo ($10^{1.5}$), 18mo, 10mo ($10^{1.5} - 10^2$)
$\boldsymbol{\mathcal{H}}_{\text{Ek}}$	$>$ 32mo ($10^{1.5} - 10^2$), 9mo ($10^{0.5}$)	32mo ($10^{1.5}$), 9mo ($10^{0.5}$)
$\boldsymbol{\mathcal{H}}_{\text{Qnet}}$	$>$ 35mo ($10^1 - 10^{1.5}$), 13mo ($10^{0.5}$)	40mo ($10^{0.5} - 10^1$), 13mo ($10^{0.5}$)

Table 3.4: The list of important periods in the spectra of "no smoothing" signal and the 6-50 month variability. The "no smoothing" signal indicates the detrended time series with seasonal cycle removed. In the parenthesis are the orders of magnitude of the power spectral density at the corresponding periods on the spectra, in the unit of ZJ^2 Month

OHC	1.6ZJ					
$\boldsymbol{\alpha}$	48.5	-				
$\boldsymbol{\mathcal{H}}_{\textbf{Geo}}$	37.8	26.3	1.2ZJ			
$\boldsymbol{\mathcal{H}}_{\textbf{Ek}}$	45.4	25.5	2.5	0.7ZJ		
$\mathbf{Q}_{\textbf{net}}$	26.1	31.0	1.4	30.5	0.5ZJ	
$\boldsymbol{\mathcal{H}}_{\textbf{Mix}}$	0.3	2.2	0.9	9.1	2.2	0.0ZJ
	OHC	$\boldsymbol{\alpha}$	$\boldsymbol{\mathcal{H}}_{\textbf{Geo}}$	$\boldsymbol{\mathcal{H}}_{\textbf{Ek}}$	$\mathbf{Q}_{\textbf{net}}$	$\boldsymbol{\mathcal{H}}_{\textbf{Mix}}$

Table 3.5: Similar to Table 3.3, except the 15-50 month variability.

3.3.5 OHC explained variance

The Ekman heat advection explains 45.4% of the variance of OHC in the 15-50 month variability (Table 3.5), increasing from 28.3% in the 6-50 month variability. The air-sea surface heat flux explains 26.1% of the variance of OHC in the 15-50 month variability, increasing from 17.0% in the 6-50 month variability. The geostrophic heat advection explains 37.8% of the variance of OHC in the 15-50 month variability, decreasing from 53.0% in the 6-50 month variability. However, the mixing terms on both time scales have small explained variance to OHC, about $0.3 - 0.5\%$.

Following the heat equation (Equation 2.4), we examined OHC contributed by the heat advection due to geostrophy, the heat advection due to Ekman current, the air-sea surface heat flux, and the mixing term. In the interannual variability (6-50 month filter), the geostrophic heat advection explains the most variance of the OHC among all examined factors. In the 15-50 month variability, the Ekman heat advection explains the most variance of OHC among all examined factors.

3.3.6 Recirculation gyre

The geostrophic heat advection is a complex term. To seek the dominant contribution, we decomposed this term and investigated the temperature advection due to geostrophic current from each boundary of the domain of analysis.

The interannual variability of geostrophic heat advection is a heat convergence of geostrophic heat fluxes from all boundaries of the domain of analysis (Figure 3-7a). Of all boundaries, the geostrophic heat advection is the most correlated with the volume flux at the southern boundary (Figure 3-7c). Their correlation coefficient is 0.59. The correlation reaches 0.62 when adding the southern boundary flux with the western boundary positive-only flux (Figure 3-7b). However the correlation between the geostrophic heat advection and the western boundary positive-only flux (Figure 3-7d) is -0.1 lower than all those aforementioned.

The southern branch of the subtropical recirculation gyre, mainly westward, passes by the southern boundary of the domain of analysis (branch C in Figure 3-6). The sum of volume fluxes of western and southern boundary reflects the volume flux of the North Atlantic current (branch A in Figure 3-6), the northern cyclonic recirculation gyre (branch D), and part of the subtropical recirculation gyre coming out of the eastern boundary (branch B). Our finding indicates that Gulf Stream strength regulated with the subtropical recirculation gyre is responsible to advect heat into the domain of analysis.

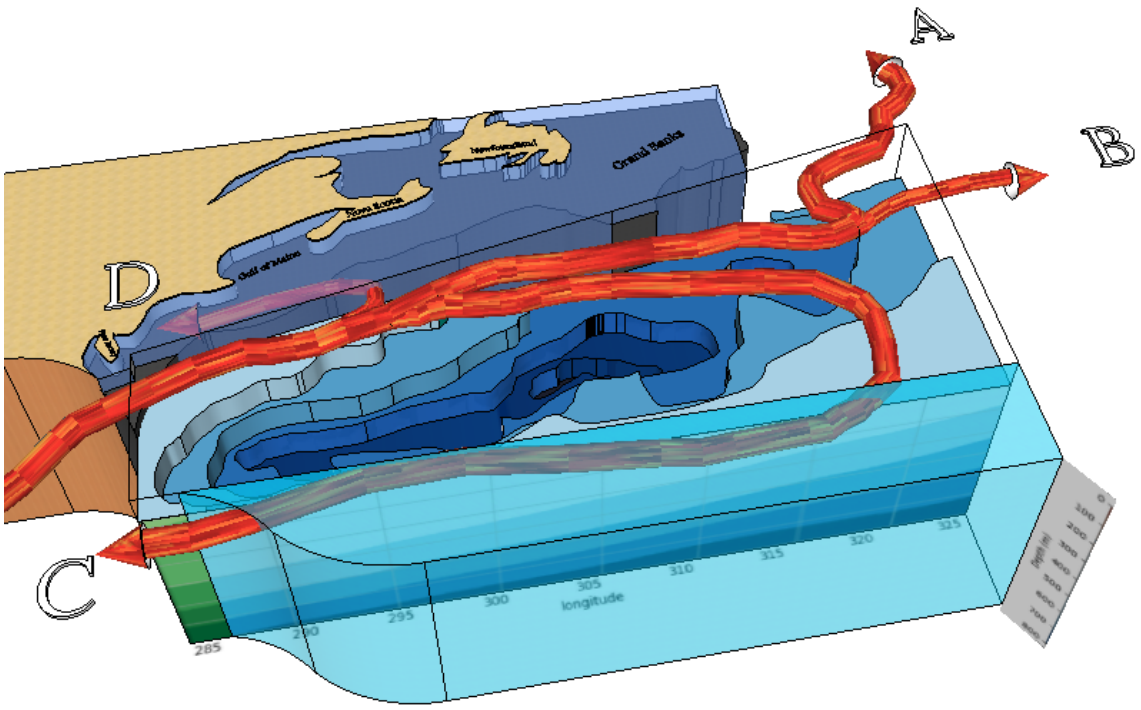

Figure 3-6: The schematic of the Gulf Stream system in the western subtropical North Atlantic. The blue colored contours in depth indicate the deepest mixed layer depth. The green colored contours indicate the climatologically averaged isotherms ranging from $11 - 19^{o}$C. The branch A indicates the North Atlantic Current. The branch B indicates the eastward traveling subtropical recirculation gyre. The branch C indicates the westward traveling subtropical recirculation gyre. The branch D indicates the northern cyclonic recirculation gyre.

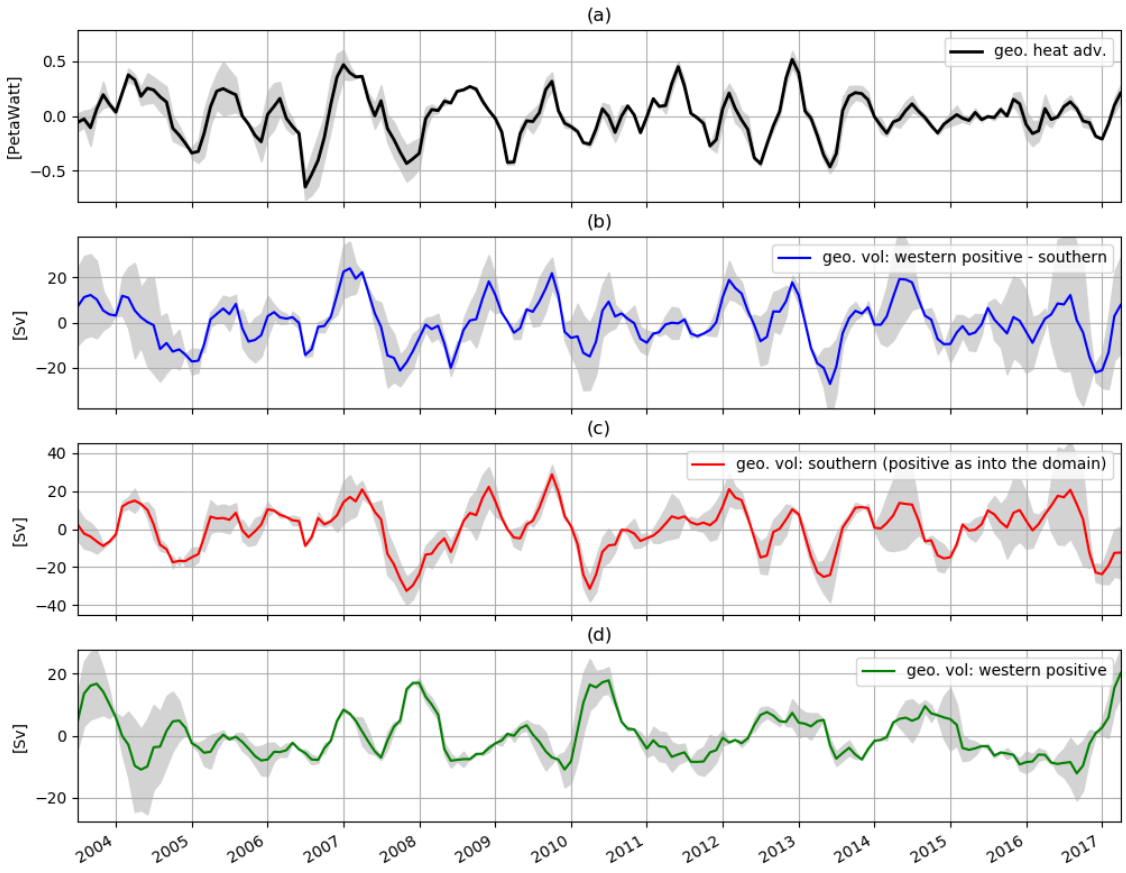

Figure 3-7: 2003-2018 interannual variability of (a) geostrophic heat advection convergence, in the unit of PetaWatt (black line), (b) The geostrophic heat advection going into the western boundary, subtracted by the geostrophic heat advection going out of the southern boundary (c) The geostrophic heat advection going out of the southern boundary, and (d) geostrophic volume flux going into the western boundary of the domain of analysis. (b), (c), and (d) are in the unit of Sv. Shaded in light grey are the unbiased standard deviations among all datasets (ISAS, EN4, Scripps, and IPRC for the ocean. ERA and NCEP for the atmosphere).

3.3.7 Gulf Stream positioning

The Gulf Stream positioning on an interannual time scale is correlated with OHC. We examined the Gulf Stream meridional positioning by introducing the index α. It is the ratio between the part south of the Gulf Stream and the overall domain of analysis. Note that α is not directly expressed in the heat equation (Equation 2.4). Yet, the Gulf Stream meridional positioning is important as it is linked to NAO. For example, Taylor and Stephens (1998) showed that the Gulf Stream positioning reacts to the NAO with a 2-year lag. A larger (smaller) α indicates the Gulf Stream meridionally displaced further north (south). On the interannual variability, the index α explains 51.4% (namely, the correlation coefficient $r = 0.72$) of the variance of OHC (Table 3.3). On the 15-50 month variability, the high frequency fluctuation around 10 months is removed. α stays as correlated to OHC on 15-50 month variability (Table 3.5). This means that the Gulf Stream located further north (south) in latitude indicates an increase (decrease) in volume of the warm water over the domain of analysis. However, this cannot represent the local trends of heat content change in certain areas in the domain of analysis, for example, the Panulirus station near Bermuda.

3.3.8 Air-sea heat fluxes

In this section, we examined the interannual variabilities of the surface sensible heat flux and the surface latent heat flux (Figure 3-8). Both the sensible heat flux and the latent heat flux are correlated with the air-sea heat flux, with coefficients of 0.96 and 0.99 respectively.

On the 6-50 month variability, the air-sea heat flux explains only 17% of the variance of OHC (Table 3.3). On the 15-50 month variability, the air-sea heat flux explains 26% of the variance of OHC (Table 3.5). Similarly, on the 6-50 month variability, the air-sea heat flux explains only 16% of the variance of the Gulf Stream positioning index α. It increases to 31%, on the 15-50 month variability. Among the examined factors, the air-sea heat flux has the highest percentage of explained variance with the Ekman heat advection, about 36.5% on the 6-50 month variability (Table 3.3).

3.3.9 OHC extreme occurrences

We aimed to seek the recipe for OHC extreme occurrences. From previous sections, we have found that the Ekman heat advection and the air-sea surface heat loss have the leading explained variance to OHC compared with geostrophic heat advection, at

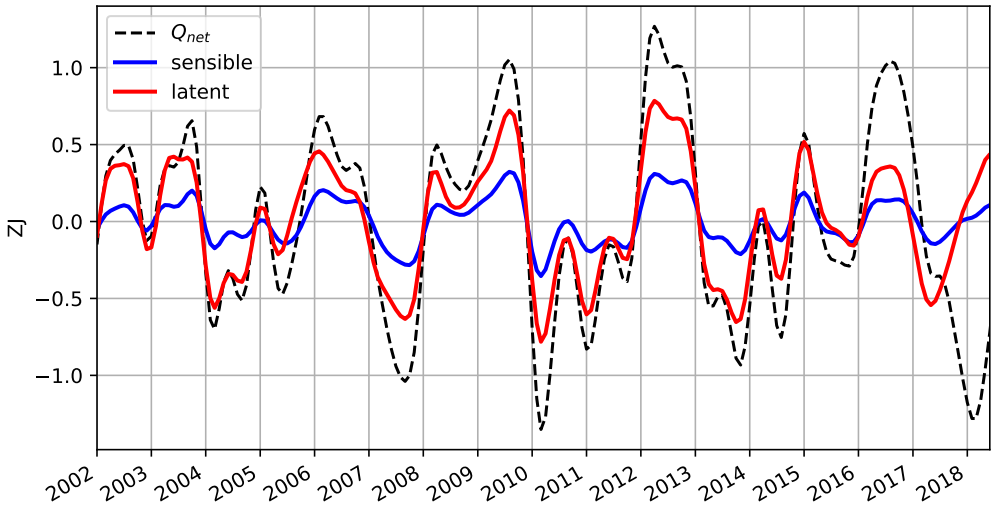

Figure 3-8: 2002-2020 6-50 month variability of accumulated surface sensible heat flux (blue solid line) and accumulated surface latent heat flux (red solid line), in the unit of ZJ. The black dotted line represents the air-sea heat flux. ERA and NCEP datasets were averaged to produce the plot.

low frequencies (30-35 months). The geostrophic heat advection, associated with the Gulf Stream, is dominant term for OHC at high frequencies ($<$ 30months). However, we see from Figure 3.3 that Ekman (geostrophic) advection is the leading term that explain the extreme occurences for 2009-10 and 2012 (2006, 2013). Yet, we found no clear links between the terms of the budget and the occurrences of OHC extremes.

3.4 Discussion

3.4.1 AMOC: the 1990s sudden increase and 2009-2010 slowdown

We observed that a cluster of interannual OHC extreme occurrences is centered around the 1990s (namely, from 1990s to 2000. See details in Figure 3-1). Caesar et al. (2020) observed around the 1990s, the AMOC experienced increase, on a multi-decadal time scale. Similarly, we observed that a cluster of interannual OHC extreme occurrences is centered around the period of 2009-2010 (namely, from 2006 to 2014. See details in Figure 3-1). Caesar et al. (2020) observed that, from the mid-2000s, AMOC experienced on its multidecadal time series a weakening that intensified in 2009 on the interannual time scale as shown by the RAPID time series. In this case, the cluster of the OHC extremes corresponds with the AMOC minimum

in the late 2000s. In short, the variability of the AMOC multidecadal signal appears to "organise" the clusters of the interannual OHC extremes in the western subtropical North Atlantic. The centers of the OHC interannual extreme clusters correspond with AMOC strength changes (or extrema) on the multidecal time scale.

In addition, we estimated the OHC reduction corresponding to the 2009-2010 AMOC decrease. The upper 800-m ocean heat content in the western subtropical North Atlantic experienced a reduction of 8.0 ZJ in the period of 2009-2010 (Figure 3-2). The 2009-2010 slowdown of MOC is responsible for a heat reduction of 14.5 ZJ (Bryden et al., 2014). They showed that this heat reduction agrees with the heat reduction of the upper 1000-m ocean in their domain of $25 - 45^{o}$N and $60 - 20^{o}$W, 13.5 ZJ. Our finding is in the same order of magnitude as the literature. The heat content reduction of our domain of analysis is smaller than that of Bryden et al. (2014) by about 41%. One explanation for this can be that the area of our domain of analysis is smaller than that of Bryden et al. (2014) by about 35%. In addition, our domain of analysis is further to the west than that of Bryden et al. (2014).

3.4.1.1 Two periods of OHC extreme absence

From the mid 1990s-late 2000s, we observed a relatively sparce distribution of the monthly OHC extreme occurrences in the western subtropical North Atlantic region. Particularly, there was an absence of the OHC extreme from 2000-2005 (Figure 3-1).

On a decadal time scale, in the period of 1990-2006, the North Atlantic region experienced warming (Fig.2E in Cheng et al., 2017). This warming took place between the AMOC at the trough of low strength in 1990s and the AMOC at the peak of high strength towards the mid 2000s (Figure 1-8, Caesar et al., 2020) .

The OHC extremes can be part of the red-noise response of the upper ocean to the atmospheric forcing (Frankignoul and Hasselmann, 1977). We showed the power spectrum density of OHC, geostrophic heat advection, and Ekman heat advection. The spectrum of Ekman heat advection shows larger power spectrum density at the lower frequency (Figure 3-5b). This resembles the red-noise like upper ocean response to the atmosphere forcing. Admittedly, we did not calculate the confidence interval of these power spectrum densities relative to the red noise. Typically, the atmosphere has a decorrelation of about 10 days, and the ocean of about several months. The OHC extremes alternating between positive and negative every 5-10 years on the OHC interannual time series can result from a progressive integration of signals from the atmosphere-ocean coupling.

3.4.2 Meridional heat transport due to mesoscale / submesoscale eddies

The mesoscale / submesoscale eddy heat transport over the Gulf Stream region is very important, making up 1/4 to 1/3 of the total meridional transport at Gulf Stream extension region (Hecht and Smith, 2009; Smith et al., 2000; Tréguier et al., 2012). It is about 0.3 PW at 36.6°N (Tréguier et al., 2017). Tréguier et al. (2017) captured the eddy heat flux using the altimetry data ($0.25^{\circ} \times 0.25^{\circ}$). We smoothed the altimetry data to coarser ocean data grids (Table 2.1) to calculate the heat transport due to geostrophy. The coarser resolution smoothed the mesoscale eddies from the altimetry data. In addtion, we removed the mesoscale / submesoscale eddies by applying 6 month low-pass filter. We removed the eddies of which the decorrelation scale is less then 6 months.

The heat transport due to mesoscale eddies was taken into account in the mixing term in our heat equation (Equation 2.1). We parameterized the mixing term using horizontal and vertical eddy mixing diffusivity. We chose $10^3\,\mathrm{m^2\,s^{-1}}$ as the horizontal eddy diffusive coefficient for the mesoscale eddy mixing. $10^3\,\mathrm{m^2\,s^{-1}}$ is reasonable at the southern and eastern boundaries of our domain of analysis. It is especially an underestimate near the Gulf Stream region, by at least one order of magnitude (Groeskamp et al., 2020). However, it does not affect our heat budget because it redistributes heat inside our domain of analysis. Mesoscale / submesoscale eddies near the Gulf Stream region serve to flatten the isopycnals. Namely, we may underestimate the impact of warm eddies traveling across the Gulf Stream exiting our domain of analysis from the northern boundary.

We chose $\kappa_{\mathrm{v}} = 10^{-5}\,\mathrm{m^2\,s^{-1}}$ as the vertical eddy diffusivity due to mixing. Frants et al. (2013) estimated the Antarctic polar front region, another eddy active region, with an eddy diffusivity of $\kappa_{\mathrm{v}} = O(10^{-5}) - O(10^{-3})\,\mathrm{m^2 s^{-1}}$. Our vertical eddy diffusivity due to mixing at the Gulf Stream region can be underestimated. With a smaller κ_{v}, less cold water from underneath the permanent pycnocline enters into our domain of analysis.

Despite an underestimate of eddy mixing near the Gulf Stream region, our estimate regarding the eddy mixing should be reasonable. We argue that the eddy mixing largely takes place within our domain of analysis, given that our northern boundary is north of the Gulf Stream extension. At the eastern and western boundaries where the Gulf Stream enters and exits the domain of analysis, the eddies travel along both boundaries. Thus, even an underestimate of eddy activity would not influence the heat budget. The southern boundary, chosen at 30°N, is far away from the Gulf Stream region enough that our choice of eddy diffusivity is within a reasonable order

of magnitude. Most likely, even an underestimate of the eddy diffusivity due to mixing would only result in a redistribution of the heat in our domain of analysis.

3.4.3 Interannual band-pass filter

To study the interannual time series, we chose 50 months as the lower boundary of the band-pass filter window on the spectrum. Classically the band-pass filter is chosen to cut at the "spectrum gap" to avoid introducing artificial peaks to the filtered signal. Our spectrum of geostrophic heat advection, for example, has a peak value at 65 months (the green line in Figure 3-5a). With the 50-month high-pass filter added, the artificial peak at 35 months nontheless remains an important frequency band with large power spectrum density (the orange and blue lines in Figure 3-5a).

3.5 Summary

1. On the interannual time series of ocean heat content, groups of extreme occurrences are centered 10-15 years apart, for the period 2006-2014 and for the period 1990-2000. These two periods are notoriously known for the MOC slowdown and strengthening. On a multi-decadal time scale, it is known that the strong (weak) phase of AMOC corresponds with warming (cooling) in the subtropical North Atlantic. Based on that, we further observed that this low frequency variability of AMOC has an impact on OHC interannual variability by organising its extreme occurrences.

2. On the interannual time scale, the Ekman heat advection contains an important frequency band of > 32 months, and the air-sea heat flux of > 40 months. Both Ekman heat advection and the air-sea heat flux are the direct indicators of the weather regimes, through surface wind stress, and through latent and sensible heat fluxes respectively. The Gulf Stream explains the variance of the air-sea heat flux on the interannual time scale (15-50 month window filter).

3. The geostrophic heat advection contains important frequency bands of > 40 months, 18 months, 13 months, and 7-10 months. At 18 months, the geostrophic heat advection is a dominant part of OHC, compared with the Ekman heat advection and the air-sea heat flux. The geostrophic heat advection is influenced by the strength of subtropical North Atlantic recirculation gyre. The eddy heat transport is parametrized by the eddy diffusivity.

4. The extreme occurrences of wintertime OHC have not become more frequent

since the last decade. Most recently, we observed no extreme occurrences in the period of 2014-2019, the longest period without OHC extremes since 1950.

5. The Gulf Stream positioning is correlated with the OHC at 15-50 month variability ($r = 0.7$). The correlation is larger than with any other major contributing factors. The Gulf Stream positioning explains the variance of the air-sea heat on an interannual variability (15-50 month). We observed no correlation between the Gulf Stream volume transport and interannual variability of OHC in the western subtropical North Atlantic region. But rather, the strength of its subtropical recirculation gyre impacts the OHC through geostrophic heat advection.

6. The OHC of our domain analysis, situated at the western North Atlantic, as the "context" of EDW, is rather complex. Too many possible interactions between the components of the OHC budget and/or the atmospheric forcing do not lead to a clear recipe for extremes. In the next chapter, we will analyse the extremes of EDW formation rates, as well as identify the major forces leading to the EDW extremes.

CHAPTER 4

Eighteen Degree Water extreme formation years

4.1 Abstract

The North Atlantic Subtropical Mode Water has been experiencing a volume decrease since 2010 (Stevens et al., 2020). We observed in the previous chapter, on an interannual time scale, the ocean heat content (OHC) in this region experiencing an absence of extremes since 2014. Yet, we observed no correlation between EDW seasonal-maximum outcropping volume and OHC due to too large the domain of analysis. However, we investigated the air-sea heat flux, the Ekman heat advection, and the preconditioning to the extreme EDW outcropping events. To explain the extreme years of strong EDW formation, we found strong heat divergence due to Ekman advection, which is the key physical process. Conversely, the less intense air-sea surface heat loss coupled with unfavorable preconditioning are the driving mechanisms behind the weak EDW formation years. In addition, a strong wintertime EDW renewal encourages a vigorous subduction through the southward geostrophic advection at 30°N. We addressed the following questions:

1. Are there, and if any, what are the extreme years in EDW outcropping volume?
2. Are the occurrences of extreme EDW renewal becoming more and more frequent?
3. On the interannual time scale, how do the air-sea heat flux and the heat convergence due to Ekman advection have an impact on the EDW formation?
4. Are there certain atmospheric patterns that correspond to the extreme occurrences of EDW renewal?

The extremes of the interannual EDW renewal take place on average every 3 years. The interannual EDW renewal has been experiencing a period absent of extremes since 2014, the longest period since 1950.

We found that the OHC variability heralds the EDW renewal in a complex manner. The Gulf Stream passed through the domain of analysis near its northern boundary. The interannual variability of OHC and that of EDW outcropping volume are not correlated ($|r| < 0.1$). In addition, we found little correlation between the winter-time change of OHC (September-December) and the interannual variability of EDW outcropping volume ($|r| < 0.1$).

Concerning the air-sea heat flux, we observed more intense air-sea surface heat loss in the domain of analysis during the extreme years of strong EDW renewal. During the extreme years of weak EDW renewal, we observed less intense air-sea surface heat loss.

Concerning the Ekman heat advection, in the subtropical region, we observed a heat divergence during the extreme years of strong EDW renewal, as well as a heat convergence during weak years.

The NAO patterns well corresponds with the EDW extreme years. NAO- (NAO+) corresponds with extreme a strong (weak) year of EDW renewal. Between strong and weak years, anomalies of the wind stress curl and the air-sea heat fluxes are asymmetric, especially in the subpolar region. This suggests NAO+ as an asymmetric counterpart of NAO-.

In this chapter, firstly we examined the extreme occurrences of interannual EDW renewal. We investigated the distribution of EDW renewal on a multidecadal time axis, as well as its spacial distribution. Secondly, we examined how the extreme occurrences of EDW renewal are signaled by the subtropical OHC, the Ekman heat advection, and the air-sea heat flux. Then we investigated the role of preconditioning in extreme EDW renewal events. Lastly, we estimated the EDW subduction rate on an interannual time scale.

4.2 Introduction

4.2.1 Extreme years in EDW freshly ventilated volume

The EDW renewal in the winter of 2007-2008 and in the winter of 2011-2012 was particularly weak (Billheimer and Talley, 2013). They attributed the weak EDW formation to the weak and late winter buoyancy forcing associated with NAO+. Neither the increased Gulf Stream heat advection nor the preconditioning played a role in these two winters of weak EDW ventilation. In addition, they showed that in the winter of 2009-2010, the EDW ventilation is strong. They showed that despite an unfavorable preconditioning in the fall of 2009 and a low geostrophic heat advection in the wintertime of 2009-2010, the high winter buoyancy loss in the water column

is mainly due to large surface heat loss. Correspondingly, they also showed that the winter of 2009-2010 is under strong NAO-. In the winter of 2004-2005, they showed a high buoyancy loss in the water column, but neither air-sea surface heat loss nor geostrophic heat advection was strong. The NAO- in the winter of 2004-2005 was not strong either. None can explain the high winter buoyancy loss. We aim to understand: 1, in the winter of 2004-2005, does the large buoyancy content reduction correspond to an anomalous EDW renewal? 2. What's the driving mechanism behind the large buoyancy content reduction in the winter of 2004-2005?

4.2.2 Ekman current

The horizontal Ekman advection is a buoyancy sink term in the subtropical North Atlantic region, associated with southward advection of cold subpolar surface water (Billheimer and Talley, 2013; Thomas, 2005; Thomas et al., 2013). In multi-decadal time scales, the Ekman current is found to be the lead driving force to the North Atlantic subtropical stratification (Seidov et al., 2018). On interannual time scales, Evans et al. (2017) showed that the variabilities of both Ekman pumping and thermocline depth are strongly correlated with the volume transport anomaly at the subtropical gyre. However, in the studies of Billheimer and Talley (2013) and Dong and Kelly (2004), the horizontal Ekman advection is within the error bar, thus considered negligible on interannual time scales. We aim to verify if horizontal Ekman advection on interannual time scales is a term negligible for the heat budget and the EDW formation in the subtropical North Atlantic region.

4.2.3 EDW subduction and obduction

Subduction is when a water parcel leaves the mixed layer and enters the main pycnocline definitively. One of the classic approaches to calculate the subduction rate is the "Stommel's demon" (Stommel, 1979), which was more widely employed in the early literature. Qiu and Huang (1995) estimated that for the $26.2 - 26.6\,\mathrm{kg\,m^{-3}}$ water in North Atlantic, the annually averaged subduction rate and obduction rate are 3.0 Sv and 1.75 Sv respectively. However, they did not specify the vorticity criteria in order to identify the EDW. Forget et al. (2011) estimated that the annually averaged EDW formation rate due to air-sea surface heat fluxes and mixing is 2.0 Sv. In this analysis, we chose to investigate the freshly ventilated EDW before subduction, which serves as a more direct response to the atmospheric impact.

Qu et al. (2016) observed that the subduction takes place to the east of the EDW formation areas (Fig. 4a), in the northern Sargasso Sea region (32^{o}N, $60^{o} - 70^{o}$W),

as well as to the southern flank of the Gulf Stream (35°N, 45° − 55°W). Kelly and Dong (2013) located the subduction region to the south of the EDW formation region (Fig.3c), 27° − 32°N, 75° − 55°W.

Many ocean state variables played a role in the subduction in the subtropical North Atlantic. Dong et al. (2007); Kelly and Dong (2013) adopted in their model the southward geostrophic advection between the formation region and subduction region as the proxy of the EDW subduction. They observed a mean southward velocity of $-0.010\,\mathrm{m\,s^{-1}}$, with a standard deviation of $0.0038\,\mathrm{m\,s^{-1}}$, more than 30% of the mean value. They addressed that the subduction driven by the southward geostrophic velocity ("transfer" as they referred to) is insufficient to transport freshly ventilated EDW to the core of their subduction region within a delay of 6-9 months. Apart from the geostrophic advection, the Ekman effects can contribute to subduction. Thomas (2005) showed that the cross-front Ekman transport generated by an along-front wind reduces the stratificaiton, expands the outcropping region, and induces the subduction. Maze and Marshall (2011); Maze et al. (2013) compared the mechanical forcing associated with Ekman-driven convection to the diabatic forcing associated with the air-sea surface buoyancy loss. Maze et al. (2013) concluded that the mechanical forcing is one order of magnitude smaller than the diabatic forcing. Yet they identified the EDW subduction at regions 2 degrees south of Gulf Stream. These regions are located at 31 − 37°N, 46 − 64°W and 31 − 33°N, 65 − 72°W, where, correspondingly, the EDW thickness exceeds 300m (Maze et al., 2013). We used geostrophic volume transport at 30°N and SST to investigate the subduction.

4.2.4 EDW formation volume

The term "EDW formation" was firstly introduced by Walin (1982) as the increase of EDW due to the wintertime anomalous air-sea buoyancy flux. Under "Walin framework", Forget et al. (2011); Maze et al. (2009) evaluated the EDW formation induced by air-sea heat fluxes. In their work, the EDW formation is used to describe the wintertime EDW volume change due to the wintertime anomalous air-sea heat flux. Peng et al. (2006) followed the idea of Marshall et al. (1993) and Marsh and New (1996) to examine the subduction/renewal rate of EDW in their model. In their analysis, the EDW renewal rate measures the newly formed EDW that enters the permanent thermocline diabatically and that actually ventilated the thermocline. We are interested in the early spring freshly ventilated EDW volume, when its outcropping surface reaches annual maximum. We aim to investigate all the factors, the wintertime forcing as well as the preconditioning in September before the EDW renewal. All these factors are potentially responsible to hinder or increase the wintertime EDW

renewal. A positive anomalous EDW renewal indicates an increase in the freshly ventilated volume.

4.3 Results

4.3.1 Extreme occurrences over a multi-decadal period

The EDW outcropping volume reaches its seasonal maximum in the spring (February-April, the black line in Figure 4-1).

We aimed to capture the interannual variability of this seasonal-maximum EDW outcropping volume. To obtain this time series, firstly, we selected the seasonal maximum of the EDW outcropping volume within a year. Then we applied a high-pass filter of 10 years to remove the multidecadal signal. From here on, unless specially specified, the EDW outcropping volume refers to the seasonal maximum.

In this section, we investigated the extreme occurrences of the interannual variability of EDW outcropping volume since 1950 (Figure 4-1). The extremes are chosen to exceed $\pm 3.39\,\mathrm{Svy}$ ($1\,\sigma$) threshold of the interannual variability of the EDW outcropping volume. Under this criteria, 22 years out of 71 total yearly samples (31% of the total years) are chosen as extremes using σ, where 16.9% are positive extremes, and the remaining 14.1% are negative.

To see the trend of extreme occurrences, we divided the time axis into 15-year segments. Since the most recent 15 years, from 2006-2020, only 3 extremes: a negative extreme in 2008, two positive extremes in 2010 and 2013 (Table 4.1). Since 2014, we observed a period absent of EDW outcropping extremes, the longest period since 1950 (Figure 4-1). Aside from this 7-year absence of EDW extremes, we observed another 6-year absence in the mid-1990s (Figure 4-1). The frequency of the extremes could be related to the state of the decadal variability. Stevens et al. (2020) found that the EDW renewal volume experienced a decrease since 2010.

From 1950-1960, the fraction of extreme occurrences for EDW outcropping volume is every 2.2 years. The most frequent among all segments. Note that in this period, only the EN4 dataset, among all the employed datasets, is available, and with limited precision (Figure 7 in Good et al., 2013).

In the wintertime of 2010, the EDW outcropping volume interannual mean reaches to $7\,\mathrm{Svy}$, exceeding the $1\,\sigma$ line (the blue line in Figure 4-1). In addition, its unbiased standard deviation range around this peak exceeds the $1\,\sigma$ line. This extreme occurrence is robust.

In the wintertime of 2005, the EDW outcropping volume interannual mean is $3.4 \pm 1.4\,\mathrm{Svy}$, exceeding the $1\,\sigma$ line (the blue line in Figure 4-1). Its unbiased standard

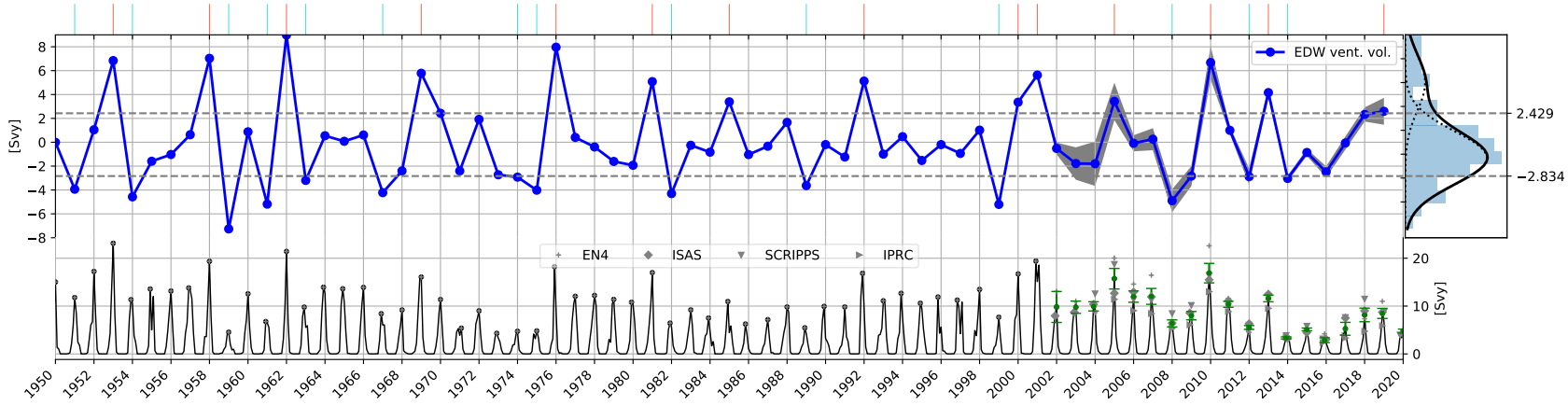

Figure 4-1: 1950-2020 interannual variability of EDW outcropping volume and its extreme occurrences in years. (Upper) The interannual variability of seasonal-maximum EDW outcropping volume is in the solid blue line with dots. The unbiased standard deviation of OHC among datasets is shaded in grey. The grey dashed lines are the standard deviation σ of the time series. The histogram of interannual OHC values is to the right (the blue bars). The black solid line indicates the non-Gaussian kernel of this histogram, containing two superimposed Gaussian kernels (dashed black curves) The months with OHC greater than σ are in short solid red lines in the "rug" plot, and those smaller than $-\sigma$ are in cyan. (Lower) The orignal time series of the EDW outcropping volume is in solid black line with dots. The black dots on the curve marks the EDW outcropping volume in March. The green errorbars indicate the unbiased standard deviation among several data products at the seasonal maximum. We used the EN4, ISAS, Scripps, and IPRC datasets to produce the time series.

deviation is 2.8 Svy, only part of which exceeds the $1\,\sigma$ line. This extreme occurrence is not as robust compared with 2010. In the original time series of the EDW outcropping volume (the black line in Figure 4-1), the examined datasets show an error bar of 5 Svy, due to the over estimate using the EN4 and Scripps datasets, and the under estimate using the ISAS and IPRC datasets.

In the wintertime of 2008, the EDW outcropping volume interannual mean reaches to -5.0 ± 0.6 Svy, with both the mean value and the error bar exceeding the $-\sigma$ line (the blue line in Figure 4-1). This extreme occurrence is robust. In the original time series the seasonal-maximum EDW outcropping volume is well-agreed upon by all the employed datasets. The error bar of unbiased standard deviation contains a range of 2.0 Svy.

In the wintertime of 2019, the EDW outcropping volume interannual mean reaches 2.2 ± 0.3 Svy, larger than that of 2011 (the blue line in Figure 4-1). In the error bar of unbiased standard deviation surpasses the $1\,\sigma$ line, and the mean doesn't. In the original time series the seasonal-maximum EDW outcropping volume is 8.0 ± 1.0, Sv, smaller than that of 2011. This difference between 2019 and 2011 reflects the role of the decadal signal in shaping the interannual extremes.

In short, the EDW outcropping extreme occurrences take place every 3 years on average. Since 1950s we observed two periods absent of EDW extremes: 2014-2020 and the mid-1990s. The extreme occurrences of EDW is not becoming more frequent. In the recent years (since 2000, for example), the noticable strong extreme years of EDW renewal are: 2001, 2005, 2010, and 2013. Since 2000, the noticable weak extreme years are 2008, surpassing the $-\sigma$ line, as well as 2012, 2014, 2015, 2016 and 2020, which are close to $-\sigma$ line.

Note that the distribution of the interannual variability of EDW outcropping volume has a high skewness in the positive extremes and a low skewness in the negative extremes, in comparison to a standard Gaussian distribution (Figure 4-1). Using the standard deviation as the cut-off line for selecting extremes can result in an overestimate of numbers of positive extremes as well as an underestimate of negative extremes.

From 1950-2020, we observed as the extreme years of strong EDW renewal: 1992, 1985, 1981, 1976, 1962, 1958, and 1953. In addition, we observed as the extreme years of weak EDW renewal: 1999, 1989, 1982, 1975, 1967, 1961, 1959, 1954, and 1951.

Year range	extreme [yr]	frac [yr]	positive	frac	negative	frac
2006-2020	6	2.5	3	5.0	3	5.0
1991-2005	5	3.0	4	3.8	1	15.0

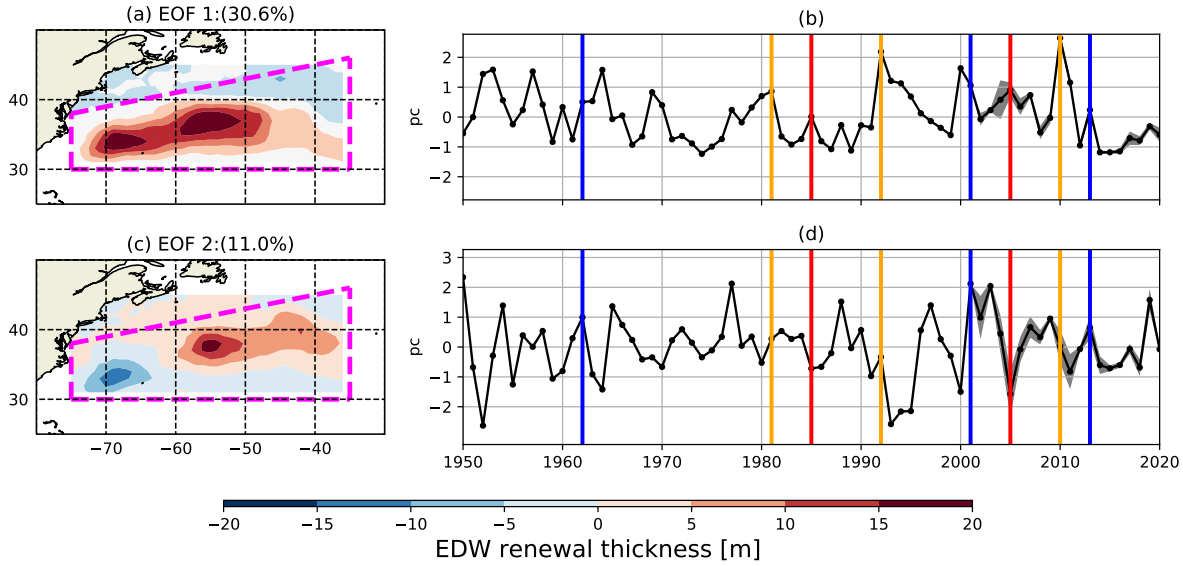

Figure 4-2: The first two EOFs (a, c) and the corresponding standardized PCs (b, d) of the interannual EDW outcropping volume variability (6-50 month filter). The percentage numbers indicate the explained variances. Highlighted are the strong extreme years of the interannual EDW outcropping volume variability. See Section 4.3.2 for the details. In blue are the years with strong EDW renewal to the south of the Gulf Stream flanc region (the red contours in c). In red are the years with strong EDW renewal in the northern Sargasso Sea region (the blue contours in c). In orange are the years with strong formation in both aforementioned regions. See Table 4.2 for the summary of the extreme years and their corresponding PCs.

1976-1990	5	3.0	3	5.0	2	7.5
1961-1975	7	2.1	2	7.5	5	3.0
1950-1960	5	2.2	2	5.5	3	3.7
1950-2020	28	2.0	14	5.0	14	5.0

Table 4.1: The 1950-2020 EDW renewal volume monthly extreme occurrences and corresponding fraction extremes in 15-year increments. Fraction extremes are the average number of months between two extreme occurences. For example, from 2006-2020, there is an average of 1 extreme occurence every 2.5 years.

4.3.2 EDW renewal spatial distribution

To investigate the spatial distribution of the EDW cropping, we performed EOF analysis (Figure 4-2). We observed two sections of EDW outcropping regions in the western subtropical North Atlantic. The western part is centered at $65-70^{o}$W, 35^{o}N. The eastern part is centered at 55^{o}W, 37^{o}N. These two regions correspond with two types of EDW, with the western one near the northern Sargasso Sea, as well as the eastern one at the southern flanc of the Gulf Stream front (Joyce, 2011). We aimed to use the principal component time series of the first two EOFs (Figure 4-2 b and d) to understand of each extreme years, the contribution of EDW renewal from each region. We also synthesized the time series into Table 4.2 to compare among all years the contributions of the two spacial patterns.

We observed that among the strong extreme years, 2010, 1992, and 1981 show peaks in the first PC, namely 2.8, 2.2, and 1.0 respectively (the orange lines in Figure 4-2b). In addition, we observed that the year 2010, 1992, and 1981 have small second PCs. Their magnitudes are < 1.0. The PCs are standardized in Figure 4-2 (b) and (d). In these years large EDW formation took place in both northern Sargasso Sea region as well as the Gulf Stream frontal region. The difference of renewal volumes in these two regions are comparably small.

We observed that among the strong extreme years, 2013, 2001, and 1962 show peaks in the second PC, namely 1.0, 2.0, and 1.0 respectively (the blue lines in Figure 4-2d). In addition, these years have small or average values in the first PC, compared with 2010, 1992, 1981. In these years large EDW formation took place predominantly in the Gulf Stream frontal region.

Similarly we observed that large EDW formation took place predominantly in the northern Sargasso Sea region in 2005 and 1985 (the red lines in Figure 4-2b).

The extreme years of weak EDW renewal correspond with troughs on the PC1 time series (Table 4.2). Note the exceptions of 1963, 1954, and 1951, where the first principle components are not negative, but the EDW renewals are weak.

Year	PC1		PC2		Reference
	< 0 (Weak)	> 0 (Strong)	< 0 (N. Sargasso)	> 0 (Gulf Stream)	
2019	-	-	-	Peak, $> \sigma$	
2014	Trough, $< -\sigma$	-	Non-extreme	-	
2013	-	Peak	-	Peak	
2012	Trough	-	-	-	Billheimer and Talley 2013
2010	-	Peak, $> \sigma$	-	-	Billheimer and Talley 2013
2008	Trough	-	-	-	Billheimer and Talley 2013
2005	-	Peak	Trough, $< -\sigma$	-	Billheimer and Talley 2013

2001	-	Near peak, $> \sigma$	-	Peak, $> \sigma$	
2000	-	Peak, $> \sigma$	Trough, $< -\sigma$	-	
1999	Trough	-	-	-	
1992	-	Peak, $> \sigma$	-	-	
1989	Trough, $< -\sigma$	-	-	-	Klein and Hogg 1996
1985	-	Peak	Trough	-	
1982	Near trough	-	-	Non-extreme	
1981	-	Peak	-	-	
1976	Non-extreme	-	-	Non-extreme	Diaz and Quayle 1978, Klein and Hogg 1996
1975	Near trough	-	-	-	Diaz and Quayle 1978, Klein and Hogg 1996, Worthington 1977, Jenkins and WJ 1982
1974	Trough, $< -\sigma$	-	-	Non-extreme	Diaz and Quayle 1978, Klein and Hogg 1996, Worthington 1977, Jenkins and WJ 1982
1969	-	Peak	Non-extreme	-	
1967	Trough	-	-	-	
1963	-	Non-extreme	Near trough	-	Klein and Hogg 1996
1962	-	Non-extreme	-	Peak	
1961	Trough	-	-	-	
1959	Trough	-	Trough, $< -\sigma$	-	
1958	-	-	-	Non-extreme	
1954	-	Non-extreme	-	Peak, $> \sigma$	
1953	-	Peak, $> \sigma$	-	-	
1951	-	-	Non-extreme	-	

Table 4.2: The summary of the EDW extreme years and their first two principle components since 1950. This table is based on Figure 4-2. Shaded in red are the extreme years of strong EDW renewal, and shaded in blue the weak EDW renewal. The principle components are calculated based on the interannual variability of EDW seasonal-maximum outcropping volume (6-50 month filter). The first principle component (PC1) indicates the strength of EDW renewal over the entire EDW formation region. The second principle component (PC2) indicates the strength of the dipole structure shown in EOF2. This dipole structure corresponds with the eastern and the western part of the EDW formation region, namely the southern flanc of the Gulf Stream and the northern Sargasso Sea. See Section 4.3.2 for details.

4.3.3 Interannual variability of EDW ventilated volume

In this section, we focused on the Argo era (after 2000) to examine the extreme EDW renewal years among different Argo observational reanalysis products. We examined

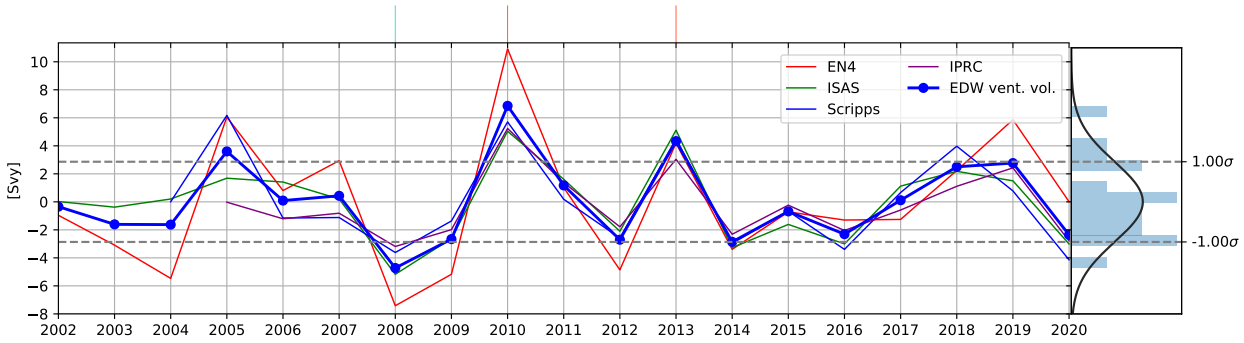

Figure 4-3: 2002-2020 interannual variability of EDW ventilated volume, in the unit of Svy (the blue curve). The averaged EDW renewal volume is in solid blue line with dots. The blue dots on the solid black line indicate the EDW renewal volume in March. In green is EDW calculated using the ISAS dataset, EN4 in red, Scripps in blue, and IPRC in purple. The grey dashed lines are the standard deviation ($\sigma = 2.86\,\mathrm{Svy}$) of the interannual EDW ventilated volume time series. The histogram of interannual EDW renewal volume values is represented to the right, superimposed with a Gaussian fit (solid black curve). The months with EDW renewal volume in all examined datasets greater than σ are in short solid red lines in the "rug" plot, and those smaller than $-\sigma$ are in cyan.

the interannual variability of EDW ventilated volume (the blue line with dots in Figure 4-3). We chose as the extreme years of the EDW renewal the years with all data products exceeding the standard deviation $\sigma = 2.86\,\mathrm{Svy}$. The years 2010 and 2013 are extreme years of strong EDW ventilation, as well as 2008 is an extreme year of weak EDW ventilation. They are robust signals as the EDW outcropping volumes calculated using all the employed datasets surpass the $\pm 1\,\sigma$ lines.

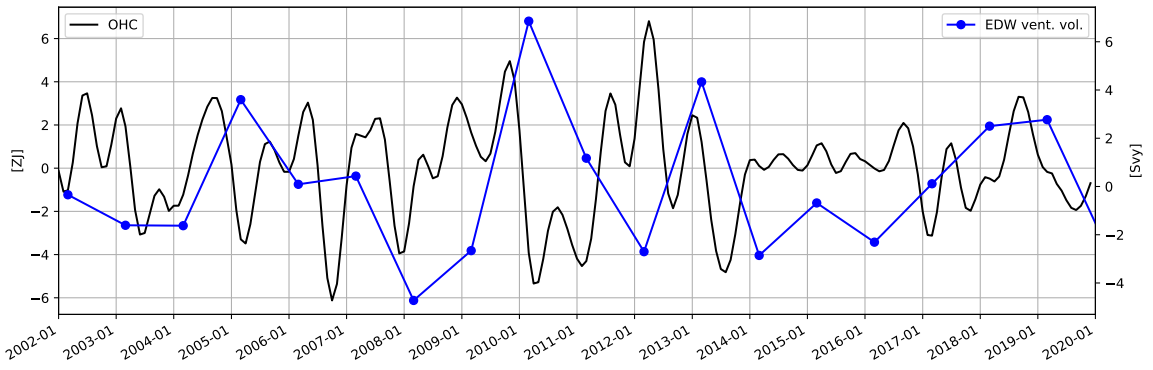

Figure 4-4: The comparison between OHC and EDW seasonal-maximum outcropping volume on the interannual time scale (with 6-50 month band pass filters).

4.3.4 OHC of the September-March period

We obtained the interannual time series of OHC from the previous Chapter. We compared this OHC time series with the EDW outcropping volume (Figure 4-4). One would expect an anti-correlation between these two time series. In the early spring of 2005 and 2010, peaks of large newly renewed EDW volume correspond with troughs of low OHC. In the early spring of 2012, the trough of a weak EDW renewal corresponds with the peak of high OHC. However, the renewed EDW volume exhibits extreme values in 2008, 2013, and 2014-2016 that correspond to OHC anomalies in a counter-intuitive manner.

Using the interannual time series of OHC with a 6-50 month filter, we investigated the OHC change (ΔOHC) over a fixed period of September-March (referred to as the wintertime) to corroborate our previous findings, as well as to reveal other extreme years (Figure 4-5a). We also provided the ΔOHC calculated using the original time series without filter (Figure 4-5b). We employed 1 standard deviation of ΔOHC in the winter time to select the extreme years with large ΔOHC

Concerning large ΔOHC decrease extremes, in Winter 2010, ΔOHC is about $-12.0\,\mathrm{ZJ}$, the largest wintertime decrease in the period of 2002-2019 (the thick grey line with + in Figure 4-5b). Correspondingly in the 6-50 month variability, ΔOHC, the OHC experienced a decrease of $-6.0\,\mathrm{ZJ}$ from September to March, 50% of the decrease observed in the original time series (the thick grey line with + in Figure 4-5a). The ΔOHC in 2010 with 6-50 month filter makes it second after 2005.

In Winter 2005, ΔOHC is $-7\,\mathrm{ZJ}$ (the thick black line with + in Figure 4-5b), second after 2010. However the 2005 ΔOHC with 6-50 month filter is $-7.5\,\mathrm{ZJ}$, becoming the largest in the period of 2002-2019, even larger than 2010.

In Winter 2019, ΔOHC is about $-4.5\,\mathrm{ZJ}$. The ΔOHC in Winter 2019 surpasses the $1\,\sigma$ threshold, and is selected as a negative extreme. Correspondingly in the 6-50 month variability, ΔOHC, the OHC experienced a decrease of $-3.7\,\mathrm{ZJ}$ from September to March, 82% of the decrease observed in the 6-50 month variability.

Both 2005 and 2010 are known as the extreme years of strong EDW renewal. The year 2019 is also an extreme year of strong EDW renewal in the interannual time variability (Figure 4-1 and Figure 4-3).

Concerning positive ΔOHC extremes, in Winter 2014 and 2012, ΔOHC is about $6.3\,\mathrm{ZJ}$, and $4.0\,\mathrm{ZJ}$ respectively. Of both years, the ΔOHC with a 6-50 month filter are still extremes, exceeding the $1\,\sigma$ line (Figure 4-5a).

Note that the wintertime OHC change in 2008 and 2013 are not able to directly herald their extreme EDW renewal. The EDW renewal in 2008 and 2013 corresponds with wintertime ΔOHC in a counter-intuitive manner. In Winter 2008, ΔOHC is about $-2.7\,\mathrm{ZJ}$ (Figure 4-5b). The year 2008 is an extreme weak year of EDW renewal. In Winter 2013, ΔOHC is about $2.0\,\mathrm{ZJ}$. The year 2013 is an extreme strong year of EDW renewal. Both 2008 and 2013 have wintertime ΔOHC corresponding with the EDW renewal in a counterintuitive manner. In addition, though 2007 is an extreme year of the wintertime OHC increase, it is not an extreme year of EDW renwal.

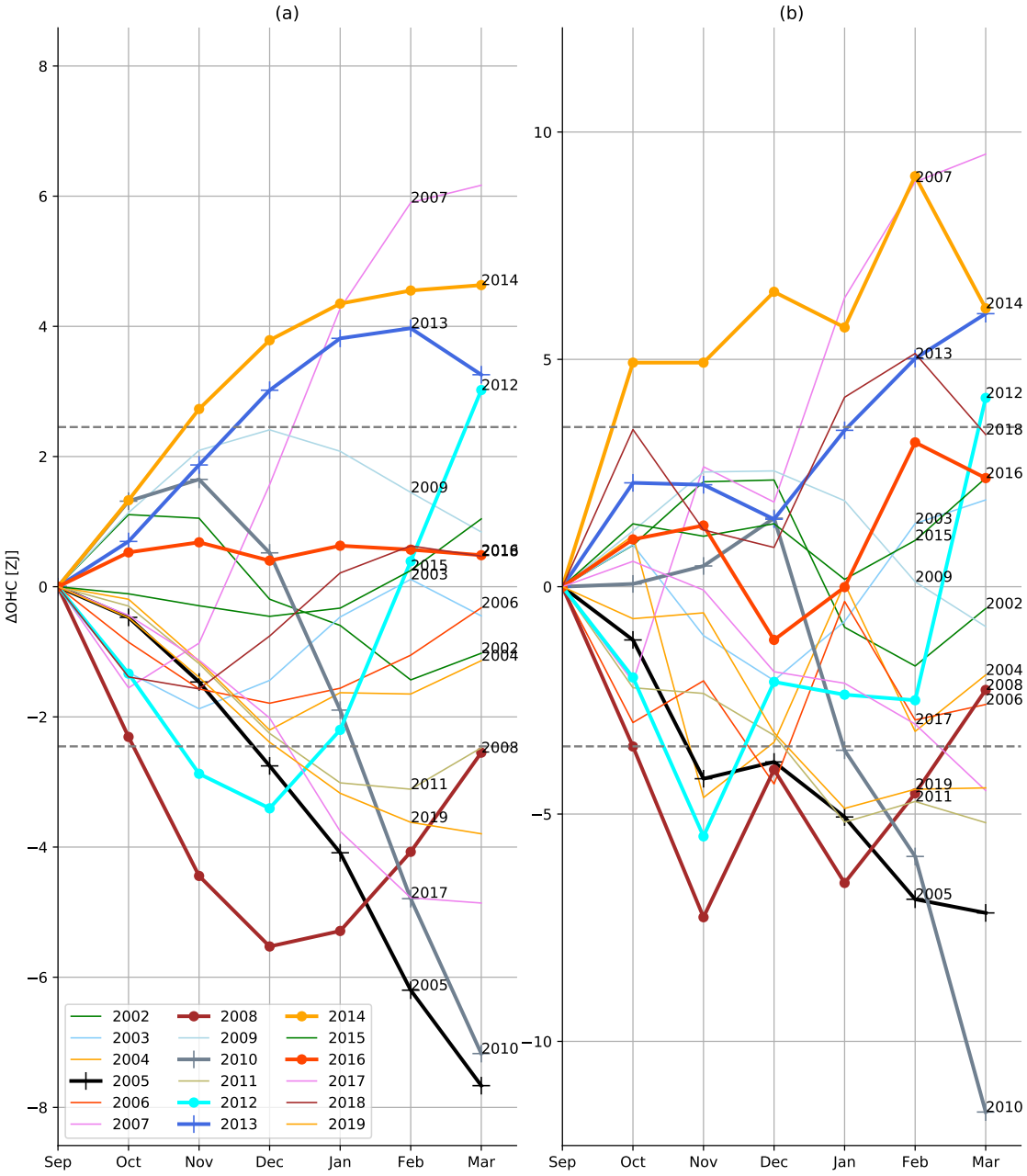
(a)
(b)
ΔOHC [ZJ]
Sep
Oct
Nov
Dec
Jan
Feb
Mar
2002
2003
2004
2005
2006
2007
2008
2009
2010
2011
2012
2013
2014
2015
2016
2017
2018
2019

Figure 4-5

Figure 4-5 *(previous page)*: The 2002-2019 September-March OHC change (ΔOHC), in the unit of ZJ, of (a) the interannual variability with a 6-15 month filter, and (b) the "no-smoothing" time series. The standard deviation of winter time ΔOHC is indicated as $\sigma = 2.42\,\mathrm{ZJ}$ in (a) and $\sigma = 3.51$ in (b). The ± 1 standard deviation are in dashed grey lines. The thick solid lines with dots are EDW formation extreme years. The extreme years of strong EDW formation are indicated in +, and the weak extreme years in $\bullet$. The variable is calculated as the average of ISAS, EN4, Scripps, and IPRC datasets. The correlation coefficient between ΔOHC and EDW ventilated volume based on interannual time scale (6-50 month filter, in a) is -0.43. The correlation coefficient between ΔOHC and EDW ventilated volume based on the original unfiltered time series is -0.47.

4.3.5 Air-sea heat flux

We examined the wintertime air-sea heat flux change and its relation to the EDW renewal extremes (Figure 4-6b).

The increase (decrease) in wintertime air-sea heat flux change ΔQ_{net} indicates a weak (strong) air-sea surface heat loss in the western subtropical North Atlantic region. Among the weak extreme EDW renewal years, 2008, 2012, 2014-2016 experienced large wintertime air-sea heat flux increase, with a magnitude exceeding the $1\,\sigma$ line, considered as positive extremes. In both 2010 and 2013, the ΔQ_{net} exceed the $-\,\sigma$ line, considered as negative extremes.

Note that 2005 is an extreme year of strong EDW renewal. However, the 2005 wintertime ΔQ_{net} is $-0.7\,\mathrm{ZJ}$ (Figure 4-6b), within the $\pm\sigma$ range. This indicates a less intense air-sea surface heat loss in 2005 than in 2010 and 2013.

On an interannual time scale, the impact of wintertime accumulated air-sea heat flux to the extreme years of EDW renewal is examined (Figure 4-6a). We compared the orginal unfiltered time series of air-sea heat flux to the interannual time series with a 6-50 month filter (Figure 4-6a). Among the weak EDW renewal years, the original unfiltered air-sea heat flux time series exhibited more clearly positive extremes than with the interannual time series. In 2005, an extreme year of strong EDW renewal, the orignal unfiltered time series showed more negative air-sea surface heat loss than with the interannual time series.

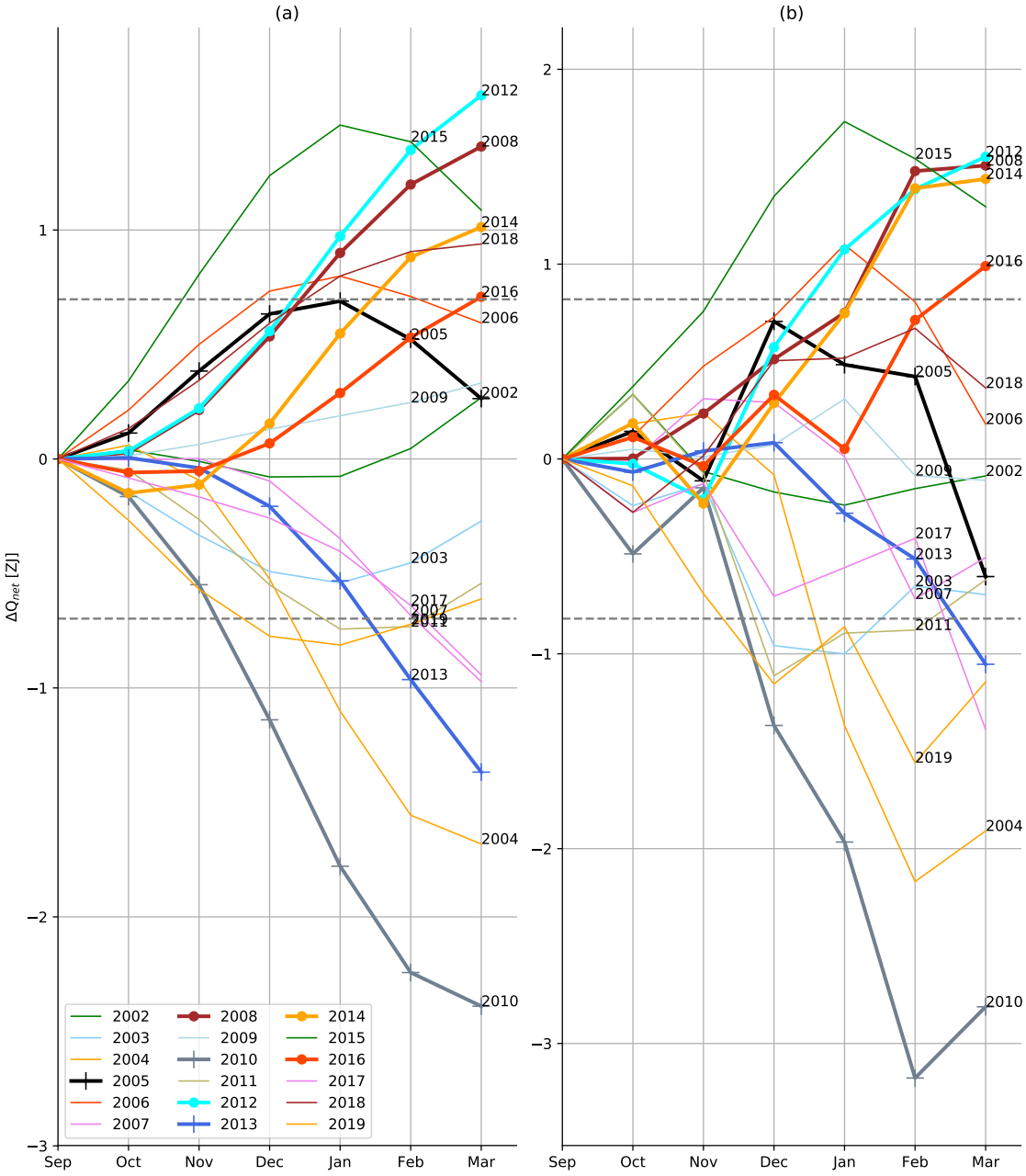
(a)
(b)
ΔQ_{net} [ZJ]
Sep
Oct
Nov
Dec
Jan
Feb
Mar
2002
2003
2004
2005
2006
2007
2008
2009
2010
2011
2012
2013
2014
2015
2016
2017
2018
2019

Figure 4-6

Figure 4-6 *(previous page)*: The 2002-2019 September-March air-sea heat flux change (ΔQ_{net}), in the unit of ZJ, of (a) the interannual variability with a 6-15 month filter, and (b) the "no-smoothing" time series. The positive and negative standard deviation of wintertime air-sea heat flux, $\sigma = 0.7$ ZJ in (a), and $\sigma = 0.82$ ZJ in (b), are in dashed grey lines. The thick solid lines with dots are EDW formation extreme years. The extreme years of strong EDW formation are indicated in +, and the weak extreme years in •. The variable is calculated as the average of ERA and NCEP datasets.

We observed negative (positive) air-sea heat flux anomalies in the subtropical gyre attributed to extreme years of strong (weak) EDW renewal (Figure 4-7 and Figure 4-8, c and d).

On an interannual time scale, a warming (cooling) due to an air-sea heat flux corresponds with a positive (negative) SST. Large troughs in the early spring of 2010 and 2011 are observed on the SST curve with amplitudes of -0.23^{o}C--0.25^{o}C (Figure 4-13b). Similarly large troughs are observed in the air-sea heat flux interannual variability curve (the dashed black line in Figure 4-13b). Note that in the early spring of 2007, the SST curve shows trough with an anomaly of -0.1^{o}C (Figure 4-13b), while the air-sea heat flux curve also shows a trough with a magnitude of -1 ZJ in spring and summer of 2017 (the dashed black line in Figure 4-13b). The peaks in the winter of 2012 and 2015 are both observed in the air-sea heat flux and the SST interannual variability curves.

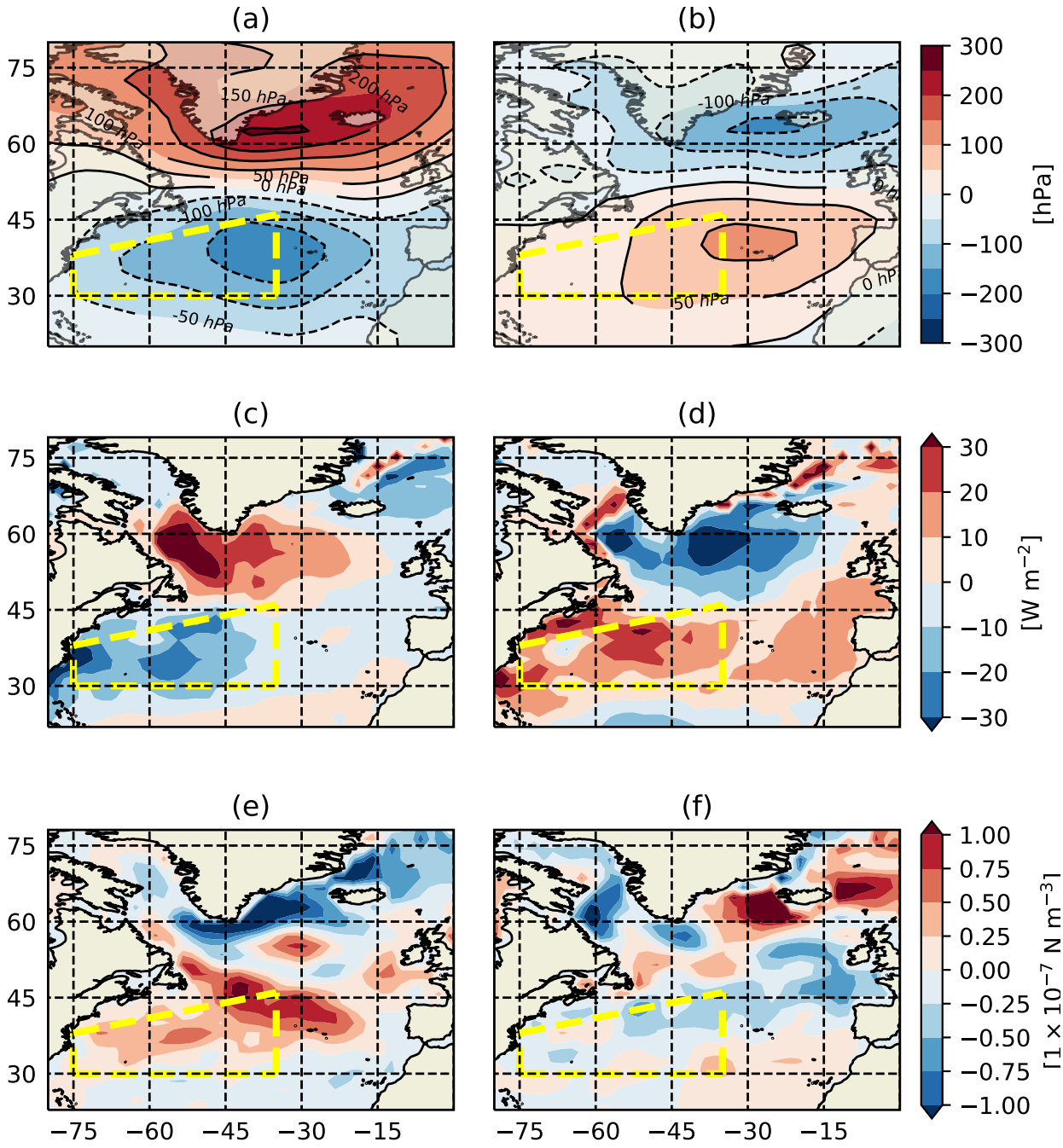
(a)
(b)
(c)
(d)
(e)
(f)
150 hPa
200 hPa
100 hPa
50 hPa
0 hPa
-50 hPa
-100 hPa
75
60
45
30
−75
−60
−45
−30
−15
300
200
100
0
−100
−200
−300
[hPa]
30
20
10
0
−10
−20
−30
[W m^{-2}]
1.00
0.75
0.50
0.25
0.00
−0.25
−0.50
−0.75
−1.00
[1 × 10^{-7} N m^{-3}]

Figure 4-7

Figure 4-7 *(previous page)*: Mapped composites of atmospheric variables onto wintertime EDW renewal extremes: (a, b) sea level pressure, in the unit of hPa, (c, d) air-sea heat flux, in the unit of W m^{-2}, and (e, f) surface wind stress curl, in the unit of 1×10^{-7} N m^{-3}. Plots on the right column are the composites onto the weak EDW renewal extremes, and plots on the left column onto the strong extremes. We used the NCEP dataset to produce this plot.

In short, in the subtropical region, more (less) intense negative air-sea heat flux corresponds with the positive (negative) extreme years of EDW renewal. In the subpolar region, we observed positive anomalies during the extreme strong EDW renewal years, as well as negative anomalies during the extreme weak EDW renewal years. In both subtropical and subpolar regions, the spacial distribution of these anomalies during strong and weak EDW renewal years are asymetric.

4.3.6 Ekman effects

We examined the wind stress curl composites attributed to the extreme years of EDW renewal (Figure 4-7e and Figure 4-8e). During the strong EDW renewal extreme years, we observed a positive wind stress curl located in the central subtropical North Atlantic region (45°N, $30^o - 45^o$W), to the northeast of the EDW formation region. The magnitude of this positive wind stress curl is $> 0.4 \times 10^{-7}$ N m^{-3}. In the subpolar region, during the strong years, we observed a negative wind stress curl along the Irminger Sea Current, distributed around the southern tip of Greenland, with a magnitude of $> 0.4 \times 10^{-7}$ N m^{-3}.

During the weak EDW renewal extreme years, we observed a negative wind stress curl in the subtropical region, with a magnitude of $< 0.1 \times 10^{-7}$ N m^{-3} (Figure 4-7f and Figure 4-8f). In the Irminger Sea region we observed a patch of positive wind stress curl, with a magnitude of $> 0.4 \times 10^{-7}$ N m^{-3}.

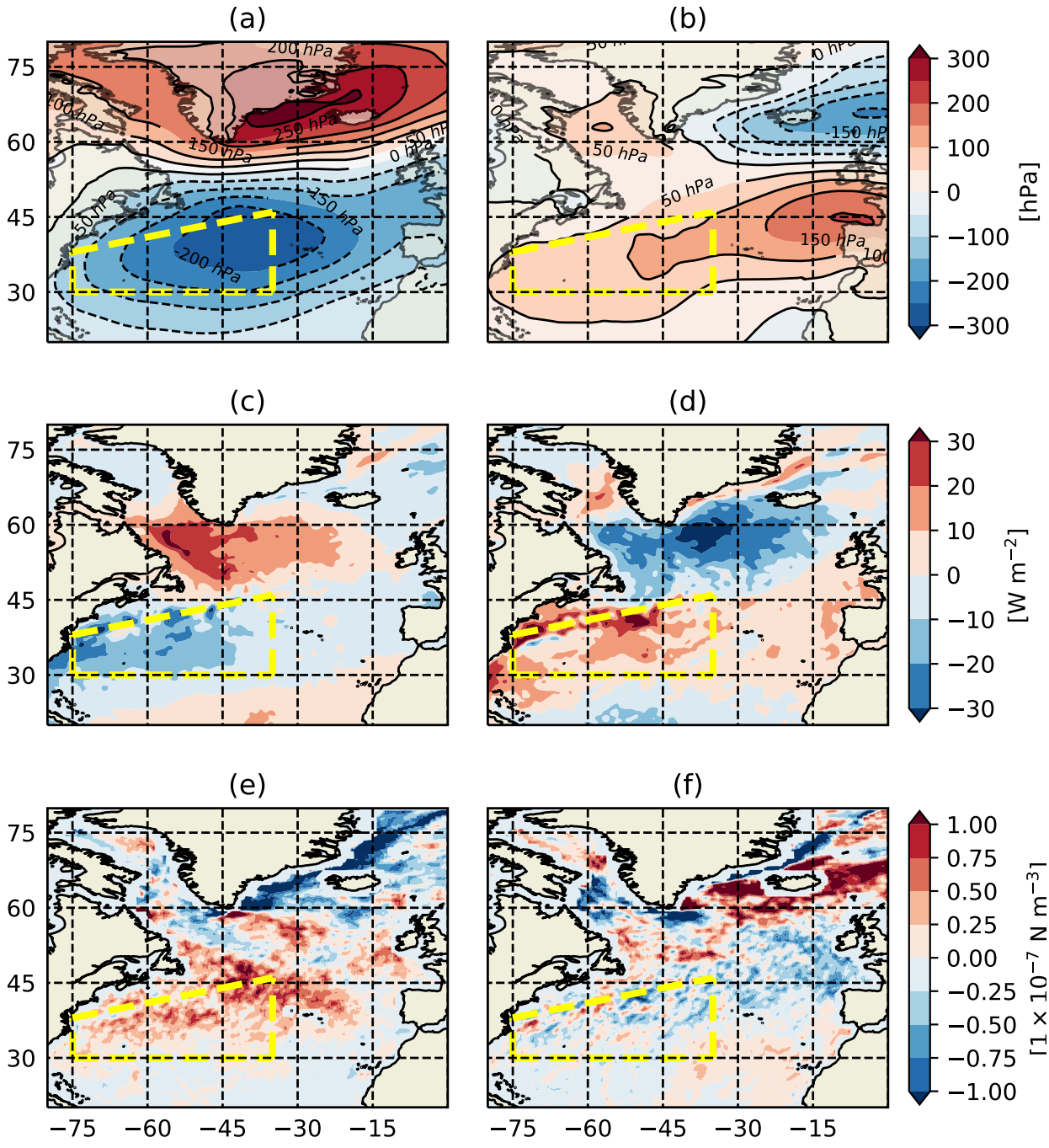

Figure 4-8: Similar to Figure 4-7, except we used the ERA dataset.

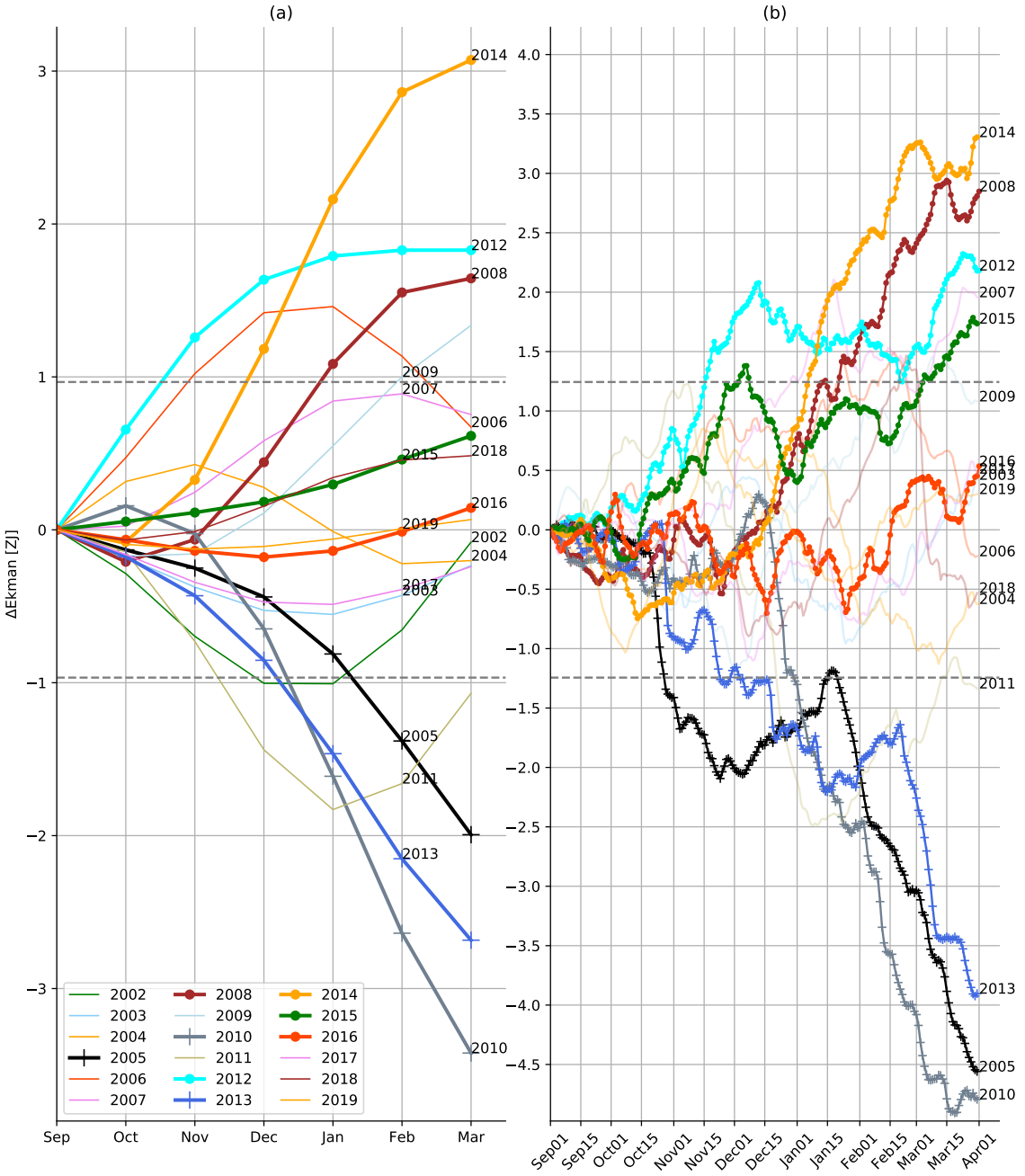
(a)
(b)
ΔEkman [Z]
Sep
Oct
Nov
Dec
Jan
Feb
Mar
Sep01
Sep15
Oct01
Oct15
Nov01
Nov15
Dec01
Dec15
Jan01
Jan15
Feb01
Feb15
Mar01
Mar15
Apr01
2002
2003
2004
2005
2006
2007
2008
2009
2010
2011
2012
2013
2014
2015
2016
2017
2018
2019

Figure 4-9

Figure 4-9 *(previous page)*: (a) The 2002-2019 September-March Ekman heat advection change (ΔEkman), in the unit of ZJ ($1\,\mathrm{ZJ} = 1 \times 10^{21}\,\mathrm{J}$). We employed the interannual variability of the Ekman heat advection, using 6-50 month filter to produce this plot. The positive and negative standard deviation of wintertime heat convergence due to Ekman advection, $\sigma = 0.97\,\mathrm{ZJ}$ are in dashed grey lines. To calculate the time series, we employed as the ocean datasets ISAS, EN4, Scripps and IPRC. We employed as the atmospheric forcing datasets NCEP and ERA. The Ekman heat advection is calculated as the average of all the employed datasets. (b) The 2003-2019 September-March, daily accumulated "no-smoothing" anomalies of the heat convergence due to Ekman advection, in the unit of ZJ. The positive and negative standard deviation of wintertime heat convergence due to Ekman advection, $\sigma = 1.24\,\mathrm{ZJ}$ are in dashed grey lines. To obtain the "no-smoothing" anomalies, we detrended and de-seasonalized the time series without applying band-pass filter. The temperature and in-situ density are from the ISAS dataset. The near-surface momentum fluxes are from the NCEP dataset. The thick solid lines with • are extreme years of weak EDW formation, and the ones with + are extreme years of strong EDW formation.

Year	**Storm-associated Ekman Convergence (ZJ)**		**Accumulated storm duration (day)**		**Ekman equivalent heat flux ($\mathbf{W\,m^{-2}}$)**	
2005	−6.0	(87.5%)	133	(max)	−106.7	(68.8%)
2008	−2.4	(18.8%)	78	(25%)	−70.8	(min)
2010	-6.9	(max)	128	(93.8%)	-126.9	(87.5%)
2012	-2.7	(31.2%)	77	(18.8%)	-82.3	(43.8%)
2013	-6.5	(93.8%)	108	(87.5%)	-140.7	(max)
2014	-1.9	(min)	60	(min)	-72.9	(12.5%)
2015	-2.6	(25.0%)	81	(31.2%)	-74.9	(18.8%)

Table 4.3: The storm-associated Ekman heat convergence, storm duration, and Ekman equivalent heat flux during the extreme EDW ventilation years. In grey are the extreme strong years of EDW ventilation. In white are the extreme weak years of EDW ventilation. In parenthesis are the percentile ranks.

The heat convergence due to Ekman advection serves as an indicator of the extreme years of EDW renewal (Figure 4-9a). Among the extreme years of weak EDW renewal, the years 2008, 2012, and 2014 correspond with extreme wintertime Ekman heat advection convergence. Among the extreme years of strong EDW renewal, the years 2005, 2013, and 2010 correspond with extreme wintertime Ekman heat advection divergence. The extreme years of weak EDW renewal, 2015, 2016 and 2019 correspond with Ekman heat advection convergence (> 0).

In extreme formation years the contribution of Ekman divergence is as large as the contribution of air-sea heat flux. For example, In 2009-2010, the heat loss due to Ekman heat divergence is $-3.5\,\mathrm{ZJ}$, and the heat loss due to air-sea surface heat flux is $-2.4\,\mathrm{ZJ}$ (Figure 4-6a and Figure 4-9a). Similarly, in 2011-2012, the heat loss due to Ekman heat divergence is $1.8\,\mathrm{ZJ}$, and the heat loss due to air-sea surface heat flux is $1.5\,\mathrm{ZJ}$.

We took one step further to understand the Ekman advection's role from the weather events perspective. We aimed to address this question: when the extreme EDW formation occurs, is it due to one single strong weather event, or due to some constant signals over a long period (i.e. wintertime). We investigated the daily progression of the Ekman heat convergence during the EDW formation period of each year (Figure 4-9b). We removed the typical seasonal cycle to produce the daily Ekman heat convergence, without band-pass filter. For example, a decrease on the accumulated Ekman heat convergence (Figure 4-9b) indicates cooling in the domain of analysis, which can be associated with low pressure systems passing by the domain of analysis.

Hurricane Sandy passed the domain of study during 26-30 in October 2012, responsible for an accumulated Ekman heat convergence of $-0.9\,\mathrm{ZJ}$ during 9 days (the blue curve in Figure 4-9b). Hurricane Sandy is responsible for 23% of the total Ekman heat convergence decrease in the wintertime of 2013. From 20 November 2012-mid-January 2013, three storms, each occurring one month apart, brought a total Ekman heat divergence of $-1.5\,\mathrm{ZJ}$, 38% of the total Ekman heat divergence in the wintertime of 2013. Included in these storms is the prelude to Wind Storm Gong, which brought dustructive high winds to Portugal (Liberato, 2014). Also included in these storms is the aftermath of the 2012 Mid-December Blizzard, featuring heavy snowfalls and gusty winds in US Midwest. From 21 February-10 March, 2013, two consecutive blizzards, namely the Late February Winter Storm and the March Nor'easter, passed the domain of study. The two typical blizzards during this time of year had a wide impact on US South, Midwest, and east coast states.

In short, the years 2005, 2010, and 2013 are identified as strong EDW formation

years. During the EDW formation period of one year, we observed the remnant storms from decaying hurricanes in the late fall, and the blizzards in winter and early spring, moved off the US east coast, that passed through the domain of study. During these strong years, these storms during the EDW formation period are responsible for the sudden decrease of the accumulated Ekman heat advection (Figure 4-9b).

We aimed to identify the storms that have a large enough impact on the domain of analysis. We selected the periods with decrease in Ekman heat convergence that lasts longer than two consecutive days. We marked these selected periods as passing storms over the domain of study. The total wintertime duration of the storms, and the storm-associated Ekman heat convergence are listed in Table 4.3. For each year, we divided the total storm-associated Ekman heat convergence by the total number of days of storms to obtain the averaged slope. We referred to this slope as the Ekman equivalent heat flux associated with storms (Table 4.3).

Of the strong extreme EDW renewal years, the Ekman heat divergence, equivalent Ekman heat flux, and storm duration are at the higher percentile ranks of the year 2003-2018 (Table 4.3). The 2005 period has the longest storm duration. The 2010 period has the largest storm-associated total Ekman heat divergence, while the 2013 period has the largest Ekman equivalent heat flux. The storm effects on Ekman heat divergence accumulate over time, and are sufficient to separate the extreme years of strong EDW formation from the remaining years.

4.3.7 NAO

We investigated the sea level pressure composites attributed to the extreme years of EDW renewal (Figure 4-7 a and b, and Figure 4-8 a and b). Among the extreme years of strong EDW renewal, the negative sea level pressure is centered in the central subtropical Atlantic region, and the positive sea level pressure is centered between Iceland and the southern tip of Greenland, above the Irminger Sea region (Figure 4-7a and Figure 4-8a). This sea level pressure pattern resembles the NAO-.

Among the extreme years of weak EDW renewal, the sea level pressure composite is almost opposite from the strong EDW renewal years. It resembles NAO+, but shifted more to the east. Note that the centers of the low and high sea level pressure patterns are shifted eastward, compared to the strong years (Figure 4-7b and Figure 4-8b).

4.3.8 Preconditioning

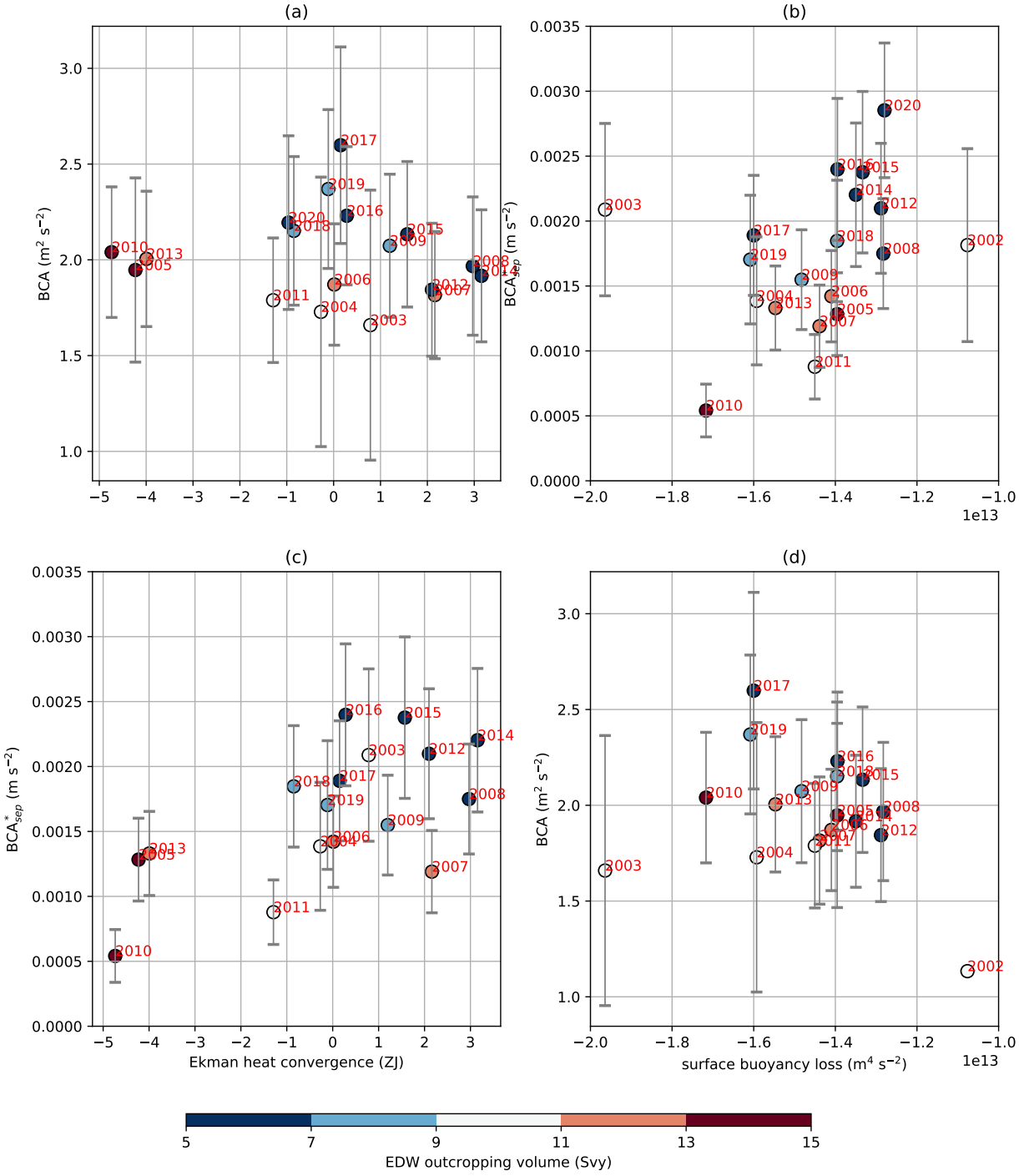
(a)
(b)
(c)
(d)
BCA (m^2 s^{-2})
BCA$^*_{sep}$ (m s^{-2})
Ekman heat convergence (ZJ)
surface buoyancy loss (m^4 s^{-2})
1e13
EDW outcropping volume (Svy)

Figure 4-10

Figure 4-10 *(previous page)*: The preconditioning measured by (a, d) the fixed domain buoyancy content anomaly (BCA), and (b, c) the $\mathrm{BCA}^*_{\mathrm{Sep}}$. The fixed domain BCA is the September buoyancy content above $\sigma_o = 26.7\,\mathrm{kg\,m^{-3}}$, in the unit of $\mathrm{m^2\,s^{-2}}$. The $\mathrm{BCA}^*_{\mathrm{Sep}}$ is the buoyancy content above the following March mixed layer depth, and then normalized by the March mixed layer depth, in the unit of $\mathrm{m\,s^{-2}}$. Both BCAs are averaged over the surface area of the domain of study. The colorbar shows the EDW outcropping volume in the early Spring of each year, in the unit of Svy. The horizontal axis in (a, c) indicates the interannual accumulated Ekman heat transport during September-March period, in the domain of study. The horizontal axis in (b, d) indicates the air-sea surface buoyancy loss, associated with the air-sea heat loss, in the unit of $\mathrm{m^4\,s^{-2}}$. The Ekman heat divergence is calculated using the NCEP dataset. The air-sea surface heat loss are calculated as the averaged of the ERA and NCEP datasets. The BCAs and its unbiased standard errors are calculated using ISAS, EN4, SCRIPPS, and IPRC datasets.

We found that the wintertime OHC change is not correlated with the EDW renewal extreme years. In this section we investigated the preconditioning in September in the domain of analysis. To describe preconditioning, we employed two metrics: the $\mathrm{BCA}^*_{\mathrm{Sep}}$ and the fixed domain BCA. The fixed domain BCA refers to the integrated buoyancy content above the permanent pycnocline (Equation 2.24). It includes the buoyancy that needs to be removed (i.e. the seasonal pycnocline) before ventilation starts. Compared with the OHC, the fixed domain BCA does not describe the part of the heat content of the subducted water underneath the permanent pycnocline. A larger (smaller) fixed domain BCA indicates an unfavorable (a favorable) preconditioning for a deep convection in the coming early spring, with more (less) buoyant upper water column (Figure 4-10a and d).

The $\mathrm{BCA}^*_{\mathrm{Sep}}$ refers to the September buoyancy values above the deepest mixed layer in early spring (March), and normalised by this deepest mixed layer depth (Equation 2.25). The $\mathrm{BCA}^*_{\mathrm{Sep}}$ describes the vertical distribution of the heat content in September that potentially turns into a deep convection in the early spring. A larger (smaller) $\mathrm{BCA}^*_{\mathrm{Sep}}$ indicates a less (more) buoyant September upper water column, an unfavorable (a favorable) preconditioning to a deep convection in the coming early spring (Figure 4-10b and c).

Of the strong EDW renewal years, 2005, 2010, and 2013 all have very similar fixed domain BCA, about $2\,\mathrm{m^2\,s^{-2}}$ (Figure 4-10a). However compared with 2005 and

2013, the September 2010 has a BCA^*_{Sep} of $5.0 \times 10^{-3}\,m\,s^{-2}$, the smallest among all the examined years (Figure 4-10b). Although 2005, 2010, and 2013 have similar and neutral preconditioning in terms of upper water buoyancy content, the stratificaiton of 2010 in the upper water column is more favorable to a deep convection than 2005 and 2013.

Of the weak EDW renewal years, 2008, 2012, and 2014 have similar and neutral fixed domain BCA, about $1.9\,m^2\,s^{-2}$ (Figure 4-10a). These three years, as we have found before, experienced large Ekman heat advection convergence. This positive anomaly of Ekman forcing is responsible for the extreme weak EDW renewal in the early spring. In comparison, 2015, 2016, and 2017 experienced less positive wintertime Ekman heat convergence. However, their larger fixed domain BCAs in September are responsible for their weak EDW renewal.

In 2007 and 2012, the fixed domain BCAs are similar in magnitude, about $1.8\,m^2\,s^{-2}$. Their forcing due to Ekman heat convergence are similar as well (Figure 4-10a). However, 2012 is a weak extreme EDW renewal year and 2007 is a strong EDW renewal year. The BCA^*_{Sep} in 2007 is smaller than that of 2012 (Figure 4-10b). This indicates that the stratification in September07 is more favorable to a deep convection in coming early spring than that in September12.

In short, in 2010, a favorable preconditioning through a weak stratification in September10 contributes to the positive extreme EDW renewal in early spring. From 2015 to 2017 unfavorable preconditioning through large upper ocean buoyancy content in September contributes to the negative extreme EDW renewal in early spring. Between 2007 and 2012, despite the same upper ocean buoyancy content in September, the stronger stratification in September12 is responsible for an extreme weak EDW renewal in 2012.

4.3.9 A brief summary of the direct results

We have examined several factors that have an impact on the EDW freshly ventilated volume in the early spring, such as the heat convergence due to Ekman current, the air-sea surface heat loss, and the preconditioning. We synthesized all the factors into Table 4.4 to corroborate our findings as well as to investigate their contributions to the extreme years of EDW early-spring renewal. For each year, we "scored" the contribution of each factor based on its Z-score, the value relative to the mean, in the unit of its standard deviation. We summed the Z-scores of all the examined factors and yielded the total score (the column "Total" in Table 4.4). For comparison, we also listed the EDW freshly ventilated volume (the column "EDW volume").

Among the extreme years of strong EDW renewal (shaded in red in Table 4.4),

the EDW ventilated volume is positive, and the total score is negative. The Ekman heat advection of 2005, 2010, and 2013 is negative with large amplitude, namely, −3.6, −3.8, and −3.1 respectively (the column Ekman, shaded in red in Table 4.4). The air-sea heat flux anomaly of 2005, 2010, and 2013 are negative. Regarding the preconditioning, although the fixed domain BCA indicates weak unfavorable preconditioning, the BCA^*_{Sep} shows that the year 2010 is −2.1 (The row of 2010 and the column of BCA^*_{Sep} in Table 4.4), an important aiding factor to the strong EDW early spring renewal. Billheimer and Talley (2013) showed a vigorous EDW associated vertical convection in the early spring of 2010. They attributed the strong 2010 EDW renewal to the large air-sea surface heat loss, despite an unfavorable preconditioning. Their calculation of preconditioning is identical to our fixed domain BCA. However, with similar buoyancy content as 2005 and 2013, the 2010 BCA^*_{Sep} added extra diagnostic value, indicating a more homogeneous stratification favorable to a vertical convection.

In 2005, the heat advection due to Ekman current is the driving mechanism responsible for the large wintertime buoyancy loss. Its Z-score is −3.6 (Table 4.4), one of the largest negative values in the period of 2003-2019, second after 2010. In comparison, the other factors are less important as contributions to the 2005 extreme EDW renewal.

Among the extreme years of weak EDW renewal, in 2012 and 2008, both the heat advection due to Ekman current and the air-sea surface heat loss are positive with large amplitudes (Table 4.4). The strong surface forcing associated with NAO+. In comparison, the preconditioning of these two years have less important impact. This is in line with Billheimer and Talley (2013).

Year	Ekman	Air-sea	Preconditioning		Total	EDW volume
			BCA^*_{Sep}	BCA_{Sep}		
2003	0.4	−0.8	0.9	−1.0	−0.5	0.3
2004	−0.5	−2.3	−0.5	−0.8	−4.0	0.5
2005	−3.6	−0.7	−0.8	−0.0	−5.1	1.8
2006	−0.1	0.3	−0.5	−0.3	−0.6	0.8
2007	1.6	−0.6	−0.9	−0.5	−0.4	0.8
2008	2.3	1.9	0.2	0.0	4.4	−0.6
2009	0.9	−0.1	−0.2	0.4	1.0	−0.2
2010	−3.8	−3.4	−2.3	0.3	−9.2	2.1
2011	−1.0	−0.7	−1.6	−0.6	−3.9	0.4
2012	1.8	1.9	0.9	−0.4	4.3	−0.9

2013	−3.1	−1.2	−0.7	0.2	−4.8	0.7
2014	2.7	1.8	1.1	−0.1	5.5	−1.4
2015	1.4	1.6	1.5	0.6	5.1	−1.0
2016	0.5	1.3	1.5	0.9	4.2	−1.5
2017	0.4	−1.6	0.5	2.1	1.4	−0.8
2018	−0.4	0.5	0.4	0.6	1.1	−0.2
2019	0.3	−1.3	0.1	1.4	0.4	−0.1

Table 4.4: 2003-2019 newly formed EDW volume, wintertime forcing, and preconditioning z-score table. The z-score is calcualted in terms of standard deviation from the mean. The table content is in the unit of standard deviation of the time series. For each variable, we employed the unfiltered time series. The preconditioning includes the fixed-domain BCA in September and the BCA^*_{Sep}. We listed as the wintertime forcing the accumulated heat convergence due to Ekman advection ("Ekman"), and the accumulated air-sea surface heat flux ("Air-sea"). Of each year, we calculated "Total" as the sum of the z-scores of the preconditioning and those of the wintertime forcing. The wintertime is defined as the period of September of previous year to March of the current year.

4.4 Discussion

4.4.1 Ventilated Volume and Subducted Volume

In this chapter, we examined the EDW outcropping volume, that reaches its seasonal maximum in early spring (e.g. March). We showed the EDW surface outcropping area (solid red contours enclosed by the domain of analysis, Figure 2-1). Qiu and Huang (1995) showed that the obduction typically takes place in the late fall and early winter, and the subduction rapidly takes place in late winter and early spring. Our EDW outcropping area matches their ambiductive region (Figure 8, Qiu and Huang 1995), an area where both subduction and obduction take place (Qiu and Huang, 1995). The freshly ventilated EDW consists of newly generated EDW by air-sea heat loss and the obducted EDW. The freshly ventilated EDW volume in March serves as a source of EDW, subject to a subduction that takes place immediately afterwards with a duration of 1-2 months.

We showed on the interannual time scale, the winter of 2010 experienced an extreme strong EDW renewal. The corresponding seasonal-maximum EDW outcropping volume anomaly is 7.0 Svy in February (Figure 4-1). We observed a positive wind stress curl in our domain of analysis among the extreme years of strong EDW renewal

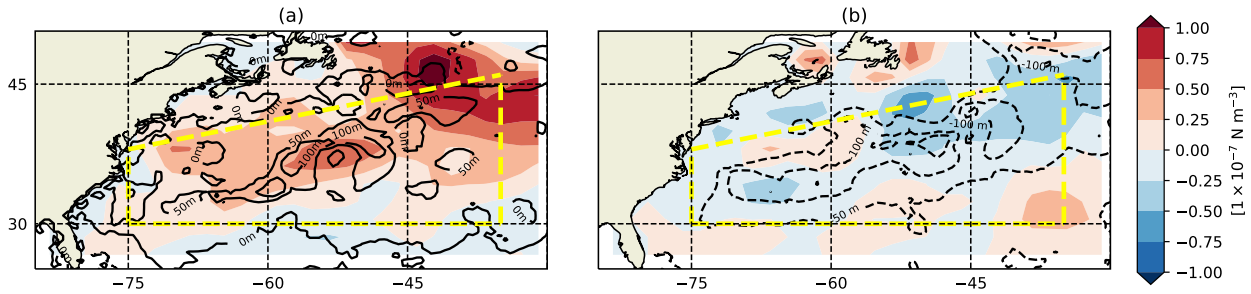

Figure 4-11: The composites of the wintertime deepest mixed layer depth onto (a) the extreme years of strong EDW renewal, and (b) the extreme years of weak EDW renewal. The solide black contours indicate positive anomalies of the wintertime deepest MLD, in the unit of m, and the dashed ones indicate negative. We employed the ISAS dataset to realize the MLD anomalies. The color contours indicate the wind stress curl anomalies, same as in Figure 4-7 e and f. We employed the NCEP dataset to realize the wind stress curl anomalies.

(Figure 4-7e and Figure 4-8e). Qu et al. (2016) showed a positive anomaly of MLD in March 2010 (Fig.12a) in the EDW outcropping region. Our finding is coherent, as the wind stress curl anomaly affected the surface layer, bringing more cold water to the surface and hence promoting convection. In addition, due to more intense air-sea heat loss, the colder SST in winter of 2010 encourages a stronger vertical convection as well as a stronger lateral induction resulting a stronger subduction.

4.4.2 Wind-driven Heaving

We found that in the extreme years with strong EDW renewal, the divergence of Ekman current corresponds with a deeper MLD (Figure 4-11). Both the heat convergence due to Ekman transport and the air-sea heat flux are indicators of the extreme years of EDW renewal. Evans et al. (2017) used modeled data showing that in the subtropical gyre, the thermocline depth is correlated with the Ekman divergence, driving the volume transport on the interannual time scales. They showed that this wind-driven heaving plays an important role to the cooling in the North Atlantic subtropical gyre, as important as the air-sea heat fluxes. They showed that the Ekman pumping lifted up the isotherms. With these uplifted isotherms, the cold and dense water underneath is prone to being entrained into the mixed layer. Here, our finding

is that the Ekman heat divergence is responsible for deep mixed layer depth. Yet, they chose as the domain of analysis the subtropical North Atlantic with a latitude range of $26^o - 45^o$N (Fig.9 in Evans et al. 2017). This is larger than our domain of analysis.

4.4.3 EDW outcropping volume

We produced the EDW outcropping volume time series, which reaches 0 in the summer and fall when EDW is capped over by the warm water. The EDW outcropping volume reaches its seasonal maximum in the early spring (Figure 4-1). Kelly and Dong (2013) examined the EDW thickness time series in the EDW formation region. Their time series of the EDW volume in the formation region does not reach 0 in the summer and fall (Fig.4a). This difference is because they examined the EDW even when its capped over in the summer and fall. We examined the volume of the EDW that is ventilated to the surface in winter. It is only meaningful to compare the two time series in early spring, when EDW renewal reaches its seasonal peak intensity.

We observed in the spring of 2001, the EDW outcropping volume reaches its seasonal maximum of 20 Svy (6.3×10^{14} m^3) (Figure 4-1). It is one of the extreme years of strong EDW renewal. Kelly and Dong (2013) showed in Fig.4(a) in spring 2001, the EDW volume in formation region reaches a peak of 16.5 Svy (5.2×10^{14} m^3), less than our estimate by 17%. We observed in the spring of 1999, the EDW outcropping volume reaches its seasonal maximum of 7 Svy (2.2×10^{14} m^3). It is one of the extreme years of weak EDW renewal. Kelly and Dong (2013) showed in Fig.4(a) in spring 1999, the EDW volume in formation region reaches a peak of 6.34 Svy (2.0×10^{14} m^3), less than our estimate by 9%. We found that the difference of the EDW outcropping volume between these two extreme years, is 12 Svy (3.78×10^{14} m^3) (Figure 4-1). Kelly and Dong (2013) showed that the difference between the two peaks in 1999 and 2001 is 12.7 Svy (4.0×10^{14} m^3). Our result is in line with that from Kelly and Dong (2013).

We reported a positive extreme EDW renewal in 1992 the EDW outcropping volume of 18.0Svy (5.67×10^{14}m^3). Their time series shows the corresponding EDW renewal volume of 9.5 Svy (3.0×10^{14} m^3), less than our estimate by 47%.

We reported a non-extreme EDW renewal in 1996, with the EDW outcropping volume of 12Svy (3.78×10^{14} m^3). However, their time series shows the corresponding EDW renewal volume of 18.4 Svy (5.8×10^{14} m^3), a peak in the 1990s.

We reported the 2007 EDW outcropping volume of 13$\pm$2 Svy (($4.1\pm0.6)\times10^{14}$ m^3). Their time series shows the corresponding EDW renewal volume of 13.3 Svy (4.2×10^{14} m^3). We observed a similar seasonal-maximum EDW outcropping volume in early

spring in 2007, calculated by two different criteria for selecting the EDW. Compared with their criteria, in the early spring, our criteria can select areas with mixed layer depth shallower than 100 m, or areas with strong but short-lived EDW convection. One possible explanation is that in 2007, the EDW convection at the outcropping area is intense, and the intense EDW convection is for a long period.

4.4.4 Annual maximum outcropping area

We showed that in the early spring, the freshly ventilated EDW volume and its averaged temperature are correlated with a correlation coefficient of 0.64 (the black and green curves in Figure 4-13c). Kwon and Riser (2004) showed that on an interannual time scale, the EDW temperature and its volume are anticorrelated with a correlation coefficient of -0.8. They measured this EDW temperature as the temperature at the PV minimmum at station S in the southwest of our domain.

This difference is due to the fact that we only took into account the freshly ventilated EDW volume situated at the outcropping area. During the extreme years of weak EDW, the outcropping area is limited to the northeast part of the domain of analysis, where the coldest flavor of EDW is formed. Peng et al. (2006) reported a mean temperature of $17.2^{o} - 17.6^{o}$C at the northeast corner of the EDW volume (northeast of, for example, 37°N, 50°W in their Fig. 7a). This temperature range is in line with our finding as the mean EDW temperature of the weak extreme years.

4.4.5 Geostrophic transport at 30°N

In the previous chapter, we found that the geostrophic volume transport at the southern boundary is the most correlated with the convergence of heat due to the geostrophic advection in our domain of analysis, compared with the transports at other boundaries. The southern boundary of the domain of analysis is 30°N (the blue dotted line in Figure 2-1). This is to the south of the southernmost position of the 19°C isotherm (the thin solid red curve in Figure 2-1).

Kelly and Dong (2013) showed in their Fig. 3c that the geostrophic volume transport across the southern boundary at 32°N serves as a good proxy to the subduction rate. They showed that the bulk of EDW south of 32°N does not usually outcrop. They also stressed that their division of "formation region" and "subduction region" is a simplified approach to understand the complex 3-D subduction process (Kelly and Dong, 2013). We chose to examine the subduction rate through the lense of the geostrophic volume transport at the southern boundary of our domain of analysis at 30°N. 30°N would cut through the center of the "subduction region" (Kelly and Dong,

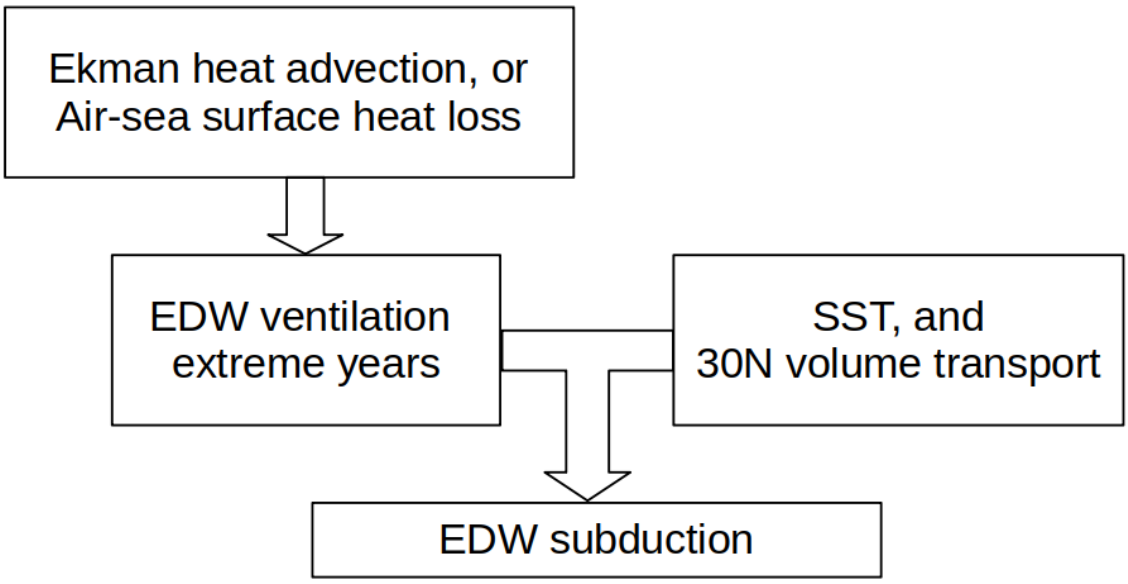

Figure 4-12: The flowchart to investigate the late spring subduction of the extreme EDW renewal years. The Ekman heat advection and the air-sea surface heat loss signal the extreme years of EDW renewal. Of each extreme year, we used SST and southward geostrophic volume transport at 30°N to infer the EDW subduction.

2013; Marshall et al., 1993). Our southern boundary is also south by 2 degrees from the Panulirus station (32°10′N, 64°30′W) near Burmuda. Qu et al. (2016) examined the subduction of the Subtropical Underwater ($50^o - 20^o$W, $20^o - 30^o$N, the black curve in Fig. 1 in Qu et al. 2016), southeast to our domain of analysis. They found that in Subtropical Underwater, the cold (warm) SST anomaly plays a favorable (unfavorable) role to the lateral induction. The annual subduction rate of the STUW varies from year to year, and most of this variability is due to lateral induction, which in turn is directly linked to the variability of the winter mixed layer depth. Therefore, they found that the SST anomaly is found anti-correlated to the mixed layer depth. Inspired by this idea, we examined the averaged SST in the domain of analysis. We aimed to examine the EDW subduction during the extreme years of EDW renewal, using the geostrophic volume transport at the southern boundary as well as the SST.

We inferred the subduction following the flowchart in Figure 4-12: The Ekman heat advection and the air-sea surface heat fluxes signal the extreme years of EDW formation. Then we examined the March geostrophic transport at 30°N of each extreme year, combined with SST to infer its corresponding subduction.

The SST over our domain of analysis and the EDW freshly ventilated volume seasonal maximum are anti-correlated with a correlation coefficient of -0.68 (Figure

4-13d). In the years 2008, 2012, 2015, 2016, the warmer SST correspond with the weak extreme EDW renewal. In the years 2010 and 2013, the colder SST correspond with the strong extreme EDW renewal. Note that the SST anomaly in early spring of 2005 is smaller in amplitude compared with those of 2010 and 2013 (Figure 4-13b). Yet, the year 2005, 2010, and 2013 are all extreme years of strong EDW renewal.

A negative value on the time series of the geostrophic transport cross the southern boundary indicates a southward-traveling flow (the red curve in Figure 4-13a). A noticeable trough towards the end of 2004 (Winter2005) has a southward anomalous volume transport of $-22\,\mathrm{Sv}$. This southward transport took place before the spring of 2005, known for strong EDW renewal (the black curve in Figure 4-13c). After the extreme strong EDW renewal of 2005, the southward geostrophic volume transport maintains weak until the fall of 2007, with a robust trough value of $-32 \pm 2\,\mathrm{Sv}$. The SST since Spring 2005 remains small in amplitude until Spring 2007, with a trough value of $-0.1^{\circ}\mathrm{C}$. The air-sea heat loss at the same time is the largest (the dashed black curve in Figure 4-13b). According to the flowchart (Figure 4-12), in 2005, strong wintertime Ekman heat advection corresponds with strong early spring EDW ventilation. In addition, we observed the warm SST from the early spring of 2005 to fall 2007. We also observed a weak southward geostrophic transport at $30^{\circ}\mathrm{N}$ from the spring of 2005-the fall of 2007, and a large southward geostrophic transport towards the end of 2007. We inferred a delayed subduction at the end of 2007 compensating the EDW that was mainly formed in 2005.

This delay of EDW subduction can be due to the Gulf Stream positioning change. The air-sea surface heat loss in the winter of 2007 is exceptionally strong, resulting in a southward moving Gulf Stream. This might encourage a southward circulation of EDW. Moreover, the southward transport at the southern edge of EDW bulk may be within an error bar of approximate of the subduction rate. The permanent pycnocline in Spring 2005 underneath the EDW bulk can go deeper. Lastly, note that we used SST to infer the EDW subduction, following the analysis performed on the Subtropical Underwater (Peng et al., 2006). This deserves more investigation to find a clear answer.

2010 and 2013 are two robust strong years of EDW renewal adjacent to each other. The Spring 2010 has a trough down to $-20\,\mathrm{Sv}$. The SST in this period experienced low anomaly, with a trough value of $-0.25^{\circ}\mathrm{C}$. The next trough after Spring 2010 is Spring 2013. In the early spring of 2013, we observed a similar southward anomalous volume transport of $-17\,\mathrm{Sv}$. Correspondingly the SST in this period experienced low anomaly, with a trough value of $-0.1^{\circ}\mathrm{C}$.

In short, in the strong year of EDW renewal, such as 2010 and 2013, a vigorous and

instantaneous subduction is suggested by the large southward geostrophic velocity. A colder SST in the springs of 2010 and 2013 is an aiding factor to extend the EDW convective activity deeply towards the thermocline.

In Spring 2011, the SST anomaly is -0.22^{o}C, comparable to 2010, encouraging water column to sink from the surface (the blue curve in Figure 4-13b). These low SST anomalies in the winters of 2009-2010 and 2010-2011 resulted from the sutropical cooling driven by the rapid slowdown of AMOC measured at 26^{o}N (Cunningham et al., 2013; McCarthy et al., 2012). However, a weak southward geostrophic transport indicates a much weaker subduction than 2010. According to the flowchart (Figure 4-12), in 2010, strong wintertime Ekman heat advection corresponds with strong early spring EDW ventilation. In addition, we observed the cold SST in both early springs of 2010 and 2011. Yet, only in the early spring of 2010 we observed the strong southward geostrophic transport at 30^{o}N, not in the early spring of 2011. We inferred that the vigorous subduction in spring 2010 was able to fully compensate the EDW formed in the Winter2010. In Spring 2011, the EDW was at low stock to be subducted, despite a favorable SST condition.

Spring 2014 experienced a weak EDW ventilation, after Spring 2013 with a strong EDW renewal. The trough in Spring 2014, indicating a strong southward geostrophic volume transport took place after the trough of Spring 2013 (Figure 4-13a). The SST in Spring 2014 shows an anomaly of -0.02^{o}C, relatively small in amplitude compared with that in Spring 2013. This suggests a continuous subduction of EDW in Spring 2014 after the strong formation in 2013, even though 2014 itself is a weak EDW renewal year.

In 2008, 2012, 2015, and 2016, positive SST in the early spring signals weak EDW renewal. In 2016, we observed a northward geostrophic volume transport anomaly crossing the southern boundary, which undermines the freshly ventilated EDW from traveling southward. Correspondingly, 2016 is a weak year of EDW renewal.

The EDW averaged temperature at the renewal period range between $17^{o} - 18^{o}$C (the green curve in Figure 4-13c). Before 2010, the EDW temperature is warmer and more flat than that after 2010. The variability of the EDW temperature does not necessarily follow the freshly ventilated EDW volume trend on the interannual time scale (Peng et al., 2006).

All strong years outcropping area extend to northern Sargasso Sea region centered at 67^{o}W, 33^{o}N, as well as the region south of the Gulf Stream $60^{o} - 65^{o}$W, $35^{o} - 40^{o}$N (the dashed black contours in Figure A-1). None of the examined weak years covers the northern Sargasso Sea region. Among all the examined weak years, only 2008 surface outcropping region fully covers the region south of the Gulf Stream.

In 2012, 2014, and 2015, the surface outcropping region only covers the western / northwestern corner of the region south of the Gulf Stream (the dashed black contours in Figure A-2). Joyce (2011) found that the EDW located at the southern flanc of the Gulf Stream is cooler and fresher than the one at the northern Sargasso Sea region. Correspondingly, the EDW temperature of 2012, and 2014-2016 are cooler than 2008 and all the strong EDW renewal years.

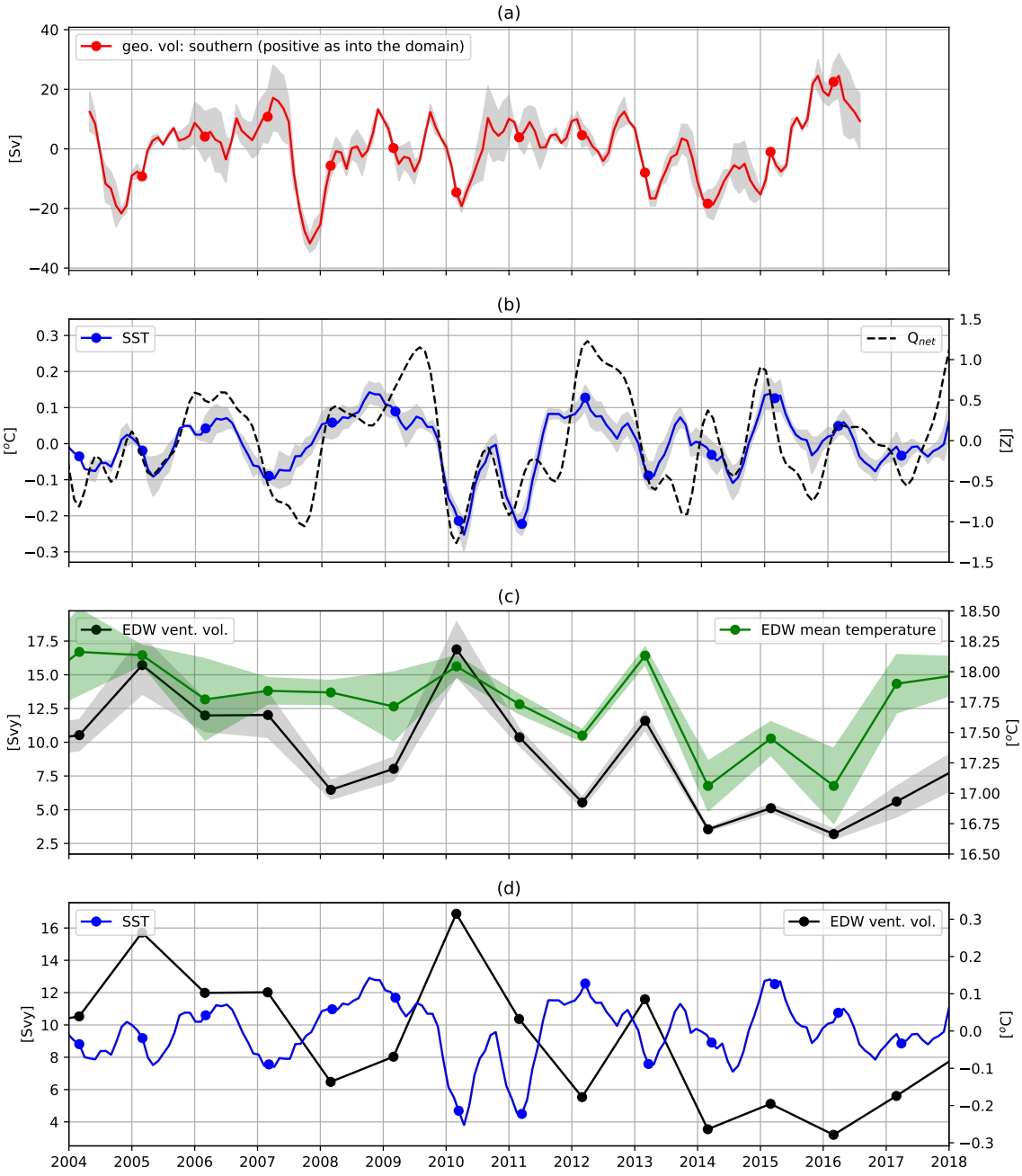
(a)
geo. vol: southern (positive as into the domain)
[Sv]
(b)
SST
Q_{net}
[°C]
[ZJ]
(c)
EDW vent. vol.
EDW mean temperature
[Svy]
[°C]
(d)
SST
EDW vent. vol.
[Svy]
[°C]
2004
2005
2006
2007
2008
2009
2010
2011
2012
2013
2014
2015
2016
2017
2018

Figure 4-13

Figure 4-13 *(previous page)*: The 2004-2017 interannual variabilities of (a) the southward geostrophic velocity, (b) the domain averaged SST in blue curve, and (c) the 2004-2017 non-filtered variabilities of the EDW early spring outcropping volume in solid black line and the EDW mean temperature of the seasonal-maximum outcropping volume. The dots indicate the March values. The correlation between these two curves are 0.64 (d) the domain averaged SST and EDW early spring outcropping volume. The green shaded area indicates the standard error of the EDW mean temperature calculated using ISAS, EN4, Scripps, and IPRC datasets. The interannual time series are generated using a 6-50 month band-pass filter. We added in dashed black curve the interannual variability of air-sea surface heat loss using 6-50 month filter, in the unit of ZJ, to compare with SST.

4.4.6 Uncertainty of geostrophic transport at 30°N

In the previous chapter, we observed that the geostrophic volume transport interannual time series is correlated with the geostrophic heat advection. We yielded the interannual variability of the southward geostrophic volume transport at 30°N (Figure 4-13b). We observed a negative volume transport peaking in the wintertime of 2008, with the magnitude of $-31 \pm 3\,\mathrm{Sv}$. The negative sign indicates a southward transport anomaly. In addition we observed a negative volume transport peaking in the wintertime of 2005, with the magnitude of $-21 \pm 2\,\mathrm{Sv}$. At these two winter periods, Kelly and Dong (2013) also observed peaks (Fig. 10b). In the wintertime of 2007, we observed a positive peak indicating a northward geostrophic transport at the southern boundary at 30°N. Kelly and Dong (2013) also observed a peak indicating a northward geostrophic transport at the southern boundary of EDW formation at 32°N. We both obtained similar interannual variability of the geostrophic transport near the boundary between EDW formation and subduction.

However, at southern boundary, we observed a climatological mean transport of $+15.7 \pm 15.9\,\mathrm{Sv}$ ($1\,\mathrm{Sv} = 1 \times 10^6\,\mathrm{m^3\,s^{-1}}$). The positive sign indicates the transport going northward into our domain of analysis. The error is calculated as the unbiased standard deviation using all examined datasets. The area of the southern boundary cross-section in our domain of analysis is $3.6 \times 10^9\,\mathrm{m^2}$ (Figure 2-1). The climatological mean of the geostrophic velocity at our southern boundary is $+0.4 \pm 0.4\,\mathrm{cm\,s^{-1}}$.

Kelly and Dong (2013) estimated a climatological mean of geostrophic velocity at the 32°N, $-1.0\,\mathrm{cm\,s^{-1}}$, with a standard deviation of $0.38\,\mathrm{cm\,s^{-1}}$. Their negative sign indicates a southward transport. Our large estimated error makes our estimate

compatible with that of Kelly and Dong (2013).

4.4.7 EDW convection due to the Ekman term

We found that the heat transport due to Ekman current is a good indicator on an interannual time scale to signal the strong years of EDW renewal. Of the strong EDW formation years, we found that in the early spring the southern boundary moves further south to increase the surface outcropping region (Figure A-1). Maze et al. (2013) showed that the air-sea surface buoyancy loss near the Gulf Stream (the diabatic PV flux) is the dominant PV sink. In comparison, the contribution of the Ekman term (the mechanical PV flux) is one order of magnitude smaller. The EDW convection due to the Ekman term (the mechanical PV flux) spatial distribution overlaps with the bulk of EDW (thickness $>$ 300m, Fig. 6b in Maze et al. 2013).

Both results showed that the Ekman heat transport plays an important role in the EDW formation. Maze et al. (2013) examined EDW in seasonal cycle / climatological scale, while our study is on the interannual time scale. We provided early-spring snapshots of the strong EDW formation years (Figure A-1). Each of these snapshots is one constituent of the many maps used to build Fig. 6b in Maze et al. 2013. In addition, Maze et al. (2013) in their Fig. 6b showed the Ekman heat transport convection in the EDW layer. They employed a Lagrangian approach. In Figure A-1, we investigated the seasonal maximum EDW outcropping position typically in early spring. This is rather an Eulerian approach.

Despite the differences, both of our findings form a coherent picture of the Ekman advection's role in EDW interannual variability. Maze et al. (2013) inferred that part of the EDW possibly migrates from the north, the region near the Gulf Stream (Maze and Marshall, 2011; Thomas and Joyce, 2010), rather than directly formed through the convection due to Ekman term (the mechanical PV flux) above. Of the strong years of EDW formation, the Ekman heat divergence is good indicator. For strong years, the heat sink due to Ekman heat divergence and the air-sea surface heat loss are in the same order of magnitude. Note that, different from Maze et al. (2013), we estimated the anomalies of the two factors on the interannual time scale, without the typical seasonal cycle. Meanwhile, Maze et al. (2013) calculated their mean state.

4.4.7.1 OHC and EDW volume

On the interannual time scale, we observed that OHC in the western subtropical North Atlantic region and the early spring EDW freshly ventilated volume are not clearly anti-correlated. In addition, we didn't observe direct link between the EDW

freshly ventilated volume and the OHC change in winter. Dong and Kelly (2004); Stevens et al. (2020) showed that the OHC in their own domains of analysis (both are in the western subtropical North Atlantic region) is anti-correlated with the EDW renewal, on decadal time scale.

In addition, in the previous chapter, we discussed that the extreme occurrences of OHC are "organised" on multidecadal scales. Namely, the clusters of OHC extreme occurrences are centered around 2009-2010, as well as 1990s. In comparison, we do not see as obvious a fashion in which the extreme occurrences of EDW are "organised" (Figure 4-1). The EDW extreme occurrences are more evenly distributed on the multidecadal time axis than OHC.

The possible explanation is that our domain of analysis to calculate the OHC is too large. As another approach, we proposed to calculate the ocean heat content at one grid point fixed at the center of EDW outcropping region. We would expect a more correlated EDW ventilated volume and OHC. However, this would not yield an OHC relevant for the box/domain, but for the EDW only.

4.5 Summary

1. On the interannual time scale, after 2002, the ventilated EDW formation has the positive extreme years as 2005, 2010 and 2013. The extreme early spring EDW renewal is robust in both 2010 and 2013 among the datasets EN4, ISAS, Scripps, and IPRC. Yet, the year 2005 being an extreme is only observed by the datasets EN4 and ISAS. The datasets Scripps and IPRC show a lower estimate of the 2005 early spring EDW freshly ventilated volume by 19% and 31%. Only 2008 is chosen as a negative extreme year in the period of 2002-2019.

   The algorithm of selecting extreme years of EDW renewal suffers a bias towards the positive extremes due to the non-Gaussian distribution of the total sampling. On an interannual variability of the seasonal maximum EDW outcropping curve, the years 2012, 2014, 2015, and 2016 are situated in the trough. In the analysis, we added these years as the extreme years of weak EDW renewal.

2. The extreme occurrences of EDW renewal since 1950s take place on average every 3 years. In the most recent periods of 2006-2020, the extreme occurrences frequency on average reduced to every 5 years. The extreme occurrences of EDW renewal are not becoming more frequent.

3. A wintertime heat divergence (convergence) due to Ekman advection corresponds with strong (weak) EDW renewal extreme years.

Concerning the air-sea heat flux, more (less) air-sea surface heat loss in the EDW formation region corresponds with the extreme years of strong (weak) EDW renewal. In particular, strong heat divergence due to Ekman advection is associated with the strong EDW renewal extreme years, while the weak air-sea heat loss is associated with the weak EDW renewal extreme years.

Concerning the Ekman pumping, during the extreme years of strong EDW renewal, vertically, the Ekman pumping in the EDW formation region elevate the isotherms. The upper 800m water column is cooled by the uplifted cold and dense water beneath the thermocline closer to the sea surface. There is then less buoyancy to be gained (or more heat to lose) in the top layer to induce vertical convention within the subsurface less stratified water. The northern boundary of the outcropping region is bordering the Gulf Stream. During the strong EDW renewal years, the southern boundary moving further southward than climatological mean.

4. NAO events coincide with EDW extreme years. NAO- (NAO+) corresponds with an extreme year of strong (weak) EDW renewal. Between strong and weak years, anomalies of the wind stress curl and the air-sea heat fluxes are asymmetric. This suggests NAO+ as an asymmetric counterpart of NAO-, comfirming the asymmetric nature of NAO in the weather regime paradigm (Cassou et al., 2004). This is examined further in Appendix A.

CHAPTER 5

Conclusions and Future Work

5.1 Conclusions

In this thesis, we investigated the EDW bulk that is renewed through surface ventilation in the early spring of each year. We employed four gridded observational data products, namely, ISAS, EN4, Scripps, and IPRC to calculate the EDW volume. Based on the mean interannual time series of the EDW volume, we determined the winters of 2004-2005, 2009-2010, and 2012-2013 to be extreme years of strong EDW formation. Out of these strong years, the events of 2009-2010 and 2012-2013 are robust and are agreed upon with all data products. We determined the winters of 2007-2008, 2011-2012, 2013-2014, 2014-2015, and 2015-2016 as the extreme years of weak EDW formation. Out of these weak years, the 2007-2008 event is robust.

During the strong EDW formation years, the western subtropical North Alantic region experienced wintertime low surface level pressure on average, as part of the NAO−. During the wintertime (September-March) of extreme EDW formation, strong wintertime NAO− is sufficiently represented by several strong passing storms, most notably, remnants of hurricanes and US east coast snowstorms. Under the low anomalous surface level pressure, these strong storms are heralded by strong air-sea surface heat loss as well as large wind stress curl anomaly of the strong EDW formation years. Particularly, extremes of wintertime large heat divergence due to Ekman advection indicate the extreme years of strong EDW formation.

During the weak EDW formation years, the western subtropical North Atlantic region experienced wintertime high surface level pressure on average, as part of the NAO+. Under the high anomalous surface level pressure, we observed less strong storms passing by the EDW formation region. Correspondingly, we observed weaker air-sea surface heat loss as well as weaker surface wind stress curl. Particularly, extremes of wintertime weak air-sea surface heat loss indicate the extreme years of weak EDW formation.

The EDW subduction impacts the EDW bulk in various ways depending on the years. Inspired by the literature, we inferred the EDW subduction rate based on the volume transport passing by 30°N and the EDW formation region average SST.

We chose 30°N, as it cuts through EDW bulk and is located south of the EDW outcropping region. 2010 and 2013, two strong EDW formation years, experienced a vigorous and instantaneous subduction after the EDW renewal. The weak years, in comparison, experienced the weak subduction. We noticed that in 2005, a strong EDW formation year, the corresponding subduction did not take place until the fall of 2007. This subduction, being delayed, was possibly hindered by the warmer than normal SST from 2005-2007 in the EDW formation region.

Note that at 30°N, the southern branch of the recirculation gyre is oriented more westward than southward. In addition, our estimated error indicates a non-significant meridional volume transport at 30°N. A more precise measure of this weak yet important meridional volume transport, demands a more pinned-down regional analysis, for example, with higher resolution, with the input of modeling simulations.

The heat advection due to the geostrophic current has important periods of 10 months, 18 months, and >35 months. Compared with air-sea heat fluxes and Ekman advection, the geostrophic advection to the best explains the high frequency, namely 10-18 months, fluctuation of the western subtropical North Atlantic ocean heat content. The geostrophic current at the western subtropical North Atlantic region is associated with the Gulf Stream. On the interannual variability, the Gulf Stream displaced further north (south) in latitude indicates an increase (decrease) in volume of the warm water in EDW formation region. Thus, the Gulf Stream positioning is correlated with the OHC of this region. In addition, the Gulf Stream strength regulated with the subtropical recirculation gyre is responsible to advect heat into the EDW formation region.

The eddy mixing near the Gulf Stream is more active than in the other parts of the recirculation gyre by an order of magnitude. Eddies restratified the EDW formation region. At the bottom of the EDW bulk, the ocean interior mixing due to internal wave breaking drives the diapycnal mixing, entraining the cold water from ocean abyss to the EDW bulk. We smoothed the altimetry data to a coarser resolution. In this way, we removed the mesoscale eddies, which are removed as well from hydrography climatologies. Meanwhile, we parameterized the eddy effects in the mixing by choosing reasonable vertical and horizontal eddy diffusivity coefficients. However, we may underestimate the horizontal eddy mixing especially at the northern boundary along the Gulf Stream extension.

We found interesting that the extreme events on the OHC interannual time series apear to be "organized" according to the variability of AMOC multidecadal signal. Groups of the extreme occurrences are centered around 1990s and 2009-2010, two periods corresponding to the AMOC increase and the sudden decrease. Alternatively,

the OHC experienced absence of extremes in the period of 2000-2005 and the period of 2014-2019. This can be due to a red-noise response of the OHC extremes to the atmospheric forcing (Frankignoul and Hasselmann, 1977).

The preconditioning plays the auxiliary role to the EDW formation. Of all the strong EDW formation years, the preconditioning does not play as dominant a role as the Ekman heat advection. However, unfavorable preconditioning can often serve as an aiding factor, combined with weak air-sea surface loss, to a weak EDW formation, for example 2014-2015, 2015-2016, and 2016-2017. Under the unfavorable preconditioning of these two periods, a more buoyant and stratified water column in the late fall, hindered the wintertime EDW ventilation to the surface. Unfavorable preconditionings of 2014-2015, 2015-2016, and 2016-2017, well correspond with the weak EDW formations from previous years, 2013-2014, 2014-2015, and 2015-2016, respectively.

5.2 Future Work

As part of the ongoing work, we investigate how the atmospheric patterns correspond to the extreme occurrences of EDW renewal. We already concluded in chapter 4 that the EDW extreme years can be signaled by the air-sea heat fluxes and the heat convergence due to Ekman advection. As the next step, we aim to understand how the weather regimes have impact on these two forcings. Thus, we employ the composites of the atmospheric forcings, such as surface wind and the air-sea heat fluxes onto the four weather regimes. Our preliminary findings suggest that the Atlantic Ridge and NAO− correspond with Ekman divergence and strong air-sea surface heat loss at the western subtropical North Atlantic region. Conversely, the Blocking and NAO+ correspond with Ekman convergence and weak air-sea surface heat loss (see details in Appendix A).

Meanwhile, we also investigate the ocean feedback to atmosphere. For example, we aim to understand if the EDW extreme events can have an impact to the weather regimes. Our preliminary results suggest that the anomalous positive EDW formation serves as a harbinger of the emergence of NAO+ 2 years later.

Another line of the ongoing work is to examin the complementary roles that the fixed-domain BCA and the $\mathrm{BCA}^*_{\mathrm{Sep}}$ play during the extreme events of EDW formatiom. We introduced in chapter 2 the fixed-domain BCA and $\mathrm{BCA}^*_{\mathrm{Sep}}$. Moreover we employed these two concepts in chapter 4 and investigated the role of preconditioning in the EDW volume interannual time series. As part of the ongoing research, we investigate how these two measures contribute to an EDW extreme formation (see de-

tails in Appendix B). We employed the fixed-domain BCA_{Sep} to indicate an absolute buoyancy content in a fixed depth water column. We employed the BCA^*_{Sep} to measure the capability of a deep ventilation due to the September vertical stratification. Our preliminary results show that a high fixed-domain BCA signals an unfavorable preconditioning. A high fixed domain BCA especially serves as a good measure of preconditioning leading to the weak EDW formation extremes. A consecutive high fixed-domain BCA_{Sep} served to sustain the 3-year weak EDW formation in 2014-2016. Meanwhile, a low BCA^*_{Sep} signals a favorable preconditioning. A low BCA^*_{Sep} especially serves as a good measure of the preconditioning leading to the strong EDW formation extremes. The BCA^*_{Sep} is able to distinguish fall vertical stratification of the strong years: 2005, 2010, and 2013, while the fixed-domain BCA of these three years are the same.

We used the observational datasets to examine the heat budget at the western subtropical North Atlantic region. To corroborate our findings, we need to use a realistic numerical simulation, where the conservations of heat and mass always hold.

We examined the EDW extremes on interannual time series using observational datasets. We proved it feasible to combine the different elements in the heat budget in a turbulent region. In the mean time, we made some key assumptions that need to be challenged.

We could use the Estimating the Circulation and Climate of the Ocean Version 4 (ECCO-v4) of the MITgcm, a 4-dimensional variational data assimilation system providing ocean state estimation (Stammer et al., 2002). The ECCO-v4 provided simulation for almost 20 years. In the simulation, the trajectory of the ocean state variable is driven by the model over time. In addition, the heat and momentum in the model is conserved.

We analysed the mapped composites of atmospheric forcing onto the positive and negative extreme years of EDW ventilation. We did not yet investigate the lagged impact from the atmospheric forcing to the ocean. For example, Frankignoul et al. (2001); Lillibridge III and Mariano (2013); Taylor and Stephens (1998) showed that a more positive (negative) NAO leads to a more northward (southward) Gulf Stream meridional position by 6 months-2 years. We will examine the persistence of an atmospheric forcing anomaly impacting the EDW ventilation in the following years.

We need to study the role of the eddies, in terms of their interaction with the Ekman current. We found that the large wintertime heat divergence due to Ekman current in the western subtropical North Atlantic indicates extremes of strong EDW early-spring formation. Thomas (2005) showed that the along front wind over intense surface front leads to the Ekman-driven convection carried by the submesoscale eddies.

Maze and Marshall (2011) addressed a possible underestimation of the submesoscale eddies' role in their PV budget calculation at the EDW bulk. We need to address how the Ekman heat advection driving EDW formation extremes is modified with submesoscale eddies.

We didn't look into the destruction rate of EDW in summer. For example, overstratifying the water colume in the summer would have an impact on the EDW formation. To fully understand the interannual variability of EDW, we need to aquire a combined understanding of the stratification both in winter and summer. We need to study the interannual variability of the EDW erosion. On a typical seasonal cycle, the EDW destruction is mainly attributed to a 1-D process of restratification due to summertime warming at the sea surface. However, the EDW destruction rate ascribable to the eddy mixing makes up 1/3 of the total EDW destruction (Billheimer and Talley, 2016b). It would be to our interest to understand if the air-sea heat flux is still the dominant factor on the interannual time scale. For example, would the role of eddy mixing still be secondary after the air-sea heat flux on the interannual variability of EDW destruction?

Would the Ekman still be the determining factor for the occurrences of the extreme formation of the North Pacific Subtropical Mode Water associated with the Kuroshio expansion? At the western boundary in the North Atlantic, the fundamental balance of processes driving the heat budget comprises the heat transport driven by the MOC and the wind-driven heat transport. However, the Kuroshio does not have MOC. The fundamental driving force in Kuroshio may not be the same as in the Gulf Stream.

We found patterns of distributions of the interannual OHC and EDW volume extreme occurrences on a multidecadal time axis. After all, our hypotheses of these patterns of distributions are only based on the reanalysis observational datasets. The robustness of these hypotheses needs to be tested in models. Then as the next step, we will investigate what would be the driving factor behind these patterns of distributions of the interannual extremes.

Appendix A

Weather conditions and Weather regimes

A.1 Introduction

Over the North Atlantic Ocean, the atmospheric mean pressure field is dominated by highs near the Azores Islands and lows near Iceland. Around this mean state takes place different variability patterns. The dominant one is a meridional pressure seesaw, the so-called North Atlantic Oscillation (Hurrell et al., 1995). Other atmospheric variability patterns are known to influence the North Atlantic Ocean and weather in Europe, like the Atlantic Ridge and Blocking (Barrier et al., 2016). To take into account the complex structure of these variablity patterns the atmospheric dynamic community has widely adopted the weather regime paradigm (Cassou et al., 2004). Weather regimes allow for positive and negative NAO patterns to be asymmetric, and to take into account a significant longitudinal shift of the NAO+ towards Europe by 30 degrees. Moreover, these regimes are shown to have the ability to effectively capture the interannual to decadal variability of the ocean surface forcing (Cassou et al., 2004). We also anticipate that the weather regime paradigm will provide a simpler and more precise description of the extreme atmospheric forcing patterns that we will ultimately focus on.

Weather regimes are asymmetric large-scale atmospheric patterns, calculated from multi-decadal variability of climatological related atmospheric variables. Over the North Atlantic region, these patterns yield NAO, Atlantic Ridge regime, and west-east dipole pattern (also known as blocking regime). The weather regimes are recurrent on a daily basis, and are quasi-stationary stable, persisting over a few consecutive days. The NAO+ and NAO- are asymmetric. Cassou et al. (2004) developed the weather regime paradigm, and obtained the asymmetric NAO+ and NAO-. Moreover, the weather regime paradigm yields two more regimes, namely Atlantic Ridge (AR) and Blocking (BLK). Barrier et al. (2013) showed AR is correlated with subtropical SSH anomalies in interannual time scales. They also concluded that the AR has an impact on the subtropical Rossby wave propagation.

The traditional Greenland Blocking regime is referred to as the high pressure over Greenland (Davini et al., 2012). The Greenland Blocking index is defined as the mean 500 hPa geopotential height for the 60˘80°N, 20˘80°W region (FANG, 2004; Hanna et al., 2013, 2014, .etc).

A.2 Results

A.2.1 Impact of NAO through Ekman heat divergence

Year	ATL	BLK	NAO−	NAO+	Weather Regime
2002	59.2 ± 1.6	58.5 ± 1.3	28.8 ± 0.2	65.5 ± 2.7	NAO+
2003	35.2 ± 4.5	94.8 ± 4.3	55.2 ± 1.7	26.8 ± 1.0	BLK
2004	69.8 ± 2.2	64.5 ± 2.1	33.0 ± 1.2	45.8 ± 0.4	ATL
2005	80.2 ± 0.4	44.8 ± 1.2	43.0 ± 1.8	44.0 ± 1.6	ATL
2006	49.0 ± 3.8	72.8 ± 3.1	52.5 ± 3.1	37.8 ± 3.1	BLK
2007	34.8 ± 1.4	49.2 ± 2.3	45.8 ± 1.4	82.2 ± 0.8	NAO+
2008	69.5 ± 2.2	56.0 ± 2.3	12.2 ± 1.2	75.2 ± 2.1	NAO+
2009	62.0 ± 1.8	58.8 ± 2.0	28.2 ± 1.6	63.0 ± 1.2	NAO+/ATL
2010	26.8 ± 2.9	45.5 ± 2.9	95.5 ± 2.8	44.2 ± 3.0	NAO−
2011	49.8 ± 4.4	45.8 ± 1.2	71.8 ± 0.7	44.8 ± 4.5	NAO−
2012	51.0 ± 2.7	79.5 ± 2.0	4.0 ± 2.0	78.5 ± 2.8	BLK/NAO+
2013	48.8 ± 3.2	32.0 ± 2.6	86.2 ± 3.3	45.0 ± 2.3	NAO−
2014	41.0 ± 2.4	45.5 ± 2.4	29.5 ± 2.5	96.0 ± 4.5	NAO+
2015	45.0 ± 2.8	71.5 ± 1.8	21.0 ± 4.3	74.5 ± 3.6	NAO+/BLK
2016	39.8 ± 1.7	66.2 ± 1.7	32.2 ± 0.5	74.8 ± 3.4	NAO+
2017	48.0 ± 3.0	99.2 ± 3.9	21.2 ± 3.5	43.5 ± 1.6	BLK
2018	66.2 ± 2.9	52.5 ± 2.8	39.5 ± 0.8	53.8 ± 0.8	ATL
2019	57.2 ± 4.1	74.5 ± 2.7	19.8 ± 2.6	60.5 ± 5.1	BLK
2020	35.8 ± 1.9	36.8 ± 2.5	40.5 ± 0.2	69.2 ± 11.0	NAO+

Table A.1: 2002-2020 wintertime weather regimes occurrences (in days) and the leading weather regimes. Shaded in orange are the years with a strong EDW renewal, and the green with a weak EDW renewal. The leading weather regimes of each year are estimated based on its wintertime occurrences in days as well as the standard errors. The occurrences are calculated as the mean occurrences among the surface level pressure and 500hPa geopotential height of NCEP and ERA datasets repectively.

The strong extreme EDW renewal years are 2005, 2010, and 2013. In Winter05, the leading weather regimes are BLK and AR (Table A.1). In Winter10 and 13, the leading weather regime is NAO-. The weak extreme EDW renewal years are 2008, 2012, 2014, and 2015. In Winter12, the leading weather regimes are Blocking and NAO+. In Winter08, 14 and 15, the leading weather regime is NAO+.

A.2.1.1 Atmospheric states

Figure A-1 and Figure A-2 show the atmospheric state variables, corresponding with early-spring EDW outcropping at the extreme years of EDW formation. We used the seasonal maximum area between $17^oC - 19^oC$ as the EDW seasonal maximum outcropping region (refered to as outcropping region, solid yellow lines in Figure A-1). In Winter05, the outcropping region is larger than that of the 2003-2018 climatological mean (solid black lines in Figure A-1a). The isotherm of 17^oC in 2005 is further northward than the climatological mean, and the isotherm of 19^oC in 2005, further southward. The zero wind stress curl line in 2005 is shifted southward compared with the mean of 2003-2018. The sea surface level pressure (SLP) anomaly has a high pressure system centered at $22N, 53W$, to the northeast of the domain of study, south of Iceland with a magnitude of $550\,hPa$. The low pressure system is centered at $30N, 45W$, on the southern boundary of the domain of study, with a magnitude of $-250\,hPa$. The wind stress curl anomaly in Winter05 are positive over the Atlantic Ridge. This positve anomaly extends from Labrador Sea to the British Islands. The negative wind stress curl anomaly of 2005 is located in the subtropical region, and fully covering the domain of study. The Ekman transport advects the temperature exiting from the northeastern boundary of the domain of study, with an order of magnitude of about $10^oC\,m\,s^{-1}$, the largest of all boundaries.

In comparison, the surface wind stress curl of 2010 and 2013 have their positive anomalies centered further north at a latitude of about 65N. In both years, the west of British Islands and the northern half of the domain of study are occupied by negative wind stress curl anomaly. The southern half of the domain of study, south of 35N, is occupied by a positive wind stress curl anomaly.

In general, among the extreme strong years of EDW formation, namely, 2005, 2010, and 2013, the SLP anomaly has a low pressure system in the domain of study, and a high pressure system to its north or northeast. The wind stress curl is negative, responsible for the horizontal Ekman heat divergence in the domain of study, dominated either by a strong northward transport from the northern boundary, as in 2005, a strong southward transport at southern boundary, as in 2010, or both, as in 2013. The zero wind stress curl line shifts further southward. The EDW outcropping

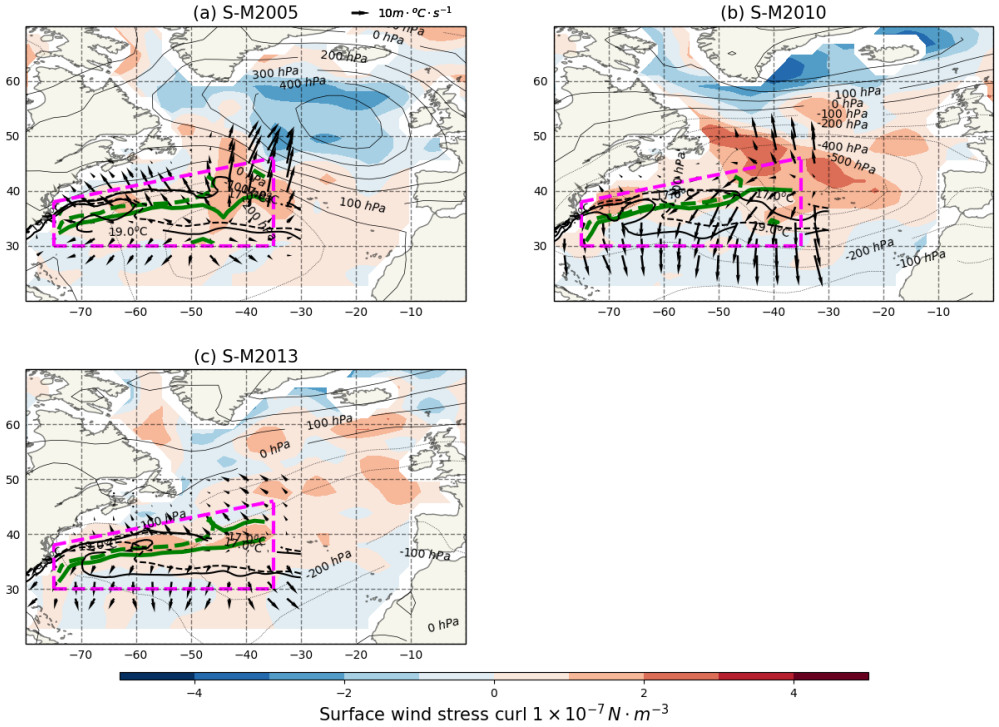

Figure A-1: The interannual SLP anomalies, near-surface wind stress curl anomalies, near-surface zero wind stress curl line position, and surface EDW outcropping region anomalies during the EDW ventilation season of the strong EDW ventilation years: (a) 2005, (b) 2010, and (c) 2013. The colored contours denote the September-March mean of the near-surface wind stress curl interannual anomalies. The thick green solid contours and the thick green dashed contours denote respectively the interannual mean position and the each-year positions of near-surface zero wind stress curl in the period of September-March. The thin grey solid contours and the thin grey dashed contours denote of the September-March mean surface level pressure interannual anomalies, positive and negative values respectively, in the unit of hPa. The black arrows denote the Ekman temperature transport in the unit of $\mathrm{m}^o\mathrm{C} \cdot \mathrm{s}^{-1}$. The yellow and bold black solid contours denote respectively the interannual mean position and the each-year positions of 17^oC and 19^oC isotherms at the ocean surface at the time of the annually deepest mixed layer.

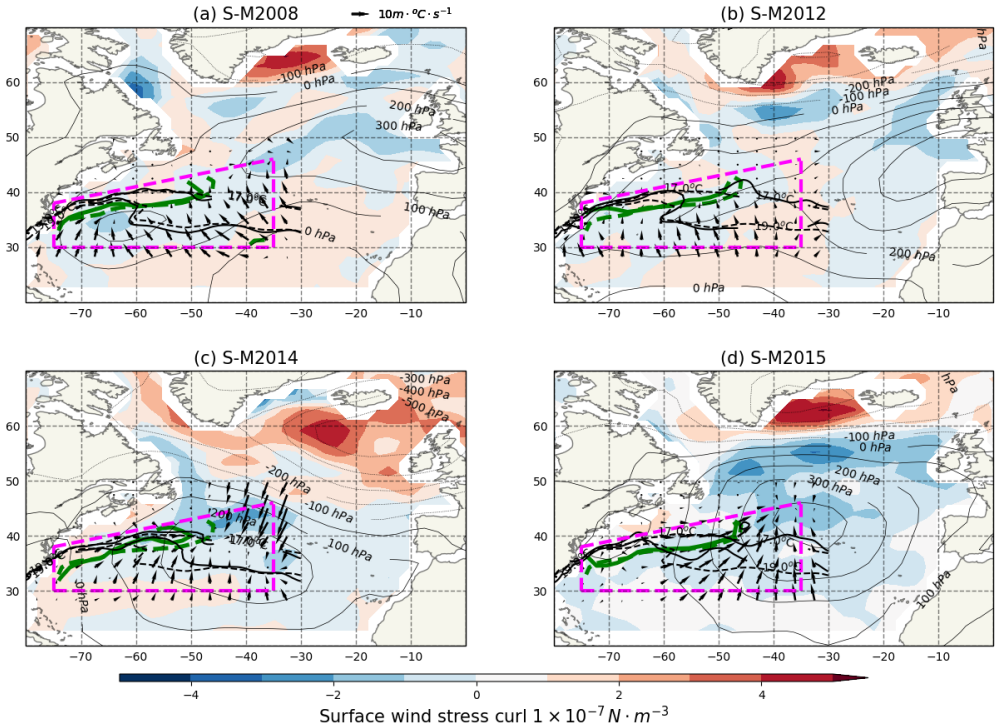

Figure A-2: The same as Figure A-1, of the weak EDW ventilation years: (a) 2008, (b) 2012, (c) 2014, and (d) 2015.

area is larger than the 2003-2018 climatological mean.

In Winter08, the EDW outcropping area is roughly equal to the 2003-2018 mean (Figure A-2a). The zero wind stress curl line of 2008 is roughly the same as the 2003-2018 mean. The SLP anomaly has two high pressure systems, with one centered at 47N, 10W, west of Europe, with a magnitude of 350 hPa, and the other at 35N, 62W, in the domain of study, with a magnitude of 250hPa. The two low pressure systems are located at southern Greenland, with an amplitude of -150 hPa, and at the equator to the west of the African continent, with an amplitude of -50 hPa. The negative surface wind stress curl anomaly is centered between Greenland and Iceland, at around 65N in latitude. To the south of 60N, The positive anomaly extends from the British Islands to the domain of study in a diagnal manner. The Ekman heat advection in 2008 in the domain of study is convergent, dominated by the northward Ekman temperature transport at the southern boundary, with an order of magnitude of $10^{\circ}\mathrm{C\,m\,s^{-1}}$.

In comparison, the surface stress curl anomaly in 2012 and 2015 are similar to that in 2008. Meanwhile in 2014, the negative wind stress curl anomaly moved further southward than that of 2008, centered at a latitude of 60N.

In general, among the extreme weak years of EDW formation, namely, 2008, 2012, 2014, and 2015, the SLP anomaly has a high pressure system in the domain of study. The wind stress curl is positive, responsible for the horizontal Ekman heat convergence in the domain of study, dominated either by a strong northward transport from the southern boundary alone (as in 2008, 2012, and 2015), or in combination with a strong southward transport from the northern boundary, as in 2014. The zero wind stress curl line shifts slightly northward. The EDW outcropping area is smaller or is shifted without changing the size compared with the 2003-2018 climatological mean.

A.2.1.2 Weather conditions

So far, we found the Ekman heat advection a "direct" indicator of extreme EDW formation years. In this section, we aimed to link the EDW extreme years to the storms. We investigated the daily progression of the Ekman heat convergence during the EDW formation period of each year (Figure 4-9b). We calculated the Ekman heat convergence accumulated from September 1 of each year. In Winter10, the total change of Ekman heat convergence is -4.7 ZettaJ, the most negative during the period of 2003-2018. In Winter05 and 13, the total change of Ekman heat convergence is -4.1 ZettaJ and -4.0 ZettaJ respectively, two of the most negative throughout the period of 2003-2018, second only to Winter10.

Conversely, in Winter14, the total change of Ekman heat convergence is 3.1 ZettaJ, the most positive during the period of 2003-2018. In Winter08, 12, and 15, the total

change of Ekman heat convergence is 3.1 ZettaJ, 2.1 ZettaJ, and 1.5 ZettaJ respectively, the most positive throughout the period of 2003-2018, second only to Winter14.

In short, the wintertime change of Ekman heat convergence well separates the extreme strong EDW formation years from the extreme weak EDW formation years.

In Figure 4-9b, a decrease on the accumulated Ekman heat convergence indicates a cooling due to the divergent Ekman current in the domain of analysis. This Ekman divergence can be associated with low pressure systems passing by the domain of analysis. We marked as passing storms over the domain of study the parts of the accumulated Ekman heat convergence curves with more-than-two-day consecutive descending slopes (Figure 4-9b). During each storm period, we estimated the corresponding accumulated Ekman heat advection by the decrease on the accumulated Ekman heat convergence curve. We divided this accumulated Ekman heat advection by the storm duration, and by the surface area of the domain of study, to obtain the Ekman equivalent heat flux, in the unit of $\mathrm{W\,m^{-2}}$. We used the equivalent heat flux to measure the impact of the storms over the domain of study in terms of Ekman heat transport.

We presented the large Ekman heat divergence signaling strong EDW formation in Section 4.3.6. As part of the complementary material, here we dicuss the weak EDW formation years and its winter Ekman heat convergence.

In Winter14, for example, the accumulated heat advection in the domain of study during the EDW ventilation season is convergent, about 3.1 ZettaJ, the most positive among the years 2003-2018. The total Ekman heat divergence in 2014 due to storms is -1.9 ZettaJ, the smallest among these years (Table 4.3). The total duration of storms in 2014 is 60 days, the shortest among these years. The average Ekman equivalent heat flux in 2014 is $72.9\,\mathrm{W\,m^{-2}}$, one of the weakest among these years, second only to 2008.

The years 2008, 2012, 2014, and 2015 are identified as weak EDW formation years. During the EDW formation of these years, the total storm-associated Ekman heat divergence, the total storm duration, and the average Ekman equivalent heat flux are at the lower percentile rank.

A.2.2 Winter storm watch

A.2.2.1 Strong EDW formation years: 2005, 2010, and 2013

In Winter05, the accumulated Ekman heat advection in the domain of analysis is divergent, about -4.2 ZettaJ (the green dotted line in Figure 4-9b. The negative sign indicates the divergence). The total Ekman heat divergence in 2005 due to storms

is $-6.03\,\mathrm{ZettaJ}$, with a percentile rank of 87.5% among the 2003-2018 period. The total duration of storms in 2005 is 133 days, the longest duration among the years 2003-2018. The average Ekman equivalent heat flux in 2005 is $106.74\,\mathrm{W\,m^{-2}}$, with a percentile rank of 68.8% among the years 2003-2018.

From 19-30 October, 2004, the accumulated Ekman heat advection experienced a sudden decrease by $-1.2\,\mathrm{ZettaJ}$ within 12 days (Figure 4-9b), composing 20% of the total storm-associated Ekman heat divergence in 2005. This divergence corresponds with a low pressure system self-developping off the coast of US Carolinas, which remained in the domain of analysis during this period. The low pressure system exited domain of analysis from the northeast corner on 26th October, 2004, and evolved into the wind storm of 27th-29th October 2004. This storm caused gale-force winds and flooding rains on the southwest coast of Great Britain (Met Office, 2013). From 20 January-5 February, 2005, the accumulated Ekman heat advection experienced a decrease by $-1.2\,\mathrm{ZettaJ}$ within 17 days, 20% of the total storm-associated Ekman heat divergence in 2015. This Ekman heat divergence was prompted by a low pressure system, associated with the 2005 North American Blizzard. After impacting the US Mid-Atlantic states, the storm moved off the coast into domain of analysis on 20 January, 2005. From 1 -18 March, two consecutive typical major North American winter storms (NWS, 2007, 2014d) passed through the northeastern US. The two storms remained in the domain of analysis for a total of 17 days, responsible for a decrease of the accumulated Ekman heat advection of $-1.1\,\mathrm{ZettaJ}$, 18% of the total storm-associated Ekman heat divergence.

In Winter10, the accumulated Ekman heat advection in the domain of analysis is divergent, about $-4.5\,\mathrm{ZettaJ}$ (the grey dotted line in Figure 4-9b). The total Ekman heat divergence in 2010 due to storms is $-6.9\,\mathrm{ZettaJ}$, the highest among the years 2003-2018. The total duration of storms in 2010 is 128 days, with a percentile rank of 93.8% among these years. The average Ekman equivalent heat flux in 2010 is $126.9\,\mathrm{W\,m^{-2}}$, with a percentile rank of 87.5% among these years.

Hurricane Ida-associated 2009 snowstorm caused strong rainfall and gusty wind along the US east coast (Collins, 2016). The low pressure system associated with this storm passed through the domain of analysis during 11-14 October, 2009 (Table A.2). The accumulated Ekman heat advection experienced a decrease of $-0.3\,\mathrm{ZettaJ}$ within 4 days, 4% of the total storm-associated Ekman heat divergence in 2010. From December 15-December 27, 2009, the low pressure system associated with the 2009 December North American Blizzard passed through the domain of analysis. This blizzard brought record-breaking snowfalls in U.S. Philadelphia and Washington D.C. (NWS, 2014c, 2016b). The accumulated Ekman heat advection experienced a

decrease of -1.5 ZettaJ within the 13 days, 22% of the total storm-associated Ekman heat divergence in 2010. It is the largest Ekman heat divergence associated with a single storm during the 2010 EDW ventilation period. From 1-14 January, 2010, the low pressure system associated with the 2010 January North American Blizzard passed through the domain of analysis. The accumulated Ekman heat advection experienced a decrease by -1.0 ZettaJ within the 14 days, 14% of the total storm-associated Ekman heat divergence in 2010. From 3 February-7 March, 2010, three consecutive blizzards passed through the domain of analysis after impacting US New England, Mid-Atlantic and Washington D.C. area, with flooding rains, hurricane-force sustained winds, and massive snowfalls (Horvitz, 2010; Livingston and Ambrose, 2015; NWS, 2014a). The associated low pressure systems remained a total of 29 days in the domain of analysis, and the accumulated Ekman heat advection divergence is about -2.3 ZettaJ, 1/3 of the total storm-associated Ekman heat divergence in 2010 (Table A.2).

About Winter13, we have presented the impact of Hurricane Sandy and Wind Storm Gong in Section 4.3.6. Apart from those two well known storms, the north America snowstorms, comparably less known, as well contribute to the large heat divergence due to Ekman heat advection. From 20-24 November, 2012, a subtropical depression self-developed and remained in the domain of analysis, which was responsible for an accumulated Ekman heat divergence of -0.5 ZettaJ (Table A.2). From 18-21 December, the 2012 Mid-December Blizzard, featuring heavy snowfalls and gusty winds in US Mid-West, entered the domain of analysis, responsible for an accumulated Ekman heat divergence of 0.5 ZettaJ. From 9-13 January, 2013, a subtropical depression self-developed at the US east coast and remained in the domain of analysis, which was responsible for an accumulated Ekman heat divergence of -0.5 ZettaJ. From 21 February-10 March, 2013, two consecutive blizzards, namely the Late February Winter Storm and the March Nor'easter, passed through the domain of analysis. The two typical blizzards during this time of year had a wide impact on US South, Mid-west, and east coast states, which was responsible for an accumulated Ekman heat divergence of -1.9 ZettaJ for a duration of 19 days (Table A.2), 29% of the total storm-associated Ekman heat divergence in 2013. From 23-30 March, 2013, the Late March Storm Complex passed through the domain of analysis, responsible for an accumulated Ekman heat divergence of $-0.5,$ ZettaJ, 8% of the total storm-associated Ekman heat divergence in 2013.

A.2.2.2 Weak EDW formation years: 2008, 2012, 2014, and 2015

Meanwhile, in Winter08,the accumulated heat advection in the domain of analysis is convergent, about 3.0 ZettaJ, the second most positive among the years 2003-2018. The total Ekman heat divergence in 2008 due to storms is −2.4 ZettaJ, with a percentile rank of 18.8% among the years 2003-2018. The total duration of storms in 2008 is 78 days, with a percentile rank of 25.0% among the years 2003-2018. The average Ekman equivalent heat flux in 2008 is $-70.8\,\mathrm{W\,m^{-2}}$, the weakest among the years 2003-2018.

In Winter12, the accumulated heat advection in the domain of analysis is convergent, about 2.1 ZettaJ. The total Ekman heat divergence in 2012 due to storms is −2.7 ZettaJ, with a percentile rank of 31.2% among the years 2003-2018. The total duration of storms in 2012 is 77 days, with a percentile rank of 18.8% among the years 2003-2018. The average Ekman equivalent heat flux in 2012 is $-82.3\,\mathrm{W\,m^{-2}}$, with a percentile rank of 43.8% among the years 2003-2018.

In Winter14, the accumulated heat advection in the domain of analysis is convergent, about 3.1 ZettaJ, the most positive among the years 2003-2018. The total Ekman heat divergence in 2014 due to storms is −1.9 ZettaJ, the smallest among these years. The total duration of storms in 2014 is 60 days, the shortest among these years. The average Ekman equivalent heat flux in 2014 is $72.9\,\mathrm{W\,m^{-2}}$, one of the weakest among these years, second only to 2008.

In Winter15, the accumulated heat advection in the domain of analysis is convergent, about 1.5 ZettaJ. The total Ekman heat divergence in 2015 due to storms is 2.6 ZettaJ, with a percentile rank of 25.0% among the years 2003-2018. The total duration of storms in 2015 is 81 days, with a percentile rank of 31.2% among these years. The average Ekman equivalent heat flux in 2015 is $74.9\,\mathrm{W\,m^{-2}}$, with a percentile rank of 18.8% among these years.

The years 2008, 2012, 2014, and 2015 are identified as weak EDW formation years. During the EDW formation of these years, the total storm-associated Ekman heat divergence, the total storm duration, and the average Ekman equivalent heat flux are at the lower percentile rank.

A.2.2.3 Intermediate EDW formation years: 2011 and 2018

In Winter11, the accumulated Ekman heat advection in the domain of analysis is divergent, about −1.8 ZettaJ. A continuous series of storms during the winter of 2010-2011 are shown as large decreases on the accumulated Ekman heat convergence curve in the domain of analysis (the solid yellow curve in Figure 4-9b). From 9-11

November, a low pressure system associated with Huricane Thomas, after a strong impact at St. Lucia, Curcao, Martinique, and Haiti, passed through the domain of analysis. Within 12 days, this low pressure system led to a decrease of the accumulated Ekman heat advection of −0.9 ZettaJ, 17.3% of the 2011 total storm-associated Ekman heat divergence. Three days after, a low pressure system associated with the 2010 Thanksgiving weekend storm entered domain of analysis (Table A.2). This storm remained in the domain of analysis for 14 days, responsible for a decrease of the accumulated Ekman heat advection of −1.0 ZettaJ, 19.2% of the total Ekman heat divergence in 2011 due to storms. A week after, during 13 December 2010-1 January 2011, several low pressure systems associated with the December 2010 North American Blizzard passed through the domain of analysis. Within 27 days, these low pressure systems led to a decrease of the accumulated Ekman heat advection of −2.1 ZettaJ, 40.4% of the total Ekman heat divergence in 2011 due to storms.

The total Ekman heat divergence in 2011 due to storms is −5.2 ZettaJ, with a percentile rank of 81.2% among the years 2003-2018. Yet, the total duration of storms in 2011 is 89 days, with a percentile rank of 62.5%. The average Ekman equivalent heat flux in 2011 is 136.5 $\mathrm{W\,m^{-2}}$, with a percentile rank of 93.8% among the years 2003-2018. The Ekman equivalent heat flux in 2011 is the strongest, second only to 2013, even stronger than 2005 and 2010. However, its short storm duration yielded a weak total storm-associated Ekman heat divergence compared with 2005 and 2010.

In Winter18, the accumulated Ekman heat advection in the domain of analysis is divergent, about −0.9 ZettaJ. The total Ekman heat divergence in 2018 due to storms is −4.7 ZettaJ, with a percentile rank of 75.0% among the years 2003-2018. The total duration of storms in 2018 is 93 days, with a percentile rank of 68.8% among these years. The average Ekman equivalent heat flux in 2018 is 119.9 $\mathrm{W\,m^{-2}}$, with a percentile rank of 81.2% among these years. Notably, during 1-7 March, 2018, the low pressure system associated with the 2018 Early March Nor'easter passed through the domain of analysis (the solid grey line in Figure 4-9b). The accumulated Ekman heat advection of this period experienced a decrease of −1.6 ZettaJ within 7 days (Table A.2).

Storm	**Time**	**duration (days)**	**Ekman (ZettaJ)**	**Majorly Impacted regions**
September-March, 2013				
Hurricane Sandy, 2012	26/10-30/10	5	−0.9	Jamaca, Cuba, Bahamas, and US east coast states, particularly New Jersey and New York (Blake et al., 2013)

Subtropical depression, 2012	20/11-24/11	5	−0.5	off US east coast
Mid-December Blizzard, 2012	18/12-21/12	4	−0.5	US midwest(NWS, 2015a, 2016a)
Subtropical depression, 2013 Prelude of Wind Storm Gong	9/01-13/01	5	−0.5	Iberia (Liberato, 2014)
Late February Winter Storm & March Nor'easter, 2013	21/02-10/03	19	−1.9	US Texas, Midwest, Ohio valley, Mid-Atlantic, and eastern New England (NWS, 2019; Ryan et al.)
Late March Storm Complex, 2013	23/03-30/03	8	−0.5	Colorado, Illinois, Maryland, and Washington D.C. (Ryan et al.)
September-March, 2010				
Hurricane Ida November Nor'easter, "Nor'Ida", 2009	11/10-14/10	4	−0.3	US Mid-Atlantic, South and Southeast (Collins, 2016)
December North American Blizzard, 2009	15/12-27/12	13	−1.5	Eastern US and Canada (Phillips, 2011)
January New England Snow Storm, 2010	1/1-14/1	14	−1.0	US Vermont(NOAA, 2010)
North American Blizzard "Snowmageddon", 2010	3/2-7/2	5	−0.5	Washington D.C. and Maryland (Horvitz, 2010)
North American Blizzard "Snoverkill", 2010	9/2-23/2	15	−1.1	Washington D.C. and Maryland (Livingston and Ambrose, 2015)
North American Blizzard "Snowicane", 2010	27/2-7/3	9	−0.7	US Mid-Atlantic and New England (NWS, 2014a)
September-March, 2005				
the storm of 27th-29th October, 2004	19/10-30/10	12	−1.2	UK Devon, Cornwall, and South Wales (Met Office, 2013)
North American Blizzard, 2005	20/1-5/2	17	−1.2	US Pennsylvania, Maryland, Delaware and New Jersey (NWS, 2014b)
Feb 28-March 1 Winter Storm, 2005	01/03-10/03	10	−0.6	Northeastern US (NWS, 2014d)
St Patrick's Day Nor'easter, 2005	12/03-18/03	7	−0.5	Northeastern US, and Canada St. Lawrence River Valley (NWS, 2007)
September-March of other years				
March 1-3 Nor'easter, 2018	1/3-7/3	7	−1.6	US New York and Pennsylvania (NWS, 2018)
Hurricane Tomas, 2010	9/11-20/11	12	−0.9	St. Lucia, Curacao, Martinique, and Haiti (Pasch and Kimberlain, 2011)
Thanksgiving weekend storm, 2010	23/11-7/12	14	−1.0	US west coast, Mid-west, and South (Pereira, 2011)

December North American Blizzard, 2010	13/12-7/1,2011	27	−2.1	Contiguous US Cananda (NWS, 2015c, 2016c)
January North American Ice Storm, 2007	20/1-26/1	7	−0.7	US Mid-west: Kansas and Missouri(NWS, 2015b)
March North American major winter storm, 2006	18/3-26/3	9	−0.8	US Colorado, Wyoming, Nebraska, South Dakota, and Kansas (Otto, 2006)

Table A.2: The major North Atlantic subtropical storms during the period of September-March of 2003-2018 that passed through the domain of analysis (name, time of passing through the domain, duration in the unit of day, and majorly impacted regions). Also recorded are their accumulated Ekman heat convergence while passing through the domain of analysis, in the unit of ZettaJ.

A.2.2.4 Surface wind stress curl

Figure A-3 shows the composites of surface wind stress curl to the four WRs. Under AR (Figure A-3a), the positive wind stress curl anomaly is centered at 55N, and the negative wind stress curl anomaly in the subtropical region. The averaged wind stress curl anomaly in Winter05 resembles its composite onto AR; however, the amplitude of the Winter05 is half of that of the composite.

Under BLK (Figure A-3b), the negative wind stress curl anomaly is centered on the east coast of Greenland at 63N. The positive wind stress curl anomaly extends, in a diagonal manner, from the southern US coastal region at west to the British Islands and Northern Europe at the East. Under BLK, the domain of study is covered with a positive anomaly. The averaged wind stress curl anomalies in Winter08, 12, and 15 resemble their composites onto BLK.

Under NAO- (Figure A-3c), the positive wind stress curl in the subpolar region is centered between Iceland and Greenland, at approximately 63N. The negative wind stress curl in the subtropical region is between $35\text{N} - 57\text{N}$. The positive wind stress curl in the subtropical region is located south of 35N. Under NAO-, the northern part of the domain of analysis is covered by a negative anomaly. The wind stress curl anomalies of Winter10 and 13 resemble its composite onto NAO-.

Under NAO+ (Figure A-3d), the negative wind stress curl anomaly is centered between Greenland and Iceland at approximately 60N. The positve wind stress curl anomaly is between roughly $30\text{N} - 65\text{N}$. Under NAO+, the northern part of the domain of study is covered by a positive anomaly. The averaged wind stress curl anomaly of Winter14 resembles its compisite onto NAO+.

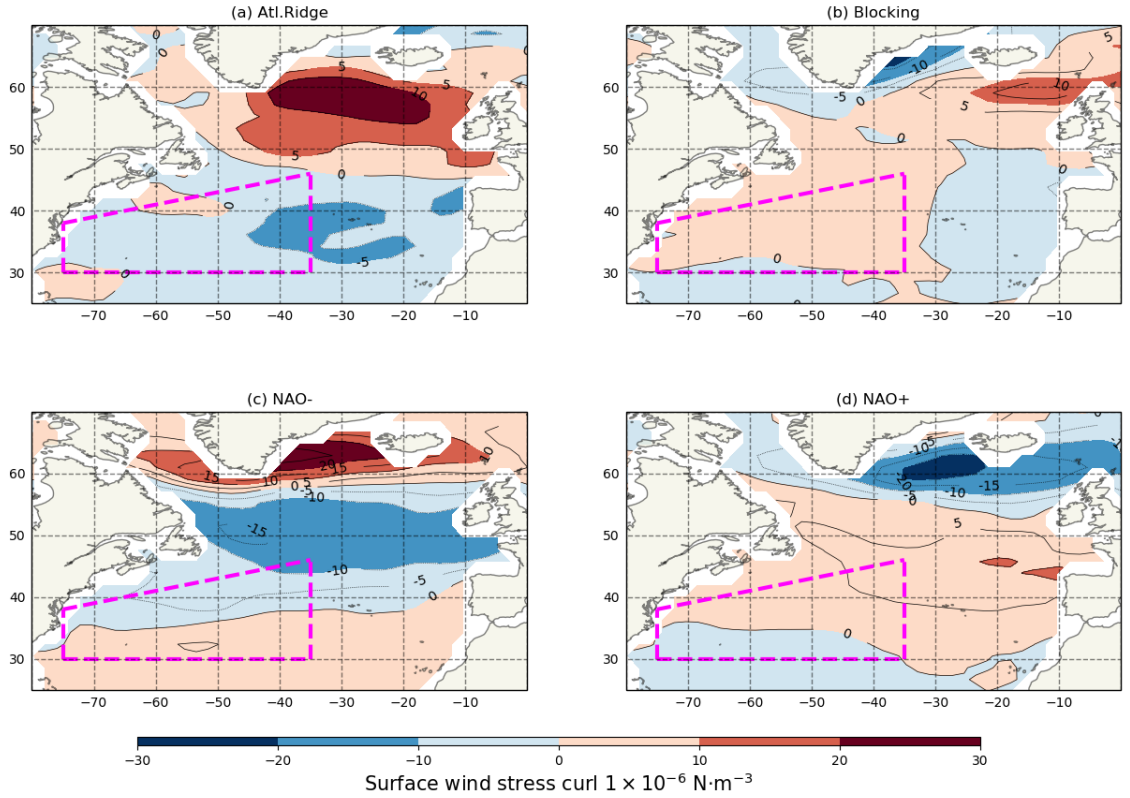

Figure A-3: Mapped composites of surface wind stress curl, in the unit of $\mathrm{N\,m^{-3}}$, onto the four WRs. (a) AR, (b) BLK, (c) NAO-, and (d) NAO+. The pink dashed contours denote the domain of analysis.

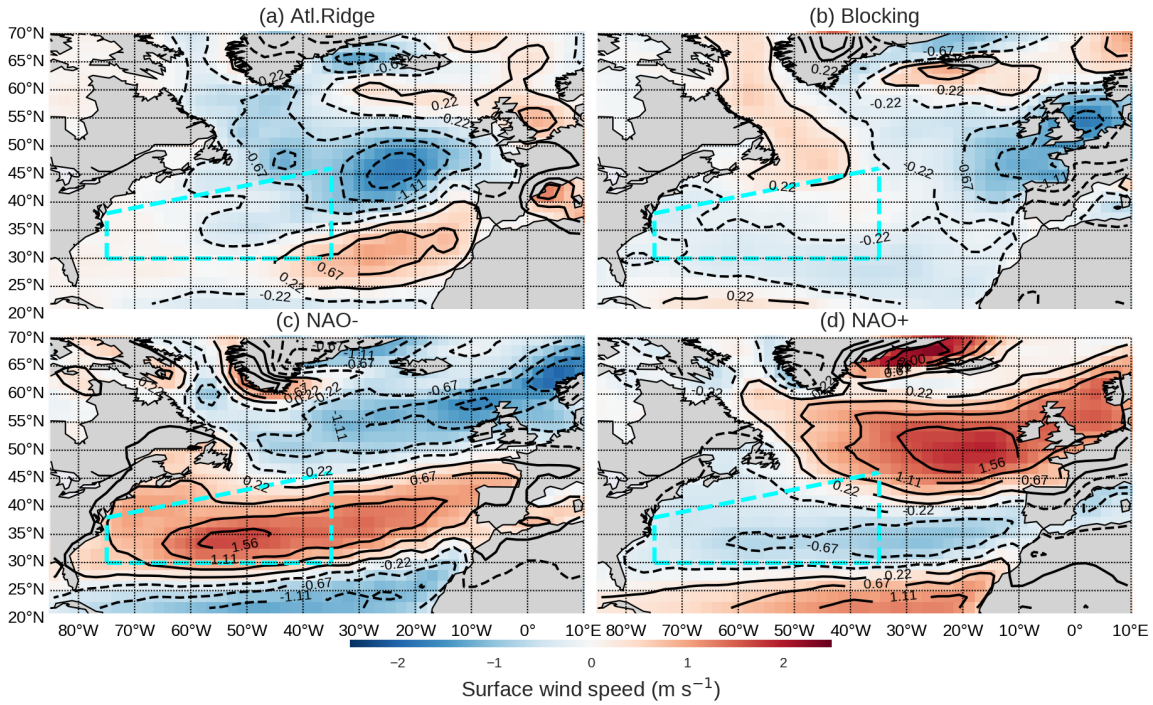

Figure A-4: Mapped composites of 10m surface wind speed, in the unit of $\mathrm{m\,s^{-1}}$, onto the four WRs. (a) AR, (b) BLK, (c) NAO-, and (d) NAO+. The cyan dashed contours denote the domain of analysis.

A.2.3 Impact of Atlantic Ridge/Blocking through Air-sea heat fluxes

A.2.3.1 10m surface wind speed

We examined the 0-year lag impact of the weather regimes on surface wind speed (Figure A-4). Under AR, the 10m surface wind speed anomaly is $-0.57 - 0.0\,\mathrm{m\,s^{-1}}$ (Figure A-4a). Under BLK, the 10m surface wind speed anomaly is $0 - 0.22\,\mathrm{m\,s^{-1}}$ (Figure A-4b). Under NAO-, the 10m surface wind speed anomaly is positive, with an "elongated" core value of $1.6\,\mathrm{m\,s^{-1}}$ at $46 - 58^{o}\mathrm{W}, 35^{o}\mathrm{N}$ (Figure A-4c). Under NAO+, the 10m surface wind speed anomaly is negative, with an "elongated" core value of $-0.7\,\mathrm{m\,s^{-1}}$ at $35 - 60^{o}\mathrm{W}, 35^{o}\mathrm{N}$ (Figure A-4d). The composite of 10m surface wind speed onto NAO- is inversed from that onto NAO+.

A.2.3.2 Air-sea surface heat fluxes

We examined the 0-year lag impact of the weather regimes on air-sea surface heat fluxes (Figure A-5). Under AR, positive air-sea surface heat flux anomaly is at $35 - 45^{o}\mathrm{W}/42 - 52^{o}\mathrm{N}$, at the northeast part of the domain of analysis (Figure A-5a). The

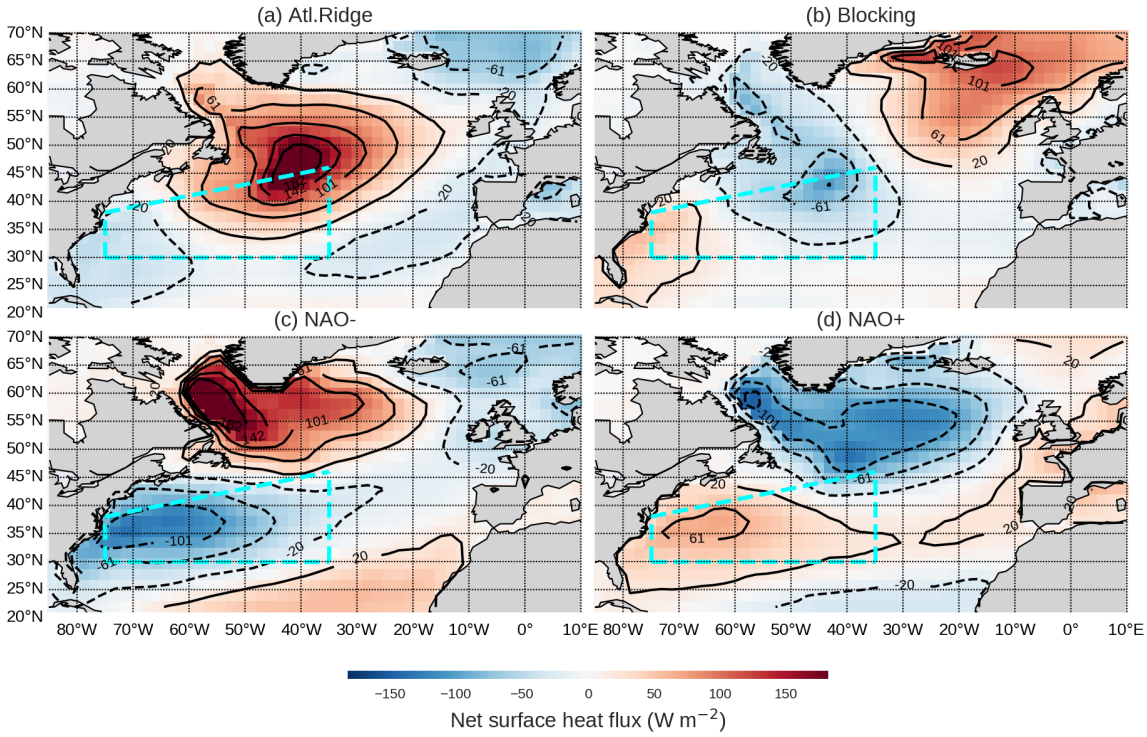

Figure A-5: Mapped composites of air-sea surface heat fluxes, in the unit of $\mathrm{W\,m^{-2}}$, onto the four WRs. The negative sign indicates losing heat to the atmosphere. (a) Atlantic Ridge, (b) Blocking, (c) NAO-, and (d) NAO+. The cyan dashed contours denote the domain of analysis.

core of this anomaly is $182\,\mathrm{W\,m^{-2}}$. The negative anomaly of the air-sea heat flux is located at the western part of the domain of analysis, at $60-75^{o}$W. The spacial pattern of air-sea heat flux composites onto BLK is inversed from that onto AR. Under BLK, positive air-sea surface heat flux anomaly is at the western part of the domain of analysis, at $60-75^{o}$W (Figure A-5b). The positive anomaly of the air-sea heat flux is at the northeastern part of the domain of analysis. The core value is $-61\,\mathrm{W\,m^{-2}}$, located at 45^{o}W 43^{o}N.

Under NAO-, negative air-sea surface heat flux anomaly occupies the domain of analysis, with a core of $-101\,\mathrm{W\,m^{-2}}$ at the northwestern part. Under NAO+, positive air-sea surface heat flux anomaly occupies the domain of analysis, with a core of $61\,\mathrm{W\,m^{-2}}$ at the northwestern part. The patterns of air-sea heat flux composites onto NAO+ and NAO- are inversed.

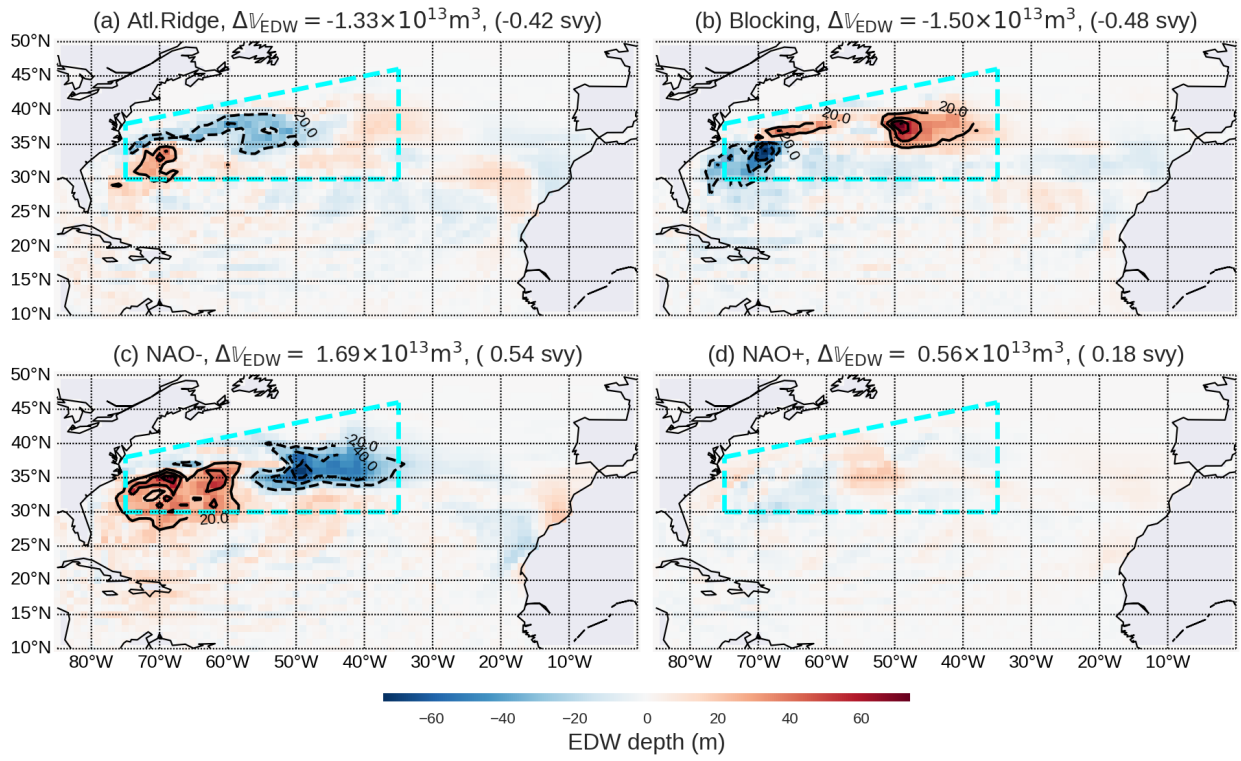

Figure A-6: EDW thickness composites attributed to weather regimes. The weather regimes are calculated using the springtime (April-June) NCEP dataset in the period of 1966-2017. The domain of study is represented in cyan dashed line.

A.2.3.3 EDW volume composites

To investigate the 0-year lag impact of the weather regimes on the EDW total volume, we computed the composites of the EDW thickness onto the weather regimes. Note that we used the EDW spring time thickness in order to capture the freshly ventilated mode water signal that, we assume, is related to the winter time dominating weather regime.

Figure A-6 shows the EDW thickness composite with each weather regimes. The EDW thickness anomaly associated with AR (Figure A-6a) shows a positive thickness anomaly located at 70W/32N of about 20m. A negative anomaly of about 30m is found all along the Gulf Stream and over a broader region centered at 55W/37N. The positive anomaly is located precisely on top of the eastern EDW thickness standard deviation maximum and is about 10% of the local EDW mean thickness value.

The EDW thickness anomaly associated with BLK (Figure A-6b) shows one large positive anomaly of about 60m in the region located at 35N-40N/40W-50W. A smaller positive anomaly of about 30m is located along the Gulf Stream. A negative anomaly

of about 60m is found around 30N-35N/70W.

The EDW thickness anomaly associated with NAO- (Figure A-6c) shows a positive anomaly of about 60m in a large region at 58W-75W/27N-37N. A negative anomaly of about 60m is located in the region of 35W-55W/33N-40N.

Under NAO+ regime (Figure A-6d), the EDW thickness anomaly appears to be smaller than 20m.

When integrated in space, the thickness anomalies provide EDW volume anomalies associated with weather regimes. For AR, the EDW volume anomaly is $-1.33 \times 10^{13}\mathrm{m}^3$; for BLK, it is $-1.5 \times 10^{13}\mathrm{m}^3$; for NAO-, it is $1.69 \times 10^{13}\mathrm{m}^3$; and for NAO+, it is $0.56 \times 10^{13}\mathrm{m}^3$.

A.2.3.4 Impact of NAO through Gulf Stream

We found that the interannual NAO- winter daily occurrence time series is anticorrelated with the Gulf Stream positioning (α), with a lagged correlation coefficient of -0.81 (the black line in Figure A-7a and the dashed red line in Figure A-7b). The time lag is 9 month with NAO- leading the Gulf Stream positioning. From 2003-2007, we demonstrated that the Gulf Stream positioning α and NAO- occurrences are out of phase. Lillibridge III and Mariano (2013) compared the NAO index with the Gulf Stream positioning. They applied a 1-year running mean to both time series. They showed a maximum correlation of 0.51 at a lag of 6 months with NAO leading. They showed that 1995-1998 and 2002-2007 are two periods with out-of-phase relationship between NAO index and the Gulf Stream meridional shift. The negative sign indicates the NAO- occurrences being opposite from NAO index. Our result shows better correlation than theirs. The possible explanation about the difference in correlation coefficents is due to the asymmetry of NAO+ and NAO-, and resemblence between NAO- and Atlantic Ridge, provided by the weather regimes. Frankignoul et al. (2001) showed a northward (southward) meridional shift of Gulf Stream has a 11-18 month lag following the NAO reaches positive (negative) extrema. Taylor and Stephens (1998) showed high values of NAO corresponds with northerly Gulf Stream, with a 2-year time lag. Our results are in line with the literature. The Gulf Stream positioning is correlated with the interannual NAO+ winter daily occurrence time series, with a lagged correlation coefficient of 0.73 (Figure A-7b). The time lag is 16 months (1.3 years) with Gulf Stream positioning time series leading NAO+.

The NAO- has a lagged correlation with the NAO+, coefficient of 0.56 (the black lines in Figure A-7a and b). The time lag is 2 years with NAO- leading NAO+. The interannual NAO- accumulated winter (September-March) daily occurrence time series is correlated with the March EDW ventilated volume time series (the blue dots

in Figure A-7a), with a 0-year lag correlation coefficient of 0.85.

A.3 Discussion

A.3.1 Wind stress curl

We showed that the average wind stress curl of Winter10 is negative in the subpolar region, centered at above the Irminger Sea (37 W, 62 N), with a magnitude of $-4.0 \times 10^{-7}\,\mathrm{N\,m^{-3}}$. The average wind stress curl of Winter10 is positive between $35-65$ N in the North Atlantic, with a magnitude of $3.0 \times 10^{-7}\,\mathrm{N\,m^{-3}}$, located at 45 N, 42 W, east of New Foundland. Häkkinen et al. (2013) showed in Figure 7b the DJF average of wind stress curl in the winter of 2009-2010. Our finding is in line with the litterature.

In addition, Häkkinen et al. (2013) investigated the subpolar region SSH increase that is correlated with $0-700$ m OHC. They also showed in Figure 5C that the subtropical SSH has very low correlation with subtropical OHC. They also showed that the drastic change in the winter of 2009-2010 corresponds with a frequent occurrences of the Greenland Blocking.

A.3.2 Zero-year lag impact

To investigate the impact of the dominant atmospheric forcing patterns onto the subtropical stratification, we computed EDW thickness composites with each of the four weather regimes. We found a clear correlation indicating that the EDW is indeed impacted by weather regimes. We found complex patterns whereby the integrated volume anomaly is a residual of large positive and negative regional thickness anomalies. Hence, the regional impact of the weather regimes should play a crucial role in understanding the integrated time series of mode water properties.

The composite maps (Figure A-6) show clear patterns of positive and negative regional anomalies of EDW thickness that are either "patchy" or "elongated". AR and BLK have opposite but very similar patterns with "patchy" anomalies collocated with the maximum of EDW thickness standard deviation (Figure 2-1), and an anomaly elongated on the Gulf Stream. On the other hand, the NAO- composite does not show anomalies along the Gulf Stream but rather larger "patches". This is especially true for the western EDW thickness anomaly that significantly overlap with the maximum EDW thickness at 60W. Maybe surprisingly, the NAO+ composite shows very small anomalies compared with the other three.

It is also worth noting that AR and NAO- composites resemble each other. However, in the integral sense, these two patterns lead to opposite EDW volume anomalies

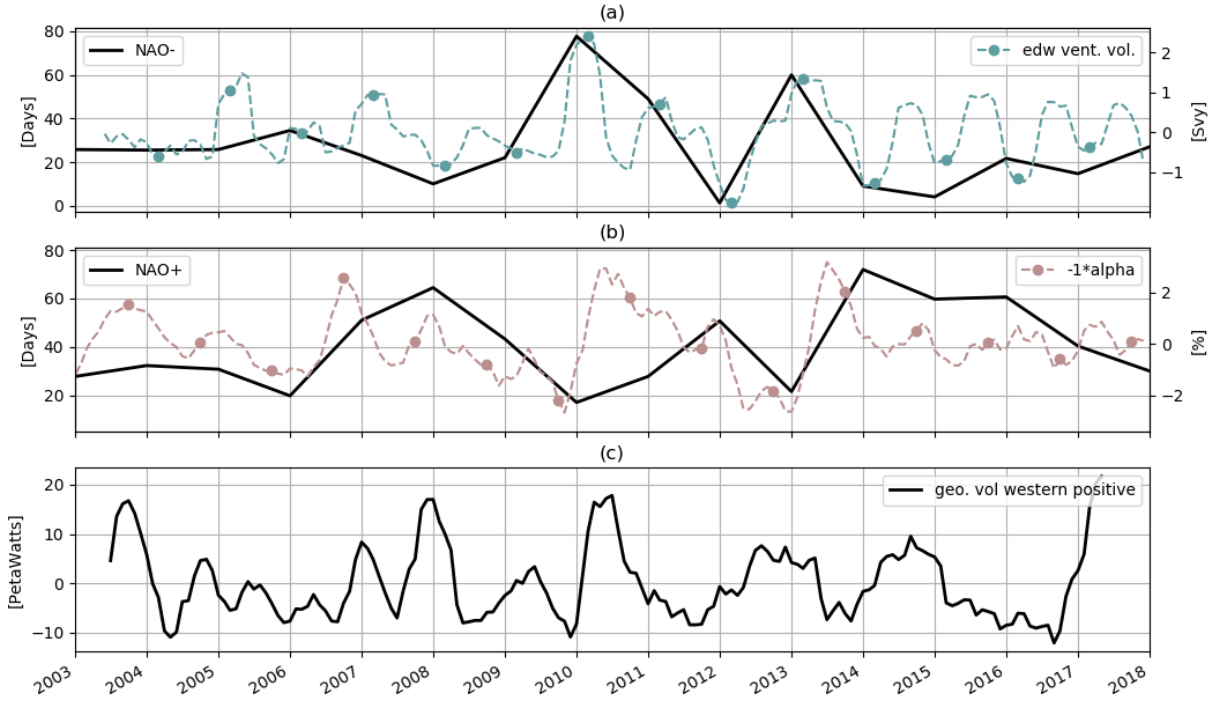

Figure A-7: Top panel (a) shows the annual NAO- total number of days during the period of September-March (thick solid black line). The dashed light blue line with dots represents the interannual variability of EDW ventilated volume, same as Figure 4-3a, and the dots represent the EDW ventilated volume in March of each year. Middle panel (b) shows the annual NAO+ total number of days during the period of September-March (thick solid black line). Both NAO- and NAO+ time series are averaged over NCEP and ERA using the variables of surface level pressure and the 500 hPa geopotential height. The dashed light red line with dots represents the interannual variability of index α, in percentage, same as Figure 2-12. This index indicates the average Gulf Stream positioning in the domain of analysis. The dots represent the α values in September of each year. The bottom panel (c) shows the interannual variability of geostrophic volume flux coming into the domain of analysis from the western boundary, positive only.

($-1.33 \times 10^{13}\mathrm{m}^3$ v.s. $1.69 \times 10^{13}\mathrm{m}^3$).

The fact that the mode water thickness anomaly are collocated with the largest thickness standard deviation regions (Figure 2-14) is strongly indicative of how the atmospheric forcing impact the mode water variability. Indeed, we selected the spring time thickness of the EDW to compute the composite in order to precisely target the freshly formed mode water signal. Thus, we infer that the atmospheric forcing impact onto the EDW thickness variability is primarily through the EDW formation mechanisms.

The NAO and the corresponding ocean circulations are substantially correlated with a 0-year lag. Gangopadhyay et al. (1992) showed that this 0-year lag can be a quick Ekman layer response to the atmosphere variability, in the sense that ocean reponds to the atmosphere. Joyce et al. (2019) showed that the zero-lag correlation between NAO and Gulf Stream can be as well an ocean-driven effect upon atmosphere. They demonstrated a lagged correlation between the Gulf Stream positioning and both North Atlantic wintertime storm track and Greenland blocking. The lagged time is about 3 months with the Gulf Stream leading. DiNezio et al. (2009) demonstrated a lagged correlation between the Florida Current transport at 26°N and the NAO. The time lag is about 3-10 months with the Western boundary current leading. They explained with the impact of North Atlantic subtropical gyre onto the wind forcing.

It is also evident that the impact of AR and BLK onto the EDW thickness has a component concentrated along the Gulf Stream Extension. This may not be surprising because any small meridional variations of the Gulf Stream frontal structure maximizes local signals. In fact, Levine et al. (2011) and Joyce et al. (2000) have already suggested that for instance the NAO- forcing leads to a southward shift of the Gulf Stream that in turn leads to a shallower mixed layer south of the Gulf Stream, a smaller EDW outcropping and an decrease in EDW volume. Joyce et al. (2000) showed that in decadal time scales, a low (high) NAO corresponds with high (low) thickness of mode water at Bermuda and a southerly (northerly) Gulf Stream path. Our results suggest that, as the 0-year lag impact, these mechanisms are at play with AR rather than NAO-. This is supported by Barrier et al. (2016), who found that the subtropical variability at Bermuda is under the dominant influence of AR rather than NAO.

Under NAO +/-, the EDW volume ditribution does not match neither wind speed, air-sea heat loss, nor wind stress curl. We inferred that NAO has an indirect impact on EDW volume, for example, with a time lag, through ocean structure / dynamics. The EDW volume composites onto NAO- and AR are similar. We inferred that despite sharing the similar pattern, they are caused by different dynamics / time scales.

Under AR, in the region east (west) of 60°W of the domain of analysis, the negative (positive) EDW volume anomaly corresponds with weak (strong) near-surface wind and negative (positive) air-sea heat surface loss (Figure A-4a and A-5a). Under BLK, the patterns are the inverse from AR (Figure A-4b and A-5b). Under AR and BLK, the EDW volume distribution matches wind speed and air-sea heat loss . We inferred that AR and BLK have a direct impact on EDW volume, through air-sea heat loss.

From Forget et al. (2011), we know that the typical seasonal cycle amplitude of the EDW volume is about $23.3 \times 10^{13}\mathrm{m}^3$. Then our weather regime composite anomalies is about 5% of the seasonal cycle amplitude. From Kwon and Riser (2004), we can infer the amplitude of the interannual to decadal EDW volume time series. From their Figure 2, we determined this amplitude to be $40 \times 10^{13}\mathrm{m}^3$. As already mentioned, this makes the EDW water mass low frequency variability strikingly larger than its seasonal cycle. Yet our weather composite anomalies are about 3% of the Kwon and Riser (2004) estimate for the low frequency EDW volume variability. A possible explanation for such a small signal from our computation would be that Kwon and Riser (2004) increased their signal to noise ratio by selecting the poorly stratified part of the EDW layer, whereas we did not.

A.3.3 Lagged correlation

We found that the interannual variability of NAO- is anticorrelated with the Gulf Stream positioning, with NAO- leading by 9 months. In addition, previously we showed that the northward (southward) shift of Gulf Stream reflects a high (low) heat content on the interannual time scale (See Section 3.3.7 in detail). It is fair to infer that, on the interannual time scale, a high (low) winter NAO- occurrences would lead to a low (high) heat content in the following September, which corresponds with a favorable (unfavorable) preconditioning for the EDW formation during the following winter.

Frankignoul et al. (2001) showed that there is no clear evidence that the Gulf Stream has direct impact to atmosphere. However, we found that, on interannual time scales, strong (weak) NAO- leads the southward (northward) shift of Gulf Stream positioning by 9 months. The southward (northward) shift of Gulf Stream leads to strong (weak) NAO+ by 16 months.

Frankignoul et al. (2001) showed that Florida current transport at 26N has been shown to have negative correlation with NAO index. However, in our analysis, no correlation is found between the NAO and the geostrophic volume flux, flowing into the domain from the western boundary.

A.4 Summary

1. On the interannual time scale, a high (low) winter NAO- occurrences would lead to a low (high) heat content in the following September, which corresponds with a favorable (unfavorable) preconditioning for the EDW formation during the following winter.

2. We found that the Ekman heat advection the driving mechanism to explain the EDW extreme occurrences. Among the extreme strong years of EDW formation, the SLP anomaly has a low pressure system in the domain of study, and a high pressure system to its north or northeast. The wind stress curl is negative, responsible for the horizontal Ekman heat divergence in the domain of study, dominated either by a strong northward transport from the northern boundary, as in 2005, a strong southward transport at southern boundary, as in 2010, or both, as in 2013. The heat divergence due to the Ekman current corresponds with larger EDW outcropping area. The EDW outcropping area is larger than the 2003-2018 climatological mean. The zero wind stress curl line shifts further southward.

   Among the extreme weak years of EDW formation, the SLP anomaly has a high pressure system in the domain of study. The wind stress curl is positive, responsible for the horitontal Ekman heat convergence in the domain of study, domainated either by a strong northward transport from the southern boundary alone (as in 2008, 2012, and 2015), or in combination with a strong southward transport from the northern boundary, as in 2014. The heat convergence due to the Ekman current prevent the EDW outcropping. The EDW outcropping area is smaller or is shifted without changing the size compared with the 2003-2018 climatological mean. The zero wind stres curl line shifts slightly northward.

3. Concerning a passing storm over the domain of analysis, both intensity and duration have an impact on extremity of EDW ventilation. During the EDW formation period of one year, we observed that passed through the domain of study remnant storms from decaying hurricanes in the late fall, or blizzards in winter and early spring, moved off the US east coast. Of these strong years, these storms during the EDW formation period are responsible for the sudden decrease of the accumulated Ekman heat advection. The Ekman heat divergence, equivalent Ekman heat flux, and storm duration are at the higher percentile ranks of the year 2003-2018. Particularly, the 2005 period has the longest storm duration. The 2010 period has the largest storm-associated total

Ekman heat divergence, while the 2013 period has the strongest rate of total heat loss due to the Ekman current divergence. The storm effects on Ekman heat divergence accumulate over time, and are sufficient to separate the extreme years of strong EDW formation from the remaining years. During the EDW formation of these years, the total storm-associated Ekman heat divergence, the total storm duration, and the rate of heat loss due to Ekman divergence are at the lower percentile rank.

Appendix B

Buoyancy Budget

B.1 A hybrid buoyancy model

We investigated the 0-year lagged response of early-spring ventilated EDW volume to the winter atmospheric conditions through the winter accumulated surface air-sea heat loss. In comparison, other physical processes have as strong an impact on the ventilated EDW volume, in the EDW formation region. Horizontal heat advection-diffusion associated with the Gulf stream system (Dong and Kelly, 2004) and preconditioning are estimated on their contributions to the winter surface upper ocean heat content change.

B.1.1 Results

Figure B-1 and Figure B-2 correlate the ventilated EDW volume in March to: the upper ocean buoyancy content anomaly change, surface heat loss, and preconditioning.

In Figure B-1, the average of winter buoyancy content anomaly change over the EDW formation region is about $-4.0 \times 10^{12}\,\mathrm{m^4\,s^{-2}}$. The average winter surface buoyancy loss due to air-sea heat flux is $-6.0 \times 10^{12}\,\mathrm{m^4\,s^{-2}}$, this being the most dominant factor contributing to the upper water heat content change, in line with Dong and Kelly (2004). 2010 was a particularly extreme year, in that it had a large EDW formation of $6 \times 10^{14}\mathrm{m^3}$ (also noted by Billheimer and Talley, 2013) and a strong surface buoyancy loss of about $-8.5 \times 10^{-12}\,\mathrm{m^4\,s^{-2}}$. In 2012, known as an extreme year of weak EDW formation (Billheimer and Talley, 2013), the surface buoyancy loss due to Q_{net} is $-6.2 \times 10^{12}\,\mathrm{m^4\,s^{-2}}$, and the ventilated EDW volume is only $1.0 \times 10^{14}\,\mathrm{m^3}$.

In Figure B-2, the average of $\mathrm{BCA^*_{Sep}}$ is about $1.2 \times 10^{10}\,\mathrm{m^3\,s^{-2}}$. For a similar winter surface buoyancy loss, one would expect more EDW volume if $\mathrm{BCA^*_{Sep}}$ is small. In this case, the preconditioning is more favorable to EDW formation. In 2010, the $\mathrm{BCA^*_{Sep}}$ is the lowest since 1979, about $0.7 \times 10^{10}\,\mathrm{m^3\,s^{-2}}$, and that year corresponded with a large ventilated EDW volume. In 2004, the $\mathrm{BCA^*_{Sep}}$ is closer to the average, about $1.1 \times 10^{10}\,\mathrm{m^3\,s^{-2}}$; However even with strong winter heat loss in

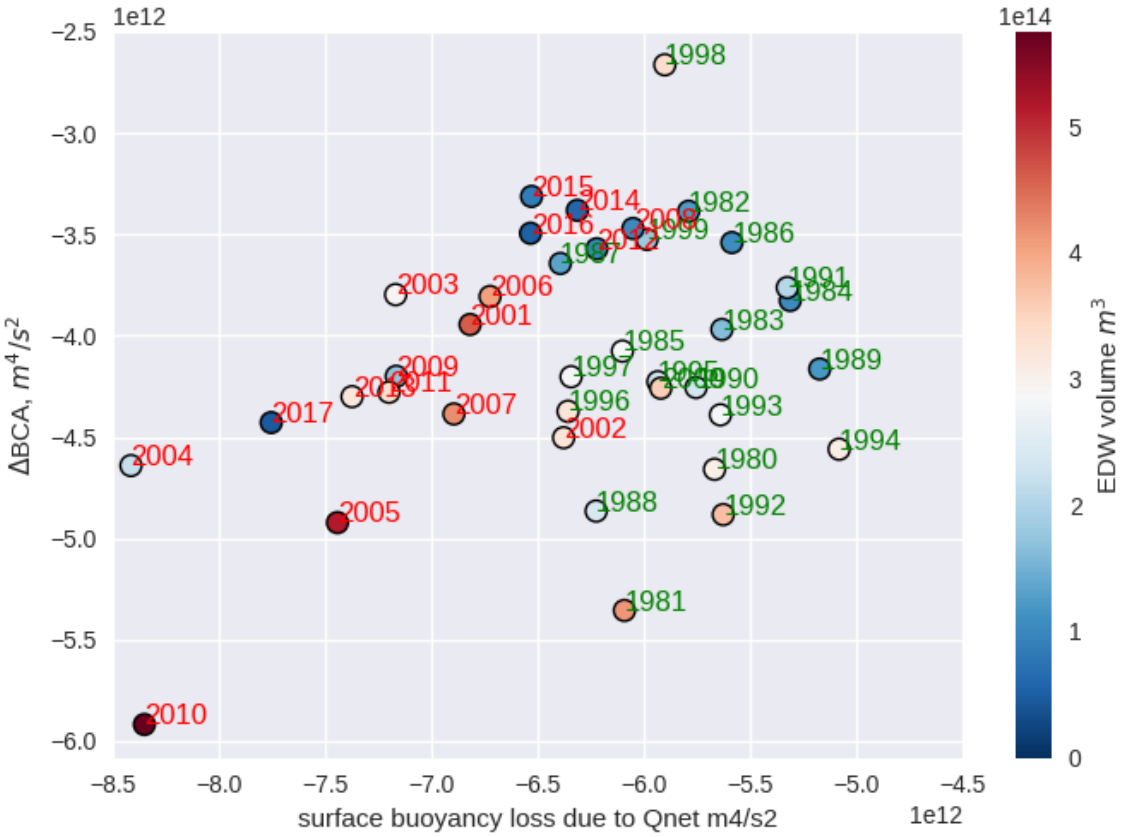

Figure B-1: The winter time surface heat loss and winter buoyancy content anomaly change from 1979-2017, with ventilated mode water volumes in color. The recent years since the year 2000, the starting of the argo era, are marked in red, and the years before 2000 argo era marked in green. The buoyancy content and the EDW ventilated volume is calculated using the ISAS dataset. The air-sea surface buoyancy loss is calculated using the NCEP dataset.

Figure B-2: The interannual variability of the buoyancy content anomaly scaled by the mixed layer depth (in the unit of $\mathrm{m}^3\,\mathrm{s}^{-2}$) as preconditioning at the beginning of EDW formation season (September). Horizotal axis is the surface buoyancy loss due to Q_{net} ($\mathrm{m}^4\,\mathrm{s}^{-2}$), and the color scale indicates the ventilated EDW volume ($1 \times 10^{14}\,\mathrm{m}^3$).

Figure B-3: The interannual variability of the difference between BCA reduction and surface buoyancy loss in winters ($m^4\,s^{-2}$). The horizontal axis and color scales are the same as the previous plot.

the surface, this year showed a ventilated EDW smaller ($2.2 \times 10^{14}\,\mathrm{m}^3$) than 2010. In 2012, the $\mathrm{BCA}^*_{\mathrm{Sep}}$ is higher than average, about $1.45 \times 10^{10}\,\mathrm{m}^3\,\mathrm{s}^{-2}$, and the winter surface buoyancy loss Q_{net} is average ($-6.2 \times 10^{12}\,\mathrm{m}^4\,\mathrm{s}^{-2}$), thus the ventilated EDW volume is small ($1.0 \times 10^{14}\,\mathrm{m}^3$).

Note that in 2014, 2015, and 2016, the water column has a quite unfavorable preconditioning ($1.7 - 1.9 \times 10^{10}\,\mathrm{m}^3\,\mathrm{s}^{-2}$), which reasonably corresponds with weak ventilated EDW volume for about similar surface buoyancy loss.

In Figure B-3, we inferred the horizontal buoyancy advection-diffusion convergence according to Equation 2.25, by subtracting the surface buoyancy loss from the winter buoyancy heat content anomaly reduction. Both 2004 and 2010 have the same winter surface buoyancy loss, and 2004 has larger horizontal warm advection/diffusion convergence ($3.7 \times 10^{12}\,\mathrm{m}^4\,\mathrm{s}^{-2}$) larger than that of 2010 ($2.5 \times 10^{12}\,\mathrm{m}^4\,\mathrm{s}^{-2}$). This leads to a smaller ventilated EDW volume in 2004 than 2010.

Calculated using the NCEP dataset, the surface buoyancy loss due to winter air-sea flux in the 2000s is generally larger than before the 2000s. This may be due to the improvement of the NCEP data quality around this time. We emphasize more on the winter events during the 2000s, where the ocean data has more samplings as a result of Argo installation.

B.2 Fixed-domain $\mathrm{BCA}_{\mathrm{Sep}}$

B.2.1 Role of preconditioning for extreme years

Figure B-4 shows the role of preconditioning in the EDW ventilation of each year in the period of 2003-2018. The 2003-2018 September BCA has an average of $2.42\,\mathrm{m}^2\,\mathrm{s}^{-2}$. The strong EDW formation years 2005, 2010 and 2013 have similar September BCAs, that are close to the average. The Ekman heat advections in 2005, 2010, and 2013 are -4.2 ZettaJ, -4.7 ZettaJ, and -4.0 ZettaJ, the top three strongest heat sink due to Ekman heat divergence among the years 2003-2018.

Among the weak EDW formation years, the year 2014 has about an average Septebmer BCA of $2.37\,\mathrm{m}^2\,\mathrm{s}^{-2}$. Meanwhile this year experienced a positive Ekman heat advection of 3.3 ZettaJ, the strongest Ekman-heat-advection associated warming among the years 2003-2018. Compared with 2014, the year 2015 experienced less of a warming due to Ekman heat convergence of 1.7 ZettaJ (only 50.0% of that in 2014). However, the September BCA in 2015 of $2.55\,\mathrm{m}^2\,\mathrm{s}^{-2}$ is larger than that in 2014. This large September BCA in 2015 is responsible for a less favorable preconditioning than 2014 in terms of the EDW ventilation in the early spring. The year 2016 has an Ekman heat convergence of 0.5 ZettaJ, even smaller than that in 2015, and only 29.4%

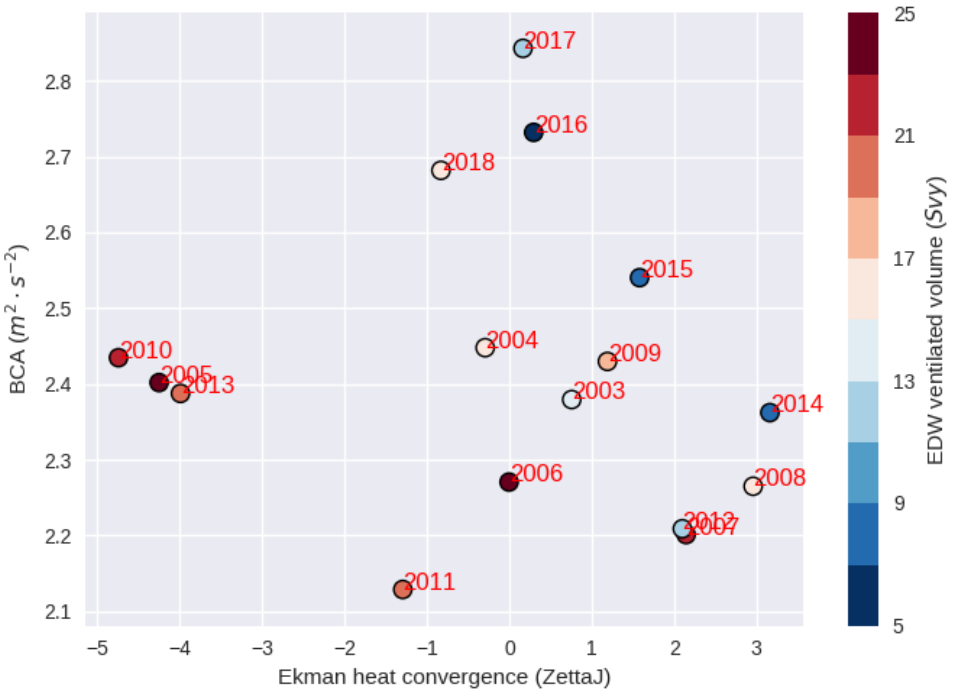

Figure B-4: The preconditioning at the beginning of EDW formation period using the buoyancy content anomaly (BCA) in September, spatially averaged over the the domain of study, in the unit of $\mathrm{m}^2\,\mathrm{s}^{-2}$. The colorbar shows the EDW ventilated volume in the early spring of each year, in the unit of Svy. The horizontal axis indicates the interannual accumulated Ekman heat transport in the period of September-March, in the domain of study. The preconditioning and Ekman heat transport convergence are calculated with the temperature and in-situ density from ISAS data. The near-surface momentum flux is from NCEP reanalysis data.

of that in 2014. Meanwhile, the September BCA of 2016 is about $2.73\,\mathrm{m^2\,s^{-2}}$, one of the largest among these years. It is larger than that in 2015 by 7.5%, and larger than that in 2014 by 15.2%. This extremely unfavorable preconditioning in 2016 becomes a factor more dominant than the Ekman heat advection, responsible for its poor EDW ventilation.

The year 2007 has an Ekman heat advection of 1.9 ZettaJ comparable to that of the year 2015. However, its September BCA is about $2.20\,\mathrm{m^2\,s^{-2}}$, one of the lowest of 2003-2018. This favorable preconditioning BCA in 2007 is responsible for its high EDW ventilation, comparable to 2005 and 2010 (Figure 4-3). The year 2007 and 2012 indeed have very similar Ekman heat convergence and September BCA, but the EDW ventilated volume in 2007 is close to 21.5 Svy, almost twice as much as that of the year 2012. The larger interannual accumulated air-sea heat flux in 2012 than that in 2007 can explain their EDW volume difference.

B.3 Discussion

We investigated preconditioning from both fixed-domain $\mathrm{BCA_{Sep}}$ and $\mathrm{BCA^*_{Sep}}$. In addition, we examined surface heat flux, and their relation with winter BCA change.

B.3.1 Seasonal cycle

Our estimate of the seasonal cycle of the EDW buoyancy budget terms is shown Figure B-5. In summer, the air-sea buoyancy flux (blue curve) is positive as ocean gains heat from the atmosphere: hence BCA peaks in late fall. In winter, the air-sea buoyancy flux is negative as ocean loses heat to the atmosphere: hence BCA is the smallest of the year in the early spring. Correspondingly, in the summer and early fall, the EDW is underneath the seasonal pycnocline and starts to ventilate (black curve) in the early winter (December) as the surface water buoyancy reduces up to the point of total erosion of the seasonal pycnocline. The ventilated EDW volume (black curve) reaches maximum in the early spring (March). Then, as the surface heat loss reduces and switches to surface heat gain from the atmosphere in April, a seasonal pycnocline is formed on top of the EDW, ceasing its ventilation window. This is in accord with air-sea flux impact on EDW at the seasonal time scale analysed from Maze et al. (2009), Maze and Marshall (2011) and Forget et al. (2011).

We also found that on the seasonal cycle, the winter surface buoyancy loss is only responsible for part of the buoyancy content anomaly change in winter. We computed the winter BCA change as if only associated with surface buoyancy loss (green curve in the grey shaded region in Figure B-5) and found it much larger than

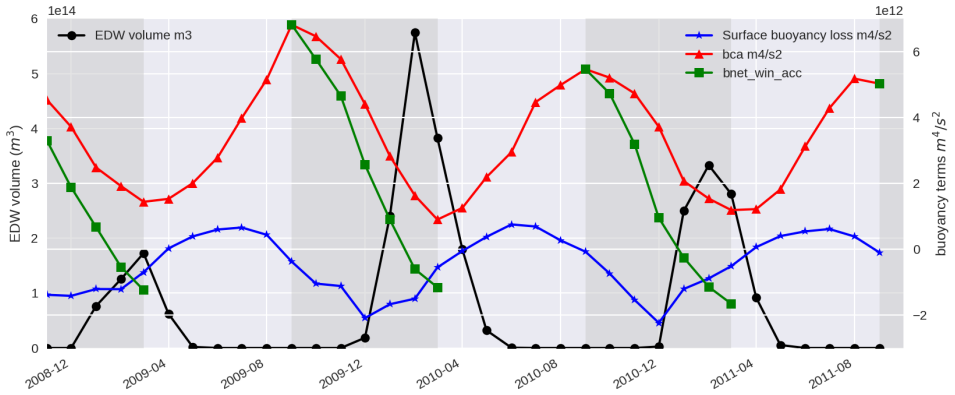

Figure B-5: The ventilated EDW volume (black line with circles), the buoyancy content anomaly (red line with triangles), the air-sea buoyancy flux (blue line with stars, downward positive) in the period of December 2008-October 2011. The green line with squares indicates the BCA in the late fall and winter, as if only impacted by surface heat loss. The winter period is shaded in grey.

the actual winter buoyancy loss ΔBCA (red curve). According to Equation (2.25), a buoyancy source associated with the convergence of horizontal advection/diffusion accumulated in winter must have compensated this buoyancy difference. Dong and Kelly (2004) found the surface heat flux the primary term and the horizontal heat advection/diffusion associated with the Gulf Stream strength the secondary term to have an impact on the upper 800m water column in the EDW ventilation region. However, we found that the net surface heat loss from Dong and Kelly (2004) is $50\,\mathrm{W\,m^{-2}}$ larger in amplitude compared to our estimate based on the NCEP dataset. We cross-validated our estimate with another heat flux product (OAFLUX, Yu and Weller 2007) and obtained similar estimates, also in line with Marshall et al. (2009, fig. 1). This may be the case that Dong and Kelly (2004) used poorly constrained air-sea heat flux from the 90s and obtained results not corroborated with more recent and modern heat flux datasets.

B.3.2 Interannual variability

Joyce et al. (2000) suggested that the NAO index is correlated with the Subtropical Mode Water (STMW) PV at Burmuda station, a good indicator of EDW formation when fewer ocean datasets were available in the late 90s. As an NAO- extreme year (NAO index of -2.0, the largest since 1987, Yashayaev 2007), 2010 corresponds with the largest amount of surface heat loss and the largest ventilated EDW volume since 1979 (Figure B-1). To the opposite, 2012 and 2014-2016 are extreme NAO+ years

(largest NAO+ values since the mid 90s, Yashayaev 2007). These years correspond with weak surface heat loss, and they correspondingly ventilated less than $1.0\times10^{14}\mathrm{m}^3$ EDW, one of the lowest ventilated EDW volumes from 1979-2017.

Preconditioning plays an important role in EDW formation. 2010 ventilation had the least buoyant preconditioning of all 1979-2017, favorable to the largest ventilalted EDW volume (Figure B-2). The 2004 event, with less favorable preconditioning than 2010, had more buoyant seasonal mixed layer, causing more difficulty for the EDW to ventilate to the surface. The year 2004 corresponds with the same amount of winter surface heat loss as 2010. Even though both 2004 and 2010 experienced the largest amount of heat loss, less EDW was ventilated in 2004 than 2010. In 2012, preconditioning in the late fall is even less favorable for the ventilation of EDW than 2004, which contributes to even weaker EDW ventilation. 2014-2016 have the least favorable preconditionings for EDW ventilation of since 1979, which also contribute to their weak EDW formations.

Note that in 2010, the winter ΔBCA is $-6.0\times10^{12}\mathrm{m}^4\,\mathrm{s}^{-2}$ (Figure 2-15) over the EDW formation area (the 75 m yellow dashed contour in Figure 2-1). The surface averaged ΔBCA in 2010 is about $-2.0\,\mathrm{m}^2\,\mathrm{s}^{-2}$. Similarly in 2012, the winter ΔBCA is $-3.5\times10^{12}\,\mathrm{m}^4\,\mathrm{s}^{-2}$, while the surface averaged ΔBCA in 2012 is about $-1.17\,\mathrm{m}^2\,\mathrm{s}^{-2}$. Both winter surface averaged buoyancy content anomaly changes are in line with Billheimer and Talley (2013). However our analysis shows preconditioning of 2010 as an aiding factor to the EDW formation compared with 2012, different from Billheimer and Talley (2013). This difference has to do with the fact that we used fixed depth as the integration domain to calculate BCA. Billheimer and Talley (2013) used as the bottom of the integration domain the depth of $\sigma = 26.7$ isopycnal, in which the heaving of the isopycnal surfaces and horizontal entrainment needs to be taken into account.

In winter, the magnitude of the convergence of horizontal buoyancy advection-diffusion in the EDW formation region is on average $2.5\times10^{12}\mathrm{m}^4\,\mathrm{s}^{-2}$ (as seen in Figure B-3. Also see in Figure B-5 the difference between green and red curves in March). This makes up 1/3 of winter surface buoyancy loss and about 1/2 of upper-ocean ΔBCA, thus it is a dominant term as described in Dong and Kelly (2004). Moreover, we observed a clear trend in Figure B-3, that over the EDW formation region, more surface heat loss corresponds with a larger convergence of horizontal buoyancy advection-diffusion. This verifies Dong and Kelly (2004) in that the heat advected by the Gulf Stream, which tends to increase the upper ocean heat content in the EDW formation region, positively correlated to flux to the atmosphere. Further, we compared those years of the same surface heat loss but with different

horizontal buoyancy advection-diffusion convergence. The years 2012 and 2014-2016 have smaller ventilated EDW than 1996 and 1997. This can be explained by the fact that the years 2012 and 2014-2016 have larger convergence of horizontal advection-diffusion than 1996 and 1997 (Figure B-3). 2004 surface buoyancy loss is compensated by a large horizontal convergence of buoyancy advection-diffusion associated with the Gulf Stream, in comparison with 2010. This explains the reason that although both years have the the largest amount surface heat flux ($-8.4 \times 10^{12} \mathrm{m}^4\,\mathrm{s}^{-2}$) of the years ranging from 1979-2017, 2004 ventilated only half the volume of EDW as that of 2010.

B.3.3 $\mathrm{BCA}^*_{\mathrm{Sep}}$ v.s. fixed-domain $\mathrm{BCA}_{\mathrm{Sep}}$

Here we discuss the two approaches to estimate the September preconditioning: (1) the $\mathrm{BCA}^*_{\mathrm{Sep}}$ and (2) the fixed-domain $\mathrm{BCA}_{\mathrm{Sep}}$.

We use 2007 and 2012 as an example. The $\mathrm{BCA}^*_{\mathrm{Sep}}$ of 2007 is smaller than that of 2012. Even though the fixed domain $\mathrm{BCA}_{\mathrm{Sep}}$ of 2007 is about the same as 2012, The preconditioning of the wintertime of 2007 is more favorable than 2012. We inferred that the $\mathrm{BCA}_{\mathrm{Sep}}$ distribution, associated with the vertical density profile, is more favorable to deep convection in 2007 than in 2012. Piron et al. (2017) utilized the similar analysis to diagnose the anomalously deep wintertime ventilation in the Irminger Sea in 2014-2015. They comapared the 2014-2015 deep convection with 2013-2014 deep convection. They showed a favorable vertical buoyancy distribution as a contributer to a favorable preconditioning. They also showed that the favorable vertical buoyancy distribution in September 2014 in the Irminger Sea, compared to September 2013, can be responsible for a stronger convection deeper by another 800m, even with the same amount of surface heat loss.

Among 2005, 2010, and 2013, the fixed domain $\mathrm{BCA}_{\mathrm{Sep}}$ is about the same. The $\mathrm{BCA}^*_{\mathrm{Sep}}$ in 2010 is the most negative and that in 2013 is the most positive among all strong EDW formation extreme years. It is fair to infer that the Fall2010[1] density vertical profile is the most favorable to a deep convection among the strong EDW formation years. Similarly, the Fall2013 vertical density profile is the least favorable to a deep convection among the strong EDW formation years.

[1] Actually referring to the fall of 2009. It is the fall of the wintertime of 2009-2010.

Appendix C

Effective Resolution

C.1 Signal smoothing: Gaussian kernel optimization

The altimetry dataset and ISAS15-ARGO dataset have different effective resolutions. The surface geostrophic velocities are calculated using two approaches: firstly from the altimetry data using geostrophy, and secondly from the density fields of ISAS15-ARGO dataset using the thermal wind relation with a reference level set at 2000m depth. Two velocity fields are showing a large difference in decaying slopes for a common chosen time and longitude (for example, the red and purple curves in Figure C-1) in the meridional autocorrelation diagrams. A larger slope in the autocorrelation curve (for example, the altimetry dataset in red curve in Figure C-1) indicates a smaller effective resolution, giving a less "blurred" point of view centered on each grid points.

To adjust the effective resolutions in altimetry dataset towards that of ISAS15-ARGO, a pool of grid points and its neighboring grid points within a distances of 3σ are selected, where σ indicates the standard deviation of a Gaussian kernel. Then a Gaussian weighted mean is calculated with σ for the Gaussian kernels at each grid point.

The meridional autocorrelations, which use smoothed altimetry data, are calculated with different σ values (for example, 100, 150, and 200 km) for a few selected time steps and longitudes. We compared the curves of the smoothed altimetry data to that of the ISAS15-ARGO, in order to find the appropriate σ, with which both datasets would have similar decaying slopes of autocorrelation curves. This would occur particularly with a small shift in latitude (for example less than 2 degrees shift).

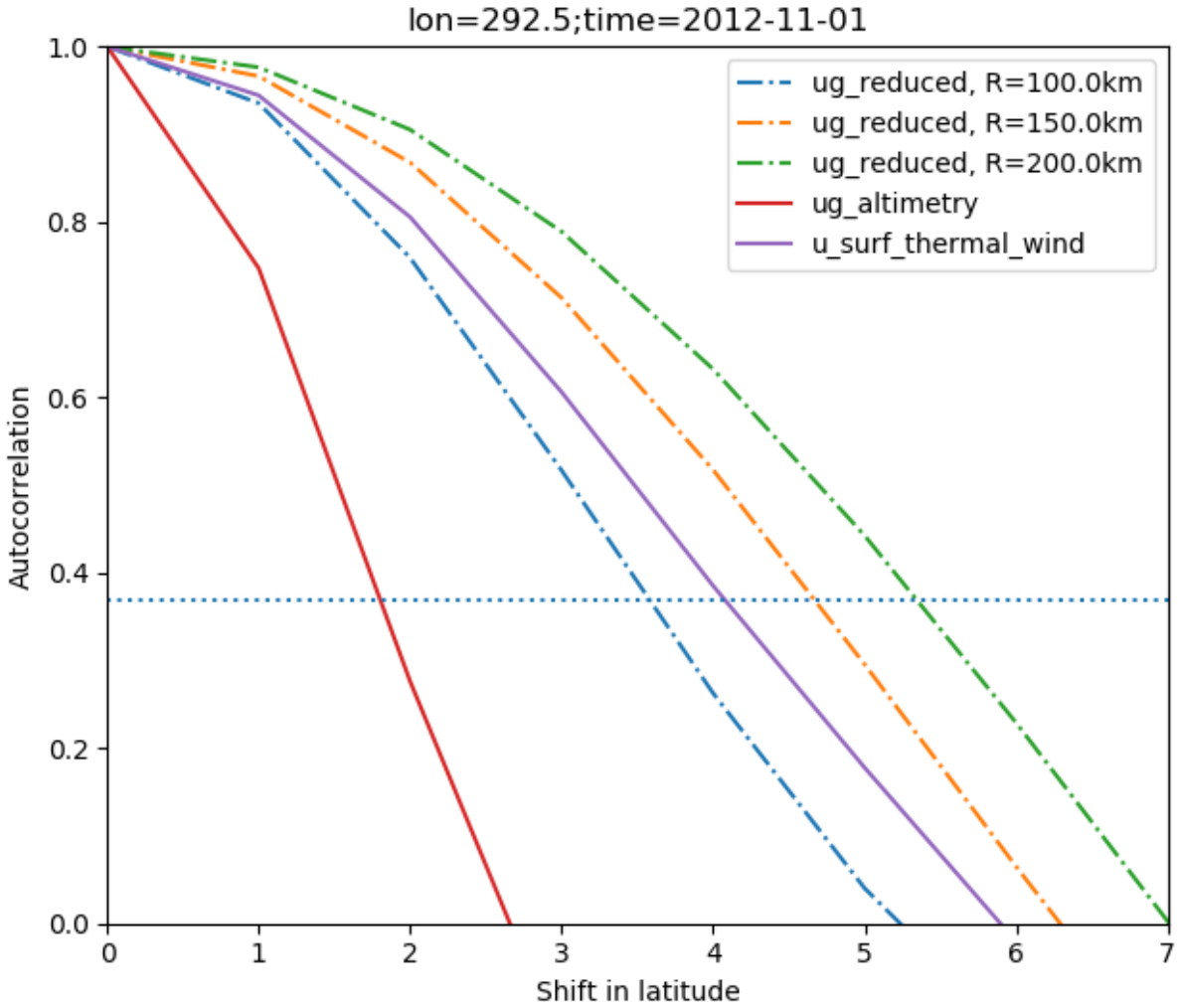

Figure C-1: Meridional autocorrelations of surface velocities by the thermal wind relation using density field in ISAS15-ARGO dataset (solid line in purple), surface geostrophic velocity calculated from altimetry data (solid line in red), and surface geostrophic velocities calculated from smoothed altimetry data using different standard deviations in the Gaussian kernels used for smoothing (dashed solid lines). Horizontal axis is the shift in degrees along latitude. The dashed line is the 1/e value.

Appendix D

Heat budget climatology and seasonal cycle

D.1 Climatology

Table D.1 shows the climatological means of the air-sea heat flux, geostrophic advection, Ekman advection, heat diffusion due to turbulence mixing, and the net change rate of ocean heat content. In the domain of study, the climatological mean of the total heat source due to geostrophic advection and Ekman advection, converted to the unit of equivalent heat flux at the surface, is $79.9\,\mathrm{W\,m^{-2}}$. The geostrophic advection mean is $45.8\,\mathrm{W\,m^{-2}}$, and the Ekman advection mean is $34.1\,\mathrm{W\,m^{-2}}$. The largest heat sink is air-sea heat flux (Q_{net}) with a climatological mean of $-78.5\,\mathrm{W\,m^{-2}}$, compensating for 98% of the total heat source. The climatological mean of the heat storage rate measured by OHC is $2.8\,\mathrm{W\,m^{-2}}$, only 3.5% of the total heat source, while the diffusion is estimated to be $-6.06\,\mathrm{W\,m^{-2}}$, compensating for 7.6% of the total heat source.

At the entrance of the Gulf Stream, the geostrophic advection of $399.0\,\mathrm{W\,m^{-2}}$ enters from the western boundary, 72.9% of which exits the domain from the northern boundary, about $-290.7\,\mathrm{W\,m^{-2}}$. In comparison, the geostrophic advection at the southern and eastern boundaries are relatively insignificant. In total, 11.5% of the heat advected from the western boundary serves as a net heat source in the domain of study, about $45.8\,\mathrm{W\,m^{-2}}$.

The Ekman temperature transport entering at the northern boundary is $35.5\,\mathrm{W\,m^{-2}}$, the strongest of those at all boundaries. In total, 96% of this temperature transport is stored in the domain of study, about $34.1\,\mathrm{W\,m^{-2}}$.

		mean ($\mathrm{W\,m^{-2}}$)	standard error ($\mathrm{W\,m^{-2}}$)	relative error (%)
Air-sea heat flux		-78.5	15.7	20.0
Geostrophic advection	Net	45.8	7.1	15.5
	North	-290.7	13.2	4.5
	South	106.0	18.7	17.6

	East	-140.4	6.8	4.8
	West	399.0	18.0	4.5
	Bottom	-28.1	1.5	5.3
Ekman advection	Net	34.1	3.0	8.8
	North	35.5	2.3	6.5
	South	3.3	2.5	75.8
	East	-4.7	0.7	14.9
	West	0.0	0.4	-
Diffusion		-6.1	0.5	8.2
Ocean heat content net rate of change		2.8	17.9	639.3

Table D.1: 2003 – 2018 heat budget climatology and standard errors over the domain of study, in the unit of $\mathrm{W\,m^{-2}}$. The heat advections are all converted to the equivalent heat flux averaged over the surface area of the domain of study. The geostrophic advection and Ekman advection include the temperature transports at each boundaries. Negative sign indicates heat going out of the domain of study.

D.2 Seasonal cycle

In a typical seasonal cycle, the ocean heat content rate of change $\partial_t \mathrm{OHC}$ has a standard deviation of $156.4\,\mathrm{W\,m^{-2}}$ (the dashed red line with dots in Figure D-1). $\partial_t \mathrm{OHC}$ becomes positive in mid-March, and reaches to the seasonal maximum in mid-May. This maximum stays flat from mid-May to early July, about $200\,\mathrm{W\,m^{-2}}$. In mid-September, $\partial_t \mathrm{OHC}$ becomes negative, and reaches to the seasonal minimum in December, about $-200\,\mathrm{W\,m^{-2}}$. The seasonal variability of air-sea heat flux Q_{net} resembles that of $\partial_t \mathrm{OHC}$ (the solid blue line in Figure D-1), with a standard deviation of $132.6\,\mathrm{W\,m^{-2}}$, contributing 84.8% of that of $\partial_t \mathrm{OHC}$. The air-sea heat flux becomes positive in mid-March, and reaches the seasonal maximum in mid-June, about $200\,\mathrm{W\,m^{-2}}$. The air-sea heat flux becomes negative in mid-September, and reaches the seasonal minimum in mid-December, about $-190\,\mathrm{W\,m^{-2}}$. In comparison, the seasonal variabilities of Ekman heat convergence and geostrophic heat convergence are much less influential to that of $\partial_t \mathrm{OHC}$, with the standard deviations of $17.2\,\mathrm{W\,m^{-2}}$ and $33.0\,\mathrm{W\,m^{-2}}$, contributing 11.0% and 21.1% to that of $\partial_t \mathrm{OHC}$, respectively.

The ocean heat content peaks in early September (the solid red curve in Figure D-1), after $\partial_t \mathrm{OHC}$ is positive since mid-March and turns negative in early September. The OHC reaches its minimum towards the end of March, as $\partial_t \mathrm{OHC}$ turns positive. The typical seasonal cycle of OHC has a standard deviation of 4.3 ZettaJ, with a total

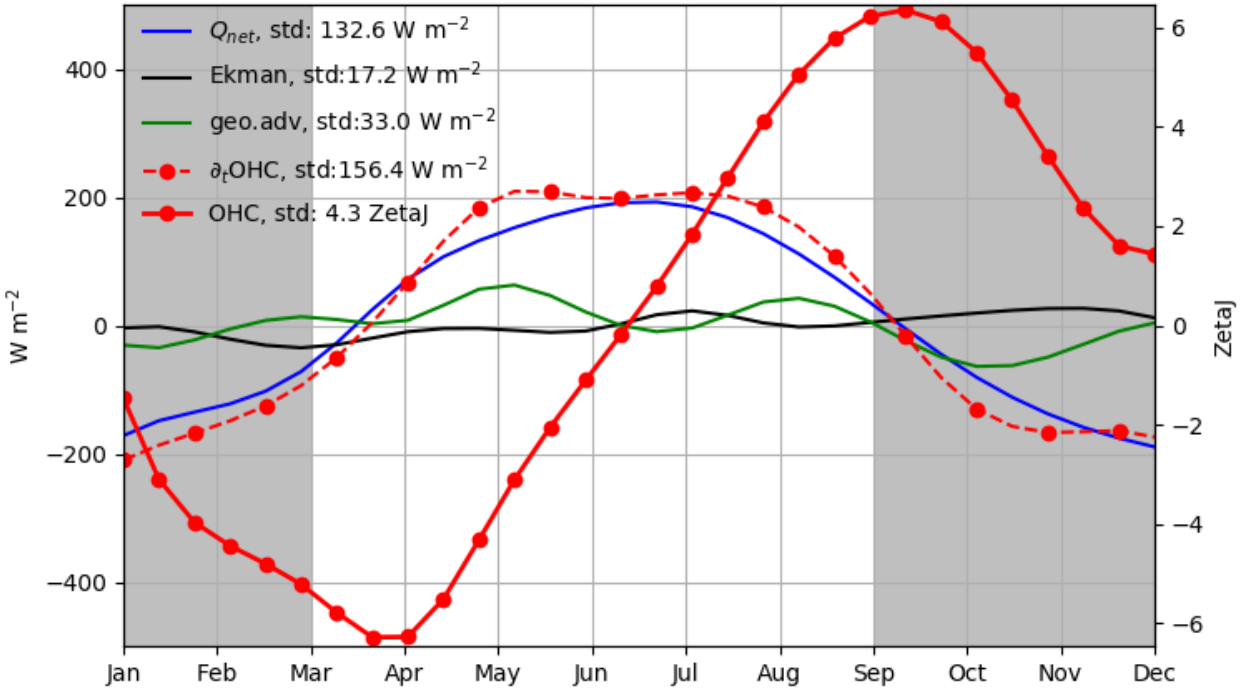

Figure D-1: The typycal seasonal cycles of surface heat loss (solid blue line), of the Ekman heat advection (solid black line), of the geostrophic heat advection (solid greenline), and of the ocean heat content rate of change (dashed red line with dots) in the unit of W m^{-2}. The typical seasonal cycle of the ocean heat content is represented in solid red line, in the unit of ZettaJ. The seasonal cycles are calculated in the domain of study with a surface area of $S = 4.918 \times 10^{12}$ m^2. 1 ZettaJ $= 1 \times 10^{21}$ J.

span of about 12 ZettaJ.

Appendix E

Heat budget error estimates

Here we provided a brief discription on how we estimated the heat budget errors for OHC as well as the geostrophic heat advection, the Ekman heat advection, and air-sea surface heat flux.

E.1 2002-2019 time series

To calculate the OHC, we employed ocean datasets of ISAS, EN4, IPRC, and Scripps (the red line in Figure E-1a). The error bar is calculated using unbiased estimator of the variance of infinite population, written as the following:

$$S(t) = \sqrt{\frac{\sum[X(t) - \bar{X}(t)]^2}{N(t) - 1}}$$

where S^2 is the unbiased estimator of the variance of infinite population. $X(t)$ indicates the OHC time series. $\bar{X}$ indicates the sample mean at each time step calculated from all datasets. N indicates the number of datasets at each time step. The average of the OHC error bar is 15.4 ZettaJ. The standard deviation of the OHC mean time series is 11.1 ZettaJ. The OHC error has an average value 1.4 times as large as the standard deviation of the mean OHC time series.

Note that the datasets are not independant from each other, thus the number of independent sample should be smaller than $N(t) - 1$. Using $S(t)$ as the error bar calculation would be subject to an underestimate.

Similarly, to calculate the geostrophic heat advection, we employed the aforementioned ocean datasets as well as the atmosphere datasets: ERA and NCEP, providing 8 datasets in combination (the green line in Figure E-1b). The average of the geostrophic heat advection error bar is 0.4 PetaWatt, while the standard deviation of the geostrophic heat advection mean time series is 0.6 PetaWatt. The average of the geostrophic heat advection error consists of 67% of the standard deviation of its mean time series.

To calculate the Ekman heat advection, we employed same datasets as the geostrophic heat advection (the black line in Figure E-1c). The average of the Ekman heat advection error bar is 0.03 PetaWatt, while the standard deviation of the Ekman heat advection mean time series is 0.2 PetaWatt. The average of the Ekman heat advection error consists of 15% of the standard deviation of its mean time series.

To calculate the air-sea surface heat flux, we employed the atmosphere datasets: ERA and NCEP (the blue line in Figure E-1d). The average of the air-sea heat flux error bar is 0.08 PetaWatt, while the standard deviation of the air-sea heat flux mean time series is 0.7 PetaWatt. The average of the air-sea heat flux error consists of 11% of the standard deviation of its mean time series.

E.2 Interannual variabilities

We estimated the errors in the 2013-2017 interannual variabilities of OHC, geostrophic heat advection, Ekman heat advection, and air-sea surface heat flux.

The averaged error of the OHC interannual variability is about 0.6 ZettaJ. The OHC interannual variability has a standard deviation of 2.0 ZettaJ (the red line in Figure E-2a). In the interannual time scale, the OHC averaged error consists of 30% of the standard deviation of its mean time series.

The averaged error of the geostrophic heat advection interannual variability is about 0.07 PetaWatt. The geostrophic heat advection interannual variability has a standard deviation of 0.2 ZettaJ (the green line in Figure E-2b). In the interannual time scale, the geostrophic heat advection averaged error consists of 35% of the standard deviation of its mean time series.

The averaged error of the Ekman heat advection interannual variability is about 0.004 PetaWatt. The Ekman heat advection interannual variability has a standard deviation of 0.08 PetaWatt (the black line in Figure E-2c). In the interannual time scale, the Ekman heat advection averaged error consists of 5% of the standard deviation of its mean time series.

The averaged error of the air-sea heat flux interannual variability is about 0.07 PetaWatt. The air-sea heat flux interannual variability has a standard deviation of 0.05 PetaWatt (the blue line in Figure E-2d). In the interannual time scale, the air-sea heat flux averaged error consists of 14% of the standard deviation of its mean time series.

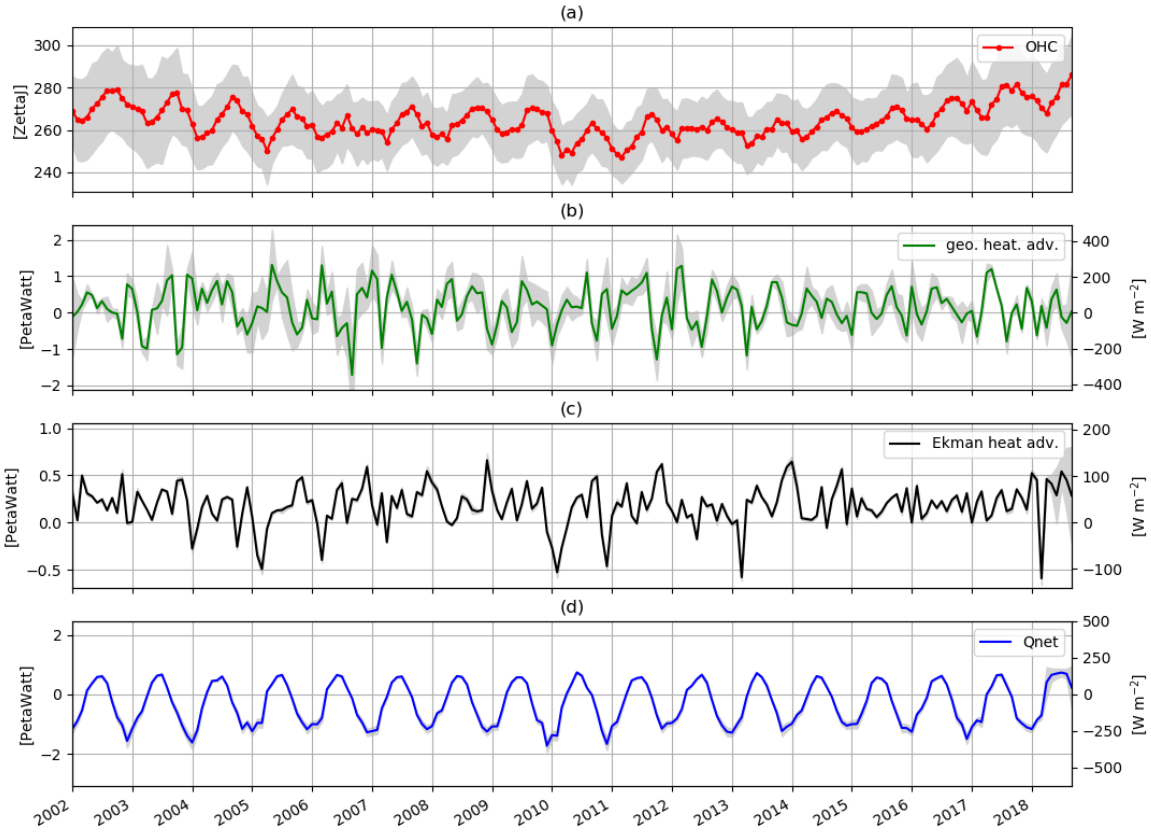

Figure E-1: The 2002-2019 OHC time series and its major contributing factors. (a) The OHC is represented by the red line with dots. The unit is in ZettaJ. (b) The geostrophic heat advection is represented by the green line. (c) The Ekman heat advection is represented by the black line. (d) The air-sea surface heat flux is represented by the blue line. (b), (c), and (d) are in the unit of PetaWatt and $\mathrm{W\,m^{-2}}$. The horizontal surface area of the domain of study is $4.918 \times 10^{12}\,\mathrm{m^2}$. Shaded in light grey are the unbiased standard deviation among all data sets, namely ISAS, EN4, IPRC, and Scripps datasets concerning the ocean, and ERA and NCEP concerning the atmosphere.

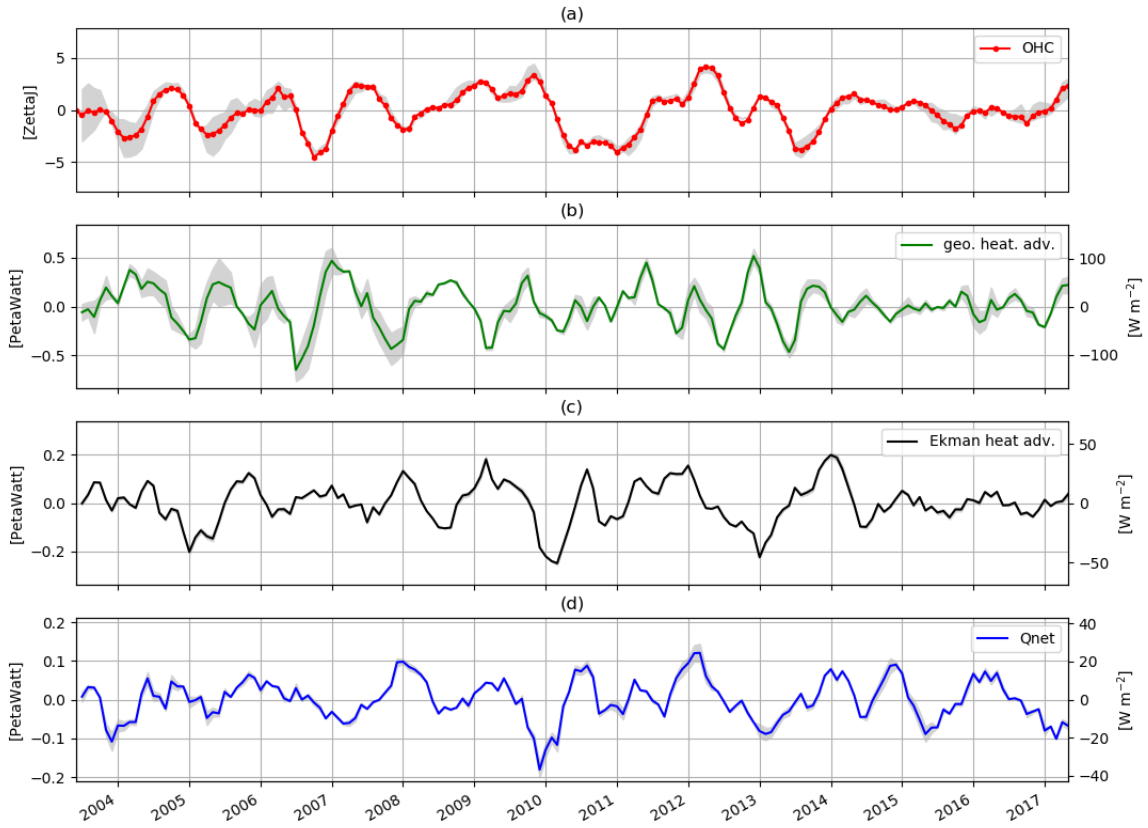

Figure E-2: The 2003-2017 interannual variability of OHC and its major contributing factors. Similar to Figure E-1.

Bibliography

APDRC. International pacific research center. *Asia-Pacific Data-Research Center*, June 2009. URL `http://apdrc.soest.hawaii.edu/projects/Argo/data/Documentation/gridded-var.pdf`.

Nicolas Barrier, Anne-Marie Treguier, Christophe Cassou, and Julie Deshayes. Impact of the winter north-atlantic weather regimes on subtropical sea-surface height variability. *Climate dynamics*, 41(5-6):1159–1171, 2013.

Nicolas Barrier, Anne A Petrenko, and Yann Ourmieres. Strong intrusions of the northern mediterranean current on the eastern gulf of lion: insights from in-situ observations and high resolution numerical modelling. *Ocean Dynamics*, 66(3): 313–327, 2016.

S Billheimer and LD Talley. Extraordinarily weak eighteen degree water production concurs with strongly positive north atlantic oscillation in late winter 2014/15 [in "state of the climate in 2015"]. *Bull. Amer. Meteor. Soc*, 97(8):S78–S79, 2016a.

Sam Billheimer and Lynne D Talley. Near cessation of eighteen degree water renewal in the western north atlantic in the warm winter of 2011–2012. *Journal of Geophysical Research: Oceans*, 118(12):6838–6853, 2013.

Sam Billheimer and Lynne D Talley. Annual cycle and destruction of e ighteen d egree w ater. *Journal of Geophysical Research: Oceans*, 121(9):6604–6617, 2016b.

Eric S Blake, Todd B Kimberlain, Robert J Berg, John P Cangialosi, and John L Beven Ii. Tropical cyclone report: Hurricane sandy. *National Hurricane Center*, 12:1–10, 2013.

Harry L Bryden, William E Johns, Brian A King, Gerard McCarthy, Elaine L McDonagh, Ben I Moat, and David A Smeed. Reduction in ocean heat transport at 26°N since 2008 cools the eastern subpolar gyre of the north atlantic ocean. *Journal of Climate*, (2019), 2019.

HL Bryden, BA King, GD McCarthy, and EL McDonagh. Impact of a 30% reduction in atlantic meridional overturning during 2009-2010. *Ocean Science*, 10(4):683–691, 2014.

L Caesar, S Rahmstorf, and G Feulner. On the relationship between atlantic meridional overturning circulation slowdown and global surface warming. *Environmental Research Letters*, 15(2):024003, 2020.

Jörn Callies and Raffaele Ferrari. Baroclinic instability in the presence of convection. *Journal of Physical Oceanography*, 48(1):45–60, 2018.

Tonia Astrid Capuano, Sabrina Speich, Xavier Carton, and Bruno Blanke. Mesoscale and submesoscale processes in the southeast atlantic and their impact on the regional thermohaline structure. *Journal of Geophysical Research: Oceans*, 123(3): 1937–1961, 2018.

Christophe Cassou. Intraseasonal interaction between the madden-julian oscillation and the north atlantic oscillation. *Nature*, 455(7212):523, 2008.

Christophe Cassou, Laurent Terray, James W Hurrell, and Clara Deser. North atlantic winter climate regimes: Spatial asymmetry, stationarity with time, and oceanic forcing. *Journal of Climate*, 17(5):1055–1068, 2004.

Lijing Cheng, Kevin E Trenberth, John Fasullo, Tim Boyer, John Abraham, and Jiang Zhu. Improved estimates of ocean heat content from 1960 to 2015. *Science Advances*, 3(3):e1601545, 2017.

Lequan Chi, Christopher LP Wolfe, and Sultan Hameed. Intercomparison of the gulf stream in ocean reanalyses: 1993- 2010. *Ocean Modelling*, 125:1–21, 2018.

CMEMS. Global ocean gridded l4 sea surface heights and derived variables reprocessed (1993-ongoing). *E.U. Copernicus Marine Service Information*, 2020. URL `https://resources.marine.copernicus.eu/?option=com_csw&view=details&product_id=SEALEVEL_GLO_PHY_L4_REP_OBSERVATIONS_008_047`.

Sylvia T Cole, Cimarron Wortham, Eric Kunze, and W Brechner Owens. Eddy stirring and horizontal diffusivity from argo float observations: Geographic and depth variability. *Geophysical Research Letters*, 42(10):3989–3997, 2015.

Alain Colin de Verdière and Michel Ollitrault. A direct determination of the world ocean barotropic circulation. *Journal of Physical Oceanography*, 46(1):255–273, 2016.

Chris Collins. Nor'ida storm, november 12-13, 2009. *National Weather Service*, Jan 2016. URL `https://www.weather.gov/mhx/Nov132009EventReview`.

Stuart A Cunningham, Christopher D Roberts, Eleanor Frajka-Williams, William E Johns, Will Hobbs, Matthew D Palmer, Darren Rayner, David A Smeed, and Gerard McCarthy. Atlantic meridional overturning circulation slowdown cooled the subtropical ocean. *Geophysical Research Letters*, 40(23):6202–6207, 2013.

Maria Valdivieso Da Costa, Herlé Mercier, and Anne Marie Treguier. Effects of the mixed layer time variability on kinematic subduction rate diagnostics. *Journal of physical oceanography*, 35(4):427–443, 2005.

Paolo Davini, Chiara Cagnazzo, Richard Neale, and Joe Tribbia. Coupling between greenland blocking and the north atlantic oscillation pattern. *Geophysical research letters*, 39(14), 2012.

de Boyer Montégut. Surface mixed layer depth. *French Research Institude for Exploration of the Sea*, Jan 2015. URL `http://www.ifremer.fr/cerweb/deboyer/mld/Surface_Mixed_Layer_Depth.php`.

Clément de Boyer Montégut, Gurvan Madec, Albert S. Fischer, Alban Lazar, and Daniele Iudicone. Mixed layer depth over the global ocean: An examination of profile data and a profile-based climatology. *Journal of Geophysical Research: Oceans*, 109(C12):n/a–n/a, 2004. ISSN 2156-2202. doi: 10.1029/2004JC002378. URL `http://dx.doi.org/10.1029/2004JC002378`. C12003.

Dick P Dee, S M Uppala, AJ Simmons, Paul Berrisford, P Poli, S Kobayashi, U Andrae, MA Balmaseda, G Balsamo, d P Bauer, et al. The era-interim reanalysis: Configuration and performance of the data assimilation system. *Quarterly Journal of the royal meteorological society*, 137(656):553–597, 2011.

Damien Desbruyères, Herlé Mercier, Guillaume Maze, and Nathalie Daniault. Surface predictor of overturning circulation and heat content change in the subpolar north atlantic. *Ocean Science*, 15(3):809–817, 2019.

Henry F Diaz and Robert G Quayle. The 1976–77 winter in the contiguous united states in comparison with past records. *Monthly weather review*, 106(10):1393–1421, 1978.

Pedro N DiNezio, Lewis J Gramer, William E Johns, Christopher S Meinen, and Molly O Baringer. Observed interannual variability of the florida current: Wind forcing and the north atlantic oscillation. *Journal of Physical Oceanography*, 39(3): 721–736, 2009.

Shenfu Dong and Kathryn A Kelly. Heat budget in the gulf stream region: The importance of heat storage and advection. *Journal of physical oceanography*, 34(5): 1214–1231, 2004.

Shenfu Dong, Susan L Hautala, and Kathryn A Kelly. Interannual variations in upper-ocean heat content and heat transport convergence in the western north atlantic. *Journal of Physical Oceanography*, 37(11):2682–2697, 2007.

Aurelie Duchez, Damien Desbruyères, Joel JM Hirschi, Eleanor Frajka-Williams, Simon Josey, and Dafydd Gwyn Evans. The tale of a surprisingly cold blob in the north atlantic. *US Clivar Variations*, 14(2):19–23, 2016.

Dafydd Gwyn Evans, John Toole, Gael Forget, Jan D Zika, Alberto C Naveira Garabato, AJ George Nurser, and Lisan Yu. Recent wind-driven variability in atlantic water mass distribution and meridional overturning circulation. *Journal of Physical Oceanography*, 47(3):633–647, 2017.

CW Fairall, Edward F Bradley, JE Hare, AA Grachev, and JB Edson. Bulk parameterization of air–sea fluxes: Updates and verification for the coare algorithm. *Journal of climate*, 16(4):571–591, 2003.

ZHI-FANG FANG. Statistical relationship between the northern hemisphere sea ice and atmospheric circulation during wintertime. In *Observation, Theory and Modeling of Atmospheric Variability: Selected Papers of Nanjing Institute of Meteorology Alumni in Commemoration of Professor Jijia Zhang*, pages 131–141. World Scientific, 2004.

Charlène Feucher, Guillaume Maze, and Herlé Mercier. Subtropical mode waters and permanent pycnocline properties in the world ocean. *Journal of Geophysical Research: Oceans*, February 2019.

Gaël Forget, Guillaume Maze, Martha Buckley, and John Marshall. Estimated seasonal cycle of north atlantic eighteen degree water volume. *Journal of Physical Oceanography*, 41(2):269–286, 2011.

Claude Frankignoul and Klaus Hasselmann. Stochastic climate models, part ii application to sea-surface temperature anomalies and thermocline variability. *Tellus*, 29 (4):289–305, 1977.

Claude Frankignoul, Gaelle de Coëtlogon, Terrence M Joyce, and Shenfu Dong. Gulf stream variability and ocean–atmosphere interactions. *Journal of physical Oceanography*, 31(12):3516–3529, 2001.

Marina Frants, Gillian M Damerell, Sarah T Gille, Karen J Heywood, Jennifer MacKinnon, and Janet Sprintall. An assessment of density-based finescale methods for estimating diapycnal diffusivity in the southern ocean. *Journal of Atmospheric and Oceanic Technology*, 30(11):2647–2661, 2013.

Avijit Gangopadhyay, Peter Cornillon, and D Randolph Watts. A test of the parsons–veronis hypothesis on the separation of the gulf stream. *Journal of Physical Oceanography*, 22(11):1286–1301, 1992.

Simon A Good, Matthew J Martin, and Nick A Rayner. En4: Quality controlled ocean temperature and salinity profiles and monthly objective analyses with uncertainty estimates. *Journal of Geophysical Research: Oceans*, 118(12):6704–6716, 2013.

Jeremy P Grist, Simon A Josey, Zoe L Jacobs, Robert Marsh, Bablu Sinha, and Erik Van Sebille. Extreme air–sea interaction over the north atlantic subpolar gyre during the winter of 2013–2014 and its sub-surface legacy. *Climate dynamics*, 46 (11-12):4027–4045, 2016.

Sjoerd Groeskamp, Joseph H LaCasce, Trevor J McDougall, and Marine Rogé. Full-depth global estimates of ocean mesoscale eddy mixing from observations and theory. *Geophysical Research Letters*, page e2020GL089425, 2020.

Anselm Grötzner, Mojib Latif, and Timothy P Barnett. A decadal climate cycle in the north atlantic ocean as simulated by the echo coupled gcm. *Journal of Climate*, 11(5):831–847, 1998.

Sergey K Gulev, Thomas Jung, and Eberhard Ruprecht. Climatology and interannual variability in the intensity of synoptic-scale processes in the north atlantic from the ncep–ncar reanalysis data. *Journal of Climate*, 15(8):809–828, 2002.

Sirpa Häkkinen, Peter B Rhines, and Denise L Worthen. Northern north atlantic sea surface height and ocean heat content variability. *Journal of Geophysical Research: Oceans*, 118(7):3670–3678, 2013.

Edward Hanna, Julie M Jones, John Cappelen, Sebastian H Mernild, Len Wood, Konrad Steffen, and Philippe Huybrechts. The influence of north atlantic atmospheric and oceanic forcing effects on 1900–2010 greenland summer climate and ice melt/runoff. *International Journal of Climatology*, 33(4):862–880, 2013.

Edward Hanna, Xavier Fettweis, Sebastian H Mernild, John Cappelen, Mads H Ribergaard, Christopher A Shuman, Konrad Steffen, Len Wood, and Thomas L Mote.

Atmospheric and oceanic climate forcing of the exceptional greenland ice sheet surface melt in summer 2012. *International Journal of Climatology*, 34(4):1022–1037, 2014.

MW Hecht and RD Smith. Towards a physical understanding of the north atlantic. *Ocean Modeling in an Eddying Regime*, 2009.

Steven Herbette, Yves Morel, and Michel Arhan. Subduction of a surface vortex under an outcropping front. *Journal of physical oceanography*, 34(7):1610–1627, 2004.

Andrew Horvitz. February 2010: Snowmageddon, blizzard of 2010 winter: Unprecedented snowfall impacts region. *PREcipitation Summary and Temperature Observations For the Washington, DC and Baltimore, MD Area (PRESTO)*, 2010. URL `https://www.weather.gov/media/publications/presto/2010feb.pdf`.

Rui Xin Huang. On the three-dimensional structure of the wind-driven circulation in the north atlantic. *Dynamics of Atmospheres and Oceans*, 15(1-2):117–159, 1990.

James W Hurrell et al. Decadal trends in the north atlantic oscillation: regional temperatures and precipitation. *Science-AAAS-Weekly Paper Edition*, 269(5224): 676–678, 1995.

David D Jackson. The use of a priori data to resolve non-uniqueness in linear inversion. *Geophysical Journal International*, 57(1):137–157, 1979.

IN James and PM James. Ultra-low-frequency variability in a simple atmospheric circulation model. *Nature*, 342(6245):53–55, 1989.

William J Jenkins and JENKINS WJ. On the climate of a subtropical ocean gyre: decade time scale variations in water mass renewal in the sargasso sea. 1982.

Simon A Josey, Joel J-M Hirschi, Bablu Sinha, Aurelie Duchez, Jeremy P Grist, and Robert Marsh. The recent atlantic cold anomaly: Causes, consequences, and related phenomena. *Annual Review of Marine Science*, 10:475–501, 2018.

Terrence M Joyce. New perspectives on eighteen-degree water formation in the north atlantic. In *New Developments in Mode-Water Research*, pages 41–48. Springer, 2011.

Terrence M Joyce, Clara Deser, and Michael A Spall. The relation between decadal variability of subtropical mode water and the north atlantic oscillation. *Journal of Climate*, 13(14):2550–2569, 2000.

Terrence M Joyce, Leif N Thomas, and Frank Bahr. Wintertime observations of subtropical mode water formation within the gulf stream. *Geophysical research letters*, 36(2), 2009.

Terrence M Joyce, Young-Oh Kwon, Hyodae Seo, and Caroline C Ummenhofer. Meridional gulf stream shifts can influence wintertime variability in the north atlantic storm track and greenland blocking. *Geophysical Research Letters*, 46(3): 1702–1708, 2019.

Eugenia Kalnay, Masao Kanamitsu, Robert Kistler, William Collins, Dennis Deaven, Lev Gandin, Mark Iredell, Suranjana Saha, Glenn White, John Woollen, et al. The ncep/ncar 40-year reanalysis project. *Bulletin of the American meteorological Society*, 77(3):437–472, 1996.

Dujuan Kang and Enrique N Curchitser. Gulf stream eddy characteristics in a high-resolution ocean model. *Journal of Geophysical Research: Oceans*, 118(9):4474–4487, 2013.

Kathryn A Kelly and Shenfu Dong. The contributions of atmosphere and ocean to north atlantic subtropical mode water volume anomalies. *Deep Sea Research Part II: Topical Studies in Oceanography*, 91:111–127, 2013.

Kathryn A Kelly, Michael J Caruso, Sandipa Singh, and Bo Qiu. Observations of atmosphere-ocean coupling in midlatitude western boundary currents. *Journal of Geophysical Research: Oceans*, 101(C3):6295–6312, 1996.

Kathryn A Kelly, R Justin Small, RM Samelson, Bo Qiu, Terrence M Joyce, Young-Oh Kwon, and Meghan F Cronin. Western boundary currents and frontal air–sea interaction: Gulf stream and kuroshio extension. *Journal of Climate*, 23(21):5644–5667, 2010.

Birgit Klein and Nelson Hogg. On the variability of 18 degree water formation as observed from moored instruments at 55 w. *Deep Sea Research Part I: Oceanographic Research Papers*, 43(11-12):1777–1806, 1996.

Nicolas Kolodziejczyk, Annaig Prigent-Mazella, and Fabienne Gaillard. Isas-15 temperature and salinity gridded fields. *SEANOE, http://doi.org/10.17882/52367*, 10: 52367, 2017.

Young-Oh Kwon and Stephen C Riser. North atlantic subtropical mode water: A history of ocean-atmosphere interaction 1961–2000. *Geophysical research letters*, 31(19), 2004.

Mojib Latif and Timothy P Barnett. Causes of decadal climate variability over the north pacific and north america. *Science*, 266(5185):634–637, 1994.

Naomi Marcil Levine, Scott C Doney, Ivan Lima, Rik Wanninkhof, Nicholas R Bates, and Richard A Feely. The impact of the north atlantic oscillation on the uptake and accumulation of anthropogenic co2 by north atlantic ocean mode waters. *Global Biogeochemical Cycles*, 25(3), 2011.

S Levitus. Climatological atlas of the world ocean. noaa prof. paper 13. *Washington, DC: US Government Printing Office*, 1982.

Xinfeng Liang, Michael Spall, and Carl Wunsch. Global ocean vertical velocity from a dynamically consistent ocean state estimate. *Journal of Geophysical Research: Oceans*, 122(10):8208–8224, 2017.

Margarida LR Liberato. The 19 january 2013 windstorm over the north atlantic: large-scale dynamics and impacts on iberia. *Weather and Climate Extremes*, 5: 16–28, 2014.

John L Lillibridge III and Arthur J Mariano. A statistical analysis of gulf stream variability from 18+ years of altimetry data. *Deep Sea Research Part II: Topical Studies in Oceanography*, 85:127–146, 2013.

Ling Ling Liu and Rui Xin Huang. The global subduction/obduction rates: Their interannual and decadal variability. *Journal of Climate*, 25(4):1096–1115, 2012.

Ian Livingston and Kevin Ambrose. Second blizzard of february 2010, snoverkill: A frigid and windy finale to the snowiest winter on record. *The Washington Post*, Feb 2015. URL `https://goo.gl/fZqCsf`.

Susan Lozier, Laifang Li, and Feili Li. The north atlantic "cold blob": an alternate explanation. *European Geophysical Union*, 2019. URL `https://meetingorganizer.copernicus.org/EGU2019/EGU2019-3412.pdf`.

CR Mann. The termination of the gulf stream and the beginning of the north atlantic current. In *Deep Sea Research and Oceanographic Abstracts*, volume 14, pages 337–359. Elsevier, 1967.

Robert Marsh and Adrian L New. Modeling 18 water variability. *Journal of physical oceanography*, 26(6):1059–1080, 1996.

J Marshall, Raffaele Ferrari, G Forget, G Maze, A Andersson, N Bates, W Dewar, S Doney, D Fratantoni, T Joyce, et al. The climode field campaign: Observing

the cycle of convection and restratification over the gulf stream. *Bulletin of the American Meteorological Society*, 90(9):1337–1350, 2009.

John Marshall, Daniel Jamous, and Johan Nilsson. Entry, flux, and exit of potential vorticity in ocean circulation. *Journal of physical oceanography*, 31(3):777–789, 2001.

John C Marshall and AJ George Nurser. A continuously stratified thermocline model incorporating a mixed layer of variable thickness and density. *Journal of physical oceanography*, 21(12):1780–1792, 1991.

John C Marshall and AJ George Nurser. Fluid dynamics of oceanic thermocline ventilation. *Journal of physical oceanography*, 22(6):583–595, 1992.

John C Marshall, Richard G Williams, and AJ George Nurser. Inferring the subduction rate and period over the north atlantic. *Journal of Physical Oceanography*, 23 (7):1315–1329, 1993.

Jonathan E Martin. The virtical circulation at fronts. In *Mid-latitude atmospheric dynamics: a first course*, chapter 7. John Wiley & Sons, 2013.

Guillaume Maze and John Marshall. Diagnosing the observed seasonal cycle of atlantic subtropical mode water using potential vorticity and its attendant theorems. *Journal of Physical Oceanography*, 41(10):1986–1999, 2011.

Guillaume Maze, Gael Forget, Martha Buckley, John Marshall, and Ivana Cerovecki. Using transformation and formation maps to study the role of air–sea heat fluxes in north atlantic eighteen degree water formation. *Journal of Physical Oceanography*, 39(8):1818–1835, 2009.

Guillaume Maze, Herlé Mercier, Virginie Thierry, Laurent Memery, Pascal Morin, and Fiz F Pérez. Mass, nutrient and oxygen budgets for the northeastern atlantic ocean. *Biogeosciences*, 9(10):4099–4113, 2012.

Guillaume Maze, Julie Deshayes, John Marshall, Anne-Marie Tréguier, Alexandre Chronis, and Lukas Vollmer. Surface vertical pv fluxes and subtropical mode water formation in an eddy-resolving numerical simulation. *Deep Sea Research Part II: Topical Studies in Oceanography*, 91:128–138, 2013.

Gerard McCarthy, E Frajka-Williams, William E Johns, MO Baringer, CS Meinen, HL Bryden, D Rayner, A Duchez, C Roberts, and SA Cunningham. Observed interannual variability of the atlantic meridional overturning circulation at 26.5 n. *Geophysical Research Letters*, 39(19), 2012.

Herlé Mercier. Determining the general circulation of the ocean: a nonlinear inverse problem. *Journal of Geophysical Research: Oceans*, 91(C4):5103–5109, 1986.

Met Office. October 2004. *Met Office*, Feb 2013. URL `https://www.metoffice.gov.uk/climate/uk/summaries/2004/october`.

Paul-Antoine Michelangeli, Robert Vautard, and Bernard Legras. Weather regimes: Recurrence and quasi stationarity. *Journal of the atmospheric sciences*, 52(8): 1237–1256, 1995.

NOAA. State of the climate: National snow & ice for january 2010. *NOAA National Centers for Environmental Information*, February 2010. URL `https://www.ncdc.noaa.gov/sotc/snow/201001`.

NWS. St. patrick's day nor'easter 16-17 march 2007. *National Weather Service*, Mar 2007. URL `https://www.weather.gov/media/btv/events/StPatricks07.pdf`.

NWS. Winter storm summary for february 25, 2010 to february 26, 2010 event. *National Weather Service*, Apr 2014a. URL `https://www.weather.gov/phi/02252010wss`.

NWS. Winter storm summary for january 22, 2005 to january 23, 2005 event. *National Weather Service*, Mar 2014b. URL `https://www.weather.gov/phi/01222005wss`.

NWS. Winter storm summary for december 19, 2009 to december 20, 2009 event, philadelphia/mt holly. *National Weather Service*, Apr 2014c. URL `https://www.weather.gov/phi/12192009wss`.

NWS. Winter storm summary for february 28, 2005 to march 1, 2005. *National Weather Service*, Mar 2014d. URL `https://www.weather.gov/phi/02282005wss`.

NWS. December 19-20, 2012 blizzard. *National Weather Service*, Mar 2015a. URL `https://www.weather.gov/dmx/dec20blizzard`.

NWS. Historic ice storm of january 12-14, 2007. *National Weather Service*, Mar 2015b. URL `https://www.weather.gov/sgf/events_2007jan12`.

NWS. Blizzard / winter storm of december 10-12, 2010. *National Weather Service*, Feb 2015c. URL `https://www.weather.gov/arx/dec1110`.

NWS. December 20, 2012 blizzard. *National Weather Service*, Aug 2016a. URL `https://www.weather.gov/dvn/Blizzard2012Recap`.

NWS. Dc winters: Snow, wind, ice and cold. *National Weather Service*, Feb 2016b. URL https://www.weather.gov/lwx/winter_DC-Winters.

NWS. December 26-27th 2010 blizzard. *National Weather Service*, Oct 2016c. URL https://www.weather.gov/okx/storm12262010.

NWS. Winter storm of march 02 to 03, 2018. *National Weather Service*, Mar 2018. URL https://www.weather.gov/bgm/pastwintermarch022018.

NWS. February 25, 2013 blizzard. *National Weather Service*, 2019. URL https://www.weather.gov/ama/feb25blizzard.

OACP-Argo. Argo, mean structure of the north atlantic subtropical permanent pycnocline. *IFREMER/LOPS*, 2020. URL http://www.ifremer.fr/erddap/tabledap/OACP-Argo.graph.

Otto. March 19-21, 2006 - major winter storm: Plains to midwest, Mar 2006. URL https://www.wpc.ncep.noaa.gov/winter_storm_summaries/2006/storm11/storm11_archive.shtml.

Jérôme Paillet and Herlé Mercier. An inverse model of the eastern north atlantic general circulation and thermocline ventilation. *Deep Sea Research Part I: Oceanographic Research Papers*, 44(8):1293–1328, 1997.

Richard J. Pasch and Todd B. Kimberlain. Tropical cyclone report: Hurricane tomas. *National Hurricane Center*, March 2011. URL https://www.nhc.noaa.gov/data/tcr/AL212010_Tomas.pdf.

Joseph Pedlosky and Paul Robbins. The role of finite mixed-layer thickness in the structure of the ventilated thermocline. *Journal of physical oceanography*, 21(7):1018–1031, 1991.

Ge Peng, Eric P Chassignet, Young-Oh Kwon, and Stephen C Riser. Investigation of variability of the north atlantic subtropical mode water using profiling float data and numerical model output. *Ocean Modelling*, 13(1):65–85, 2006.

Frank Pereira. Thanksgiving week 2010 arctic outbreak and storms. *Storm Summaries*, Mar 2011. URL https://www.wpc.ncep.noaa.gov/storm_summaries/event_reviews/2010/Thanksgiving2010.pdf.

Tillys Petit, Herlé Mercier, and Virginie Thierry. First direct estimates of volume and water mass transports across the reykjanes ridge. *Journal of Geophysical Research: Oceans*, 123(9):6703–6719, 2018.

Anthony David Phillips. The north american blizzard of 2009: A synoptic review. 2011.

Anne Piron, Virginie Thierry, Herlé Mercier, and Guy Caniaux. Gyre-scale deep convection in the subpolar north atlantic ocean during winter 2014–2015. *Geophysical Research Letters*, 44(3):1439–1447, 2017.

Bo Qiu and Rui Xin Huang. Ventilation of the north atlantic and north pacific: subduction versus obduction. *Journal of Physical Oceanography*, 25(10):2374–2390, 1995.

Tangdong Qu, Linlin Zhang, and Niklas Schneider. North atlantic subtropical underwater and its year-to-year variability in annual subduction rate during the argo period. *Journal of Physical Oceanography*, 46(6):1901–1916, 2016.

Stefan Rahmstorf, Jason E Box, Georg Feulner, Michael E Mann, Alexander Robinson, Scott Rutherford, and Erik J Schaffernicht. Exceptional twentieth-century slowdown in atlantic ocean overturning circulation. *Nature climate change*, 5(5): 475, 2015.

Monika Rhein, Stephen Rintoul, Shigeru Aoki, Edmo Campos, Don Chambers, Richard Feely, Sergey Gulev, Gregory Johnson, Simon Josey, Andrey Kostianoy, Cecilie Mauritzen, Dean Roemmich, Lynne Talley, and Fan Wang. Observations: Ocean, ipcc chapter 3. *IPCC*, 2018. URL `https://www.ipcc.ch/report/ar5/wg1/observations-ocean/`.

MH Rio. A new mean dynamic topography computed over the global ocean from grace data, altimetry and in situ measurements. In *Poster communication at OceanObs09 symposium, 21-25 September 2009, Venice*, 2009.

Jon Robson, Pablo Ortega, and Rowan Sutton. A reversal of climatic trends in the north atlantic since 2005. *Nature Geoscience*, 9(7):513, 2016.

Dean Roemmich and John Gilson. The 2004–2008 mean and annual cycle of temperature, salinity, and steric height in the global ocean from the argo program. *Progress in oceanography*, 82(2):81–100, 2009.

Dean Roemmich, O Boebel, H Freeland, B King, PY LeTraon, R Molinari, WB Owens, SC RISER, U Send, K Takeuchi, et al. On the design and implementation of argo-a global array of profiling floats. *Argo Science Team*, 1999.

T Rossby and E Gottlieb. The oleander project: Monitoring the variability of the gulf stream and adjacent waters between new jersey and bermuda. *Bulletin of the American Meteorological Society*, 79(1):5–18, 1998.

Michael S Ryan, Mary Beth Gerhardt, David Hamrick, Paul J Kocin, Kwan-Yin Kong, Richard Otto, Frank J Pereira, and Brendon Rubin-Oster. Major winter weather events during the 2012-2013 cold season.

Dan Seidov, Alexey Mishonov, James Reagan, and Rost Parsons. Eddy-resolving in situ ocean climatologies of temperature and salinity in the northwest atlantic ocean. *Journal of Geophysical Research: Oceans*, 2018.

Richard D Smith, Mathew E Maltrud, Frank O Bryan, and Matthew W Hecht. Numerical simulation of the north atlantic ocean at 1/10. *Journal of Physical oceanography*, 30(7):1532–1561, 2000.

Kevin Speer and Gael Forget. 3.5 global distribution and formation of mode waters. 2013.

Detlef Stammer, Carl Wunsch, R Giering, C Eckert, P Heimbach, Jochem Marotzke, A Adcroft, CN Hill, and J Marshall. Global ocean circulation during 1992–1997, estimated from ocean observations and a general circulation model. *Journal of Geophysical Research: Oceans*, 107(C9):1–1, 2002.

Samuel W Stevens, Rodney J Johnson, Guillaume Maze, and Nicholas R Bates. A recent decline in north atlantic subtropical mode water formation. *Nature Climate Change*, 10(4):335–341, 2020.

Henry Stommel. Determination of water mass properties of water pumped down from the ekman layer to the geostrophic flow below. *Proceedings of the National Academy of Sciences*, 76(7):3051–3055, 1979.

Shusaku Sugimoto, Kimio Hanawa, Tomowo Watanabe, Toshio Suga, and Shang-Ping Xie. Enhanced warming of the subtropical mode water in the north pacific and north atlantic. *Nature Climate Change*, 7(9):656, 2017.

Arnold H Taylor and John A Stephens. The north atlantic oscillation and the latitude of the gulf stream. *Tellus A: Dynamic Meteorology and Oceanography*, 50(1):134–142, 1998.

The Ring Group. Gulf stream cold-core rings: Their physics, chemistry, and biology. *Science*, pages 1091–1100, 1981.

Leif N Thomas. Destruction of potential vorticity by winds. *Journal of physical oceanography*, 35(12):2457–2466, 2005.

Leif N Thomas and Terrence M Joyce. Subduction on the northern and southern flanks of the gulf stream. *Journal of physical oceanography*, 40(2):429–438, 2010.

Leif N Thomas and Craig M Lee. Intensification of ocean fronts by down-front winds. *Journal of Physical Oceanography*, 35(6):1086–1102, 2005.

Leif N Thomas, John R Taylor, Raffaele Ferrari, and Terrence M Joyce. Symmetric instability in the gulf stream. *Deep Sea Research Part II: Topical Studies in Oceanography*, 91:96–110, 2013.

Anne-Marie Tréguier, Julie Deshayes, Camille Lique, Raphaël Dussin, and Jean-Marc Molines. Eddy contributions to the meridional transport of salt in the north atlantic. *Journal of Geophysical Research: Oceans*, 117(C5), 2012.

Anne-Marie Tréguier, Camille Lique, Julie Deshayes, and Jean-Marc Molines. The north atlantic eddy heat transport and its relation with the vertical tilting of the gulf stream axis. *Journal of Physical Oceanography*, 47(6):1281–1289, 2017.

Frédéric Vivier, Kathryn A Kelly, and Lu Anne Thompson. Heat budget in the kuroshio extension region: 1993–99. *Journal of physical oceanography*, 32(12):3436–3454, 2002.

Gösta Walin. On the relation between sea-surface heat flow and thermal circulation in the ocean. *Tellus*, 34(2):187–195, 1982.

Bruce A Warren. Insensitivity of subtropical mode water characteristics to meteorological fluctuations. In *Deep Sea Research and Oceanographic Abstracts*, volume 19, pages 1–19. Elsevier, 1972.

CB Whalen, LD Talley, and JA MacKinnon. Spatial and temporal variability of global ocean mixing inferred from argo profiles. *Geophysical Research Letters*, 39 (18), 2012.

RG Williams. Ocean subduction. *Management*, 25(1), 2001.

Richard G Williams. The influence of air–sea interaction on the ventilated thermocline. *Journal of Physical Oceanography*, 19(9):1255–1267, 1989.

Richard G Williams. The role of the mixed layer in setting the potential vorticity of the main thermocline. *Journal of Physical Oceanography*, 21(12):1803–1814, 1991.

Richard G Williams, John C Marshall, and Michael A Spall. Does stommel's mixed layer "demon" work? *Journal of Physical Oceanography*, 25(12):3089–3102, 1995.

LV Worthington. On the north atlantic circulation. the johns hopkins oceanographic studies, number 6, 1976.

LV Worthington. Intensification of the gulf stream after the winter of 1976-77. *Nature*, 270(5636):415–417, 1977.

Igor Yashayaev. Hydrographic changes in the labrador sea, 1960–2005. *Progress in Oceanography*, 73(3):242–276, 2007.

L Yu and RA Weller. Objectively analyzed air-sea heat fluxes for the global ice-free oceans (1981–2005), b. am. meteorol. soc., 88, 527–539, doi: 10.1175. Technical report, BAMS-88-4-527, 2007.

Xubin Zeng, Ming Zhao, and Robert E Dickinson. Intercomparison of bulk aerodynamic algorithms for the computation of sea surface fluxes using toga coare and tao data. *Journal of Climate*, 11(10):2628–2644, 1998.

Patricia Zunino, Herlé Mercier, and Thierry Virginie. Why did deep convection persist over four consecutive winters (2015-2018) southeast of cape farewell? 2019.

DOCTORAT SCIENCES BRETAGNE DE LA MER LOIRE ET DU LITTORAL

UBO Université de Bretagne Occidentale

Titre: Le transport d'Ekman comme déclencheur des extrêmes de formation de l'Eau Modale à 18 degrés aux échelles de temps interannuelles

Resumé: La gyre subtropical de l'Atlantique Nord montre depuis 1970 une tendance au réchauffement. Cette tendance se superpose à une variabilité interannuelle intense, mais dont les mécanismes ne sont pas encore bien connus, en particulier, à l'égard des évènements extrêmes hivernaux. Dans cette thèse, nous avons développé, sur la base d'observations, un bilan de chaleur océanique, au-dessus de 800 m dans la région ouest subtropicale de l'Atlantique Nord, une région où la chaleur est presque entièrement stockée dans l'Eau Modale à 18°C (Eighteen Degree Water, EDW).

A l'échelle de temps interannuelle, la variabilité de l'advection géostrophique est presqu'entièrement contrôlée par le Gulf Stream, qui est le facteur dominant de la variabilité du contenu de chaleur océanique, 2,5 fois plus important que l'advection d'Ekman, et presque 4 fois plus que les flux de chaleur de surface (mais qui dominent dans le cycle saisonnier). En revanche, le volume d'EDW ventilé en hiver est anti-corrélé aux anomalies de contenu de chaleur en 2008, 2013 et 2015. Nous avons montré que l'advection d'Ekman est le meilleur indicateur de ces occurrences d'extrêmes, grâce à un processus de divergence qui favorise l'approfondissement de la couche de mélange et donc la ventilation de l'EDW. De plus, nous avons montré les liens entre la distribution spatiale de cet indicateur et les tempêtes atmosphériques: l'intensité et la durée des tempêtes hivernales jouent toutes deux un rôle dans la ventilation de l'EDW des années extrêmes.

Title: Ekman transport: a trigger of interannual extreme formation rates of Eighteen Degree Water

Key words: weather regimes, ocean stratification, subtropical gyre, Ekman current, North Atlantic subtropical mode water, Argo floats

Abstract: The North Atlantic subtropical gyre was shown to have experienced warming since 1970s. But this trend sits on top of a large interannual variability driven by mechanisms that are yet to be clarified, especially with regard to extreme winter events. In this research, we developed an observation-based ocean heat budget of the upper 800 m in the western subtropical North Atlantic, a region where heat is mostly stored in the Eighteen Degree mode Water (EDW).

In interannual time scale, the variability of geostrophic advection, mostly driven by the Gulf Stream, is the most dominant factor to that of the ocean heat content (OHC) variability, 2.5 times as large as that of Ekman advection and almost four times as large as that of surface heat loss (which dominates at the seasonal cycle only). However, the annually ventilated EDW exhibits extreme values in 2008, 2013, and 2015 that correspond to opposite OHC anomalies. We will show that Ekman advection is the best indicator and driving mechanism explaining these extreme occurrences. We have further shown that such extreme Ekman advection patterns can be linked to large scale atmospheric weather storms and that both storm intensity and duration have an impact on the extreme of EDW ventilation and that of the heat content in the western subtropical North Atlantic.